THÈSE

En vue de l'obtention du

DOCTORAT DE L'UNIVERSITÉ DE TOULOUSE

Délivré par : *l'Université Toulouse 3 Paul Sabatier (UT3 Paul Sabatier)*

Présentée et soutenue le *12/10/2016* **par :**

YOUNES MONJID

Concept de corrélation dans l'espace fréquentiel de Fourier pour la télédection passive de la Terre: Application à la mission SMOS-Next

---

JURY

YANN H. KERR	Ingénieur CESBIO	Directeur de thèse
BERNARD ROUGÉ	Ingénieur CMLA/CESBIO	Co-directeur de thèse
FRANÇOIS MALGOUYRES	Professeur UPS	Président du Jury
ANDRÉS ALMANSA	Professeur Paris Descartes	Rapporteur
JEAN-PIERRE WIGNERON	Chercheur INRA	Rapporteur
DIDIER MASSONNET	Ingénieur CNES	Examinateur

École doctorale et spécialité :
SDU2E : Océan, Atmosphère et Surfaces Continentales
Unité de Recherche :
CESBIO
Directeur(s) de Thèse :
Yann H. Kerr et *Bernard Rougé*
Rapporteurs :
Andrés Almansa et *Jean-Pierre Wigneron*

Résumé

La *synthèse d'ouverture* est une technique interférométrique similaire à la synthèse par rotation de la terre utilisée en radioastronomie où les signaux reçus par une paire de petites antennes sont traités de telle manière à synthétiser une seule grande antenne [1]. Le concept de synthèse d'ouverture a été réadapté pour l'observation de la terre dans le cas de la télédétection de sources étendues de température. L'utilisation de cette technique pour l'observation de la terre a permis de contourner les limitations sur la taille d'antenne en télédétection passive [2].

La fonction de corrélation, ou de visibilité, obtenue en inter-corrélant les signaux reçus par les antennes d'un système interférométrique employant une synthèse d'ouverture est définie comme étant la transformée de Fourier de la carte des *températures de brillance* de la scène observée. Cette relation est connue sous le nom du théorème de *Van Cittert–Zernike* pour des observateurs en repos par rapport aux sources de température. La forme classique de ce théorème a été dérivée en inter-corrélant les échantillons temporels instantanés du champ électrique mesurés par différentes antennes [3].

Un nouveau concept basé une **interférométrie spatio-temporelle** passive a été proposé comme étant la nouvelle génération qui succédera à la mission SMOS (Soil Moisture and Ocean Salinity) opérant dans l'espace depuis Novembre 2009 [4]. Celui-ci a pour objectif principal l'amélioration de la résolution spatiale à des ordres pouvant répondre aux applications hydrologiques à l'échelle locale où des résolutions kilométriques sont exigées [5].

Ce concept interférométrique se base sur l'idée d'intégrer le déplacement de l'observateur (l'antenne) et ainsi la variable temps dans le calcul de la fonction de corrélation. Ceci engendre la création de nouvelles lignes de base virtuelles entre les positions des antennes à des instants différents, en plus des lignes de base physiques formées entres les positions des antennes instantanées. L'étude de ce concept de corrélation a malheureusement démontré la suppression exacte de l'information additionnelle due aux lignes de base virtuelles par le *décalage Doppler* induit par le déplacement [6].

Une seconde étude du concept d'interférométrie spatio-temporelle combinée à une nouvelle procédure d'imagerie par **corrélation dans l'espace fréquentiel**, accomplie en inter-corrélant les spectres fréquentiels des champs électriques mesurés par une paire d'antennes séparées d'une distance Δr à bord d'un satellite à une hauteur h, a démontré l'obtention d'une information en 2D en températures de brillance de la scène observée [7]. En plus, le développement théorique de la fonction de corrélation a mis en évidence une relation liant les visibilités aux températures de brillance par l'intermédiaire d'un noyau hautement oscillatoire.

L'élément nouveau apporté par la corrélation dans l'espace fréquentiel consiste à exploiter l'information de corrélation acquise par les antennes du satellite pour des fréquences présentant de petites différences et pas seulement l'auto-corrélation. Cette propriété permet une reconstruction en 2D des températures de brillance avec seulement deux antennes.

Dans le cadre des travaux de cette thèse, la méthode de corrélation dans l'espace fréquentiel a été, dans un premier temps, théoriquement testée par la reconstruction de l'image d'un point source. On obtient des résolutions géométriques de l'ordre de $hc/(\Delta r \omega_0)$ ($\sim$ quelques kms) dans les deux directions, avec c la vitesse de la lumière et ω_0 la fréquence centrale, en utilisant une paire d'antennes espacée d'une

centaine de mètres. Quant à la sensibilité radiométrique, une valeur de l'unité a été mise en évidence par simulation.

Dans un deuxième temps, l'évaluation numérique du concept, intégralement développée au cours de cette thèse, a nécessité l'introduction de plusieurs méthodes de simplification, notamment les méthodes numériques d'inversion des noyaux fortement oscillants, pour ainsi permettre de contourner le besoin d'un grand effort de calcul pour l'implémentation des quantités physiques en bande L (1.4 GHz). Ceci a conduit au développement de plusieurs versions d'un processeur numérique pour la reconstruction des températures et la dérivation des paramètres fonctionnels d'intérêt, et par conséquent à la validation numérique des propriétés du concept de corrélation en fréquentiel.

Abstract

Aperture synthesis is an interferometric technique similar to Earth rotation synthesis employed in radio astronomy in which the signals received by a pair of small antennas are processed in a way to synthesize a single large antenna [1]. The aperture synthetic concept used in radioastronomy was readapted to Earth remote sensing for large thermal sources. Thanks to this technique, limitations on antenna size in passive microwave remote sensing have been overcome [2].

The correlation, or visibility, function obtained by cross-correlating the signals received by the antennas of an interferometric system using aperture synthesis is linked to the *brightness temperature* map of the observed scene by means of a Fourier-transform law. This is know as the standard form of the *Van Cittert–Zernike* theorem for fixed observers with respect to sources of temperature [3]. This standard formulation is derived by cross-correlating the instantaneous temporal components of the measured electric fields by different antennas.

A new concept based on a passive **spatio-temporal interferometry** was proposed as the new generation to follow the well-known SMOS (Soil Moisture and Ocean Salinity) mission successfully operating since November 2, 2009 [4]. The aim of the proposed concept is a jump in the current achieved geometric resolution to orders capable of meeting the stringent users' needs for the study of hydrological applications in the local scale where sub-kilometric resolutions are required [5].

This interferometric concept is based on the idea of integrating the displacement of the observer (satellite's antenna), and hence the time variable, in the calculation of the correlation function, which yields the creation of virtual baselines between the positions of antennas at different instants, in addition to the physical ones formed between the instantaneous antennas' spatial positions. Sadly, the additional information due to the virtual baseline was shown to be exactly canceled by the induced *Doppler shift* due to the observer's motion [6].

We show furthermore that when using the aforementioned spatio-temporal interferometric system combined with a revolutionary **Fourier Correlation Imaging** (FouCoIm) procedure, consisting in cross-correlating, at slightly different frequencies, the Fourier components of the fluctuations of the received electric fields by a pair of antennas separated by a distance Δr on board of a satellite flying at height h, the 2D position-dependent brightness temperature can be reconstructed [7]. Besides, the analytical derivation of the correlation function gives rise to a relationship linking the measured correlations to the position-dependent brightness temperatures by means of a Highly Oscillatory Integral (HOI) kernel.

Interestingly, the analytical study of the HOI kernel showed the remarkable property that a correlation between both antenna-signals remains within a small frequency interval (different frequencies) outside the simple auto-correlation (same frequency). As a matter of fact, while existing systems had, until now, only considered the simple 1D information contained in the auto-correlation, it appears that the resulting correlation function from this concept bears a 2D information for the measurement of the position-dependent brightness temperature. Based on this, one is capable of reconstructing 2D brightness temperatures starting from a simple 1D geometry (two antennas arranged perpendicularly to the flight direction).

On one hand, we theoretically test this method of FouCoIm by reconstructing the image of a single point-like source. Based on this, we arrive, at a first estimation, to a spatial resolution of the order of $hc/(\Delta r \omega_0)$ ($\sim$ few kms), where c refers to the speed of light and ω_0 to the central frequency, using a pair of antennas separated by a distance of 100 m. A first theoretical calculation of the radiometric sensitivity verified by simulation yielded a value of unity and a study of a possible amelioration of the latter using an array of antennas is to be conducted.

On the other hand, the numerical evaluation of the FouCoIm, entirely derived in the framework of this thesis, required the introduction of several simplification approaches, particularly the use of highly oscillatory quadrature methods, in a way to bypass the needed high computational effort for the implementation of the physical quantities in the L-band (1.4 GHz). Based on these approaches, we developed different versions of a numerical processor for the reconstruction of temperatures and the derivation of the functional parameters, which therefore allowed the numerical validation of the concept's properties.

Bibliography

[1] A. R. Thompson, J. M. Moran, and G. W. Swenson, "Interferometry and Synthesis in Radio Astronomy," New York: Wiley, 1986.

[2] David M. Le Vine, "The sensitivity of synthetic aperture radiometers for remote sensing applications from space," *Radio Sci.*, vol. 25, no. 4, pp. 441-453, 1990.

[3] I. Corbella, N. Duffo, M. Vall-llossera, A. Camps, "The visibility function in interferometric aperture synthesis radiometry," *IEEE Transaction on Geoscience and Remote Sensing*, vol. 42, No. 8, pp. 1677-1682, ISSN: 0278-0062.

[4] Y.H. Kerr, P. Waldteufel, J.-P. Wigneron, S. Delwart, F. Cabot, J. Boutin, M. J. Escorihuela, J. Font, N. Reul, C. Gruhier, and al. "The SMOS mission: new tool for monitoring key elements of the global water cycle," *IEEE, Institute of Electrical and Electronics Engineers*, 2010, 98 (5), pp. 666-687.

[5] Marc F. P. Blerkens, "Global hydrology 2015: State, trends, and directions," *AGU Publications: Water Resources Research*, 17 Jul, 2015.

[6] D. Braun, Y. Monjid, B. Rougé, and Y. Kerr, "Generalization of the Van Cittert-Zernike theorem: observers moving with respect to sources," *Measurement and Science Technology*, November, 2015.

[7] D. Braun, "Fourier Correlation Imaging," Unpublished, 2012.

à ma famille, pour n'avoir jamais cessé de me soutenir et de croire en moi, et d'avoir su m'apporter le réconfort et le soutien les moments difficiles, je leur dois tout,

à Bernard Rougé, mon directeur de thèse au quotidien, pour sa disponibilité, son inébranlable soutien, ses longues discussions, sa capacité à prendre les bonnes décisions, d'avoir su d'une manière parfois forte me pousser à donner le meilleur de moi-même, ..., je lui dois énormément,

à Yann Kerr, mon directeur de thèse, pour sa présence, son soutien, ses sages conseils, son cadrage, et plein d'autres choses ...,

à Daniel Braun, pour sa superbe collaboration et implication dans les travaux, ses précieux conseils, et sa stricte approche scientifique,

à Ali Khazaal et Ahmad Al Bitar, pour leurs longues conversations et précieuses aides,

à Marie Parrens, d'avoir été une merveilleuse collègue de bureau,

à François, Eric, Christophe, Philippe, Arnaud, Delphine, Ali, Beatriz, à tout membre du CESBIO et plus particulièrement de l'équipe SMOS,

à tous ceux qui ont contribué de près ou de loin à ce travail.

Contents

List of Figures

List of Tables

Introduction

Ce document résume les travaux effectués entre octobre 2013 et septembre 2016, au Centre d'Études Spatiales de la Biosphère (CESBIO), dans le cadre d'une thèse cofinancée par le Centre National d'Études Spatiales (CNES) et la région Midi-Pyrénées en vue de l'obtention du doctorat de l'université Toulouse 3 (Paul Sabatier).

Le sujet de cette thèse porte sur le modélisation théorique et numérique d'un nouveau concept d'interférométrie spatio-temporelle pour le développement d'une nouvelle mission d'observation de la terre depuis l'espace pour la gestion des ressources en eau.

Les travaux effectués tout au long de ces trois années englobent deux volets majeurs: un volet théorique et un volet numérique. Le premier volet a été entièrement consacré au développement théorique du nouveau concept en partant des équations de bases en électromagnétisme jusqu'à la dérivation des paramètres fonctionnels. Quant au deuxième volet, il a principalement concerné toute la partie numérique de validation des résultats théoriquement obtenus.

Ce mémoire de thèse est rédigé en grande partie en anglais à l'exception de l'introduction, du contexte, des conclusions et des perspectives qui sont rédigés en français.

Guide de lecture

Après une introduction générale au contexte d'étude, le 1er chapitre fait l'objet de l'état de l'art des différentes missions et techniques d'observation de la terre et traite, plus particulièrement, de la télédétection par radiométrie passive en bande L.

Le 2ème chapitre décrit les différentes applications d'observation de la terre, les nombreux défis à surmonter par la nouvelle génération de missions à venir et les besoins des utilisateurs en terme de produits délivrés par les missions spatiales.

Le 3ème chapitre décrit une première étude du concept d'interférométrie spatio-temporelle combiné à une méthodologie de corrélation en temporel. Cette étude s'est soldée par la généralisation du plus important théorème en observation de la terre par synthèse d'ouverture, connu sous le nom du théorème de *Van Cittert-Zernike*, au cas d'observateurs en mouvement par rapport aux sources de température.

Une deuxième étude du concept d'interférométrie spatio-temporelle combiné à une méthodologie de corrélation en fréquentiel a été largement détaillée au 4ème chapitre. Une propriété remarquable de cette méthode d'imagerie a été découverte en mettant en perspective une nouvelle information jusqu'à lors jamais exploitée.

L'étude menée au chapitre précédent a mis en évidence l'apparition d'un noyau intégral hautement oscillant liant les valeurs de corrélation aux températures à reconstruire. La première partie du 5ème chapitre a été donc consacrée à l'étude détaillée de l'approximation de ce noyau intégral par l'utilisation des méthodes numériques d'inversion des noyaux fortement oscillants. La deuxième partie, quant à elle, reprend les différents développements numériques compris dans le deuxième volet de ces travaux de thèse. Elle s'intéresse plus particulièrement à la reconstruction des températures par l'utilisation de plusieurs méthodes d'inversion des fonctions de corrélation ainsi qu'à la dérivation des différents paramètres fonctionnels du concept à l'étude.

Finalement, une conclusion générale reprend les résultats significatifs à l'issu de cette thèse et discute des perspectives et des travaux à venir.

Publications

Articles publiés:

- Un article publié sur la généralisation du théorème de Van Cittert-Zernike au cas d'observateurs en mouvement par rapport aux sources:
"*Generalization of the Van Cittert–Zernike theorem: observers moving with respect to sources*", Measurement Science and Technology, vol. 27, no. 1, Nov. 2015.

- "*Generalization of the Van Cittert–Zernike theorem: observers moving with respect to sources*", IEEE Xplore, 2016.

Articles en préparation:

- Un article en cours de publication sur le nouveau concept de corrélation dans l'espace fréquentiel:
"*Fourier-Correlation Imaging*", to be submitted soon.

- Un article en cours de préparation sur l'approximation numérique du noyau intégral hautement oscillant intervenant dans la fonction de corrélation du concept de corrélation dans l'espace fréquentiel:
"*Numerical quadrature of a highly oscillatory integral kernel*", in preparation.

- Un article de revue en cours de finalisation sur les différentes missions et techniques d'observation de la terre par radiométrie passive en bande L:
"*Microwave Remote Sensing: An Overview of Recent Missions*", to be submitted soon.

Présentations orales à des conférences:

- "*Fourier Correlation Imaging for passive Earth remote sensing: a proposal for SMOS-Next*", MicroRad 2016, Espoo, Finland.

- "*Generalization of the Van Cittert–Zernike theorem: observers moving with respect to sources*", MicroRad 2016, Espoo, Finland.

Contexte

Une meilleure compréhension de la planète sur laquelle nous vivons, sa constante évolution, sa capacité à supporter la vie et dans quelle mesure elle serait impactée par l'activité humaine est le grand enjeu que confronte l'humanité dans le futur. Le sort de l'humanité est plus que jamais lié au sort, encore incertain, de la planète sur laquelle elle évolue.

L'un des faits majeurs de notre époque est le changement climatique dont le constat devient de plus en plus évident. Le réchauffement de l'atmosphère et des océans, l'augmentation des niveaux des mers et la fonte des glaces aux pôles sont parmi les plus importants indicateurs d'un réchauffement de la planète.

"L'homme est-il directement responsable du changement climatique ?" est là la question que nombreux scientifiques souhaitent élucider. Du fait de la grande complexité de la nature scientifique du problème, la réponse à cette question requiert la prise en compte d'un nombre considérable de paramètres physiques qui définissent le comportement à l'origine des différents phénomènes régissant le climat terrestre. S'ajoute à cela le caractère global de tels phénomènes dont la modélisation passe par une connaissance à la fois à l'échelle spatiale et temporelle. De ce fait, malgré le nombre croissant d'études sur la relation entre l'activité humaine et le changement climatique, nulle évidence scientifique n'a permis, à ce jour, de déclencher des actions à l'échelle globale. En outre, les études sur le lien entre le changement climatique et l'augmentation du nombre de catastrophes naturelles sont encore prématurées et ne permettent guère de statuer sur la gravité de la situation et encore moins servir de base scientifique pour inciter des mesures politiques d'envergure internationale.

Climat terrestre:

Le climat et la météo font partie intégrante de la vie humaine de tous les jours et ont un impact direct sur la santé et la production de nourriture. La météo est définie comme étant les fluctuations de l'état de l'atmosphère terrestre sous l'impact d'un ensemble complexe de paramètres tels que la température, le vent et les nuages. Le climat, quant à lui, désigne l'état moyen météorologique et sa variabilité sur une période de temps ou sur une zone particulière.

La dénomination "changement climatique" fait référence à un changement significatif de l'état moyen du climat et de sa variabilité s'opérant sur une durée pouvant dépasser la décennie. Les changements au niveau du climat terrestre ont un caractère lent et périodique (figure 1), mais depuis quelques décennies on a assisté à une augmentation globale de la température moyenne d'à peu près 0.8°C (figure 2). Ceci a été accompagné d'une augmentation de la température des océans et des niveaux des mers et d'un déclin sans précédent de la calotte glacière [1].

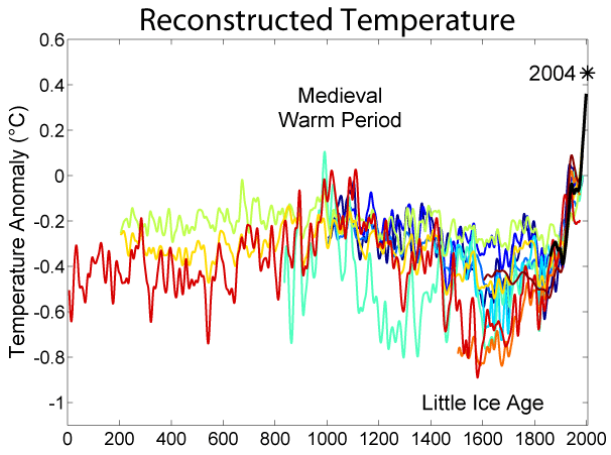

Figure 1: Moyenne globale de la température terre/océan relative à la moyenne entre 1951 et 1980 (Source: NASA GISS)

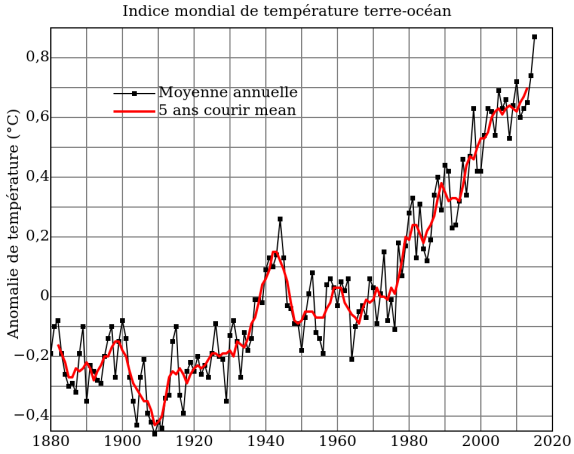

Figure 2: Température reconstruite en utilisant différentes méthodes proxy

Le cinquième rapport d'évaluation IPCC (Intergovernmental Panel on Climate Change) de 2013 a scientifiquement mis en évidence que l'activité humaine a commencé à influencer le climat terrestre, et

ce depuis la révolution industrielle, par la génération effrénée de gaz à effets de serre augmentant la concentration atmosphérique du CO_2 jusqu'à 40% depuis 1970 (figure 3).

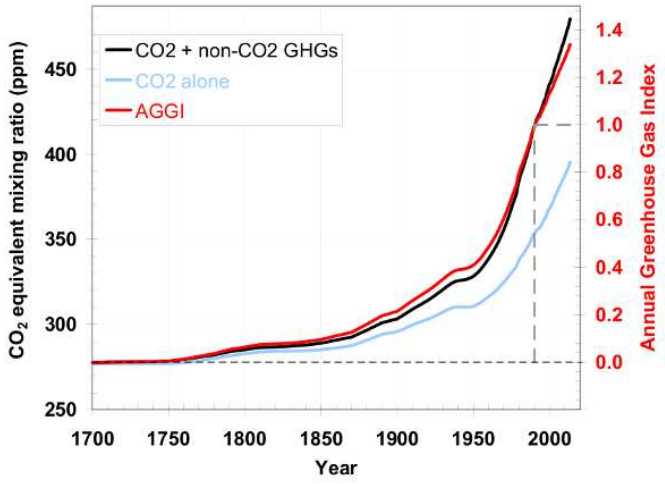

Figure 3: Concentration en CO_2 (The Keeling curve)

Une vue d'ensemble:

Avoir une vue d'ensemble sur la planète semble être plus que jamais déterminant dans la perspective d'une meilleure compréhension des phénomènes gouvernant le changement climatique et d'une illustration précise de l'influence humaine sur le climat terrestre.

Une telle vision, à la fois globale et récurrente, est devenue disponible grâce au grand déploiement des missions spatiales d'observation de la terre. Cette nouvelle aire de missions spatiales a permis la naissance d'un grand spectre d'applications scientifiques, en partant de l'étude du changement climatique jusqu'à la gestion des ressources en eau en passant par les prédictions météorologiques [2].

Paramètres déterminants:

En plus du vent et de la topographie des sols, l'*humidité des sols* et la *salinité des océans* constituent les paramètres essentiels qui gouvernent les interactions à l'interface entre la surface de la terre et l'atmosphère. Une modélisation à l'échelle globale des processus d'échange entre la terre et son atmosphère requière donc une cartographie à l'échelle de la planète de ses paramètres d'influence.

L'humidité du sol, où teneur en eau, représente la quantité d'eau stockée dans un volume donné du sol qui est en interaction directe avec l'atmosphère par l'intermédiaire de différents processus tels que l'évaporation, l'évapotranspiration, ou encore l'infiltration. De ce fait, une connaissance globale de la distribution de l'humidité des sols est d'une grande utilité dans la détermination des ressources en eau et l'estimation des précipitations, et sert d'entrée à nombreux modèles de prédiction météorologique [3, 4].

La salinité désigne la concentration en sel dissout dans l'eau mesurée en grammes de sel par litre d'eau (practical salinity unit (psu)). La salinité des océans sert d'indicateur de la formation des masses d'eau, de la circulation des courants marins, de la distribution de l'eau fraîche, etc., ce qui rend sa cartographie à l'échelle globale primordiale dans la compréhension du rôle de l'océan dans le système

climatique terrestre [5].

À ce jour, les missions comme SMOS (Soil Moisture and Ocean Salinity) ont fait leurs preuves quant à la provision en données d'observation nécessaires à une multitude d'applications. Cela dit, des progrès sont encore à réaliser en terme de précision, de finesse et de temps de disponibilité dans le design des missions à venir.

Bibliography

[1] "Summary for Policymakers," 1. Observed changes in climate and their effects, in IPCC AR4 SYR 2007.

[2] P. Kansakar and F. Hossain, "A review of applications of satellite earth observation data for global societal benefit and stewardship of planet earth," ELSEVIER: Space Policy, no. 36, pp 46-54, 2016.

[3] A. C. M. Beljaars, P. Viterbo, M. J. Miller, and A. K. Betts, "The anomalous rainfall over the United States during July 1993: Sensitivity to land surface parameterization and soil moisture," *Mon. Weather Rev.*, vol. 124, pp. 362-383, 1996.

[4] G. Balsamo, J. F. Mahfouf, S. Belair, and G. Deblonde, "A land data assimilation system for soil moisture and temperature: An information content study," *J. Hydrometeorol.*, vol. 8, pp. 1225-1242, 2007.

[5] Y.H. Kerr, P. Waldteufel, J.-P. Wigneron, S. Delwart, F. Cabot, J. Boutin, M. J. Escorihuela, J. Font, N. Reul, C. Gruhier, and al., "The SMOS mission: new tool for monitoring key elements of the global water cycle," *IEEE, Institute of Electrical and Electronics Engineers*, 2010, 98 (5), pp. 666-687.

Chapter 1

STATE OF THE ART: AN OVERVIEW OF RECENT MISSIONS

Contents

1.1 Introduction

Microwave remote sensing is one of the widespread techniques in Earth observation, it is particularly used to monitor the key parameters that govern the major exchange processes between the Earth's surface and the atmosphere. The large-scale monitoring of the Earth's environmental variables is of crucial importance to better understand the interactions at the land/atmosphere interface and constitutes a valuable base to a broad range of scientific applications in hydrology and climatology.

When compared to optical and infrared spectral images, Earth's microwave emissions yield a complete different physical information on the surface-atmosphere system. Microwave Earth's emissions are particularly sensitive to the dielectric properties of the near-surface, and thus act as a complementary information to the one available in other frequency regions.

Starting from airborne campaigns until spaceborne missions, microwave remote sensing of the Earth has gained over the decades a major importance within the scientific community. Earth observation systems operating in the microwave regime apply either passive or active radiophysical devices to measure *Soil Moisture* [1] and *Sea Surface Salinity* [2] which are the governing variables in numerous scientific applications including water monitoring, climate forecasting, carbon cycles determination, etc.

The aim of the present chapter is to give an overview of L-band dedicated Earth observation missions and techniques using microwave remote sensing.

1.2 Introduction to microwave remote sensing

1.2.1 Why microwave remote sensing ?

Earth remote sensing is the science of retrieving the properties of the Earth's surface/atmosphere system at a distance from it by measuring the emitted electromagnetic radiations [3].

Observations of the Earth's emissions in the microwave domain, and particularly at around 1.4 GHz, present many advantages: i) the capability of penetrating clouds, and to some extent rain, ii) a higher penetration depth through vegetation and iii) an all-day-around operability due to their independence of sun as a source of illumination.

Microwaves, in the sense of the retrieved information, act as a complementary information to the one available in the visible and infrared frequency regions. While waves in the visible and near-infrared regions are sensitive to the molecular resonances at the surface, microwaves are more particularly sensitive to the in-depth geometric and bulk-dielectric properties of the soil surface, and more precisely to its *dielectric constant* [4].

Furthermore, microwave emissions from the ice-covered and ice-free sea surface are highly contrasted, which renders microwave radiometry particularly effective for monitoring the temporal and spatial changes in the sea-ice cover in oceans.

1.2.2 Radiometry

All matter, under the influence of an incident illumination, radiates a certain amount of electromagnetic energy which results from the interaction between the atoms and the molecules in the material. At thermodynamic equilibrium, a real material absorbs and emits the same amount of energy in contrast to a *blackbody* which is defined as an ideal material that absorbs all the incident radiation.

In Planck's quantum theory, the emission spectrum of a blackbody is expressed by the Planck's blackbody radiation law. The latter is considered to be the reference relative to which the thermal

radiation mechanism of any real (or grey) material can be described, and is given by

$$B_f = \frac{2hc^2}{\lambda^5}\Big(\frac{1}{e^{hc/(\lambda kT)} - 1}\Big), \tag{1.1}$$

where B_f refers to the black-body spectral brightness (in $\mathrm{W.m^{-2}.sr^{-1}.Hz^{-1}}$), h is the Planck's constant ($= 6.63 \times 10^{-34}$ joules), λ is the wavelength (in m), c is the speed of light ($= 3 \times 10^8$ $\mathrm{m.s^{-1}}$), k is the Boltzmann's constant ($= 1.38 \times 10^{-23}$), and T is the absolute temperature (in K).

In the case of extended sources of incoherent radiation (such as the sky), the physical temperature is related to the so-called *brightness temperature*, defined as the radiated power per unit of solid angle per unit of area,

$$B = \frac{F_t}{A_t}, \tag{1.2}$$

of units $W.sr^{-1}.m^{-2}$, by means of the *emissivity* whose amount depends on the dielectric constant of the emitting body.

The incident radiation toward a real material (grey body), in contrast to an ideal black-body, is partially absorbed and reflected depending on the emissivity. The *brightness temperature* of a real body of physical temperature T in the direction (θ, ϕ), $T_B(\theta, \phi)$ is thus expressed as

$$T_B(\theta, \phi) = e(\theta, \phi)T, \tag{1.3}$$

where $e(\theta, \phi)$ represents the emissivity in the direction (θ, ϕ). Based on this, the brightness of a real material in the direction (θ, ϕ) is defined, for a narrow frequency bandwidth Δf, by means of its brightness temperature as follows

$$B(\theta, \phi) = \frac{2k}{\lambda^2} T_B(\theta, \phi)\Delta f. \tag{1.4}$$

In practice, depending on the type of the measured radiation, either a natural emission from the Earth's surface and its atmosphere or a backscattered artificial signal, microwave remote sensing sensors are either **passive** or **active**.

1.2.2.1 Active microwave remote sensing

The monostatic active type creates its own electromagnetic energy which is propagated from the sensor toward the ground and through their interaction a backscatter is produced and returned to the sensor. The transmitter and the receiver are collocated in the same system in contrary to the bistatic type where they are separated by a distance of the order of the expected target distance.

Active microwave remote sensing is performed using a RAdio Detection And Ranging (RADAR) system, which is a radio device composed of a transmitter, responsible of the illumination of the ground using an artificial radiation, and a receiver, which measures the backscattered signal after the interaction with the ground [4].

Active microwave remote sensing using radars fall into three categories:
ii) *Synthetic aperture radars* (SARs), widely used in active remote sensing applications, create their own illumination, propagate it toward the Earth's surface and measure the strength and round-trip time of the backscattered response. SAR systems are capable of achieving high spatially resolved images, but are strongly impacted by the surface topography (rougher areas will induce brighter pixels on the image),
iii) *Scatterometers* are essentially dedicated instruments to map the ocean wind circulation and some other geophysical variables from space. They actively transmit electromagnetic pulses toward the Earth's

surface and measure the backscattered response to derive the surface properties. Due to their relatively coarse spatial resolution (of the order of radiometer's), scatterometers are mainly sued to provide a global coverage mapping, and
iii) *Altimeters*, usually employed in combination with radars, are especially intended to provide auxiliary data to the radar's output such as wind speed or sea surface roughness. By exploiting the ranging capability of the radar, altimeters are capable of measuring the precise satellite's altitude and mapping the surface topography profile in the flight direction. However, altimeters' measurements are highly affected by the surface roughness, which renders them mostly effective over smooth surfaces such as oceans and low relief land surfaces.

1.2.2.2 Passive microwave remote sensing

The passive type measures the self-emitted microwave radiation from objects on the ground as a result of sun illumination by means of a **radiometer**. The measured spectral brightness by radiometers is expressed by the *Rayleigh-Jeans law* derived from the *Planck's law* (1.1) in the regime $kT \gg hc/\lambda$,

$$B_f = \frac{2f^2kT}{c^2}. \tag{1.5}$$

A radiometer is thus a sensor capable of converting the receiver's output voltage V_{out} into an effective apparent temperature T_{ML}. T_{ML} represents the brightness distribution of the incident radiation (containing the scene self-emitted radiation and other emissions) carried by the solid angle subtended by the main lobe of the receiving antenna. The physical temperature is afterwards deduced by means of the relationship linking the power generated by a matched load as function of its physical temperature.

Spaceborne radiometers are highly accurate but at the expense of a coarse spatial resolution (typically 25 to 50 km in L-band) essentially dictated by the antenna's diameter; the larger the antenna's diameter is, the higher the achieved spatial resolution will be. For this reason, enhancing the radiometer's spatial resolution requires the use of very large antennas (typically a 16m-diameter low-orbit antenna to achieve a 10-km spatial resolution at around 1.4 GHz) unsuitable for a spaceborne use. This limitation was overcome by the introduction of the *Synthetic Aperture* technique [5].

1.2.3 Aperture Synthesis

Aperture synthesis is an interferometric technique similar to Earth rotation synthesis employed in radioastronomy in which the signals received by a pair of small antennas are processed in such a way to synthesize a single large antenna of narrow beamwidth with the intent of observing typically punctual celestial sources [6]. Instead of looking upward, Earth rotation synthesis was readapted to Earth remote sensing by looking downward and dealing with large thermal sources. Thanks to this technique, limitations on antenna size in satellite-based passive radiometers were overcome [7].

Aperture synthesis uses the basic idea that the coherent product (cross-correlation) of the received signals by a pair of different antennas defines a sample point in the Fourier transform of the brightness temperature map of the observed scene. Thus, instead of a power measurement in real aperture systems, a synthetic aperture radiometer measures the cross-correlation product between the measured signals by a pair of antennas (figure 1.1),

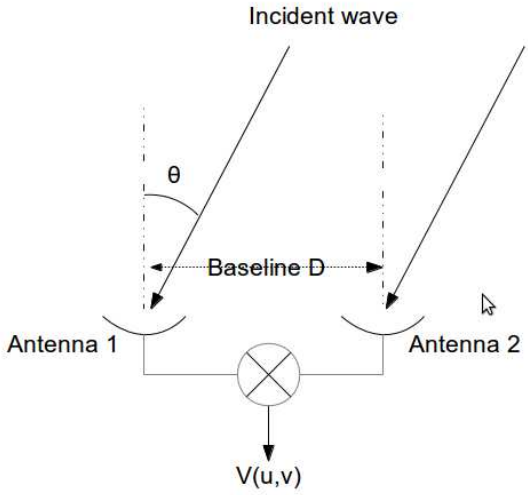

Figure 1.1: Schematic diagram of a two-element interferometer

expressed for an ideal two-element interferometer as [8],

$$V(u,v) = \iint \frac{T_B(\xi,\eta)}{\sqrt{1-\xi^2-\eta^2}} e^{-j2\pi(u\xi+v\eta)} du dv, \tag{1.6}$$

where $V(u,v)$ is the so-called visibility function, $(u,v) = (x_1 - x_2, y_1 - y_2)/\lambda$ is the baseline vector normalized by the wavelength, (ξ,η) is the direction cosine of the incident wave and $T_B(\xi,\eta)$ is the brightness temperature distribution of the scene. The Fourier-transform relationship linking the visibilities to the brightness temperature distribution is straightforward from (1.6) and is classically known as the *Van Cittert–Zernike* theorem.

When observing a scene using synthetic aperture systems, the Fourier-transform of the brightness temperature map of the observed scene is constructed by cross-correlating the pair of signals collected by an array of antennas of various baselines (spacings between the antennas). Then, using inversion and regularization techniques, the brightness temperature distribution of the scene can be reconstructed [9] and the spatial resolution of the reconstructed image is found to be directly dictated by the longest baseline of the array instead of the antenna diameter in real aperture systems.

However, employing aperture synthesis by means of small antennas to bypass the need of large antennas comes at the cost of a reduced accuracy in addition to a complex electronic hardware, data processing, and calibration procedures. Fortunately, one shows that the radiometric accuracy of interferometric systems can be improved by increasing the time-bandwidth product to approach real aperture radiometers [7].

More generally in aperture synthesis, a tradeoff between the spatial resolution (dictated by the longest baseline) and the radiometric sensitivity (dictated by the maximal integration time) is always set depending on each mission's objectives. The optimality of an interferometric configuration relies on the trade-off between filling as much as possible the $(u,v)-$plane and reducing the minimal required number of radiating elements for mass optimization.

One of the famous applications of the synthetic aperture technique are the Electronically Scanned Thinned Array Radiometer (ESTAR), the Microwave Imaging Radiometer with Aperture Synthesis (MIRAS), and the *Atacama Large Millimeter Array* (ALMA) in Chile [10] used for radioastronomical observations.

1.2.3.1 ESTAR

ESTAR is a 1D push-broom system composed of an array of antennas oriented in the flight-direction which employs a combination of real aperture and interferometric imaging methodologies (figure 1.2).

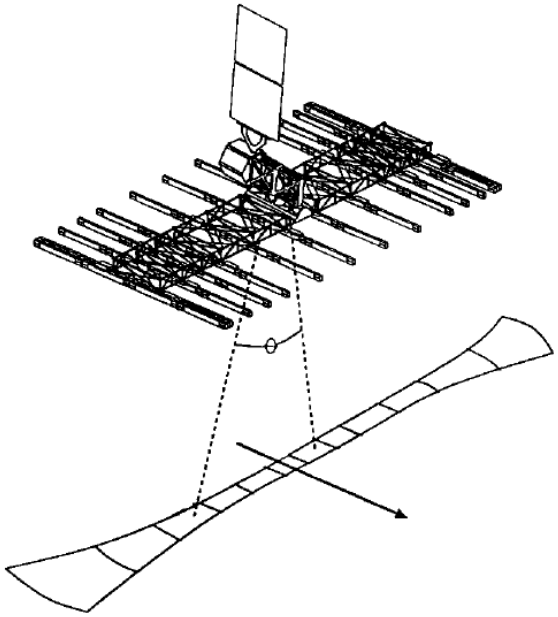

Figure 1.2: 1D push-broom interferometric imaging radiometer

The imaging in the along-track direction is performed through a classical real aperture technology, whereas in the cross-track direction a synthetic aperture technique is employed. This configuration was for the first time tested on board of the NASA P-3B Orion aircraft, incorporating a ESTAR instrument developed as part of the cooperative research between the NASA and the university of Massachusetts, between July 8-20, 1999 as an experiment (Southern Great Plains (SGP)) to demonstrate the feasibility of aperture synthesis for remote sensing purposes [11]. As firstly developed, the ESTAR system consisted of a L-band (1.4 GHz) instrument composed of five real "stick" antennas providing the resolution in the along-track direction, and the equivalent beam synthesized by means of seven unique baselines of width at half power of 7° produces the resolution in the other direction.

ESTAR allowed for the first time to show the feasibility of synthetic aperture for the measurement of soil moisture and ocean salinity [12].

1.2.3.2 SMOS

The MIRAS instrument on board of the SMOS mission employs a 2D interferometry in both directions by collocating a set of small antennas to achieve the best trade-off between the instrument weight and the spatial resolution.

MIRAS operates in the L-band (1.4 GHz) and is composed of 69 dual-polarized antennas arranged along a three-arm Y-shaped configuration [13]. Using a 2D synthetic aperture, this configuration allows to synthesize an equivalent 8m-diameter real aperture antenna and a mean ground spatial resolution of 40-50 km.

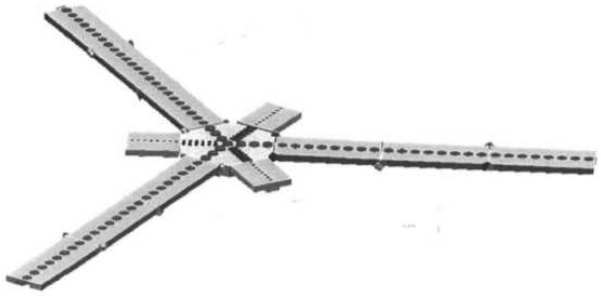

Figure 1.3: SMOS radiometer

MIRAS constituted the first spaceborne demonstration of the feasibility of a 2D interferometry to Earth observation and provided a new means for the measurement of soil moisture and ocean salinity [46].

1.2.3.3 ALMA

ALMA is a complete astronomical imaging and spectroscopic instrument incorporating an array of up-to 80 12m-diameter antennas at different baseline configurations raging from 15 m to 18 km (figure 1.4). By combining the signals from different antenna-pairs, ALMA continuously synthesizes very narrow beams yielding the provision of radio-astronomical images of resolution as fine as 0.005".

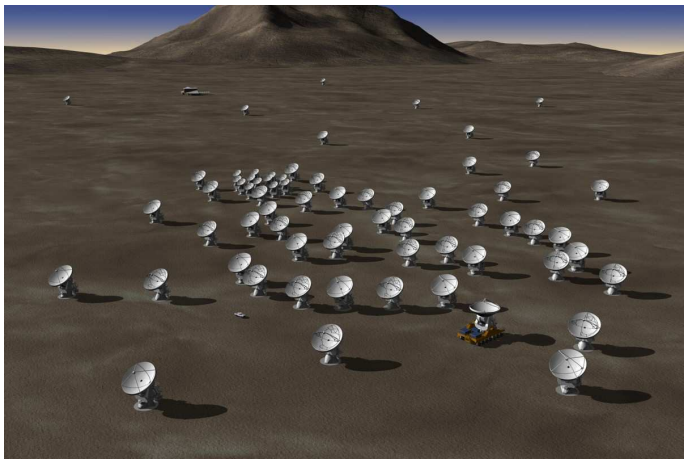

Figure 1.4: ALMA artist's view

1.3 History of microwave remote sensing

1.3.1 Radars

The first radio experiment was conducted by Heinrich Hertz, 1886, where he experimentally demonstrated the Maxwell's electromagnetic theory. His experiment allowed the discovery of radio waves and showed that reflections could be received from metallic and nonmetallic objects. In 1903, Christian Hulsmeyer obtained a patent for the detection of ships using radars.

The pulse radar system was originally developed by A. H. Taylor and the U. S. Naval Research Laboratory to detect and track ships and aircrafts. While the first practical radar system for aircraft detection was designed by Sir Robert Watson-Watt in 1937.

During World War II, the first military reconnaissance imaging radars employed the *plan-position indicator* (PPI) to produce an accurate ground mapping. Later in 1950s, the use of real aperture *side-looking airborne radar* (SLAR) has led to even finer resolution ground maps compared to PPI systems.

In June 1951, Carl A. Wiley invented a new system called "Doppler beam-sharpening", which exploited the Doppler shifts of the returned signals to significantly improve the resolution. This technique led afterwards to the current *synthetic aperture radar* (SAR). During 1950s and 1960s, Goodyear Aircraft introduced numerous advancements in SAR technology.

Early experiments using artificial Earth satellites had demonstrated that the Doppler frequency shifts of signals traveling through the ionosphere and atmosphere were stable enough to permit fine and achievable resolutions even at ranges of hundreds of kilometers. The application of SAR systems to Earth remote sensing and geoscience radar reconnaissance was primarily deployed with the first radar mapping mission launched in 1967 using the Westinghouse AN/APQ 97 system and the development of multi-channel airborne SAR systems. Later, the Apollo Lunar Sounder experiment launched in 1972 constituted the first use a SAR system on board of a spaceborne instrument.

In the recent past, SAR and InSAR (interferometric SAR) remote sensing technologies have been largely widespread. While the U.S. haven't had any operational civilian satellites carrying a SAR system since the short-lived SEASAT program launched in 1978, many non-U.S. spaceborne SAR systems have been deployed for the imaging of the Earth's surface, namely the ESA satellites ERS-1, ERS-2, ENVISAT and the Canadian satellites Radarsat-1 and Radarsat-2.

1.3.2 Radiometers

The first apparition of microwave radiometric systems goes back to 1930s and 1940s for essentially radioastronomical applications, namely the measurement of the extraterrestrial electromagnetic energy. In 1962, radiometric measurements at 15.8- and 22.0-GHz were performed using a two-channel microwave radiometer on board of the *Mariner 2* spacecraft providing, for the first time, observations of Venus [14].

After two decades of outward-looking radioastronomical and atmospheric studies, scientists from the university of Texas pointed an antenna downward, for the first time, from an airborne platform achieving radiometric measurements at 4.3-mm wavelength to measure the microwave-emitting properties of water, grass, and asphalt (Straiton et al. 1958).

The derivation of the physical properties of the Earth's surface and atmosphere using spaceborne microwave radiometry initially began in 1968 with the *Cosmos 243* mission (Basharinov et al. 1971). In the same perspective, several satellites have carried aboard microwave radiometers including *Cosmos 384*, *Nimbus 5*, 6 and 7, *Skylab*, *TIROS*, and *Seasat*.

The single-frequency electrically scanning microwave radiometer (EMSR) system flown aboard Nimbus 5 and Nimbus 6 (Zwally and Gloersen) provided global microwave observations at 19.35-GHz, which allowed the first analyses of sea ice (Wilheit et al.). Since 1978, multi-frequency and dual-polarized observations of the Earth's microwave emissions started to be used to assess the extent of sea ice and Earth's geophysical parameters, particularly using the scanning multi-channel microwave radiometer (SMMR) flown aboard *Seasat-A* and *Nimbus 7*, which comprised five different frequency H- and V-polarized channels. The richness of these observations motivated the development of improved algorithms for the retrieval of ice-concentration and ice-type estimates (Cavalieri and Zwally).

The Special Sensor Microwave Imager (SSM/I) and the Special Imager Sounder (SSMIS) carried aboard the Defense Meteorological Satellite Program (SMSP) satellites since 1987 referred to as F08,...,F19 (currently operating systems F15, F16, F17, and F18) are dedicated to ocean measurements including Surface Wind Speed, Rain Rate, Cloud Liquid Water, and Atmospheric Water Vapor. Similarly, the conically scanning passive Advanced Microwave Scanning Radiometer (AMSR) carried aboard the NASA's EOS Aqua spacecraft (2002-2011) and the JAXA's spacecrafts (2002-2003 and 2012-present) provide ocean measurements of sea surface temperature. Before that, the Tropical Rainfall Measuring Mission (TRMM), launched on November 27, 1997 carried the multi-channel, dual polarized, conical scanning passive TRMM Microwave Imager (TMI) designed to measure rain rates over a wide swath.

Mainly motivated by the successful application of such airborne and spaceborne sensors for monitoring the Earth's geophysical parameters, numerous recent concepts have been developed with the primary focus on providing global observations of the Earth to the scientific community.

1.4 Rationale for the use of L-Band

Figure 1.5 shows the sensitivity to geophysical parameters as function of increasing frequency. For the parameters of interest (soil moisture and ocean salinity) microwave frequencies, and more specifically at L-band, are to be preferred [27, 28].

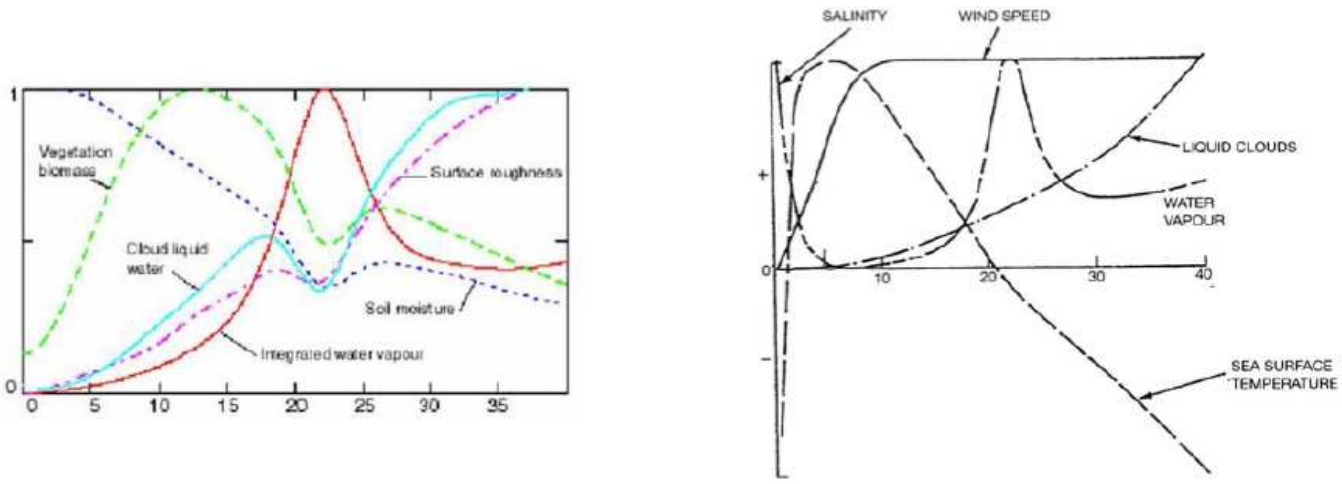

Figure 1.5: Sensitivity to SM and OS as function of increasing frequency [29, 30]

On one hand, figure 1.6 shows the modeled microwave transmissivity as function of increasing biomass at L-band (1.4 GHz), C-band (6 GHz), and X-band (10 GHz) frequencies. In the case of vegetated surfaces, L-band frequencies have the significant advantage of a higher penetration depth than higher frequencies. Based on this, remote sensing in the L-band allows a global and widest estimation of soil moisture [31].

On the other hand, figure 1.7 shows the penetrating depth in bare soils as function of increasing frequency. Emissions at low frequencies thus originate from deeper layers in the soil (higher than 5 cm) than in higher frequency regimes which usually don't exceed 1 cm.

Although the undeniable advantages of measuring T_B at low frequencies, highly contaminating emissions originating from manmade ground-based instruments and the galaxy must be handled. To this end, a protected frequency band within the L-band (1.400-1.427 GHz) was exclusively allocated for Earth radiometric observations.

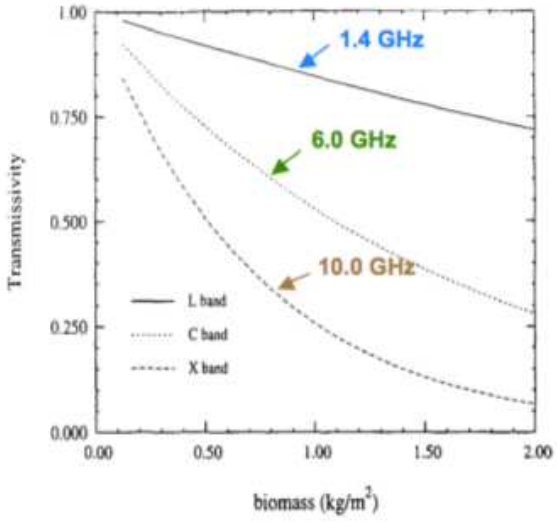

Figure 1.6: Microwave transmissivity as function of increasing biomass [31]

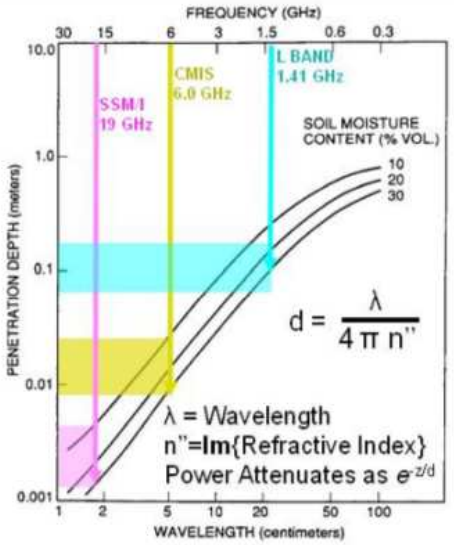

Figure 1.7: Sensitivity of L-band T_B observations as function of soil depth [31]

1.5 Earth observation using microwave remote sensing

1.5.1 Science motivation

At L-band, soil moisture from the near-surface is directly linked to the emitted brightness temperature T_B through a straightforward relationship [15, 16]. An other significant advantage of imaging in the L-band is the fact that the Earth's microwave emissions are weakly impacted by the atmosphere, the clouds and the rain [17]. Besides, at around sunrise, when the thermal equilibrium is most probably reached, the thermal infrared radiations from the surface can be directly used, in addition to other relatively stable parameters (surface roughness, soil topography, vegetation type) [18], to assess the effective surface temperature T_e.

1.5.2 Soil Moisture (SM)

1.5.2.1 Rationale for measuring SM

Soil Moisture generally refers to the amount of available water in the near-surface, which directly interacts with the atmosphere through various exchange processes, such as evaporation, infiltration, etc. This amount of water in the first centimeters (5 cm) of the soil layer constitutes the needed storage to ensure the vegetation's growth and health and a key parameter that governs the transfers between the surface and the atmosphere. As a result, an all-time knowledge of SM is of crucial importance in the determination of i) water availability, ii) mass transfer between the surface and the atmosphere, iii) rainfall, and iv) the energy budget at the surface/atmosphere interface, and thus in the accuracy of several prediction models such as weather and extreme events [19, 20].

1.5.2.2 How to measure SM ?

Several approaches have been considered to measure the volumetric SM which corresponds to the ratio between the volumes of water and the containing soil, such as ground measurements using gravimetric sampling which provide accurate data but only at very local areas. These measurements are essentially dedicated to validate microwave remote sensed data provided by airborne or spaceborne systems.

SAR systems offer an all weather capability with a fine spatial resolution but at the cost of a low temporal sampling and a high dependence on the surface topology. Scatterometers, in turn, allow a much wider swath leading to a higher temporal resolution but are still highly impacted by surface roughness and vegetation. Finally, the use of microwave radiometers to infer SM is based on the induced change of emissivities between land and water due to the variation of their corresponding dieletric constants. The acquired signal by radiometers is weakly impacted by roughness and vegetation structure but yields a low spatially resolved information.

1.5.3 Sea Surface Salinity (SSS)

1.5.3.1 Rationale for measuring SSS

Salinity refers to the concentration of dissolved salt in water, measured in practical salinity unit (psu) which corresponds to grams of salt water per litter of water. SSS has a direct impact on the thermohaline circulation and the distribution of mass and heat whose variations result from the exchange processes of water between the ocean and the atmosphere, essentially due to sea-ice freezing and melting, and continental runoff.

Monitoring SSS for the estimation of the global distribution of salt and its annual and seasonal variability is of crucial importance to understand the role of ocean in the climate system. Particularly, salinity acts as an indicator of water masses formation, precipitation and evaporation, ocean circulation, fresh water budget, extreme events, etc.

1.5.3.2 How to measure SSS ?

The measurement of SSS is either performed using i) sampling by the deployment of ARGO profiling floats and drifting buoys for conductivity measurements which produces sparse maps with few data of salinity or ii) remote sensing by means of passive radiometers exploiting the idea that sea surface emissivity, known as the *brightness temperature* (T_B), is directly impacted by the dielectric constant of seawater which is, in turn, a function of salinity and temperature [21].

1.6 Retrieval algorithmic schemes

Based on the scientific properties of the emitted Earth's radiations, several algorithmic approaches were developed for the retrieval of the geophysical parameters from Earth observations by means of remote sensing.

Data processing in Earth observation mission is generally performed along various levels of treatment (see section 1.7 for more details on the processing levels). The level 1 (L1) usually contains the derived T_B product from raw data as received from the imaging instrument, which serves as inputs to the level 2 (L2) where the retrieval process is performed. Hereafter are described some of the most-used retrieval schemes.

1.6.1 Iterative approach

1.6.1.1 Overview

Starting from an initial value of the brightness temperature (T_B), the retrieval algorithm aims at iteratively minimizing a cost function that takes as principal component the squared weighted differences between the measured and modeled T_B for a set of different incidence angles. The objective is to derive the set of parameters (soil moisture and vegetation characteristics) yielding the best match between modeled and measured T_B's.

The iterative retrieval algorithm is summarized through the following steps [27]:

- identification of the Earth's surface area (or target) responsible of a particular set of the multi-angular acquired signals,
- determination of the area's characteristics and its position within the target area,
- assuming known states from other sources (default contributions) such as the sky and atmosphere,
- estimation of the states from other contributions (SM and optical thickness), and
- iteratively adjusting the parameters until reaching the minimum distance between the observed and modeled value.

1.6.1.2 Input data

Several operations are performed on the T_B product derived in level 1 (L1), including time-ordering, geolocalization, calibration, resampling with respect to the fixed 36-km updated Equal-Area Scalable Earth-2 (EASE2) grid [18], and correction for atmospheric effects and Faraday rotation, in order to derive the final L1 T_B product used as inputs to the level 2 (L2) where the retrieval process is performed.

1.6.1.3 Iterative retrieval scheme

The algorithm tries to retrieve the physical parameters p_i included in the forward model which yield the best match between measured (T_{B_M}) and modeled (T_{B_S}) brightness temperatures. Once computed, T_{B_S} is transported to the antenna reference frame using a matrix transformation, that takes account of the Faraday rotation (due to the ionosphere) and the geometric transformations between the Earth- and antenna-fixed frames, and finally compared to T_{B_M} by minimizing the following cost function

$$f_{\text{COST}} = {}^t(T_{B_{Mm}} - T_{B_{Sm}}(\theta_m, p_i \ldots)) \times C_T^{-1} \times (T_{B_{Mm}} - T_{B_{Sm}}(\theta_m, p_i \ldots)) + \sum_{i=1}^{NP} \frac{(p_i - p_{i0})^2}{\sigma_{i0}^2}, \qquad (1.7)$$

with $m = 1 \ldots NT$ the index over the set of considered measurement incidence angles, C_T the variance matrix for the observed T_{B_M}, and p_{i0} are prior estimates of the NP free physical parameters of prior variances σ_{i0}. The iterative minimization of the cost function is performed using the principle of the *Levenberg-Marquardt algorithm* [22].

1.6.2 Soil moisture retrieval

1.6.2.1 Auxiliary inputs

In order for soil moisture to be accurately retrieved, a variety of global static and dynamic ancillary data are required. These parameters, including surface temperature, vegetation opacity and single

scattering albedo, surface roughness information, land cover type classification, soil texture, and data flags for case identification are mapped to the 36-km EASE2 grid prior going through the L2 SM retrieval processor.

1.6.2.2 Tau-omega model

Soil moisture, as retrieved from T_B observations, is based on a variant of the radiative transfer equation, called the *tau-omega model*. The latter expresses the polarization-dependent (subscript p) T_B as the attenuation of the soil emissivity due to vegetation [23],

$$T_{B_p} = T_s e_p \Gamma + T_c(1-\omega_p)(1-\Gamma)[1 + r_p \exp(-\Gamma)], \tag{1.8}$$

where $\Gamma = \exp(-\tau_p \sec(\theta))$ refers to the canopy transmissivity, T_s, T_c the soil effective and vegetation temperatures which, at thermal equilibrium, are equal and can be replaced by T_{eff}, τ_p the nadir vegetation opacity related to the total columnar vegetation water content (VWC) through $\tau_p = b_p \text{VWC}$ with b_p a factor that reflects the dependence on the vegetation type and frequency, ω_p the vegetation single scattering albedo and r_p the reflectivity due to soil roughness.

Given T_B observations and ancillary information, the surface reflectance r_p, expressed as function of the dielectric constant using the following Fresnel equations (1.9)

$$R_h = \left|\frac{\cos(\theta) - r}{\cos(\theta) + r}\right|^2, \quad R_v = \left|\frac{\epsilon\cos(\theta) - r}{\epsilon\cos(\theta) + r}\right|^2, \tag{1.9}$$

where $r = \sqrt{\epsilon - \sin^2(\theta)}$, can be deduced. Then, soil moisture is estimated from the information on the dielectric constant using various dielectric models.

1.6.2.3 Soil dielectric models

The linkage between soil moisture and the dielectric constant is commonly described by means of various soil dielectric models depending on the observed soil type:

1.6.2.3.1 Dobson model: A semi-empirical approach that describes the dielectric properties of the soil free water using Debye equations combined with some empirical fitting parameters which depend on the soil type [24].

1.6.2.3.2 Wang & Schmugge model: A purely empirical model that describes the effect of bound water on the soil dielectric constant. It mainly uses the information on the threshold water content over which a variant of soil moisture induces a high variation on the dielectric constant [35].

1.6.2.3.3 Mironov model: A semi-empirical mixing dielectric model originally developed with a dielectric data basis covering a wide range of moisture conditions. It provides an estimation of dielectric spectra predictions for moist soils using only granulometric mineralogy data [26].

1.6.2.4 Direct model

The retrieval approach is based on the demonstrated linkage between the passive microwave emissions of non-frozen and snow-free surfaces and SM, vegetation opacity, and the effective surface temperature in the L-band.

1.6.2.4.1 Radiative Transfer Equation: The general radiative transfer equation (RTE) expresses the dependence of the measured signal at the level of the antenna on polarization and incidence angle [18] (figure 1.8):

$$T_{B_p} = T_{B_{atu}} + T_{B_{sp}} \exp(-\tau_{atu}) + (T_{B_{atd}} + T_{B_{sky}} \exp(-\tau_{atd}))r_{sp} \exp(-\tau_{atu}). \tag{1.10}$$

where τ_{atu}, τ_{atd} are the upward and downward atmospheric opacities, r_{sp} the surface reflectivity, $T_{B_{sp}} = e_{sp}T_s$ the surface brightness temperature with T_s the physical surface temperature, and $T_{B_{sky}}$ the sky background brightness temperature.

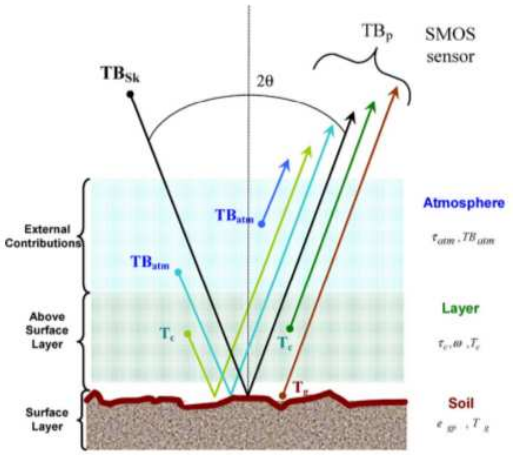

Figure 1.8: Contributions to TOA T_B [27]

1.6.2.5 Retrieval algorithms

1.6.2.5.1 Single Channel Algorithm (SCA): The retrieval process of soil moisture is performed following five main steps:
i) derivation of emissivity from T_B observations as $e = T_B/T$ by estimating the physical surface temperature from a Numerical Prediction model product,
ii) derivation of soil emissivity by getting rid of the effects of vegetation,

$$e^{surf} = \frac{e - 1 + \Gamma^2 + \omega - \omega\Gamma^2}{\Gamma^2 + \omega\Gamma - \omega\Gamma^2}, \tag{1.11}$$

with $\Gamma = \exp(-\tau \sec(\theta))$ the transmissivity of the canopy, $\tau = b \times \text{VWC}$ the optical depth, ω the single scattering albedo, b a proportionality value dependent on vegetation and frequency, and VWC the vegetation water content. b and ω are provided by means of a land cover look up table and VWC is estimated from NDVI data,
iii) accounting for the effects of the soil surface roughness that impacts the smooth soil emissivity as follows

$$e^{soil} = 1 - (1 - e^{surf}) \exp[h \cos^2(\theta)], \tag{1.12}$$

iv) linking the emissivity measurement to the soil dielectric properties using Fresnel equations (1.9), and
v) linking the derived dielectric properties to the amount of soil moisture using a dielectric mixing model.

1.6.2.5.2 Dual Channel Algorithm (DCA): The Dual Channel Algorithm (DCA) uses both H- and V-polarized T_B observations to retrieve soil moisture and VWC [33]. The inversion mechanism of the DCA is based on an iterative approach that starts by initializing the tau-omega model using guessed values of soil moisture and VWC coupled with ancillary data and, by iteratively adjusting the parameters, the algorithm determines the best match between modeled and observed T_B's.

1.6.2.5.3 Microwave Polarization Ratio Algorithm (MPRA): The MPRA, based on the Land Parameter Retrieval Model [34], allows the retrieval of soil moisture and vegetation optical depth using dual-polarized channels at a single microwave frequency. Two main assumptions are set in the radiative transfer model implemented in the MPRA: i) same temperature of soil and canopy and ii) the vegetation transmissivity Γ as well as the single-scattering albedo ω are polarization-independent. Letting e_s the soil emissivity, T_B is thus expressed by the tau-omega model as follows

$$T_B = Te_s\Gamma + T(1-\omega)(1-\Gamma)[1+(1-e_s)\Gamma], \tag{1.13}$$

with ω assumed to be globally constant by the MPRA.

In turn, the vegetation optical depth is derived by the MPRA from the Microwave Polarization Difference Index (MPDI $= (T_{BV}-T_{BH})/(T_{BV}+T_{BH})$) and the observed emissivity (e_H and e_V) through

$$\tau = \cos(\theta)\ln[ad + \sqrt{(ad)^2 + a + 1}], \tag{1.14}$$

with $a = [(e_V - e_H)/\text{MPDI} - e_V - e_H]/2$ and $d = (\omega/2)/(1-\omega)$. τ is used afterwards to estimate the transmissivity Γ.

Next, the modeled value of emissivity is derived as function of soil moisture and temperature by
i) calculating the dielectric constant as function of soil moisture, temperature and soil type using Wang and Schmugge parametrization [35],
ii) deriving the smooth surface emissivity using Fresnel equations, and
iii) correcting for roughness effects as described by Choudhury et al. [36].

Finally, soil moisture is retrieved by means of an optimization routine that determines the best-suited match between modelled and measured T_B's.

1.6.3 Sea Surface Salinity retrieval

1.6.3.1 Overview

Similarly to the SM retrieval algorithm, the ocean salinity retrieval approach uses auxiliary data (sea surface temperature (SST), wind speed, roughness and foam effects, ...) and a first guessed value of sea surface salinity (SSS) to run a set of physical models for the computation of T_B at a specific polarization and geometric configuration. These values of T_B are then transported to the antenna reference and compared to the actually measured T_B. An iterative process, by considering all measurements/views of a single grid point obtained in consecutive snapshots, allows afterwards the minimization of the difference between modeled and measured values until identifying the optimal value of the retrieved SSS for each grid point.

1.6.3.2 Algorithm description

The brightness temperature is expressed as the sum of the polarization-dependent T_B of a flat sea described by Fresnel equations and an additional δT_B induced by sea surface roughness (SSR) usually

expressed through the processes at its origin.
Taking θ to be the measurement angle, the brightness temperature is defined as

$$T_B(\theta) = e(\theta) \times \text{SST}, \tag{1.15}$$

where $e(\theta)$ is the surface emissivity at L-Band defined as

$$e(\theta, \Phi) = 1 - \Gamma(\theta, \Phi, \epsilon, \text{roughness}), \tag{1.16}$$

with Γ the reflectivity, ϵ the complex dielectric constant of sea water ($\epsilon' + j\epsilon''$), and Φ the azimuth angle.

1.6.3.2.1 Flat sea: In the case of a smooth surface, the reflectivity is directly calculated through the polarization-dependent Fresnel reflection coefficients [37], and one gets

$$T_{B_{p,flat}}(\theta, \text{SST}, \text{SSS}) = (1 - R_h(\theta, \epsilon)) \times \text{SST}, \tag{1.17}$$

where $p = h, v$. It is shown that at 1.43 GHz when SSS=20 psu and for T=20 °C, ϵ of sea water can be approximated by $75 + j42$.

1.6.3.2.2 Surface roughness: Sea surface roughness (SSR) at both large and small scales is mainly the consequence of the local/distant and instantaneous wind including dwell and wave interactions. Three different surface roughness models are used [28]:

i) Model 1:
The scattering by waves engenders a slight dependence of reflectivity on θ, Φ and roughness. For this reason, changes in the local brightness temperature over a large wave ($T_{B,l}$) with respect to T_{Bflat} are the consequence of i) the modification of incidence and azimuth angles due to large waves' tilting (θ_l, Φ_l) and ii) the presence of diffracting small-scale roughness on the large wave,

$$T_{B,l}(\theta_l, \Phi_l) = \text{SST} \times (1 - \text{Rss}(\theta_l, \Phi_l)), \tag{1.18}$$

where $\text{Rss} = R_c + R_i$ the reflectivity of small-scale rough covered surfaces, separated into a coherent component (R_c) in the specular direction and an incoherent component (R_i) in the other direction (*Yueh et al.* (1988) and *Rice* (1951)).

ii) Empirically modified SSA/SPM model:
By modeling the effect of wind and wave-generated roughness on emissivities at L-band, the small perturbation method/small slope approximation (SPM/SSA) model provides an estimation of corrections for roughness induced errors. The basic idea of this method mainly relies on the estimation of the ocean's polarimetric thermal emissions. This is achieved by applying the standard small perturbation theory to determine the bistatic scattering coefficients of a rough surface expressed in the upper atmosphere.

iii) Empirical model:
An empirical model is proposed to infer the increment to ocean brightness temperature due to SSR using the information of physically measurable parameters and measurement-based coefficients. Together with a regression with auxiliary data from ECMWF, the empirical model expresses the roughness induced T_B as function of incidence angle, neutral wind speed, wind direction, and wave height.

1.6.3.3 Iterative retrieval scheme

Several corrections are performed prior the retrieval step for i) the *Faraday rotation effect* using auxiliary Total Electron nadir Columnar Content (TEC) values, ii) the *atmospheric effects* using the radiative transfer equation, and iii) the *Galactic noise contamination* due to radiations from celestial sources and the constant cosmic background using galactic noise maps. Next, the T_B at the top of the atmosphere (TOA) is computed by summing up all the contributions to the emitted sea surface signal [38]:

1. $T_{B_{sea}} = (T_{B_{flat}} + T_{B_{rough}})(1 - F) + T_{B_{foam}}$;
2. $T_{B_{BOA}} = T_{B_{sea}} + T_{B_{ref}} = T_{B_{sea}} + (T_{B_{DN}}\Gamma + T_{gal_{ref}}e^{-\tau_{atm}})$;
3. $T^E_{B_{TOA}} = T_{B_{BOA}}e^{-\tau_{atm}} + T_{B_{UP}}$;
4. $T^A_B = [\mathrm{MR4}] \times T^E_{B_{TOA}}$,

where F is the fraction of sea foam coverage, $T_{B_{ref}}, T_{B_{DN}}, T_{gal_{ref}}, T_{B_{UP}}$ are the radiometric temperatures from the sky and atmosphere scattered by the surface, extraterrestrial sources multiplied by the reflection coefficient Γ, galactic and cosmic background multiplied by the attenuation factor due to atmosphere, and atmospheric self emissions towards the antenna, respectively, $T^E_{B_{TOA}}, T^A_B$ refer to the T_B at the TOA in the Earth and antenna reference frames, and [MR4] the transformation matrix accounting for geometry and Faraday rotation.

Lastly, for each grid point the measured T_B at the incidence angle θ_i ($T^{meas}_{B_i}$) is fitted to the corresponding modeled $T^{mod}_{B_i}$ by means of the minimization of the following cost function

$$\epsilon^2 = \sum_{i=0}^{Nm-1} \frac{[T^{meas}_{B_i} - T^{mod}_{B_i}(\theta_i, P)]^2}{\sigma_{T_{B_i}}} + \sum_{j=0}^{Np-1} \frac{[P_j - P^{prior}_j]^2}{\sigma_{P_j}}, \tag{1.19}$$

where P_j refer to the parameters influencing the T_B and P^{prior}_j the known measurement of P_j of an uncertainty σ_{P_j} and $\sigma_{T_{B_i}}$ the measurement uncertainty at each incidence angle. The outputs of the minimization step are the set of parameters included in P (SSS, SST, WS,...) responsible for the best match between modeled and measured T_B.

1.6.4 Neural Network approach for SM retrieval

An alternative approach using *neural networks* (NNs) allows to build an inverse model for the extraction of soil moisture values directly from a given set of measured T_B's. Once established, the NN can be used to predict the outcome of new set of independent input data.
NNs are intended to construct a mapping between a set of input and output data without the need of any prior estimations on their statistical behavior [39]. The functional model of NNs relies on three basic components: i) *weights* which represent the strengths of the connections between the inputs and the neurons, ii) a *linear combination* which is an adder to sum up the input signals modified by their respective weights, and iii) an *activation function* which controls the amplitude of the output of each neuron [40].
The derivation of the statistical link between observations and soil moisture is build using a global database and a neural network topology called Multi-Layer Perceptrons (MLP), without any land-cover

information to be informed to the regression models [41]. The MLP are composed of a number of neurons organized in layers. If the input to the layer j is expressed as a vector $\mathbf{i}^j$, the weights and bias of the neurons (the adaptive parameters) are respectively expressed as a matrix $\mathbf{W}^j$ and a vector $\mathbf{b}^j$, the outputs from the neurons are grouped in a vector $\mathbf{o}^j$ and the activation function of all neurons in the layer j is f_j, the output from the layer j is thus given by

$$\mathbf{o}^j = f_j(\mathbf{W}^j\mathbf{i}^j + \mathbf{b}^j). \tag{1.20}$$

Using NNs, the predicted soil moisture is thus defined as the propagation of the input observation vector $y = \mathbf{i}^1$ through the M layers of the MLP,

$$\begin{aligned} \mathbf{x}_{pre} = \mathbf{o}^M &= f_M[\mathbf{W}^M\mathbf{i}^M + \mathbf{b}^M] \\ &= f_M[\mathbf{W}^M f_{M-1}(\mathbf{W}^{M-1}\mathbf{i}^{M-1} + \mathbf{b}^{M-1}) + \mathbf{b}^M]. \end{aligned} \tag{1.21}$$

In this case, the number of layers, number of neurons at each layer and the type of the activation functions are the variables to be determined for each specific application of the MLP. Weights and biases are, in turn, determined during a training phase in which the MLP is subject to adaptation to database examples $\{X^l, Y^l\}_{l=1\ldots L}$.

More generally, NNs are a very efficient way to perform non-linear regression in the purpose of statistically deriving the relationship linking the T_B values to SM.
The used NN for the retrieval of SM in the Soil Moisture and Ocean Salinity (SMOS) processor is a feed-forward MLP network comprised of two layers [42]. The first layer contains typically 10 neurons with a non-linear sigmoid function while the second layer comprises a single node with a linear function. The input vector is multiplied at the level of each neuron of the first layer by a vector of weights and passes afterwards through the corresponding activation function. Again, the output vector of the first layer undergoes a multiplication with a vector of weights and the resultant linear combination of all is used as entry to the neuron of the second layer.
For each input vector, an associated SM value is chosen to be compared with the output of the NN. The comparison result allows to adjust the different weights by minimizing a cost function using the Levenberg-Marquard algorithm. Besides, additional information may be provided to the NN in order to optimize the SM retrieval, we quote i) soil temperature from ECMWF models or the soil texture from Ecoclimap, ii) observations at different wavelengths, including active and passive microwaves, and iii) local information on T_B's extreme values and associated SM values.

1.7 Dedicated L-band Earth observation missions

1.7.1 Soil Moisture and Ocean Salinity (SMOS) mission

Figure 1.9: SMOS artist's view

1.7.1.1 Introduction

The Soil Moisture and Ocean Salinity (SMOS) (figure 1.9) is the second mission of the ESA Earth Explorer Opportunity Programme developed with the french space agency (CNES) and the Spanish center para el Desarollo Technologico industrial (CDTI) with the main objective of a frequent and global monitoring of surface soil moisture (SM) and ocean salinity (OS) over the whole globe. The SMOS instrument uses microwave radiometry in the L-band to produce multi-angular global SM and OS measurements of a spatial resolution of 40 km and a revisit time of less than 3 days. The SMOS satellite was successfully launched on November 2, 2009.

The SMOS mission provides every 3 days global maps of soil moisture and ocean salinity which are the two key variables in the water cycle. These observations are of great importance in a variety of climate research applications, particularly in oceanography, meteorology, and hydrology. SMOS observations are intended to procure a better understanding of the governing exchange processes between the surface and the atmosphere and a valuable characterization of sea ice and snow-covered surfaces.

1.7.1.2 Mission requirements

Based on the SMOS primary scientific objectives [43], the mission functional requirements for a global and efficient monitoring of SM and OS are the following:

- a soil moisture accuracy of 0.04 m^3/m^3,
- an adequate temporal sampling to allow an acceptable estimation of evaporation and soil transfer parameters,
- a spatial resolution less than 50 km for climate, hydrology, and agronomy applications,

- a revisit time of 2-3 days corresponding to a swath of approximately 1000 km to track the quick drying period after a rainfall,
- a 6 $A.M/6$ $P.M$ sun-synchronous orbit to reach the thermal equilibrium with a minimal Faraday rotation effect.

1.7.1.3 SMOS concept

The concept of SMOS was optimally designed to meet with the predefined mission objectives. Studies in this sense have shown that the best possible configuration to satisfy the mission specifications is a Y-shape design (figure 1.10) with [45]

- a swath determined by the antennas' diameter and the platform's altitude,
- a maximal aliasing-free zone determined by the minimal distance between the antennas,
- a 50-km spatial resolution directly induced by the maximal baseline-length,
- a steer angle s (angle formed between the arms and the velocity vector) adjusted as function of the spacing between the antennas.

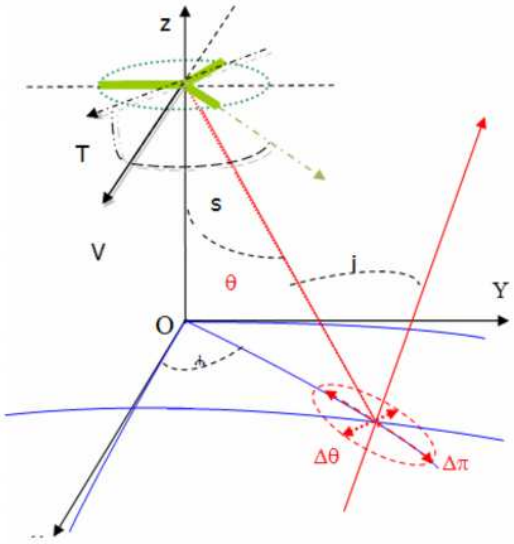

Figure 1.10: SMOS Y-shaped geometry [46]

More particularly, the SMOS imaging instrument comprises 69 antennas regularly spaced at 0.875 wavelength along a three-arm Y-shaped 2D interferometric radiometer operating in the L-band at 1.41 GHz. The 120°-apart three arms of length 4.5×0.26 m^2 are tilted at a 32.5° forward angle so as to permit a full range of angular acquisitions allowing each location at the Earth's surface to be observed with different acquisition angles. Each arm comprises 23 elementary antennas in addition to one central element and three others located on the hub. This configuration yields a dual-polarized 1000×2000 km^2 full image [46].

That being said, the hexagonal shape of the footprint (figure 1.11) dictated by the Y shape of the array is limited on the borders by aliases of the Earth. This is mainly the consequence of the violation of the Nyquist criterion ($d \leq \lambda_0/\sqrt{3}$) [47, 48].

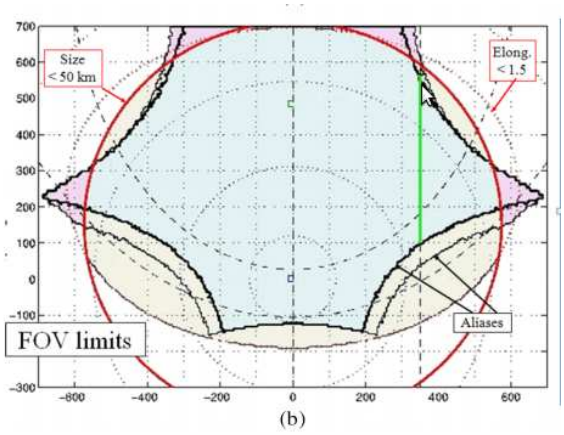

Figure 1.11: Typical SMOS field of view (X and Y axes are expressed in kilometers) [46]

Besides, a sun-synchronous low-Earth orbit at about 758 km was chosen for the SMOS mission so as to provide an efficient power availability throughout the year and to minimize the payload thermal variations.

At the same time, the concept of SMOS concept employs a 2D interferometry to reach an enhanced spatial resolution of 40 km compared to classical systems but at the cost of a degraded radiometric sensitivity. That is, studies have shown that averaging both spatially and temporally (over an integration time of 1.2 s) the dual-polarized multi-angular acquisitions provided by SMOS allows a significant improvement of the measurements' radiometric sensitivity [49].

1.7.1.4 Use of SMOS data

More precisely, the acquired signals by each pair of antennas of the interferometric array of SMOS are transferred to a correlator bank where the cross-correlation products are performed and calibrated prior any image reconstruction [50]. Each 300 ms, an image containing the Fourier components of the brightness temperatures of an observed scene (visibilities) is constructed in both polarizations [8]. These images are transferred to the Instrument Control Unit where they are averaged over time and acquisition angles producing every 1.2 s two images (one per polarization).

At this stage, the onboard treatment is finished and the 1.2s-produced images are forwarded to the ground-based image reconstruction data centers. At the ground, several reconstruction algorithms based on the Fourier-transform relationship between visibilities and T_B's and the previously described retrieval approaches are launched to reconstruct brightness temperature maps of the Earth's surface.

So far, two main classes of issues were identified as a source of contamination of quality degradation of SMOS data, radio-frequency interferences and calibration anomalies.

1.7.1.4.1 Interference correction: The Radio-Frequency Interference (RFI), essentially caused by illegal emitters and out-of-band emissions, is a highly time- and polarization-dependent variable which can occur both in aliased or alias-free regions of the reconstructed images. These contaminations were for the first time highlighted by SMOS which wasn't initially designed to deal with this type of data corruptions.

Owing to their highly corrupting effect, several RFI detection and mitigation algorithms were developed and implemented in SMOS.

The first RFI characterization approach used in SMOS is based on an iterative minimization (or

an optimization problem with a predefined criterion) of the residual between a modeled and observed brightness temperature map affected by a RFI source starting from a initial guess [51]. This approach attempts to provide an accurate estimation of the geolocation of RFI sources so as they can be turned off by the national spectrum management agencies.

An other RFI detection criterion employed in SMOS is based on the idea that a strong RFI source can be represented by an observed T_B that ranges outside from predefined dynamic thresholds. Then, lower sources are also detected using either a test on the angular signature anomaly of the halved 1^{st} Stokes parameter or, if enough T_Bs remain, a retrieval is performed and the residuals between retrieved and modeled values are compared to a threshold dictated by the observation radiometric uncertainty. At the end, flagged RFI values are removed and a new retrieval is performed using solely the clean T_B values [52].

Several other approaches were proposed but haven't been considered for implementation yet. We quote for instance an approach to be used in the full-polarimetric mode based on a first detection of RFI sources through the application of several masks, and once a pixel is flagged, a differentiation between land and ocean pixels is set to take account of their different angular signature. Next in the mitigation step, ocean corrupted pixels are replaced by their corresponding mean ones computed from all clean snap-shots during a predefined time period, while in the case of land pixels, an interpolation methodology combining object's removal and inpainting algorithms [53] is performed.

1.7.1.4.2 Calibration: It is needless to say that a good calibration scheme is essential to ensure the expected scientific return. In this view, a classical onboard calibration approach [54] is used to calibrate the very large field-of-view noise injection radiometer in SMOS in addition to an internal calibration which is performed using different noise injection sources to regularly monitor all the key elements of the interferometer.

Furthermore, external calibrations based on absolute radiometric comparisons are also performed with the interferometer pointed toward a well-known point of known temperature. This external calibration lasts less than a complete orbit period (100 min).

1.7.1.5 SMOS products

Similarly to other Earth observation missions, the SMOS products are processed along a chain of several levels starting from the downlinked payload data in their original form comprised of the instrument observation data and housekeeping telemetry. These products are classified according to the level of processing and the scientific aspect (table 1.1).

Table 1.1: SMOS products

Level	product	Sub-product	Latency	Gridding
L1	Multi-incidence angle brightness temperatures in the top of the atmosphere	Geolocated on a ISEA 4H9 grid	Near-real time	15 km
		Geolocated on a N256 gaussian grid	Near-real time	30-50 km
L2	Soil moisture	Swath-based soil moisture	8-12 hours	15 km
		Vegetation optical depth	8-12 hours	15 km
		Near real-time soil moisture	daily	1 km
	Sea surface salinity	Swath-based sea surface salinity	8-12 hours	15 km
L3	Soil moisture	Swath-based soil moisture maps	1, 3, 9 day(s), monthly, seasonal, annual	25 km
	Sea surface salinity	Swath-based sea surface salinity maps	3 and 9 days, monthly, seasonal, annual	Regular grid of 0.25°x0.25°
	Sea Ice thickness	-	Daily, monthly, seasonal, annual	12.5 km
L4	Soil moisture	Root-zone soil moisture	daily	1 km
	Sea surface salinity	Fused product	3-days, 9-days, monthly, seasonal, annual	Regular grid of 0.25°x0.25°

1.7.2 Aquarius/SAC-D

Figure 1.12: Aquarius artist's view

1.7.2.1 Introduction

Aquarius was officially declared dead on July, 2015. It was a combined active/passive L-band microwave instrument designed to map the Sea Surface Salinity (SSS) field of the oceans from space (figure 1.12). Aquarius was carried aboard the Aquarius/SAC-D (Satellite de Aplicationes Cientificas) mission as a partnership between the U.S and Argentine space agencies, NASA and CONAE, launched from the Vanderberg Air Force Base on June 10, 2011 [57].

The Aquarius primary objectives concerned the monitoring of the seasonal and inter-annual variation of the large scale features of the surface salinity field in the open ocean. Based on these observations, scientists try to model the coupling between global water cycle, ocean circulation and climate in a way to better understand the complete surface atmosphere/ocean hydrological cycle. Likewise, the Aquarius

mission was intended to reveal how oceans respond to the effects of evaporation, precipitation, ice melt, and river runoff on a seasonal time scale.

Aquarius provided SSS maps with a spatial resolution of 150 km and a global accuracy of 0.2 psu (practical salinity unit) on a monthly basis and a complete global survey every seven days.

1.7.2.2 Mission description

Aquarius operated in the L-band at 1.413 GHz, the frequency at which the brightness temperature is the more sensitive to changes in salinity (Swift and McIntosh, 1983; Lagerloef, Swift and LeVine, 1995). Since salinity measurements in the L-band are highly affected by either surface roughness (namely oceans waves) and the Faraday rotation due to propagation through the ionosphere [58], Aquarius included both a scatterometer and a radiometer that share approximately the same frequency and footprint. More precisely, the scatterometer provided auxiliary measurements to the radiometer to help correct for the roughness effect. On the other hand, additional measurements delivered by a polarimetric channel were combined to the Aquarius measurements to correct for the induced Faraday rotation angle [55].

At the same time, the Aquarius instrument provided rain, wind at ocean's surface and sea ice measurements thanks to a microwave radiometer MWR composed of two separate radiometers operating in the Ka-band (36.5 GHz) and the K-band (23.8 GHz). Each radiometer operated in a pushbroom mode and comprised eight beams providing polarimetric measurements.

Finally, a sun-synchronous orbit was chosen for the Aquarius/SAC-D mission with the antennas pointing toward the nighttime side of the orbit to reduce the effect of the ocean reflection and sun contamination. Aquarius achieved a seven-day total coverage of the Earth's surface thanks to a swath of about 390 km performed by three elliptical beam footprints (figure 1.13). Table 1.2 gives an overview of the Aquarius main functional parameters.

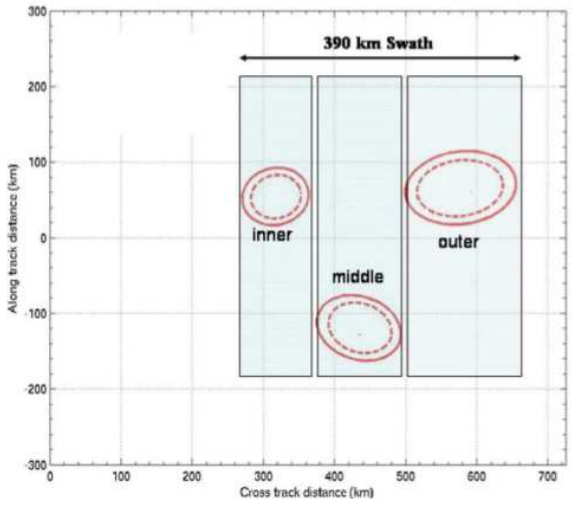

Figure 1.13: Aquarius antennas' beams [55]

Table 1.2: Aquarius measurement and instrument functional requirements [55]

Orbit		**Antenna**	
Altitude	657 km	Main Reflector	2.5 m offset
Sun-synchronous	6 pm ascend	Beam look angles (deg)	25.8, 33.8, 40.3
Inclination	98 deg	Local incidence (deg)	28.7, 37.8, 45.6
Coverage	7 day global	Resolution	76x94, 84x120,
Swath	390 km		96x156 km
Radiometer		**Scatterometer**	
Frequency	1.413 GHz	Frequency	1.26 GHz
Polarization	Polarimetric	Polarization	HH, VH, HV,
Sample time	10 ms		VV
Integration time/sample	9 ms	PRF	100 Hz
NEDT (5.76 seconds)	0.06K	Pulse width	0.98 ms
Calibration Stability	0.13K	Calibration	0.1 dB

1.7.2.3 Aquarius instrument

As originally conceived, the Aquarius instrument comprised an antenna in the form of a 2.5-m offset parabolic reflector fed by three horns and deployed using a single-fold mechanism. The reflector was designed to reflect the beams of three Dicke radiometers arranged in a pushbroom fashion through a pointing in the cross-track direction at respective angles 25.8°, 33.8° and 40.3° out from the nadir. The three beams achieve respectively the following spatial resolutions, 76×94 km, 84×120 km and 96×156 km (figure 1.13).

A long term stability (within 0.13 K) over at least 7 days and a good thermal control (changes less than 0.1°C) were required for an efficient retrieval of salinity over the entire globe [59]). To this end, the Aquarius radiometers included two internal reference sources (a noise diode and a Dicke load) for calibration and were designed in a way to reduce the impact of radio-frequency interferences (RFIs) essentially caused by ground-based air surveillance radars. Besides, the Aquarius-based RFI mitigation approach consisted in performing a sampling at a sufficiently high rate in order to relatively facilitate the identification and the mitigation of RFIs without the complete loss of information [56].

At the same time, the Aquarius instrument carried a scatterometer responsible of providing real-time estimations of sea surface roughness and wind speed. It comprised a L-band radar system which sequenced among the three radiometers feeds and at two polarizations. The synchronization between the scatterometer and the radiometers allowed the simultaneous monitoring of the same ocean pixel at VV, HV, VH and HH polarization combinations. Besides, using real data algorithms, the measured surface backscatter by the scatterometer was converted to corrections to the radiometer's brightness temperatures.

1.7.2.4 Use of Aquarius/SAC-D data

Eventhough it achieved a relatively low spatial resolution, Aquarius provided conversely salinity maps of much greater radiometric accuracy than historical data. As a matter of fact, Aquarius allowed to detect variations less than the mean change of salinity levels in the open ocean of the order of two parts per 10,000, equivalent to about one-eighth of a teaspoon of salt in a gallon of water [57].

Salinity maps were derived from the Aquarius brightness temperature measurements after the correction for other emissions sources and induced errors by surface roughness and Faraday rotation. The Aquarius ground-based reconstruction algorithms were developed using the idea that salinity modulates the seawater dieletric constant which is related to the brightness temperature at lower frequencies (Klein and Swift 1977).

More particularly, the Aquarius radiometers' measurements were converted to antenna temperatures (T_A) using a calibration approach by means of a matched load. Then, using ground-based salinity retrieval algorithms, these T_A measurements were transformed into flat ocean surface brightness temperatures (T_B) and afterwards converted to sea surface salinity maps. These maps were termed in a post-processing step with measurements provided by the scatterometer and the polarimetric channel in addition to auxiliary wind speed and wind direction data from NCEP so as to subtract contaminations due to sea surface roughness and Faraday rotation.

1.7.2.5 Aquarius/SAC-D products

Table 1.3 summarizes the main delivered products by the Aquarius/SAC-D mission during its operational phase.

Table 1.3: Aquarius/SAC-D products

Products	Sub-products	Level	Latency	Gridding
Soil Moisture products	Global SM	L2	weekly	beams'
	Global gridded SM	L3	daily, monthly, seasonally, and annually	1°
	SM climatology	L3	-	1°
Polar gridded products	Brightness temperature	L3	weekly	1°
	Sea surface salinity	L3	weekly	1°
	Normalized radar cross section	L3	weekly	1°
Additional products	Ocean surface wind speed	L3	daily, weekly, and seasonally	1°

1.7.3 Soil Moisture Active and Passive (SMAP) mission

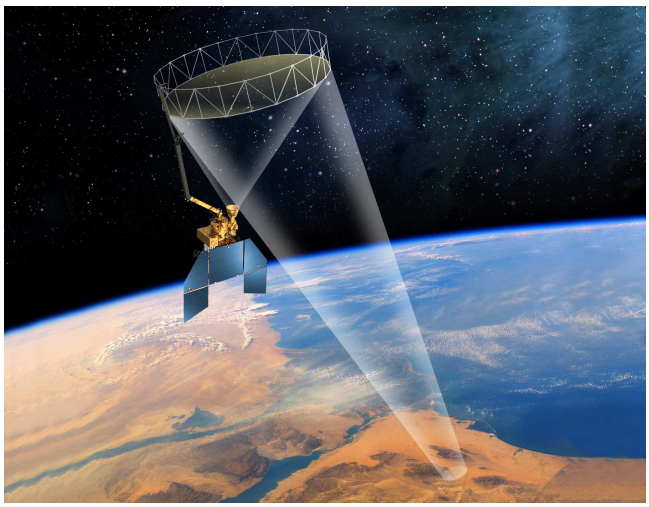

Figure 1.14: SMAP artist's view

1.7.3.1 Introduction

The Soil Moisture Active Passive (SMAP) mission was developed by the National Aeronautics and Space Administration (NASA) in response to the National Research Council's Decadal Survey (figure 1.14). The SMAP instrument was in the first place designed with the intention to map soil moisture (SM) globally with higher resolution, sensitivity, area coverage, and revisit time than recent systems [60] to significantly improve estimations of water, energy and carbon transfers between the land and the atmosphere. It was successfully launched on January 31, 2015.

This initiative comes as a response to the ongoing quest for high-resolved maps expressed across many scientific disciplines including hydrology, climatology, meteorology. In this view, the SMAP products are mainly expected to help scientists to i) enhance their understanding of the transfers between the land and the atmosphere, ii) improve their ability to predict natural hazards like floods and droughts, and iii) ameliorate weather forecasting and crop yield predictions. In this perspective, SMAP includes a combination of active and passive imaging instruments in addition to sophisticated modeling and advanced data assimilation algorithms derived from the canceled Hydros mission [61] as well as efficient radio frequency interference (RFI) detection and mitigation features.

Unfortunately, the SMAP radar stopped transmitting few months after launch due to an anomaly involving the radar's high-power amplifier (HPA). The latter was designed to boost the power level of the radar's pulse and ensure the energy scattered from Earth's surface to be accurately measured.

1.7.3.2 Mission requirements

Based on the scientific objectives of SMAP to collect measurements of surface soil moisture and freeze/thaw state, together termed with the hydrosphere state, the SMAP's measurement approach and functional requirements were accordingly established (table 1.4). Of course at the present time, only the radiometer is operating and delivering measurements.

Table 1.4: SMAP's measurement and instrument functional requirements

Orbit		**Antenna**	
Altitude	685 km	Main reflector	6.5 m
Sun-sunchronous	6 am/6 pm	Rotation	14.6 rpm
Coverage	3 days	Incidence angle	between 35-50°
Swath	~1000 km		
Radiometer		**Radar**	
Frequency	1.41 GHz	Frequency	1.26 GHz
Polarization	V, H, U	Polarization	VV, HH, HV
Resolution	40 km	Resolution	10 km
Relative accuracy	1.5 K	Relative accuracy	0.5 dB

1.7.3.3 SMAP concept

The SMAP instrument includes a 6-m diameter, conically scanning, deployable mesh reflector antenna, shared by both a radiometer and a radar that use a single L-band feed with both a dual-polarization and dual-frequency capability (1.41 GHz for the radiometer and 1.26 GHz for the radar). The reflector rotates about the nadir at 14.6 rpm, producing a conically scanned antenna beam with an incidence angle of 40° (figure 1.15).

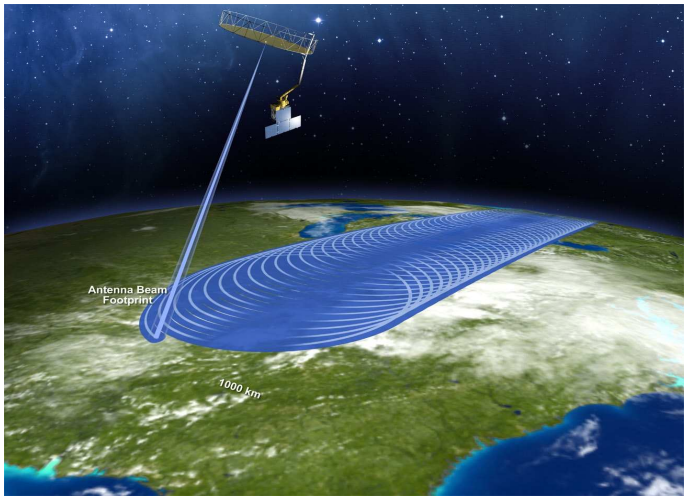

Figure 1.15: SMAP's scanning configuration

More generally, radars are capable of a highly resolved imaging but at the expense of a low accuracy and a high dependence on surface roughness, vegetation structure, and water content. Various approaches for the retrieval of soil moisture from radar backscatters were intensively investigated [62, 63], nevertheless they adequately perform only in low-vegetation and water content conditions. On the other hand, although their relatively coarse spatial resolution, L-band radiometers measure soil moisture with higher accuracy even in the presence of moderate vegetation and the retrieval processes are well established.

To overcome the individual limitations of both the passive and the active techniques, the SMAP measurement approach was thought in a way to combine both procedures to achieve an intermediate spatial resolution between radar's and radiometer's while maintaining the required retrieval accuracy.

More particularly, the SMAP's passive system consists of a Dicke radiometer that uses real aperture at 1.41 GHz to measure the Earth's brightness temperatures with a spatial resolution of 40 km. While the active system consisted of a not fully polarimetric radar that only contained VV, HH and HV channels. The radar employed pulse compression in range and Doppler discrimination in azimuth to subdivide the antenna footprint, and thus achieved during the first months, owing to the conical scan configuration, a varying spatial resolution across the swath of 360 m-1.2 km.

In order to reach the spatial resolution requirements (3-km for the freeze/thaw and 9-km for soil moisture products), the SMAP approach was thought to combine the retrieval accuracy of the radiometer with the high resolved measurements from the radar to produce a 3- and 9-km intermediate resolution soil moisture maps with the radiometer's accuracy.

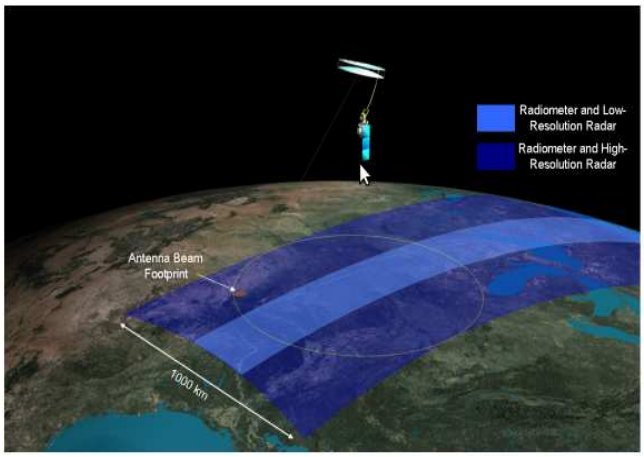

Figure 1.16: SMAP's measurement geometry

1.7.3.4 Error correction

Identically to other L-band concepts, the SMAP's 6 *A.M.*/6 *P.M.* sun-synchronous low Earth orbit measurements when termed with auxiliary U-channel data allow to correct for the Faraday rotation.

In like manner, due to the demonstrated deleterious impact of RFIs on L-band soil moisture measurements by SMOS, a set of innovative strategies for RFI characterization, detection and mitigation were from the beginning implemented in SMAP. More precisely, SMAP employs a combination of space-flight instrument hardware and ground-based science processing algorithms to relatively get rid of the corrupting effects of RFIs.

At the level of the radiometer, the SMAP characterization approach of the RFI environment is based on: i) prediction by exploiting known properties of existing sources, ii) comparison with observations from ground-based or aircraft radiometers, and iii) analysis of other satellite data sets namely from SMOS and Aquarius [64]. Also, the SMAP radiometer, unlike conventional systems, includes a new advanced digital processing (DSP) back-end which allows a synchronous sampling of the receiver output with the pulse-repetition interval of the radar and provides a large amount of telemetry data that initialize the RFI detection ground-based algorithms.

The detection of RFIs is performed using a kurtosis approach based on a test of the Gaussianity of the acquired signals and the use of data samples with different time and frequency resolutions. Once detected, RFIs are removed using a single maximum PD (MPD) algorithm [64]. Besides, the SMAP's RFI mitigation approach is performed in-between the radiometric calibration and the step of conversion of antenna temperatures.

1.7.3.5 Use of SMAP data

Regardless of the radar failure, the disaggregation methodology of brightness temperature from the SMAP active/passive measurements as originally implemented consisted in a time-series approach that exploits the relationship linking changes in brightness temperature to the radar backscatter in addition to classical passive SM retrieval processes. Besides, using a set of sequential measurements at a fixed location with the same look angle and for a particular season, previous approach yielded, at least in first months, the mapping of soil moisture with a spatial resolution of the order of 10 km [65, 66].

Not only SM measurements but also transitions between freeze/thaw landscapes were intended to be identified using SMAP by exploiting the dynamic temporal response of the radar backscatter to differ-

ences in the aggregate landscape dielectric constant particularly occurring in the freeze/thaw transitions [67].

1.7.3.6 SMAP products

At the present time, the raw data transmitted from the SMAP instrument to the ground station mainly comprise chronologically sorted radiometer measurements that are processed in four levels (table 1.5).

Table 1.5: SMAP's products

Level	Product	Gridding	Latency
L1	Radiometer data in Time-order	-	12 hours
	Radiometer TB in Time-order	36x47 km	12 hours
	Radiometer TB in Half-Orbits	36 km	12 hours
L2	Radiometer SM	36 km	24 hours
L3	Radiometer SM	36 km	50 hours
L4	Surface & root-zone SM	9 km	7 days
	Carbon Net Ecosystem Exchange	9 km	14 days

1.8 Summary

Mainly motivated by the irreversible and accelerated global warming, Earth observation from space has become, more than ever, paramount within the scientific community. The understanding of the exchange and transfer processes between the Earth's surface and the atmosphere is the major scientific objective of Earth observation airborne and spaceborne concepts through the measurement of the two key parameters, *soil moisture* and *ocean salinity*.

When interacting with the Earth's surface, microwave frequencies are to be preferred in Earth observation due to their high dependence on soil moisture and ocean salinity. They also present an all-weather and all-time capability to penetrate the surface canopy and the ground and are weakly affected by the atmosphere.

Depending on the scientific objectives, either passive or active microwaves sensors are to be chosen. In one hand, passive sensors (radiometers) are highly sensitive noise receivers but achieve coarse spatial resolutions that can be relatively enhanced using the *synthetic aperture* technique inspired from radioastronomy. On the other hand, active sensors (radars) achieve finer spatial resolutions but at the cost of a low accuracy and a high dependence on the surface topography.

As has been noted, existing Earth observation spaceborne concepts are either purely passive or combined passive/active. Table 1.6 gives an overview of recent L-band dedicated passive Earth observation remote sensing concepts.

Table 1.6: Comparative table of recent L-band dedicated Earth observation concepts

Satellite	Instruments	Swath	Orbit	Products	Accuracy	Spatial resolution	Revisit time	Science objectives
Aquarius	-2.5-m rotating antenna -3 L-band (1.41 GHz) radiometers -L-band (1.26 GHz) scatterometer	390 km	657 km Sun-synchronous 6pm ascend	Soil moisture	0.04m³/m³ for moderate vegetated areas	~100 km (1 degree)	7 days	Determination of the ocean response to effects of evaporation, precipitation, ice melt , and river runoff.
				Sea surface salinity	0.2 psu	36 km		
SMOS	2D Y-shaped interferometric radiometer (MIRAS)	~1000 km	758 km 6 A.M/ 6 P.M Sun-synchronous	Soil moisture	0.04m³/m³	Less than 50 km	2-3 days	-Enhancement of the understanding of exchange processes between the surface and the atmosphere ; and -Characterization of sea ice and snow-covered surfaces.
				Sea surface salinity	0.5 psu	Less than 50 km		
SMAP	-6-m rotating antenna -L-band (1.41 GHz) radiometer -L-band (1.26 GHz) radar	~1000 km	650 km 6 A.M/ 6 P.M Sun-synchronous	Soil moisture	No greater than 0.04m³/m³	Radar (3 km) Radiometer (~40 km)	3 days	-Understanding of the linkage between water, energy and carbon cycles; -Estimation of global water and energy fluxes at the land surface; -Improvement of climate forecasting, flood prediction and water monitoring.

1.9 Prospects

Table 1.7 depicts the expressed users' requirements in the specific Earth observation application of the study of *coastal zones* [68] (see next chapter for more details). With this in mind, current missions seem to reach their limits and fail to respond to such hydrological applications in the *local scale* where sub-kilometric resolutions are required [69].

Table 1.7: Coastal areas users' requirements [11]

	Necessary	useful	optimal
Spatial resolution (km)	**3-10**	**1-3**	**0.1-1**

Furthermore, in addition to the fact that the SMOS satellite has been successfully operating in space since 2009 with an extended end-of-life to around 2019, 2015 has known two major incidents, the official loss of Aquarius mission on July, 2015 and the radar failure of the SMAP mission few months after launch. Seeing that the expected 10-km resolution of the SMAP instrument is strictly linked to the combined passive/active observation procedure, the best optimistic spatial resolution value currently achievable by SMAP is of the order of radiometer's ($\sim$ 50 km).

As can be seen, both previous issues bring to attention that data continuity is not even ensured at the low resolution that characterizes theses sensors.

With all of this, a new mission, named of **SMOS-Next**, currently in the study phase within the SMOS team at CESBIO was proposed as the new generation to follow the SMOS mission. It comes as an

answer to previous issues with the challenging objectives of an enhancement of the spatial resolution up to sub-kilometric orders using solely passive sensors without degrading the current achievable radiometric sensitivity. The proposed concept relies on a new revolutionary spatio-temporal interferometric aperture synthesis which is currently under theoretical and numerical validation [71].

Bibliography

[1] Schmugge et al., "Passive Microwave Remote Sensing of Soil Moisture," *EARSel Advances in Remote Sensing*, vol. 2, no. 2 - VI, 1993.

[2] C.J. Koblinsky et al., "SEA SURFACE SALINITY FROM SPACE: SCIENCE GOALS AND MEASUREMENT APPROACH," *Radio Sci.*, vol. 38, p. 8064, 2003.

[3] Eugene A. Sharkov "Passive Microwave Remote Sensing of the Earth: Physical Foundations," *Springer*, 2003.

[4] F. T. Ulaby, R. K. Moore, and A. K. Fung, "Microwave Remote Sensing: Active and Passive," *Microwave Remote Sensing Fundamentals and Radiometry*, vol. 1, 1981.

[5] David M. Le Vine, "Synthetic Aperture Radiometer Systems," *IEEE transactions on microwave theory and techniques*, vol. 47, no. 12, December 1999.

[6] A. R. Thompson, J. M. Moran, and G. W. Swenson, "Interferometry and Synthesis in Radio Astronomy," New York: Wiley, 1986.

[7] David M. Le Vine, "The sensitivity of synthetic aperture radiometers for remote sensing applications from space," *Radio Sci.*, vol. 25, no. 4, pp. 441-453, 1990.

[8] I. Corbella, N. Duffo, M. Vall-llossera, and A. Camps, "The visibility function in interferometric aperture synthesis radiometry," *IEEE Transaction on Geoscience and Remote Sensing*, Vol. 42, No. 8, pp. 1677-1682, ISSN: 0278-0062.

[9] E. Anterrieu and A. Khazaal, "Brightness Temperature Map Reconstruction from Dual-Polarimetric Visibilities in Synthetic Aperture Imaging Radiometry," *IEEE transactions of geoscience and remote sensing*, vol. 46, no. 3, march 2008.

[10] Alwyn Wootten, "The Atacama Large Millimeter/Submillimeter Array," *Activity White Paper for Astro2010 Program Prioritization Panel*.

[11] D. M. Le Vine et al., "ESTAR: A synthetic aperture microwave radiometer for remote sensing applications," *Proc. IEEE*, vol 82, pp. 1787-1801, Dec. 1994.

[12] D. M. Le Vine, T. J. Jackson, C. T. Swift, M. Haken, and S. W. Bidwell, "ESTAR Measurements During the Southern Great Plains Experiment (SGP99)," *IEEE Transaction on Geoscience and Remote Sensing*, vol 39, no. 8, August 2001.

[13] M. Martin-Neira and J. M. Goutoule, "MIRAS-A two dimensional aperture synthesis radiometer for soil-moisture and ocean-salinity ob- servations," *ESA Bull.*, vol. 92, pp. 95-104, 1997.

[14] A. H. Barrett and A. E. Lilley, "Mariner 2 microsave observations of Venus," *Sky and Telescope*, 25(4), 192-195, 1963.

[15] T. J. Schmugge and T. J. Jackson, "Mapping soil moisture with microwave radiometers," *Meteorol. Atmos. Phys.*, vol. 54, pp. 213-223, 1994.

[16] A. Chanzy, T. J. Schmugge, J.-C. Calvet, Y. Kerr, P. van Oevelen, O. Grosjean, and J. R. Wang, "Airborne microwave radiometry on a semi-arid area during Hapex-Sahel," *J. Hydrol.*, vol. 188-189, pp. 285-309, 1997.

[17] Y. H. Kerr and E. G. Njoku, "On the use of passive microwaves at 37 GHz in remote sensing of vegetation," *Int. J. Remote Sens.*, vol. 14, no. 10, pp. 1931-1943, 1993.

[18] Y. H. Kerr and E. G. Njoku, "A semiempirical model for interpreting microwave emission from semiarid land surfaces as seen from space," *Int. J. Remote Sens.*, vol. 28, pp. 384-393, May 1990.

[19] A. C. M. Beljaars, P. Viterbo, M. J. Miller, and A. K. Betts, "The anomalous rainfall over the United States during July 1993: Sensitivity to land surface parameterization and soil moisture," *Mon. Weather Rev.*, vol. 124, pp. 362-383, 1996.

[20] G. Balsamo, J. F. Mahfouf, S. Belair, and G. Deblonde, "A land data assimilation system for soil moisture and temperature: An information content study," *J. Hydrometeorol.*, vol. 8, pp. 1225-1242, 2007.

[21] C.T. Swift and R.E. McIntosh, "Considerations for Microwave Remote Sensing of Ocean-Surface Salinity," *IEEE Trans. Geoscience Electronics*, vol. G.E.-21, no. 4, pp. 480-491, October 1983.

[22] D. W. Marquard, "An algorithm for least-squares estimation of non linear parameters", *J. Soc. Ind. Appl. Math*, vol. 11, pp. 431-441, 1963.

[23] Jackson, T. J. and T. J. Schmugge, "Vegetation effects on the microwave emission from soils", *Rem. Sens. Environ.*, vol. 36, pp. 203-212, 1991.

[24] M. C. Dobson, F. T. Ulaby, M. T. Hallikainen, and M. A. El-Rayes, "Microwave dielectric behavior of wet soil – Part II: Dielectric mixing models", *IEEE Trans. Geosci. Rem. Sens.*, vol. GE-23, pp. 35-46, 1985.

[25] J. R Wang and T. J. Schmugge, "An empirical model for the complex dielectric permittivity of soils as a function of water content", *IEEE Trans. Geosci. Rem. Sens.*, vol. 18, pp. 288-295, 1980.

[26] Mironov, V. L., L. G. Kosolapova, and S. V. Fomin, "Physically and mineralogically based spectroscopic dielectric model for moist soils", *IEEE Trans. Geosci. Rem. Sens.*, vol. 47(7), pp.2059-2070, 2009.

[27] CBSA, UoR, TV and INRA, "Algorithm Theoretical Basis Document for the SMOS Level 2 Soil Moisture", October 24, 2014.

[28] SMOS Team, P. Spurgeon, and S. Delwart, "SMOS L2 OS Algorithm Theoretical Baseline Document", September 5, 2014.

[29] Y. H. Kerr, J. Font, P. Waldteufel, and M. Berger, "The soil moisture and ocean salinity mission: SMOS", *ESA Earth Observation Quarterly*, no. 66, pp. 18-25, 2000.

[30] T. Wilheit, A. T. C. Chang, and A. S. Milman, "Atmospheric corrections to passive microwave observations of the ocean", *Boundary-Layer Meteorology*, vol. 18, no 1, pp. 65-77, 1980.

[31] P. O'Neill, S. Chan, E. Njoku, T. Jackson, and R. Bindlish, "Algorithm Theoretical Basis Document Level 2 & 3 Soil Moisture (Passive) Data Products", December 9, 2014.

[32] L. A. Klein and C. T. Swift, "An Improved Model for the Dielectric Constant of Sea Water at Microwave Frequencies". *IEEE Journal of Oceanic Engineering*, vol. 2, no. 1, January, 1977.

[33] E. Njoku and L. Li, "Retrieval of Land Surface Parameters Using Passive Microwave Measurements at 6-18 GHz". *IEEE Trans. Geosci. Rem. Sens.*, vol. 37, pp. 79–93, 1999.

[34] Owe, M., R. De Jeu, and J. Walker. "A methodology for surface soil moisture and vegetation optical depth retrieval using the microwave polarization difference index", *IEEE Trans. Geosci. Rem. Sens.*, vol. 39, pp. 1643-1654, 2001.

[35] Owe, M., R. De Jeu, and J. Walker, "A methodology for surface soil moisture and vegetation optical depth retrieval using the microwave polarization difference index", *IEEE Trans. Geosci. Rem. Sens.*, vol. 39, pp. 1643-1654, 2001.

[36] Choudhury, B. J., T. J. Schmugge, A. Chang, and R. W. Newton, "Effect of surface roughness on the microwave emission from soil", *J. Geophys. Res.*, vol. 84(C9): 5699-5706, 1979.

[37] F. T. Ulaby, R. K. Moore, and A. K. Fung, "Microwave Remote Sensing - Active and Passive", vol. 1. Norwood, USA: Artech House, 1981.

[38] Y. H. Kerr, P. Waldteufel, P. Richaume, P. Ferrazzoli, and J. P. Wigneron, "SMOS level 2 processor soil moisture algorithm theoretical basis document (ATBD)," CESBIO, Toulouse, France, ATBD SO-TN-ESL-SM-GS-0001, V3.a, Oct. 15, 2008.

[39] D. -H. Chang, and S. Islam, "Estimation of Soil Physical Properties Using Remote Sensing and Artificial Neural Network", *Remote Sensing of Environment*, vol. 74 (3): 534-544, 2000.

[40] D. -H. Chang, and S. Islam, "An Artificial Neural Network Approach For Soil Moisture Retrieval Using Passive Microwave Data", PhD of Curtin University of Technology, March 2010.

[41] C. Jiménez, D. B. Clark, J. Kolassa, F. Aires, and C. Prigent, "A joint analysis of modeled soil moisture fields and satellite observations", *JOURNAL OF GEOPHYSICAL RESEARCH*, vol. 118, no. 12, p. 6771-6782, 27 June 2013.

[42] N.J. Rodríguez-Fernández et al., "Soil moisture retrieval from SMOS observations using neural networks", *Summary Report of project SMOS+NN.*

[43] Y. H. Kerr, "The SMOS mission: MIRAS on RAMSES. A proposal to the call for Earth explorer opportunity mission," CESBIO, Toulouse, France, Proposal 30/11/1998.

[44] J.-P. Wigneron, P Waldteufel, A. Chanzy, J.-C. Calvet, and Y. Kerr, "Two-D microwave interferometer retrieval capabilities of over land surfaces (SMOS Mission)," *Remote Sens. Environ.*, vol. 73, no. 3, pp. 270-282, 2000.

[45] P. Waldteufel, J. Boutin, and Y. Kerr, "Selecting an optimal configuration for the soil moisture and ocean salinity mission," *Radio Sci.*, vol. 38, 2003.

[46] Y.H. Kerr et al., "The SMOS mission: new tool for monitoring key elements of the global water cycle," *IEEE, Institute of Electrical and Electronics Engineers*, 2010, 98 (5), pp. 666-687.

[47] A. Lannes, E. Anterrieu, and K. Bouyoucef, "Fourier Interpolation and Reconstruction via Shannon-type Techniques; Part I: regularization principle," *Journal of Modern Optics*, Taylor & Francis, 1994, 41(8), pp.1537-1574.

[48] A. Lannes, E. Anterrieu, and K. Bouyoucef, "Fourier Interpolation and Reconstruction via Shannon-type Techniques; Part II: technical developments and applications," *Journal of Modern Optics*, Taylor & Francis, 1996, 43(1), pp.105-138.

[49] A. Camps, M. Vall-llossera, L. Batres, F. Torres, N. Duffo, I. Corbella, "Retrieving sea surface salinity with multiangular L-band brightness temperatures: Improvement by spatiotemporal averaging," *Radio Science*, vol. 40, issue 2, April 2005.

[50] E. Anterrieu, "A resolving matrix approach for synthetic aperture imaging radiometers," *IEEE Trans Geosci. Remote Sens.*, vol. 42, no. 8, pp. 1649-1656, Aug. 2004.

[51] E. Anterrieu, A. Khazaal, F. Cabot, and Y. Kerr, "Geolocation of RFI sources with sub-kilometric accuracy from SMOS interferometric data," *Remote Sensing of Environment*, Vol. 180, pp. 76-84, 2016.

[52] P. Richaume et al., "RFI in SMOS measurements: Update on detection, localization, mitigation techniques and preliminary quantified impacts on soil moisture products," *IGARSS*, July, 2014.

[53] A. Criminisi, P. Perez, and K. Toyama, "Object Removal by Exemplar-Based Inpainting," *Proceedings of the 2003 IEEE Computer Society Conference on Computer Vision and Pattern Recognition*, Vol. 2, pp. 721-728, Madison, WI, USA, 16-22 June 2003.

[54] A. Colliander et al., "Development and calibration of SMOS reference radiometer," *IEEE Trans. Geosci. Remote Sens.*, vol. 45, no. 7, pt. 1, pp. 1967-1977, Jul. 2007.

[55] D. M. Le Vine, G. S. E. Lagerloef, F. R. Colomb, S. H. Yueh, and F. A. Pellerano, "Aquarius: An Instrument to Monitor Sea Surface Salinity From Space," *IEEE Trans. Geosci. Remote Sens.*, vol. 45, no. 7, July 2007.

[56] D. M. Le Vine, P. de Matthaeis, C. S. Ruf, and D. D. Chen, "Aquarius RFI Detection and Mitigation Algorithm: Assessment and Examples," *IEEE Trans. Geosci. Remote Sens.*, vol. 52, no. 8, August 2014.

[57] G. Lagerloef et al., "THE AQUARIUS/SAC-D MISSION," *Oceanography*, vol.21, No.1.

[58] D. M. Le Vine and S. Abraham, "The effect of the ionosphere on remote sensing of sea surface salinity from space: Absorption and emission at L-band," *IEEE Trans. Geosci. Remote Sens.*, vol. 40, no. 4, pp. 771-782, Apr. 2002.

[59] W. J. Wilson, A. Tanner, F. Pellerano, and K. Horgan, "Ultrastable radiometers for future sea surface salinity missions," JPL, Pasadena, CA, Apr. 2005. Jet Propulsion Lab. Int. Rep. D-31794.

[60] D. Entekhabi et al., "The Soil Moisture Active Passive (SMAP) Mission," *IEEE Trans. Geosci. Remote Sens.*, Vol. 98, No. 5, May 2010.

[61] D. Entekhabi et al., "The Hydrosphere State (HYDROS) mission concept: An earth system pathfinder for global mapping of soil moisture and land freeze/thaw," *IEEE Trans. Geosci. Remote Sens.*, vol. 42, no. 10, pp. 2184-2195, Oct. 2004.

[62] C. Notarnicola, M. Angiulli, and F. Posa, "Use of Radar and Optical Remotely Sensed Data for Soil Moisture Retrieval Over Vegetated Areas," *IEEE Trans. Geosci. Remote Sens.*, Vol. 44, No. 4, April 2006.

[63] Yisok Oh, "An Inversion Algorithm For Retrieving Soil Moisture And Surface Roughness From Polarimetric Radar Observation," *IEEE Trans. Geosci. Remote Sens.*, 1994.

[64] J. R. Piepmeier et al., "Radio-Frequency Interference Mitigation for the Soil Moisture Active Passive Microwave Radiometer," *IEEE Trans. Geosci. Remote Sens.*, vol. 52, no. 1, Jan. 2014.

[65] U. Narayan, V. Lakshmi, and T. Jackson, "A simple algorithm for spatial disaggregation of radiometer derived soil moisture using higher resolution radar observations," *IEEE Trans. Geosci. Remote Sens.*, vol. 44, no. 6, pp. 1545-1554, Jun. 2006.

[66] M. J. Escorihuela, Y. J. Kerr, P. de Rosnay, J.-P. Wigneron, J.-C. Calvet, and F. Lemaitre, "A simple model of the bare soil microwave emission at L-band," *IEEE Trans. Geosci. Remote Sens.*, vol. 45, no. 7, pp. 1978-1987, Jul. 2007.

[67] J. Kimball, K. McDonald, S. Frolking, and S. Running, "Radar remote sensing of the spring thaw transition across a boreal landscape," *IEEE Trans. Geosci. Remote Sens.*, vol. 89, no. 2, pp. 163-175, 2004.

[68] Guimei Liu, "Statement of guidance for ocean applications," SoG for Ocean Applications, 2014.

[69] "Earth science and applications from space: National imperatives for the next decade and beyond," Washington, DC, DC, USA, p. 400, 2007.

[70] M. Brown, S. Moran, V. Escobar, D. Entekhabi, "SMOS-Next: USERs' group meeting," Toulouse, CESBIO, January 16-17, 2014.

[71] D. Braun, Y. Monjid, B. Rougé, and Y. Kerr, "Fourier-Correlation Imaging," to be submitted soon.

Chapter 2

EARTH OBSERVATION USERS' NEEDS

Contents

2.1 Introduction

The unprecedented environmental changes globally occurring at the level the planet have risen the question of whether human activity, by its accelerated increase, contribute to a global change of the whole planet, and global warming is the best illustrating example. To answer this question, a robust understanding of the Earth as a living planet termed with its overarching geophysical phenomena is of crucial importance to ensure the emergence of wise sustainability decisions.

The provided data by space-borne Earth observation systems have a direct impact on world sustainability through their capability of providing measurements with valuable information on natural and artificial phenomena occurring at the Earth/atmosphere system. Thanks to its repetitive and frequent coverage capability, Earth observation from space allows to detect changes over various temporal and spatial scales and thus offers the most economical means per unit of coverage of assessing the environmental impact of human activity and the evolution of appropriate action plans for a sustainable development. It is also of a paramount help in the monitoring of the Earth's geophysical parameters that govern the global environmental phenomena such as climate change and natural hazards.

The last decade has known a critical decrease in the number of operating Earth observation missions and most of current remaining systems are well beyond their nominal lifetime (figure 2.1). This threatens more than ever by a dramatic cease in the provision of a wide range of measurements, including Earth radiation, sea surface winds, solar irradiance, etc., that need to be sustained in numerous critical scientific applications such as weather forecasting, El Niño and hurricane predictions, etc.

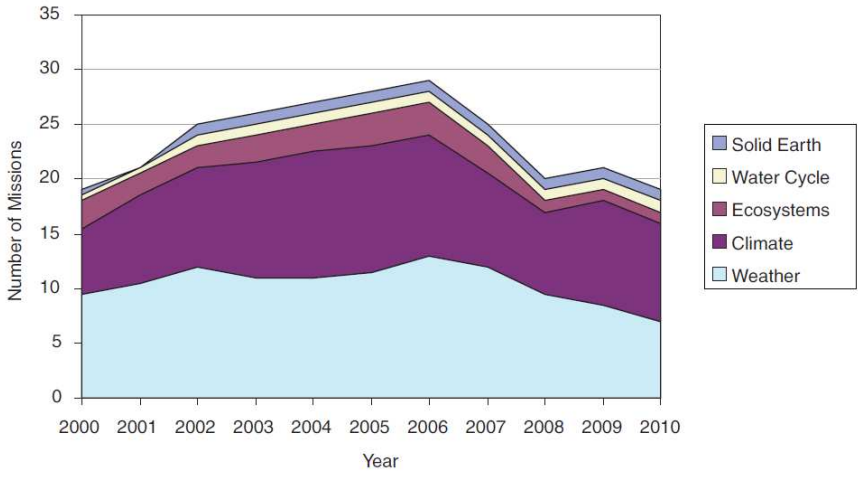

Figure 2.1: Evolution of US Earth observation dedicated missions [1]

2.2 Applications

Earth observation data derived by means of remote sensing are used in numerous critical areas such as the study of climate change, water resources monitoring, natural hazards prediction, weather forecasting, to name a few.

2.2.1 Study of climate change

Global warming, ocean water exchange, and greenhouse emissions are undoubtedly the main causes of the rising of sea levels due to ice loss which is one of the many devastating effects of climate change

particularly felt at the level of coastal areas.

Eventhough climate change has been globally well defined during the last decade, greater challenges have to be met for what concerns the characterization of its local impacts at the level of communities and individuals. To this end, a robust base of scientific information on the Earth's system is undoubtedly required in order to inform decision making and plans for environmental preservation in the local scale.

Landuse and Landcover (LULC) mapping derived from Earth observation data and the geophysical information system (GIS) represents an efficient spatio-temporal tool for the hydrological study of the causes and effects of climate change through the determination of the trend, rate, nature, location and magnitude of climate variations. Moreover, amongst the derived parameters from Earth observations, many are used in the study of climate change including the climate variability derived from precipitation rates, the global carbon cycle deduced from vegetation indices, and the impact of landuse change on climate and desertification monitoring using soil moisture products, to name a few [8].

Remote sensed Earth observation data from space are thus of valuable importance for a successful understanding and management of climate changes. More particularly, the global, frequent, and long-term records of climate variables, such as greenhouse-gas concentrations, sea-ice extent and thickness, and sea-surface temperature and salinity, are of fundamental importance in the assessment of the occurrence of disasters as function of climate changes and in the monitoring of the extent of their effects [2].

2.2.2 Weather prediction & forecasting

The day-to-day weather changes are dictated by various predominant meteorological parameters such as rainfall, temperature, wind speed and humidity. The global and continuous monitoring of these parameters using meteorological is therefore of crucial importance in weather prediction and forecasting.

In particular, weather forecasting is commonly achieved using the so-called numerical weather prediction (NWP) models constructed of the information of two main components. The first one is a model that describes the physical processes occurring in the atmosphere while the second one concerns the knowledge of the initial conditions comprised of current observational data required to run the model using data assimilation techniques. The atmospheric dynamical and physical processes, including precipitation and temperature estimates, humidity, clouds behavior dictated by wind profiles, etc., described by the numerical prediction models, are related to the outgoing terrestrial radiations measured by Earth observation satellites.

2.2.3 Drought and flood monitoring

With the rise of large-scale data, soil moisture has become one the most-used drought indicators. The monitoring and prediction of drought conditions is based on the determination of the root zone soil moisture (RZSM) following two approaches: i) the derivation of the relative & evaporation soil moisture in the root zone from land surface energy fluxes [7] or ii) the assimilation of surface soil moisture into a hydrological model to derive the RZSM. The first approach uses meteorological and remote sensed data to derive the Surface Energy Balance Index while the second approach uses Earth observation data combined with other meteorological and drought statistics as inputs to meteorological models to provide maps of soil water deficit and drought severity.

In like manner, soil moisture products derived from Earth observations termed with climate forecasts are used as entries to flood prediction and landslide susceptibility models to provide maps of flood risk zones [9], rising sea levels, water elevation of rivers and the vulnerability of an area to lanslides. This includes the use of a combination of Digital Elevation modeling derived from SAR measurements, optical

imagery of medium resolution and in-situ measurements so as to detect water level changes and flooded areas.

2.2.4 Disaster management

Natural hazards cause thousands of deaths and billions of dollars of economic losses each year all over the world. Besides, the amount of the economic cost is increasingly rising owing to population growth and coastal investments. Accurate Earth observations are certainly valuable in the determination of the causes and effects of natural hazards required in the implementation of improved prediction and warning strategies, and after-disaster crisis management policies intended to help reduce risks and damages.

In the same perspective, Earth observation using remote sensing starts to become a valuable resource for the assessment of the spatial extent of an earthquake and its effects such as landslides, tsunamis, floods, etc. Likewise, meteorological data are intensively used in hurricane and storm prediction models.

An other application of Earth observation concerns the study of the impact of climate change on human health through the modeling of the occurrence and spreading of diseases and epidemics as function of climate variations [2].

More particularly, various Earth observation parameters are characterized as beneficial in the field of extreme events prediction. We quote precipitation rates, vegetation indices and soil moisture products involved in flooding and landslides monitoring, numerical weather prediction models in addition to weather forecasting.

2.2.5 Agriculture and water resources management

An other aspect of the use of Earth observation data is to monitor global and local precipitations as an indicator parameter of water availability used in agriculture production management and food security issues prevention. Using Earth observation meteorological forecasts termed with rainfall-runoff hydrology models, scientists are able of establishing efficient water management strategies based on water availability to ensure a better balance between the human use of water and natural ecosystems water needs [5]. To this end, satellite imagery, namely visible and near infrared high and medium resolved images, is used to derive precise information on the freshwater availability including the detection of groundwater resources.

Earth observation data derived from space-based satellites such as MODIS allow to assess vegetation indices as well as their spatio-temporal variability. These variables serve to predict drought conditions and other phenomena affecting agriculture such as climate change, globalization, population growth as a result of immigration, and many others.

Since almost 38% of world's land is used for agriculture [6], it is not to mention that global Earth observations are of valuable benefits in farm and productions management. Intensively exploited in crop productions, satellite imagery provide information that serve as a basis to crop health, type and growth monitoring as well as irrigation and fertilizing requirements management.

2.2.6 Forest stocks and carbon concentration assessment

Forest biomass mapping, derived from e.g. Landsat images, is employed to infer carbon stocks in forests required for monitoring fires, one of the main causes of fauna and flora degradation and deforestation [3]. Henceforth, the frequent airborne (LiDAR) and space-borne (MODIS) surveillance termed with thermal remote sensing allow the estimation of the canopy fuel parameters used in the management of fire incidents and the modeling of their effects [8].

Also, the global knowledge of the carbon exchanges between land, atmosphere and oceans, which represents the primary parameter of carbon cycle and its seasonal and inter-annual variability, is paramount in the estimation of the impact of global climate changes, the effects of deforestation and forest participation to atmospheric CO_2 concentrations [4].

Additionally, large satellite imagery enables the monitoring of vast areas of forest through the provision of health evaluation, deforestation and fire damage/risk maps.

Last but not least, the global monitoring of greenhouse emissions is one of the overarching parameters in the assessment of the linkage between the human activity and the climate change.

2.2.7 Ocean management

Comparatively to land-oriented applications, satellite remote sensing is intensively used over oceans. Earth observations provide valuable information on the ocean surface such waves profile, wind speed, sea ice, surface temperature, sea surface salinity, etc.

These parameters are essential in various ocean-oriented applications: i) the assessment of the impact of climate change on marine ecosystems, ii) the management of ocean economic applications such as fisheries and marine transportation, etc. [2].

One of the main issues occurring at the level of the oceans is the rising of sea levels as a result of the thermal expansion of the oceans and ice melting. The monitoring of sea levels by means of space-based altimetry (such as Jason-2) is thus paramount for the determination of the effects of climate change at the local scale and more particularly threats to coastal regions [8].

2.3 Challenges

The numerous challenges that face the new generation of Earth observation systems put emphasis on both the scientific and societal aspects. The new observations are expected to notably strengthen the link between the scientific knowledge and its direct application to the societal demands. For this purpose, a better modeling of the Earth's system through the improvement of weather forecasts and natural hazards predictions, the accurate determination of water resources, the enhanced knowledge of the ocean health, etc., is undoubtedly required. This information base constitutes furthermore the needed scientific platform upon which scientists can stand to arise the alarm bell for urgent political decisions in the sense of environmental preservation.

The definition of the primary combined scientific/societal benefits is of direct influence on the design of the next generation of Earth observation missions and techniques to be developed. Besides, numerous technical, scientific, and organizational challenges need to be met in order to trigger the efficiency and usability of Earth observation data. First, due to the high amount of the generated data by current operating systems, which is expected to be notably increasing in the future, rises the challenge of building data centers capable of storing and processing Tera-bytes of raw data. In the same perspective, new algorithmic approaches engaging extensive computation methodologies need to be implemented so as to handle equivalent amounts of data within the expected delays. Second, the scientific knowledge of the different measurement processes and the various unwanted interferences must be pushed further in order to allow an efficient exploitation of Earth observation data. Last but not least, close collaborations between private/public laboratories and governmental institutions, by combining both scientific cooperation models and program findings, need to be set up for an efficient provision of high-quality scientific Earth observation products.

So far, the greatest potential of Earth observation data is not fully reached and not all users have the required technical and knowledge to get advantage of the wide range of usability of Earth observation data sets. This depicts the importance of setting more close interaction between missions' scientists and relevant scientific and non-scientific communities in a way to allow a fully and widespread use of Earth observation data and to evaluate the usability Earth observation products to the applications of interest. Numerous programs, such as "SERVIR" and "EA" (Early adopter) programs, were established in this perspective but remain insufficient to allow a global use of Earth observation data capabilities.

Last, the step forward in the efficient exploitation of Earth observations is only achievable by establishing closer synergies between in-situ and remotely sensed data.

2.4 Users' needs

Users' requirements on Earth observations widely differ from an application to another. Based on the nature of the needed information (either local or global), the requirements on the space-based mission's functional parameters (spatial and radiometric resolutions, latency, etc.) delivering the data are defined.

More particularly, a trade-off is often made between the requirement on the spatial and radiometric resolutions depending on the application of interest, e.g. when the study concerns land/ocean or open ocean areas. Table 2.1 represents the correspondent minimal users' requirements as function of the Earth observation application [11].

Table 2.1: Earth observation users' needs

Application	Spatial resolution (in km)	Accuracy (in K)	Latency
Land NWP Soil Moisture	10	3	<240 min
Catchment Hydrology Soil Moisture	4	0.04	24 hrs
Regional Hydrology Soil Moisture	10	0.04	24 hrs
Vegetation Water Management	4	0.04	2 days
Agriculture Vegetation Optical Thickness	4	0.5	2 days
Sea Ice	15	0.5	2 days
Coastal Areas Sea Surface Salinity	3-10	0.1 (rivers and ice melt) 1-3 (river estuaries)	2 days
Open Ocean Sea Surface Salinity	100	0.2	monthly
Ocean Wind	50	0.2	Near-real time

Table 2.2 gives an overview of the wide range of Earth observation applications principally exploiting the information on soil moisture and sea surface salinity [10].

Table 2.2: Earth observation applications

Area	EO scientific application	EO Products	Derived products
Weather	-Weather and Climate Forecasting	-Brightness temperature -Soil Moisture -Freeze/thaw state	-Precipitation estimates -Inundation estimates -Drought predictions
Climate change	-Climate prediction -Effects of climate change -Global warming -Sea levels rising	-Land use and land cover maps -Sea-ice extent and thickness -Sea surface temperature and salinity -Wind profiles	-Ocean water exchange -Greenhouse emissions
Droughts and wildfires	-Desertification identification -Land management -Air quality -Food security	-Soil moisture -Root-zone soil moisture	-Land surface energy fluxes -Soil water deficit -Forest Carbon stocks
Carbon concentration	-Fires monitoring -Deforestation -Fauna & Flora degradation	-Carbon stocks	-Carbon cycle
Floods and landslides	-Flood forecasting -Storms prediction	-Soil moisture -Rainfall estimates	-Flood risk mapping -Soil infiltration -Ice breakup prediction
Agriculture productivity	-Food security -Water resources management -Irrigation performance monitoring	-Soil moisture -Global & local precipitations	-Water availability -Vegetation indices
Ocean resources	-Sea-ice mapping -Ocean salinity changes -Hurricane monitoring -Fisheries management	-Sea surface temperature and salinity -Ocean wind speed	-Ocean water exchange

2.5 Conclusion

As a result of the great success of the use of Earth observations from space in a wide range of scientific applications particularly dedicated to enhance the understanding of the Earth's system, ensuring a constant provision of Earth observation products has become more than even crucial. This unprecedented success has also engendered the birth of new Earth observation applications increasingly demanding in precision and time of availability.

Users' demands mainly concern the best achievable spatial and radiometric resolutions and latency. These parameters respectively inform about the capability of the imaging instrument to distinguish the spatial features and changes in temperature, and the required time for a global coverage of the Earth's surface.

Earth observation applications are speedily becoming greedy in newer, finer and more accurate products which consequently engenders an increasing demand on the development of new Earth observation missions pushing the technology advancement to its limits. Besides, various critical Earth observation applications, e.g. weather forecasting or disaster prediction, are entirely depending on the information provided by Earth observation instruments and used as inputs to their corresponding scientific models and whose provision needs to be constantly ensured.

That being said, numerous technical and organizational challenges face the development of the new generation of Earth observation missions. It is clear that the expected data amount to be downlinked from the next generation of space-based systems will necessarily require advanced data storage capabilities and improved resource management methodologies. Also, continuous efforts must be made in

knowledge and competences sharing in order to allow a wider exploitation of Earth observation products [2].

Last but not least, the identification of the required observations is subject to societal, economical and scientific imperatives. Based on this, a considerable effort in the accurate determination of observation needs is essential in order to allow an efficient provision of data. This mainly relies on the enhanced scientific understanding of the various applications of interest.

Bibliography

[1] P. Kansakar and F. Hossain, "Earth Science and Applications from Space: National Imperatives for the Next Decade and Beyond," THE NATIONAL ACADEMIES PRESS, Washignton DC, 2007.

[2] P. Kansakar and F. Hossain, "A review of applications of satellite earth observation data for global societal benefit and stewardship of planet earth," ELSEVIER: Space Policy, no. 36, pp 46-54, 2016.

[3] V. Ramos and A. Fores, "The role of earth observation for managing biodiversity and disasters in Mesoamerica: past, present and future," in: Faisal Hossain (Ed.), Earth Science Satellite Applications: Current and Future Prospects, Springer Publishers, 2016.

[4] J.R. Cihlar et al., "Initiative to quantify terrestrial carbon sources and sinks," In: Eos, Transactions, vol. 83, no. 1: 1, 6-7., 2002.

[5] C.M. Lee et al., "Applying earth observations to water resources challenges: looking at case studies in the U.S., Africa, Asia, and the global context," in: Faisal Hossain (Ed.), Earth Science Satellite Applications: Current and Future Prospects, Springer Publishers, 2016.

[6] "Food and Agriculture Organization of the United Nations," 2013.

[7] Z. Su, "The Surface Energy Balance System (SEBS) for estimation of turbulent heat fluxes," Hydrology and Earth System Sciences, 6(1), 85-99, 2002.

[8] U.S. Group on Earth Observations, "Achieving and sustaining Earth observations," National Research Council, September, 2010.

[9] G. Schumann, D. Kirschbaum, E. Anderson, and K. Rashid, "Role of earth observation data in disaster response and recovery from science to capacity building," in: Faisal Hossain (Ed.), Earth Science Satellite Applications: Current and Future Prospects, Springer Publishers, 2016.

[10] M. Brown, S. Moran, V. Escobar, and D. Entekhabi, "Soil Moisture Active Passive (SMAP) Mission Applications Plan," July 2012.

[11] "SMOS-Next: USERs' group meeting," Toulouse, CESBIO, January 16-17, 2014.

Chapter 3

TEMPORAL CORRELATION IMAGING: GENERALIZATION OF THE VAN CITTERT–ZERNIKE THEOREM

Contents

List of standard parameters

v_s :	aircraft's speed at the Low Earth Orbit (7.5 km/s)
c :	speed of light (3.10^8m/s)
h :	aircraft's altitude at the Low Earth Orbit (750 km)
B :	Earth observation reserved frequency bandwidth (1400-1427 MHz)
f_0 :	central frequency of B (1.4135 GHz)
ω_0 :	central pulsation ($\omega_0 = 2\pi f_0$)
λ :	wavelength at f_0 ($\sim$ 21 cm)
τ :	integration time
Δr :	Distance between a pair of antennas

3.1 Introduction

Spatial aperture synthesis is a widespread technique in radio-astronomy [3]. It is based on precisely timing the arrival times of the emitted signals by a given source at spatially separated antennas and then correlating them. In the simplest case of negligible motion of the observer relative to the source and correlation of simultaneously registered signals the correlation values are related by a direct Fourier-type law to the intensity distribution of the distant incoherent source through the Van Cittert–Zernike theorem (VCZT) (see equation (3.29) below).

As classically derived, the standard form of the theorem do not take into account the relative motion of the observer with respect to sources, or equivalently neglects the Doppler shift. From the other hand, one may want to generalize the theorem to correlations of electric fields measured at *different* times in order to achieve a *temporal aperture synthesis*, where in addition to the physical baselines provided by the spatially different antennas, virtual baselines are created by means of the observer's motion. Similarly, rotational synthesis using the motion of the Earth has long been used in radio-astronomy [4, 5]. Satellite-based temporal aperture synthesis for radio-astronomy is currently being tested on board of the mission Spektr-R (Radio-Astron) [6], whose measured signals are combined with those of antennas on the Earth's surface, yielding virtual baselines of up to 350,000 km lengths.

In this chapter, we generalize the Van Cittert–Zernike theorem to the case of an observer moving relative to the sources. In the meantime, we investigate correlations of fields measured at different times, delayed by the motion of the observer along the desired virtual baseline. We put emphasis on the introduction of delay times that only depend on the motion of the antennas and not on the positions of the sources, and we answer the question of whether with such global, pixel-independent time shifts virtual baselines can still be created. Our derivation is based on first principles, using only Maxwell's equations and a Lorentz transformation from the Earth-fixed frame (where the sources of the electromagnetic fields are at rest) to the satellite-fixed frame, taken to be moving uniformly with constant speed relative to Earth. We show that there is a remarkable cancellation of the phase due to the first order Doppler effect and the phase due to the virtual baseline. This renders the idea of temporal aperture synthesis through direct correlations of electric fields shifted in time by the travel time of the satellite over the distance of the virtual baseline impossible. At the same time, our generalized derivation shows that the VCZT in its standard form is still valid to first order in the speed of the observer and provides therefore a *a posteriori* justification of the use of the theorem for satellite observations of Earth without including the Doppler shift.

The third paragraph of this chapter was initially developed in collaboration between the CESBIO SMOS team and D. Braun from the university of Tübingen, and was subject in its entirety to a recent publication in the "Measurement and Science Technology" journal [14].

3.2 Spatio-temporal interferometry

The idea at the basis of the spatio-temporal interferometry was firstly proposed as the new generation to succeed the 2D interferometry employed in the MIRAS instrument of SMOS so as to meet with the more and more demanding users' needs in terms of the achieved spatial resolution.

The Y-shaped configuration of SMOS currently achieve a 40-50-km spatial resolution which is directly dictated by its longest 8m-length baseline. Based on this, in order to improve the spatial resolution by an order of magnitude, one idea could be to simply to increase the length of the bigger baseline by the same order. Such a configuration yields indeed the synthesizing of narrower beams and thus enhanced geometric resolutions by an order of magnitude. Nonetheless, in addition to the fact that putting into

orbit a satellite of this size is unlikely to be technically feasible, we show that this configuration yields a degraded radiometric sensitivity (figure 3.1).

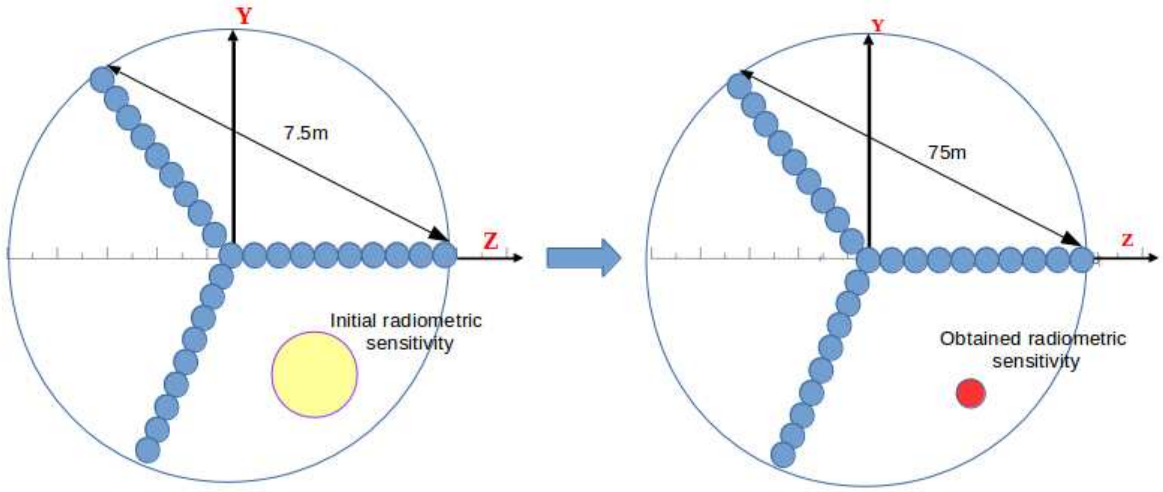

Figure 3.1: Radiometric sensitivity for an increased SMOS configuration

Due to the stringent relation between both the spatial resolution and the radiometric sensitivity (figure 3.2), the improvement of one parameter using classical methods usually goes together with the degradation of the other.

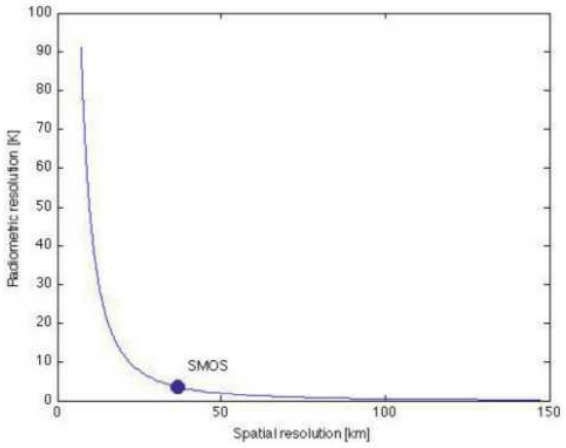

Figure 3.2: Radiometric sensitivity .vs. spatial resolution using standard parameters [2]

One can notice furthermore that the current configuration of SMOS is already close to the optimal trade-off which leaves no room for further improvement.

Now, starting from the SMOS' interferometric concept, an original idea was proposed so as to transform the complex 2D purely spatial configuration of SMOS into a simplified combined 1D-spatial/1D-temporal configuration. This simplification is reached when taking into account the observer's motion in the signal processing step. I.e. by collocating the time-dependent measured signals antennas with each other, new virtual baselines between two positions of antennas at different time samples. Figure 3.3 shows the configuration for a single pair of antennas.

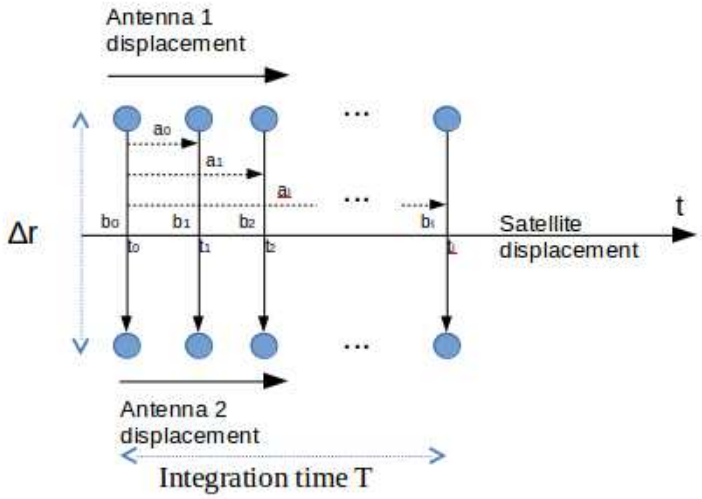

Figure 3.3: Spatio-temporal aperture synthesis

Two types of baselines are thus created: i) physical baselines b_i between the instantaneous spatial positions of the pair of antennas and ii) virtual baselines a_i between two different time-dependent positions. Based on this, one hopes, in principle, to exploit the flexibility on the virtual baselines to consequently enhance the spatial resolution.

The integration of the observer's motion in the calculation of the visibility function constitutes a generalization of the calculation procedure classically employed in purely spatial aperture synthetic systems such as SMOS. The image reconstruction procedure in interferometric imaging systems is based on the relationship linking the visibility samples to the brightness temperatures of the observed scene, known as the *Van Cittert-Zernike* theorem.

In next section, we derive a generalization of the standard form of the Van Cittert-Zernike theorem to the case of moving observers with respect to sources.

3.3 Generalization of the Van Cittert-Zernike theorem

3.3.1 Introduction

The use of the Van Cittert–Zernike theorem for the formulation of the visibility function in satellite-based Earth observation with passive radiometers does not take into account the relative motion of the observer (the satellite antenna) with respect to sources of the electro-magnetic fields at the surface of the Earth. The motion of the observer leads on the one hand to a more complex signal due to a pixel-dependent Doppler shift that is neglected in the standard derivation of the Van Cittert–Zernike theorem (Corbella et al. 2004 [1]), but on the other hand one may hope that it could be employed for a temporal aperture synthesis, where virtual baselines are created through the motion of the satellite. Here, we generalize the formulation of the aperture synthesis concept to the case of observers moving with respect to the sources, and to the correlation of fields measured at times that differ by the travel time of the observer along a virtual baseline. Our derivation is based on first principles, starting with the wave propagation in the Earth reference frame of electro-magnetic fields arising from incoherent current sources, and Lorentz transforming the fields into the reference frame of the satellite. Our detailed study leads to the remarkable conclusion that the delay time due to observer motion cancels exactly the

Doppler effect. This justifies the neglect of the Doppler effect in existing imaging systems based on the standard Van Cittert–Zernike theorem.

3.3.2 Model

Consider two antennas on board of a satellite flying at a height h with a speed v_s in the along-track (x-direction) over a current source at the Earth's surface. Let $\mathcal{R} = (O, \hat{e}_1, \hat{e}_2, \hat{e}_3)$ be the reference frame fixed with respect to Earth and $\mathcal{R}' = (O', \hat{e}'_1, \hat{e}'_2, \hat{e}'_3)$ the reference frame moving with speed $\boldsymbol{v}_s$, in which the satellite is thus at rest with the antennas at fixed positions $\boldsymbol{r}'$. At time $t = t' = 0$, the two origins O, O' are taken to coincide. Let $\boldsymbol{j}(\boldsymbol{r}, t)$ be a current density expressed at the position $\boldsymbol{r} = (x_1, x_2, x_3)$ in the reference frame $\mathcal{R}$ relative to Earth. One is interested in calculating the electric fields at points $\boldsymbol{r}' = (x'_1, x'_2, x'_3)$ relative to $\mathcal{R}'$, and with time saples t' measured by an aboard clock (figure 3.4).

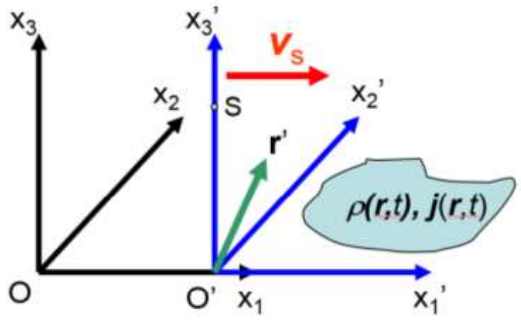

Figure 3.4: Earth frame $\mathcal{R} = (O, \hat{e}_1, \hat{e}_2, \hat{e}_3)$ and reference frame $\mathcal{R}' = (O', \hat{e}'_1, \hat{e}'_2, \hat{e}'_3)$ moving with speed $\boldsymbol{v}_s$ relative to $\mathcal{R}$. Fluctuating charge densities $\rho(\boldsymbol{r}, t)$ and current densities $\boldsymbol{j}(\boldsymbol{r}, t)$ create electric and magnetic fields. Antennas at fixed positions $\boldsymbol{r}'_i = (x'_i, y'_i, h)$ with respect to $\mathcal{R}'$ measure the electric fields at the proper time t' of the satellite S.

Under those circumstances, two types of baselines are created when considering two antennas at fixed positions $\boldsymbol{r}'_1$, $\boldsymbol{r}'_2$ with respect to $\mathcal{R}'$: A real physical baseline between the two antennas and a virtual baseline due to the displacement of each. The first one, exploited in spatial aperture synthesis and implemented in SMOS, uses fields measured at space-time points $(\boldsymbol{r}'_1, t')$ and $(\boldsymbol{r}'_2, t')$, implying a physical baseline $\boldsymbol{r}'_1 - \boldsymbol{r}'_2$. The second one uses measurements recorded in space-time points $(\boldsymbol{r}'_1, t'_1)$ and $(\boldsymbol{r}'_2, t'_2)$ for two different times t'_1, t'_2, which implies a virtual baseline in frame $\mathcal{R}$ with an additional "virtual" component $\simeq v_s(t'_2 - t'_1)$ in the direction of the motion of the satellite (neglecting here for clarity the relativistic correction, see below for the precise transformation). This is therefore a "temporal" aperture synthesis.
We now calculate the electric fields measured by the satellite that are created by charge and current densities in the Earth-fixed frame $\mathcal{R}$.

3.3.3 Electric field

3.3.3.1 Lorentz transformation

The sources of the e.m. fields are microscopic charges and currents at the surface of the Earth at some position-dependent temperature T in thermal equilibrium. They give rise to an electric field $\boldsymbol{E}(\boldsymbol{r}, t)$, and a magnetic induction $\boldsymbol{B}(\boldsymbol{r}, t)$, originally expressed in the frame $\mathcal{R}$ fixed to Earth. These fields are observed at a space-time point $(\boldsymbol{r}', t')$ in the frame $\mathcal{R}'$ relative to the satellite. The fields $\boldsymbol{E}'(\boldsymbol{r}', t')$

measured in the satellite frame $\mathcal{R}'$ can be obtained from a Lorentz transformation (LT) that describes the relation between the physical quantities measured by two observers moving at constant speed with respect to each other [9]. The electric and magnetic fields mix under the Lorentz transformation, i.e. one needs to calculate both $\boldsymbol{E}(\boldsymbol{r},t)$ and $\boldsymbol{B}(\boldsymbol{r},t)$ in order to obtain $\boldsymbol{E}'(\boldsymbol{r}',t')$. More precisely, the strategy will be the following:

- Calculate $\boldsymbol{E}(\boldsymbol{r},t)$ and $\boldsymbol{B}(\boldsymbol{r},t)$ generated by $\boldsymbol{j}(\boldsymbol{r},t)$ for every space-time point in $\mathcal{R}$,
- Apply a Lorentz transformation of these two fields in order to get $\boldsymbol{E}'(\boldsymbol{r},t)$, the electric field in the frame $\mathcal{R}'$ for every space-time point in $\mathcal{R}$, and
- Calculate the four-vector $(ct',\boldsymbol{r}')$ in the moving frame by Lorentz transforming $(ct,\boldsymbol{r})$ in order to have $\boldsymbol{E}'(\boldsymbol{r}',t') = \boldsymbol{E}'(LT(\boldsymbol{r}),LT(t))$ in $\mathcal{R}'$.

We neglect the general relativistic effects due to the acceleration on the elliptic orbit of the satellite and assume that the satellite flies with constant speed on a straight line over a plane.

For a given time-dependent charge density $\rho(\boldsymbol{r},t)$ and current density $\boldsymbol{j}(\boldsymbol{r},t)$, the exact expressions for $\boldsymbol{E}(\boldsymbol{r},t)$ and $\boldsymbol{B}(\boldsymbol{r},t)$ are (see equation (6.55) in 5th German edition of [9])

$$\boldsymbol{E}(\boldsymbol{r},t) = \frac{1}{4\pi\epsilon_0}\int d^3r''\Big\{\frac{\hat{R}}{R^2}\rho(\boldsymbol{r}'',t-R/c) + \frac{\hat{R}}{cR}\frac{\partial\rho(\boldsymbol{r}'',t-R/c)}{\partial t} - \frac{1}{c^2R}\frac{\boldsymbol{j}(\boldsymbol{r}'',t-\frac{R}{c})}{\partial t}\Big\}, \tag{3.1}$$

$$\boldsymbol{B}(\boldsymbol{r},t) = -\frac{\mu_0}{4\pi}\int d^3r''\frac{\hat{R}}{R}\times\left(\frac{1}{R}\boldsymbol{j}(\boldsymbol{r}'',t-\frac{R}{c}) + \frac{1}{c}\frac{\partial\boldsymbol{j}(\boldsymbol{r}'',t-\frac{R}{c})}{\partial t}\right), \tag{3.2}$$

where $\boldsymbol{R} = \boldsymbol{r}-\boldsymbol{r}''$, $R = |\boldsymbol{R}|$, $\hat{R}/R$ is the unit vector in $(\boldsymbol{r}-\boldsymbol{r}'')$-direction, and ϵ_0, μ_0 are the electric susceptibility and magnetic permeability of vacuum, respectively. Equations (3.1,3.2) show that the electric and magnetic fields are fully retarded with respect to the sources by the propagation time R/c. Both fields contain terms present also for static charges and currents that decay according to the Coulomb-law with distance, i.e. as $1/R^2$. However, in the far field $R \gg \lambda$, where λ is the wavelength, these terms are negligible compared to the ones decaying as $1/R$ and which arise only for time-dependent charge and current densities [10]. In the following we will take into account only these radiation fields. In the far-field approximation, the fields are thus given by

$$\boldsymbol{E}(\boldsymbol{r},t) = \frac{1}{4\pi\epsilon_0}\int d^3r''\Big\{\frac{\hat{R}}{cR}\frac{\partial\rho(\boldsymbol{r}'',t-R/c)}{\partial t} - \frac{1}{c^2R}\frac{\boldsymbol{j}(\boldsymbol{r}'',t-\frac{R}{c})}{\partial t}\Big\}, \tag{3.3}$$

$$\boldsymbol{B}(\boldsymbol{r},t) = -\frac{\mu_0}{4\pi}\int d^3r''\frac{\hat{R}}{R}\times\frac{1}{c}\partial_t\boldsymbol{j}(\boldsymbol{r}'',t-\frac{R}{c}), \tag{3.4}$$

The Lorentz transformation of the electric and magnetic fields from $\mathcal{R}$ to $\mathcal{R}'$ reads [9],

$$\boldsymbol{E}' = \gamma(\boldsymbol{E}+c\boldsymbol{\beta}\times\boldsymbol{B}) - \frac{\gamma^2}{\gamma+1}\boldsymbol{\beta}(\boldsymbol{\beta}\cdot\boldsymbol{E}), \tag{3.5}$$

$$\boldsymbol{B}' = \gamma(\boldsymbol{B}-\boldsymbol{\beta}\times\boldsymbol{E}/c) - \frac{\gamma^2}{\gamma+1}\boldsymbol{\beta}(\boldsymbol{\beta}\cdot\boldsymbol{B}), \tag{3.6}$$

where $\boldsymbol{\beta} = \boldsymbol{v}_s/c$, $\beta = |\boldsymbol{\beta}|$ and $\gamma = 1/\sqrt{1-(v_s/c)^2}$. We deduce the expression of the electric field in $\mathcal{R}'$ as function of the space-time coordinates in $\mathcal{R}$,

$$\boldsymbol{E}'(\boldsymbol{r},t) = -\frac{\gamma\mu_0}{4\pi}\int\frac{d^3r''}{R}\left[\partial_t(\boldsymbol{j}-c\hat{R}\rho) + (\boldsymbol{\beta}\cdot\partial_t\boldsymbol{j})\hat{R} - (\boldsymbol{\beta}\cdot\hat{R})\partial_t\boldsymbol{j} - \frac{\gamma}{\gamma+1}\boldsymbol{\beta}\cdot\partial_t(\boldsymbol{j}-c\hat{R}\rho)\boldsymbol{\beta}\right], \tag{3.7}$$

where the arguments of ρ and $\boldsymbol{j}$ are $(\boldsymbol{r}'', t - R/c)$.

The next step consists in Lorentz transforming the space-time coordinates in $\mathcal{R}$ in order to get the expressions of $(\boldsymbol{r}, t)$ as function of $(\boldsymbol{r}', t')$,

$$t = \gamma(t' + \frac{\boldsymbol{\beta} \cdot \boldsymbol{r}'}{c}), \tag{3.8}$$

$$\boldsymbol{r} = \boldsymbol{r}' + \frac{\gamma - 1}{\beta^2}(\boldsymbol{r}' \cdot \boldsymbol{\beta})\boldsymbol{\beta} + \gamma\boldsymbol{\beta}ct'. \tag{3.9}$$

Inserting (3.8,3.9) in (3.7), one finds that $\boldsymbol{E}'(\boldsymbol{r}', t')$ is still given by (3.7) where, however, the arguments of ρ and $\boldsymbol{j}^t$, to be inserted after differentiation with respect to t, are now $\Big(\boldsymbol{r}'', \gamma(t' + \boldsymbol{\beta} \cdot \boldsymbol{r}'/c) - R/c\Big)$, and $\boldsymbol{r}$ is to be replaced everywhere on the right hand side, including in $\boldsymbol{R}$, R, and $\hat{R}$, by (3.9).

3.3.3.2 Expansion in β

Equation (3.7) can still be further simplified if we take into account that β is typically very small. The example of SMOS with $h \simeq 700\,\text{km}$, $v_s \simeq 7\,\text{km/s}$, gives $\beta \sim v_s/c \sim 10^{-5}$. It makes therefore sense to expand in powers of β. We keep in the following systematically terms up to order β in all phases, but neglect corrections of order β in the prefactor. This is justified by the fact that in the end we calculate correlation functions, where the phase information is crucial, whereas the overall amplitudes are irrelevant, as they are, in practice, always renormalized with respect to the total intensity.

To first order in β, we have $\gamma \simeq 1$ and the following approximations

$$t \simeq t' + \frac{\boldsymbol{\beta} \cdot \boldsymbol{r}'}{c}, \tag{3.10}$$

$$\boldsymbol{r} \simeq \boldsymbol{r}' + \boldsymbol{v}_s t' \Rightarrow R \simeq |\boldsymbol{r}' + \boldsymbol{v}_s t' - \boldsymbol{r}''|. \tag{3.11}$$

With all of this, one finds

$$\boldsymbol{E}'(\boldsymbol{r}', t') \simeq -\frac{\mu_0}{4\pi} \int \frac{d^3 r''}{R} \partial_t \Big[\boldsymbol{j}(\boldsymbol{r}'', t)\Big]_{t = t' + (\boldsymbol{\beta} \cdot \boldsymbol{r}' - R)/c}. \tag{3.12}$$

Another approximation is in order: We will be interested only in times t' smaller or equal to the maximum possible averaging time. As explained below, this time is set by the time of overflight of a single pixel, assumed to be at constant temperature. With a pixel dimension $\Delta x'' \sim \Delta y''$ $\sim$ some 1-10 km, we have $v_s t/|\boldsymbol{r}' - \boldsymbol{r}''| \leq \Delta x''/h \ll 1$. For the typical values of SMOS, the maximum t' would be of order of 1 s, but the inequality shows that even substantially longer times ($t \lesssim 100$ s) can still be accommodated in the range of validity of the following approximation

$$\begin{aligned} R &\simeq \sqrt{(\boldsymbol{r}' + \boldsymbol{v}_s t' - \boldsymbol{r}'')^2} \\ &= |\boldsymbol{r}' - \boldsymbol{r}''| \sqrt{1 + 2\frac{(\boldsymbol{r}' - \boldsymbol{r}'') \cdot \boldsymbol{v}_s t'}{|\boldsymbol{r}' - \boldsymbol{r}''|^2} + \Big(\frac{\boldsymbol{v}_s t'}{|\boldsymbol{r}' - \boldsymbol{r}''|}\Big)^2} \\ &\simeq |\boldsymbol{r}' - \boldsymbol{r}''| \left(1 + \frac{(\boldsymbol{r}' - \boldsymbol{r}'') \cdot \boldsymbol{v}_s t'}{|\boldsymbol{r}' - \boldsymbol{r}''|^2}\right) \\ &= |\boldsymbol{r}' - \boldsymbol{r}''| + \hat{e}_{\boldsymbol{r}' - \boldsymbol{r}''} \cdot \boldsymbol{v}_s t'. \end{aligned} \tag{3.13}$$

As for the shift $\boldsymbol{\beta}\cdot\boldsymbol{r}'/c$ in the time argument, we have, with antennas at positions (x_i', y_i', h) and $|x_i'|, |y_i'| \simeq$ (10-100) m $\ll v_s t'$, $|\boldsymbol{\beta}\cdot\boldsymbol{r}'/c| \ll \beta^2 t'$ for almost all t', such that this term can also be neglected. Also note that this term vanishes exactly for antennas located on a line perpendicular to the displacement of the satellite, $\boldsymbol{\beta}\cdot\boldsymbol{r}' = 0$.

By neglecting again corrections of the amplitude of order β or higher, the expression of the received electric field at position $\boldsymbol{r}'$ of the antenna relative to the satellite, expressed in the frame $\mathcal{R}'$, becomes

$$\boldsymbol{E}'(\boldsymbol{r}', t') \simeq -\frac{\mu_0}{4\pi}\int \frac{d^3r''}{|\boldsymbol{r}'-\boldsymbol{r}''|}\partial_t \boldsymbol{j}(\boldsymbol{r}'', t)\,|_{t=t'-\frac{R(t')}{c}}\,, \tag{3.14}$$

with $R(t') = |\boldsymbol{r}' + \boldsymbol{v}_s t' - \boldsymbol{r}''|$. By analyzing the expression (3.14), one realizes that it could have been obtained in a naive way by simply replacing $\boldsymbol{r}$ in the far field expression of $\boldsymbol{E}(\boldsymbol{r}, t)$ with the position of the moving satellite as seen in $\mathcal{R}$, and keeping the time t. However, even the meaning of the partial time-derivative would have then remained ambiguous: does it apply to $R(t)$ or not? In the formal, rigorous derivation that we have followed here, it is clear, that it does not: one first differentiates $\boldsymbol{j}(\boldsymbol{r}'', t)$ with respect to t and then replaces t as indicated. Also, the sequence of well-controlled approximations discussed above opens the way to systematically deriving higher-order corrections, which is clearly not possible in the mentioned "naive" approach.

3.3.3.3 Fourier transform

Thermal sources at the surface of Earth, which are the origin of the thermal noise detected at the position of the satellite, are assimilated to random fluctuations as function of time. They can be expressed through their spectrum $\tilde{\boldsymbol{j}}$,

$$\boldsymbol{j}(\boldsymbol{r}'', t) = \frac{1}{\sqrt{2\pi}}\int_{-\infty}^{\infty} d\omega' e^{i\omega' t}\tilde{\boldsymbol{j}}(\boldsymbol{r}'', \omega'). \tag{3.15}$$

Inserting (3.15) in (3.14) yields

$$\boldsymbol{E}'(\boldsymbol{r}', t') \simeq -\frac{\mu_0}{4\pi\sqrt{2\pi}}\int \frac{d^3r''}{|\boldsymbol{r}'-\boldsymbol{r}''|}\int d\omega' i\omega' e^{i\omega'(t'-\frac{R(t')}{c})}\tilde{\boldsymbol{j}}(\boldsymbol{r}'', \omega'). \tag{3.16}$$

The spectrum of the electric field received at the position of the satellite corresponds to the Fourier transform of (3.16),

$$\tilde{\boldsymbol{E}}'(\boldsymbol{r}', \omega) \simeq -\frac{\mu_0}{8\pi^2}\int dt' e^{-i\omega t'}\int \frac{d^3r''}{|\boldsymbol{r}'-\boldsymbol{r}''|}\int d\omega' i\omega' e^{i\omega'(t'-\frac{R(t')}{c})}\tilde{\boldsymbol{j}}(\boldsymbol{r}'', \omega'), \tag{3.17}$$

and using the approximation (3.13), the previous expression becomes

$$\tilde{\boldsymbol{E}}'(\boldsymbol{r}', \omega) \simeq -\frac{\mu_0}{8\pi^2}\int \frac{d^3r''}{|\boldsymbol{r}'-\boldsymbol{r}''|}\int d\omega' i\omega' e^{-i\omega'\frac{|\boldsymbol{r}'-\boldsymbol{r}''|}{c}}\tilde{\boldsymbol{j}}(\boldsymbol{r}'', \omega')\int dt' e^{-i\omega t'} e^{i\omega'(1-\hat{e}_{\boldsymbol{r}'-\boldsymbol{r}''}\cdot\boldsymbol{\beta})t'}. \tag{3.18}$$

By noticing that the only remaining time dependence is in the exponent, the integral over time variable t' can thus be simplified to

$$\begin{aligned}\int dt' e^{-i\omega t'} e^{i\omega'(1-\hat{e}_{\boldsymbol{r}'-\boldsymbol{r}''}\cdot\boldsymbol{\beta})t'} &= 2\pi\delta\Big(-\omega+\omega'(1-\hat{e}_{\boldsymbol{r}'-\boldsymbol{r}''}\cdot\boldsymbol{\beta})\Big)\\ &= \frac{2\pi}{|1-\hat{e}_{\boldsymbol{r}'-\boldsymbol{r}''}\cdot\boldsymbol{\beta}|}\delta\Big(\omega'-\omega(1-\hat{e}_{\boldsymbol{r}'-\boldsymbol{r}''}\cdot\boldsymbol{\beta})^{-1}\Big)\\ &\simeq 2\pi|1+\hat{e}_{\boldsymbol{r}'-\boldsymbol{r}''}\cdot\boldsymbol{\beta}|\delta\Big(\omega'-\omega(1+\hat{e}_{\boldsymbol{r}'-\boldsymbol{r}''}\cdot\boldsymbol{\beta})\Big)\,,\end{aligned}$$

where the last expression is once more correct to order β. By neglecting again corrections of the electric field amplitude, the spectrum of the electric field measured in $\mathcal{R}'$ becomes

$$\tilde{\boldsymbol{E}}'(\boldsymbol{r}',\omega) \simeq -\frac{\mu_0}{4\pi}\int d^3r'' \frac{i\omega e^{-i\omega\frac{|\boldsymbol{r}'-\boldsymbol{r}''|}{c}(1+\hat{e}_{\boldsymbol{r}'-\boldsymbol{r}''}\cdot\boldsymbol{\beta})}}{|\boldsymbol{r}'-\boldsymbol{r}''|}\tilde{\boldsymbol{j}}\Big(\boldsymbol{r}'',\omega(1+\hat{e}_{\boldsymbol{r}'-\boldsymbol{r}''}\cdot\boldsymbol{\beta})\Big).$$

On board of the satellite, the received electric field typically passes through a filter with filter function $w(\omega)$. E.g. for SMOS, the spectrum is filtered to a narrow window corresponding to the allowed band of width $b = 2\pi \times 17$ MHz centred at $\omega_0 = 2\pi \times 1.4135$ GHz. The retrieved temporal electric field at the output of the filter is expressed by inverse Fourier transforming $\tilde{\boldsymbol{E}}'(\boldsymbol{r}',\omega)$ multiplied with the filter function,

$$\begin{aligned}\boldsymbol{E}'(\boldsymbol{r}',t') &= \frac{1}{\sqrt{2\pi}}\int d\omega w(\omega)\tilde{\boldsymbol{E}}'(\boldsymbol{r}',\omega)e^{i\omega t'} \\ &\simeq -\frac{\mu_0}{4\pi}\frac{1}{\sqrt{2\pi}}\int d\omega w(\omega)\int d^3r''\frac{i\omega}{|\boldsymbol{r}'-\boldsymbol{r}''|}e^{i\omega t'}\tilde{\boldsymbol{j}}\Big(\boldsymbol{r}'',\omega(1+\hat{e}_{\boldsymbol{r}'-\boldsymbol{r}''}\cdot\boldsymbol{\beta})\Big)e^{-i\omega\frac{|\boldsymbol{r}'-\boldsymbol{r}''|}{c}(1+\hat{e}_{\boldsymbol{r}'-\boldsymbol{r}''}\cdot\boldsymbol{\beta})}.\end{aligned} \tag{3.19}$$

Since the integration over the frequency variable ω is from $-\infty$ to $+\infty$, one can apply the change of variables $\omega(1+\hat{e}_{\boldsymbol{r}'-\boldsymbol{r}''}\cdot\boldsymbol{\beta}) \to \omega$. Neglecting once more corrections of the amplitude of order β or higher, and corrections of the phase of order β^2 or higher, this leads to

$$\boldsymbol{E}'(\boldsymbol{r}',t') \simeq -\frac{\mu_0}{4\pi}\frac{1}{\sqrt{2\pi}}\int i\omega d\omega\int d^3r''\tilde{\boldsymbol{j}}(\boldsymbol{r}'',\omega)\frac{w\Big(\omega(1-\hat{e}_{\boldsymbol{r}'-\boldsymbol{r}''}\cdot\boldsymbol{\beta})\Big)}{|\boldsymbol{r}'-\boldsymbol{r}''|}e^{i\omega(t'-\frac{|\boldsymbol{r}'-\boldsymbol{r}''|}{c})}e^{-i\omega t'\hat{e}_{\boldsymbol{r}'-\boldsymbol{r}''}\cdot\boldsymbol{\beta}}. \tag{3.20}$$

As it was to be expected, the satellite motion generates a Doppler shift of the frequency of the sources. The Doppler shift appears in the expression of the filtered electric field by means of a shift of the frequency of the filter function and the appearance of the phase factor $e^{-i\omega t'\hat{e}_{\boldsymbol{r}'-\boldsymbol{r}''}\cdot\boldsymbol{\beta}}$. The Doppler shift to linear order in β is clearly a purely longitudinal one, as is well-known. A transverse (i.e. purely relativistic) Doppler shift would appear at second order in β.

3.3.4 Correlation function

We define the correlation (also called the visibility function) of the electric fields in the frame $\mathcal{R}'$ fixed to the satellite as

$$C(\boldsymbol{r}'_1,t'_1,\boldsymbol{r}'_2,t'_2) \equiv \Big\langle \boldsymbol{E}'(\boldsymbol{r}'_1,t'_1)\boldsymbol{E}'^*(\boldsymbol{r}'_2,t'_2)\Big\rangle. \tag{3.21}$$

The thermal sources at the surface of Earth can be modeled by Gaussian stochastic processes that are uncorrelated for different frequencies and positions ([11, 12] and next chapter for more details),

$$\Big\langle\tilde{\boldsymbol{j}}\Big(\boldsymbol{r}''_1,\omega_1\Big)\tilde{\boldsymbol{j}}^*\Big(\boldsymbol{r}''_2,\omega_2\Big)\Big\rangle = \frac{l_c^3}{T_c}\delta(\boldsymbol{r}''_1-\boldsymbol{r}''_2)\delta(\omega_1-\omega_2)\Big\langle|\tilde{\boldsymbol{j}}\Big(\boldsymbol{r}''_1,\omega_1\Big)|^2\Big\rangle, \tag{3.22}$$

where l_c and T_c refer to the correlation length and the correlation time, respectively.

The averages in (3.21) and (3.22) are in principle over an ensemble of different realizations of the noise processes, but, assuming ergodicity, they may be replaced by a time average. The averaging time should be as long as possible to reduce the fluctuations of the average, but sufficiently short for not mixing different inequivalent ensembles. In our case this means that the averaging time should be comparable

to the time it takes for the satellite to fly over one pixel (with assumed constant temperature). This renders the definition (3.21) operational for a single pass of the satellite.

Let $\Delta\boldsymbol{r} = \boldsymbol{r}'_2 - \boldsymbol{r}'_1$ and $\Delta t = t'_2 - t'_1$. To first order in $|\Delta\boldsymbol{r}|/|\boldsymbol{r}'_1 - \boldsymbol{r}''| \sim 10^{-4}$, we have the following approximations

$$|\boldsymbol{r}'_2 - \boldsymbol{r}''| \simeq |\boldsymbol{r}'_1 - \boldsymbol{r}''| + \Delta\boldsymbol{r}\cdot\hat{e}_{\boldsymbol{r}'_1-\boldsymbol{r}''}, \tag{3.23}$$

$$\hat{e}_{\boldsymbol{r}'_2-\boldsymbol{r}''}\cdot\boldsymbol{\beta} \simeq \hat{e}_{\boldsymbol{r}'_1-\boldsymbol{r}''}\cdot\boldsymbol{\beta}. \tag{3.24}$$

Finally, using (3.18), (3.22), (3.23) and (3.24), the expression (3.21) of the correlation function becomes

$$C(\boldsymbol{r}'_1,t'_1,\boldsymbol{r}'_2,t'_2) \simeq \frac{l_c^3}{2\pi T_c}\Big(\frac{\mu_0}{4\pi}\Big)^2\int d\omega\omega^2\int d^3r''\Big\langle\Big|\tilde{\boldsymbol{j}}\big(\boldsymbol{r}'',\omega\big)\Big|^2\Big\rangle \tag{3.25}$$
$$\times\frac{\Big|w\big(\omega(1-\hat{e}_{\boldsymbol{r}'_1-\boldsymbol{r}''}\cdot\boldsymbol{\beta})\big)\Big|^2}{|\boldsymbol{r}'_1-\boldsymbol{r}''||\boldsymbol{r}'_2-\boldsymbol{r}''|}\exp\Big[-i\omega\Delta t + i\frac{\omega}{c}(\Delta\boldsymbol{r}+\Delta t\boldsymbol{v}_s)\cdot\hat{e}_{\boldsymbol{r}'_1-\boldsymbol{r}''}\Big].$$

We assume that $\omega^2\Big\langle\Big|\tilde{\boldsymbol{j}}\big(\boldsymbol{r}'',\omega\big)\Big|^2\Big\rangle$ which is related to the brightness temperature depends only weakly on frequency (compared to the rapid oscillations of the phase as function of ω) over the bandwidth b, $\omega^2\Big\langle\Big|\tilde{\boldsymbol{j}}\big(\boldsymbol{r}'',\omega\big)\Big|^2\Big\rangle \simeq \omega_0^2\Big\langle\Big|\tilde{\boldsymbol{j}}\big(\boldsymbol{r}'',\omega_0\big)\Big|^2\Big\rangle$. It is then convenient to invert the applied change of variables $\omega(1-\hat{e}_{\boldsymbol{r}'_1-\boldsymbol{r}''}\cdot\boldsymbol{\beta})\to\omega$, and one easily finds

$$C(\boldsymbol{r}'_1,t'_1,\boldsymbol{r}'_2,t'_2) \simeq \frac{l_c^3}{2\pi T_c}\Big(\frac{\mu_0}{4\pi}\Big)^2\int d\omega\omega_0^2|w(\omega)|^2\int d^3r''\frac{\Big\langle\Big|\tilde{\boldsymbol{j}}\big(\boldsymbol{r}'',\omega_0\big)\Big|^2\Big\rangle}{|\boldsymbol{r}'_1-\boldsymbol{r}''||\boldsymbol{r}'_2-\boldsymbol{r}''|} \tag{3.26}$$
$$\times\exp\Big[-i\omega\Delta t - i\omega\Delta t\hat{e}_{\boldsymbol{r}'_1-\boldsymbol{r}''}\cdot\boldsymbol{\beta} + i\frac{\omega}{c}(\Delta\boldsymbol{r}+\Delta t\boldsymbol{v}_s)\cdot\hat{e}_{\boldsymbol{r}'_1-\boldsymbol{r}''}\Big].$$

By noticing that $\boldsymbol{\beta} = \boldsymbol{v}_s/c$ and neglecting once more corrections of order β^2 in the phase, it follows that

$$C(\boldsymbol{r}'_1,t'_1,\boldsymbol{r}'_2,t'_2) \simeq \frac{l_c^3}{2\pi T_c}\Big(\frac{\mu_0}{4\pi}\Big)^2\int d\omega\omega_0^2|w(\omega)|^2 \tag{3.27}$$
$$\times\int d^3r''\frac{\Big\langle\Big|\tilde{\boldsymbol{j}}\big(\boldsymbol{r}'',\omega_0\big)\Big|^2\Big\rangle}{|\boldsymbol{r}'_1-\boldsymbol{r}''||\boldsymbol{r}'_2-\boldsymbol{r}''|}\exp\Big[-i\omega\Delta t + i\frac{\omega}{c}\Delta\boldsymbol{r}\cdot\hat{e}_{\boldsymbol{r}'_1-\boldsymbol{r}''}\Big].$$

We clearly see that the two phases $-\omega\Delta t\hat{e}_{\boldsymbol{r}'-\boldsymbol{r}''}\cdot\boldsymbol{\beta}$ of the Doppler shift and $(\omega/c)\Delta t\boldsymbol{v}_s\cdot\hat{e}_{\boldsymbol{r}'-\boldsymbol{r}''}$ corresponding to the virtual baseline in the direction of the motion of the satellite cancel.

Finally, by considering a simple rectangular filter function of bandwidth b,

$$w(\omega) = \begin{cases} 1 & \text{for } \omega_0 - b/2 \le \omega \le \omega_0 + b/2, \\ 0 & \text{elsewhere,}\end{cases}$$

the integral over ω can be performed. To first order in β, one finds

$$C(\boldsymbol{r}'_1,t'_1,\boldsymbol{r}'_2,t'_2) \simeq K\int d^3r''\Big\langle\Big|\tilde{\boldsymbol{j}}\big(\boldsymbol{r}'',\omega_0\big)\Big|^2\Big\rangle\frac{\exp\Big[i\omega_0\Big(-\Delta t + \frac{1}{c}\Delta\boldsymbol{r}\cdot\hat{e}_{\boldsymbol{r}'_1-\boldsymbol{r}''}\Big)\Big]}{|\boldsymbol{r}'_1-\boldsymbol{r}''||\boldsymbol{r}'_2-\boldsymbol{r}''|}$$
$$\times\operatorname{sinc}\Big[\frac{b}{2}\Big(-\Delta t + \frac{1}{c}\Delta\boldsymbol{r}\cdot\hat{e}_{\boldsymbol{r}'_1-\boldsymbol{r}''}\Big)\Big]. \tag{3.28}$$

where $\operatorname{sinc}(x) \equiv \sin(x)/x$, and the constant $K = l_c^3 b\omega_0^2\mu_0^2/(32\pi^3 T_c)$.

Equation (3.28) is our main result. It generalizes the Van Cittert–Zernike theorem to an observer moving with respect to the sources and to a finite time-interval Δt between the measurements of the electric fields, as we discuss now.

3.3.5 Discussion

A passive micro-wave interferometer for Earth observation measures the complex spatial correlation field, or the visibility function, of the incident electric field originating from thermally fluctuating sources on Earth's surface. The Van Cittert–Zernike theorem describes the Fourier transform relationship between a spatial intensity distribution of these incoherent sources of radiation and its associated visibility function. In our notation, the theorem can be written as

$$C_{VCZ}(\boldsymbol{r}'_1, t'_1, \boldsymbol{r}'_2, t'_2) \simeq K \int d^3r'' \left\langle \left| \tilde{\boldsymbol{j}}\left(\boldsymbol{r}'', \omega_0\right) \right|^2 \right\rangle \frac{\exp\left[i\omega_0 \left(\frac{1}{c} \Delta\boldsymbol{r} \cdot \hat{e}_{\boldsymbol{r}'_1 - \boldsymbol{r}''} \right) \right]}{|\boldsymbol{r}'_1 - \boldsymbol{r}''||\boldsymbol{r}'_2 - \boldsymbol{r}''|}. \tag{3.29}$$

It shows that the set of equal time visibility functions obtained from different antennas pairs is given by the spatial 2D Fourier transform of the intensity distribution of the sources, where the phases of the Fourier transform are the scalar products of the wave-vector from the source to an antenna and the vector joining two antennas.

In the standard derivation of the theorem, sources and observer are taken at rest with respect to each other, and only electric fields observed at the same time (with respect to the observer reference–frame) but at different positions are correlated. We recover the standard form of the VCZT when setting $\Delta t = 0$, and considering a small bandwidth, $b\Delta\boldsymbol{r}/c \ll 1$. The latter condition allows one to approximate the sinc-function by 1. The speed of the satellite v_s has disappeared from the expression already in (3.27) with the cancellation of the Doppler shift and the phase related to the virtual baseline created by the displacement of the satellite during time Δt. Thus, *the standard form (3.29) is valid also at finite speed to first order in* β. Our study therefore extends the validity of the standard form (3.29) of the Van Cittert–Zernike theorem to the case of an observer moving with constant speed with respect to the sources.

The cancellation of the phases due to the Doppler shift and the virtual baseline shows that it is not possible to create a temporal aperture synthesis by correlating the observed time-dependent electric fields delayed by the travel time of the satellite in the direction of the virtual baseline. In addition, a finite time interval Δt between two observations leads to i) a strong suppression of the amplitude of the correlation function and ii) a rapidly oscillating phase factor. The first effect results from the sinc-term. If $\Delta t \sim \Delta\boldsymbol{r}/v_s$, the term due to Δt in the argument of the sinc is up to a factor c/v_s larger than the second one. The second one, on the other hand, has to be of order one if the spatial aperture in the direction of the real baseline Δr is supposed to work. Therefore, the amplitude of the correlation function is suppressed by a factor $\sim v_s/c$ relative to the standard case with $\Delta t = 0$. The rapidly oscillating phase factor is given by $\exp(-i\omega_0\Delta t)$. This phase overwhelms the information in the cross-track direction contained in the phase $(\omega_0/c)\Delta\boldsymbol{r} \cdot \hat{e}_{\boldsymbol{r}'_1 - \boldsymbol{r}''}$.

Thus, while the hope of being able to use the virtual baseline created by a moving satellite for imaging purposes through correlating the time-dependent fields shifted only by the travel time over the virtual baseline is disappointed, our derivation justifies the neglect of the Doppler effect in existing satellite-based passive radiometers based on the standard Van Cittert–Zernike theorem [13].

3.3.6 Conclusion

We have examined the possibility of temporal aperture synthesis for satellite-based passive microwave observation of Earth, where a virtual baseline is created by the motion of the satellite in order to enhance the spatial resolution. Our study shows that the interesting phase information in the along-track direction obtained from a time shift of the fields corresponding to the travel time over the virtual baseline is exactly canceled by the first order (longitudinal) Doppler effect. Furthermore, the time

shift yields a large uncompensated frequency-dependent phase overwhelming the information in the cross-track direction, and a drastic reduction of the amplitude of the correlation function. Therefore, by correlating in this way the time-dependent signals received by a 1D antennas array with pixel-independent shifts corresponding only to the travel time of the satellite, one cannot reconstruct the brightness temperature in both the along- and cross-track directions.

Nevertheless, our result (3.28) constitutes a generalization of the Van Cittert–Zernike theorem (3.29) to the case of an observer moving with respect to the sources, and the correlation of electric field measurements at different times. By deriving the electric fields in the moving frame from first principles, we have shown that the longitudinal Doppler effect cancels exactly in the correlation function. The standard Van Cittert–Zernike theorem for equal time correlations therefore holds even for a moving observer with substantially different Doppler shifts in different directions of sight.

3.4 Similar concepts

3.4.1 Very Long Baseline Interferometry (VLBI)

The *Very Long Baseline Interferometry* (VLBI) is the branch of radio-interferometry whose observations currently yield the high-resolved radio-astronomical images with angular resolutions of the order of a milliarcsecond (mas). This technique relies on the use of very long baseline lengths which are either limited by the size of the Earth when considering ground-based telescopes, or unlimited as is currently the case by the use of space-based observers.

3.4.1.1 Introduction

In radio-astronomy, an interferometer allows the reconstruction of the spatial intensity distribution of the electro-magnetic radiation produced by an astronomical object from the spatial coherence function measured at two points [3]. VLBI is a technique of radio-interferometry where observations are made simultaneously by a set of radio-telescopes separated by a long distance. At the level of the participating radio-telescopes, the simultaneous observations are recorded paired with a timing information, usually from a local atomic clock, and pass through an amplification and digitization step before the final storage on tape or disk for a later post-processing, or, more recently, immediately sent over network links to the processing centers (eVLBI). The cross-correlation of the acquired signals allows to "synthesize" a radio-telescope of the size of the distance between the individual elements and thus produces extremely high-resolved measurements of the astronomical radio-source.

One of the main differences with typical connected interferometric systems is the required calibration in VLBI systems since the lines of sight from each antenna pass through totally uncorrelated atmospheres and are highly impacted by the Earth's orientation effects which are too small to affect connected interferometers. The calibration consists in precisely measuring a set of geometric quantities such as the positions of sources, the baseline vectors and the phase shifts to be integrated in the correlation step.

More particularly, the high-resolved radio-astronomical observations are exploited in various astronomical and non-astronomical applications. They are employed, for instance, using phase-referencing techniques, to determine with higher accuracy the precise celestial positions needed to calibrate the GPS system [15].

3.4.1.2 Interferometry and aperture synthesis

The monochromatic electro-magnetic field, $\mathbf{E}(\mathbf{r})$, arriving at the observer's location $\mathbf{r}$ is defined as the sum of all waves emitted by celestial bodies at that particular frequency. The correlation function, called also the visibility function, defined as the cross-correlation of the signals received at two different locations $\mathbf{r}_1$ and $\mathbf{r}_2$, $V(\mathbf{r}_1, \mathbf{r}_2) = \left\langle \mathbf{E}(\mathbf{r}_1)\mathbf{E}^*(\mathbf{r}_2) \right\rangle$, describes the similitude of the electro-magnetic field at these two positions.

If we assume that each incident radiation from the sky toward an observer at the surface of the Earth is largely spatially incoherent, except over a very small region. Based on this, the spatial correlation function at the frequency ν can be expressed as follows

$$V_\nu(\mathbf{r}_1, \mathbf{r}_2) \simeq \int I_\nu(\mathbf{s}) e^{-i2\pi \mathbf{s} \frac{\mathbf{r}_1 - \mathbf{r}_2}{c}} d\Omega, \tag{3.30}$$

where $\mathbf{s}$ is the unit vector pointing toward the source and $d\Omega$ is the surface element of the celestial sphere.

The correlation function as defined by (3.30) appears to behave as function of the relative separation and orientation of the locations of the two interferometer elements. Interestingly, when switching to the (u, v)-plane which describes the projection of the separation and orientation of the elements on a plane perpendicular to the line of sight, measured in wavelengths,

$$V_\nu(u, v) \simeq \int\int A_\nu(l, m) I_\nu(l, m) e^{-i2\pi(ul+vm)} dl dm, \tag{3.31}$$

where l and m are the direction cosines in the direction of the astronomical source and A_ν is a factor describing the response of the antennas, equation (3.31) exactly defines the standard form of the most important theorem in aperture synthesis, the *Van Cittert–Zernike* theorem. The expression of this theorem describes the Fourier transform relationship between the correlation function and the intensity distribution of the sky, which, using deconvolution techniques, allows the reconstruction of the intensity distribution of the observed region of the sky I_ν from the correlation samples.

As a result of the Earth's rotation, the relative orientation of the interferometric elements continuously changes and the ground-fixed elements will sample various aspects of the observed seen as the observation progresses. This is known as the technique of **Aperture Synthesis** employed in a wide range of radio-interferometers.

Based on this, if we consider a celestial source observed in the line-sight vector direction, $\mathbf{s}$, the sky coordinates defined through the direction cosines l and m and the antennas' coordinates projected onto the (u, v) plane, the visibility values measured at $(-u, -v)$ and (u, v) are found to be complex conjugate which allows the sampling of the whole (u, v)-plane within only 12h.

3.4.1.3 Image reconstruction

Since equation (3.31) is defined as a Fourier relationship between the correlation function and the intensity distribution of the sky, one shows that within a particular region this expression can be invertible.

However, after a VLBI observation the purely Fourier transformed image obtained by means of a direct inversion of equation (3.31) will look poor owing to the insufficient sampling of the (u, v)-plane. In reality, in aperture synthetic systems the brightness distribution is convolved with the instrument's point-spread function (PSF) defined as the Fourier transform of the (u, v) coverage. This gives rise to artefacts in the reconstructed image arising from the PSF of the interferometric array. One way to get

rid of these corrupting sidelobes is to interpolate the visibilities to the empty regions of the (u, v)-plane by means of the so-called "CLEAN" algorithm.

In general, radio-astronomical images using radio-interferometry are generated from thousands of interferometric measurements. This allows a great flexibility either on sensitivity, by ignoring measurements from the longest baselines, or resolution, by giving priority to the shortest baselines.

On the other hand, VLBI measurements are not correlated in real time, but first recorded to disks, or transmitted via high-speed networks, and then reprocessed by precise synchronized VLBI correlators. Recorded data are next cross-correlated through two different procedures: i) using a XF correlator by firstly cross-correlating and next Fourier-transforming the signals or ii) using a FX correlator based on a Fourier transformation followed by the cross-correlation of the signals. Based on the Fourier theory, one shows that both methods yield equivalent results.

During the correlation step, data from two different stations must be synchronized, in other words they must be read out with exactly the same speed. The output of the correlation stage comprised of a set a visibility measurements termed with auxiliary information on the array are stored and afterwards sent for calibration (phase and delay calibration) before any information can be extracted using deconvolution techniques such as the "CLEAN" or the "MEM" algorithms [16].

3.4.1.4 Application of the generalized VCZT to VLBI

Based on equation (3.30), the visibility function of an interferometer is expressed as function of the delay between the two interferometer's elements $(\mathbf{r}_1 - \mathbf{r}_2)/c$, and due to Earth rotation this delay is constantly changing as long as the observation progresses. Owing to this, in VLBI systems it is primordial to introduce adjustable delays τ_i to the nonretarded signal in order to compensate for the propagation delay (figure 3.5).

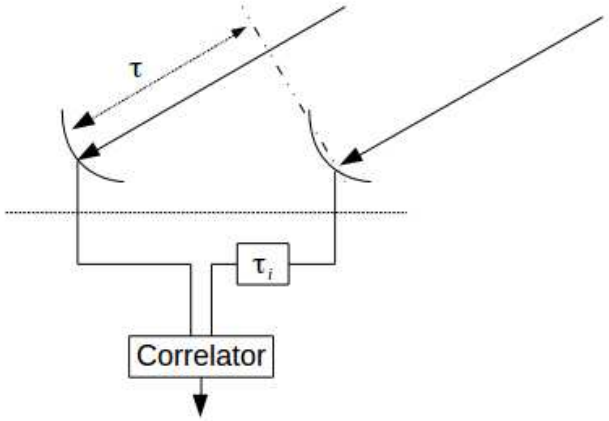

Figure 3.5: Delay in VLBI

In VLBI, observations are usually performed over a particular frequency bandwidth and the corresponding filtering transforms the expression of the visibility function (3.30) to the generalized form of the Van Cittert–Zernike theorem (3.28). In the case of a rectangular filter, an induced sinc-function, usually referred as the "fringe washing" function, appears in the expression of the visibility function. It particularly describes the change of the interferometer's response as function of the propagation delay τ. Hence, if no adjustable delays are introduced in the correlation channel, the "fringe washing" function destroys the interferometer response and no fringes remain.

For a focused celestial source in the sky, the required adjustable delays that have to be continuously introduced can be exactly determined based on the generalized form the Van Cittert–Zernike theorem for moving observers with respect to sources, which models the visibility behavior for each couple of radiating elements as function of their in-between time-dependent delay.

3.4.1.5 Conclusion

VLBI techniques have not only been used in radio-astronomy, but have also inspired scientists for a re-adaptation to microwave remote sensing of the Earth in the case of large thermal sources. More particularly, aperture synthesis used in radio-astronomy by exploiting the Earth's rotation (for an upward observation) has been re-adapted to Earth observation (for a downward observation) using the satellite's motion and gave rise to the spatio-temporal interferometry.

3.4.2 2D Doppler-Radiometer

3.4.2.1 Introduction

The detailed study of the spatio-temporal interferometry (section III) yielded the conclusion that by directly correlating the signals collected by independent antennas at different time samples the interesting phase information is exactly canceled by the Doppler shift. Moreover, one is left with an uncompensated rapidly oscillating phase factor and a strong suppression of the amplitude of the correlation function.

In VLBI observations, objects are located in the very far field region and the Earth's rotation is used to synthesize different baselines corresponding to different spatial frequencies of the visibility function found to be the Fourier transform of the brightness temperature of the observed region of the sky. A concept inspired from VLBI interferometry and the proposed concept by Mel'nik, called *2D Doppler Radiometer*, was proposed by A. Camps and C. Swift [7] to improve the achieved spatial resolution by classical space-based passive radiometers (figure 3.6).

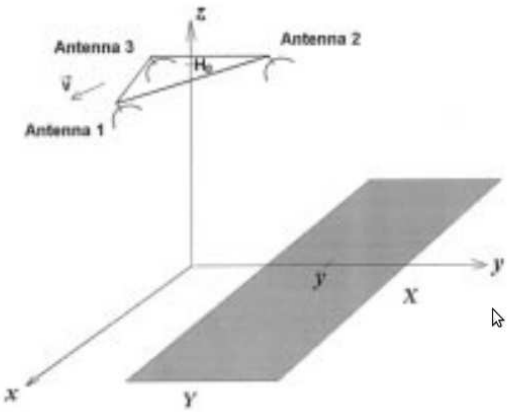

Figure 3.6: 2D Doppler radiometer [7]

3.4.2.2 Concept

The 2D Doppler Radiometer is based on a spatio-temporal interferometry by exploiting the aircraft's motion in its orbit to create additional baselines in the along-track direction. However, as Mel'nik described in [17], matched filtering techniques must be used in order to track the differential delay

induced by the satellite's motion determined for a particular pixel position, i.e. the image is continuously constructed pixel by pixel.

Similarly to VLBI interferometry, adjustable delays are introduced in the post-processing step so as to stop the fringes [18] (figure 3.7) before the cross-correlation. Nevertheless, since the observed sources in the field of Earth observation are not punctual, a pixel-by-pixel treatment by the introduction of pixel-dependent (position-dependent) delays is thus required. This yields therefore a pixel-by-pixel reconstruction of images.

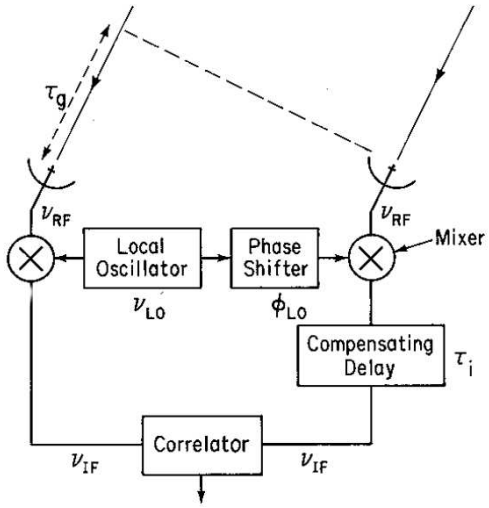

Figure 3.7: Diagram of a frequency conversion and delay tracking interferometer [7]

The 2D Doppler radiometer comprises three antennas spaced by 50m-baselines (figure 3.6). From a focused pixel, adjustable delays are applied on each channel to compensate for the differential propagation delay. The outputs are afterwards cross-correlated and filtered. One shows that the output of the low-pass filter filters down the contributions from non-focused pixels and only the contribution from the focused pixel remains [7].

More particularly, a first 1D information is retrieved through the calculation of the visibility functions V_{12}, V_{13} obtained by cross-correlating the signals received by the pair of antennas (1,2) and (1,3) after the introduction of the adjustable delays in each channel corresponding to a given pixel. One shows furthermore that the operation $\sqrt{V_{12}V_{13}}$ yields a 2D information of the focused pixel neighborhood.

Finally, it is shown in [7] that the 2D Doppler Radiometer with three 1.1m×0.64m antennas separated by a distance of 50 m yields a spatial resolution of the order of 15 km and roughly a radiometric sensitivity of the order of 2.1 K using standard parameters.

3.4.2.3 Discussion

The originality of the 2D Doppler Radiometer rests on the retrieval of a 2D information with acceptable spatial resolutions using solely a three-antenna configuration termed with an adjustable delay introduction methodology allowing a pixel-by-pixel construction of images.

However, three issues are in perspective when dealing with such a concept. First, in order to reach the expected 15-km spatial resolution, the minimal required separation between the antennas is of the order of 50 m. This rises essentially the question of whether a similar configuration is technically feasible and if a flight-formation technology is not required to ensure the required separation between antennas with its accompanying energy insurance and precise timing challenges. Second, based on what depicts

figure (3) in [7], one notices that the optimal trade-off between acceptable radiometric sensitivities and geometric resolutions is obtained for swath widths of the order of 200 km much lower than minimal required value of 1000 km to ensure a global coverage of the Earth's surface in three days. Finally, a temporal integration of 60 s is by the same token required in the light of achieving highly resolved images. Unfortunately, such a long integration deteriorates the angular resolution found to be of great advantage in SMOS since it defines the number of possible angular acquisitions of the same region and allows the improvement of the instrument's radiometric performance.

3.4.2.4 Conclusion

The study of the 2D Doppler radiometer concept showed an expected achievable spatial resolution of the order of 15 km using a 50m-separated three-antenna configuration. The basic idea was initially inspired from VLBI and consists in the introduction of instrumental delays to the different channels in order to compensate for the differential propagation delays. The image is reconstructed pixel-by-pixel by applying adjustable delays corresponding to each pixel's position, this technique allows to focus only one pixel and cancels, by destructive interferences, the contributions from other pixels.

The 2D imaging is performed by taking advantage of the 2D configuration of the Doppler Radiometer. Starting from the 1D spatial resolution retrieved from the cross-correlation of the outputs of the different pairs of antennas, the 2D spatial information is in turn reached by averaging both cross-correlation products.

Bibliography

[1] I. Corbella, N. Duffo, M. Vall-llossera, and A. Camps, "The visibility function in interferometric aperture synthesis radiometry," *IEEE Transaction on Geoscience and Remote Sensing*, vol. 42, No. 8, pp. 1677-1682, ISSN: 0278-0062.

[2] Y. Soldo, F. Cabot, B. Rougé, Y. H. Kerr, A. Al Bitar, and E. Epaillard, "SMOS-NEXT: A new concept for soil moisture retrieval from passive interferometric observations," *EAS Publications Series*, 59 (2013) 203-212.

[3] A. R. Thompson, J. M. Moran, and G. W. Swenson, "Interferometry and Synthesis in Radio Astronomy, 2nd Edition," *WILEY-VCH.*, 2001.

[4] W. N. Christiansen and J.A. Hogbom, "Radiotelescopes," *Cambridge University Press*, Cambridge, 1969.

[5] D. A. Duev et al., "RadioAstron as a target and as an instrument: Enhancing the Space VLBI mission's scientific output," *Astronomy and Astrophysics*, 573:A99, January 2015.

[6] N. S. Kardashev, Y. Y. Kovalev, and K. I. Kellermann, "RadioAstron: An Earth-Space Radio Interferometer with a 350,000 km Baseline," *The URSI Radio Science Bulletin,* no. 343, pp. 22-29, December 2012.

[7] A. J. Camps and C. T. Swift, "A two-dimensional Doppler-Radiometer for Earth observation," *IEEE Transactions on Geoscience and Remote Sensing*, 39(7):1566–1572, July 2001.

[8] Hyuk Park, Sung-Hyun Kim, Ho-Jin Lee, Nam-Won Moon, and Yong-Hoon Kim, "A Rectangular Array for Motion Induced Synthetic Aperture Radiometer," *Geoscience and Remote Sensing Symposium, 2008. IGARSS 2008. IEEE International*, vol. 2, pages II–1160–II–1163, July 2008.

[9] J.D. Jackson, "Classical Electrodynamics," *2nd edition*, Wiley, 1975.

[10] Nanzer, Jeffrey A., "Microwave and Millimeter-wave Remote Sensing for Security Applications," *Artech House*, 2012.

[11] S. M. Rytov, "Theory of electric fluctuations and thermal radiation," Technical report, July 1959.

[12] Eugene A. Sharkov, "Passive Microwave Remote Sensing of the Earth: Physical Foundations," *Springer, Berlin; New York : Chichester, UK, 2003 edition*, December 2003.

[13] Yann H. Kerr et al., "Soil Moisture Retrieval from Space: The Soil Moisture and Ocean Salinity (SMOS) Mission," *IEEE Transaction on Geoscience and Remote Sensing,* vol. 39, vo. 8, AUGUST 2001.

[14] D. Braun, Y. Monjid, B. Rougé, and Y. Kerr, "Generalization of the Van Cittert–Zernike theorem: observers moving with respect to sources," *Measurement and Science Technology*, November, 2015.

[15] E. Middelberg and U. Bach, "High resolution radio astronomy using very long baseline interferometry," *Rep. Prog. Phys.*, 71 (2008) 066901 (32pp).

[16] Peter N. Wilkinson. "An introduction to deconvolution in VLBI," *Very Long Baseline Interferometry NATO ASI Series*, Vol 283, pp. 183-197, 1989.

[17] Y. A. Mel'nik. "Space-time handling of radiothermal signals from radiators that move in the near zone of an interferometer," *Izvestiya Vysshikh Uchebnykh Zavedenii, Radiofiz.*, 15:1376–1380, Sept. 1972.

[18] G. B. Taylor, C. L. Carilli, and R. A. Perly, "Synthesis Imaging in Radio Astronomy II," *A collection of Lectures from the Sixth NRAO/NMIMT Synthesis Imaging Summer.*, pp. 17-18, June. 1998.

Chapter 4

FOURIER CORRELATION IMAGING: ANALYTICAL DERIVATION

Contents

4.1 Introduction

A new spaceborne concept is proposed as the new generation to follow the well-known ESA SMOS mission. It relies on an innovative *passive spatio-temporal interferometry* inspired from the Microwave Imaging Radiometer using Aperture synthesis (MIRAS) system. This new proposal comes in answer to the more and more greedy user-driven needs for higher spatially resolved satellite-delivered products. The new mission main functional objective is a wide jump of the currently achieved spatial resolutions by optimally a factor 10 so as to reach sub-kilometric resolutions.

Such a challenge has never been taken-up using exclusively passive radiometry for Earth observation purposes. Meanwhile the American Soil Moisture Active Passive (SMAP) mission choose the passive/active combination option as a try to answer the need for higher spatial resolutions, the new proposed mission opted for a passive radiometry system relying on an innovative interferometric approach whose objective is to exploit at maximum the acquired physical information by the imaging instrument.

The basic idea behind the spatio-temporal interferometry resulted from the enhanced understanding of the aperture synthesis technique thanks to SMOS achievements. It has been demonstrated that when using aperture synthesis for imaging the surface of the Earth by means of an antenna-array, the optimal achievable spatial resolution is directly deduced from the maximal physical distance between the antennas, also called maximal baseline. Thus, one firstly wondered whether generating *virtual* longer baselines using the motion of the instrument could have a significant impact on the achieved spatial resolution. This exactly constitutes the basis of the spatio-temporal approach that proposes to combine the time-space variables in the correlation procedure.

A preliminary study of the spatio-temporal interferometry combined with a **temporal correlation imaging** procedure based on cross-correlating the temporal samples of the acquired signals at various spatial positions of antennas was carried out in previous chapter. It leaded to the conclusion that the additional information due the observer motion is *exactly* canceled with the Doppler shift induced by the relative motion of the observer with respect to sources at the Earth's surface [1].

In this chapter, we describe the second correlation approach, proposed by D. Braun [2, 3], which, when combined with the spatio-temporal interferometric system, yields remarkable results. Instead of performing the correlation product in the time domain, we show that by correlating the *Fourier* components of the temporally acquired signals over a fixed integration time by a pair of antennas, separated by a distance Δr on board of a satellite flying at height h, at slightly different frequencies, the 2D brightness temperature of the observed scene can be reconstructed using a set of different observations of the same source. This is what we called **Fourier Correlation Imaging**. This property of the correlation function owes to the fact that the fluctuations of a source point at the surface of the Earth are seen at slightly different frequencies at the level of the pair of antennas due to the slightly different Doppler effect.

4.2 Theoretical model

4.2.1 Electric field

Consider a pair of antennas separated by a distance Δr on board of a satellite of speed v_s and height h. We assume for simplicity that the antenna-pair is arranged perpendicularly to the flight direction (figure 4.1).

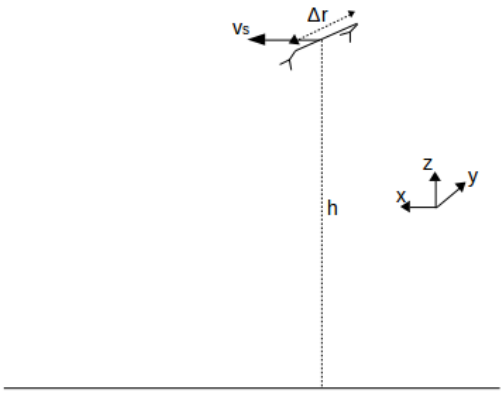

Figure 4.1: Concept's geometry

At each time sample, the microwave radiation arising from sources, that are assumed to behave as fluctuating currents of standard deviation the mean square of the physical temperature, is measured at the position of the antennas at the satellite-fixed reference frame. We showed in chapter 3 that the expression of the time-dependent electric field measured at the level of antenna 1 of time-dependent position $\mathbf{r}_1'(t) = \mathbf{r}_1 + \mathbf{v}_s t$ at instant t is given by

$$\mathbf{E}(\mathbf{r}_1', t) = -\frac{\mu_0}{4\pi} \int \frac{d^3\mathbf{r}''}{|R(t)|} \partial_t \mathbf{j}(\mathbf{r}'', t) \mid_{t=t-R(t)/c}, \tag{4.1}$$

with $R(t) = \mathbf{r}_1'(t) - \mathbf{r}''$, c the speed of light, μ_0 the magnetic permeability of vacuum, and $\mathbf{r}_1$ the initial position of the antenna at $t = 0$. $\mathbf{j}(\mathbf{r}'', t)$ denote the spatio-temporal component of the current densities of a source at position $\mathbf{r}''$ at the surface of the Earth. This expression is valid under the far field condition, namely $R(t) \gg \lambda$ with $\lambda \sim 20$ cm in the microwave regime.
Next, we express the current densities through the inverse Fourier transform of their spectrum,

$$\mathbf{j}(\mathbf{r}'', t) = \frac{1}{\sqrt{2\pi}} \int_{-\infty}^{\infty} d\omega' e^{i\omega' t} \tilde{\mathbf{j}}(\mathbf{r}'', \omega'), \tag{4.2}$$

which, together termed with (4.1), gives

$$\mathbf{E}_{\mathbf{r}_1}(t) \equiv \mathbf{E}(\mathbf{r}_1', t) = -\frac{\mu_0}{4\pi\sqrt{2\pi}} \int d^3\mathbf{r}'' \int d\omega' \frac{i\omega'}{|R(t)|} \tilde{\mathbf{j}}(\mathbf{r}'', \omega') e^{i\omega'(t-|R(t)|/c)}. \tag{4.3}$$

The previous expression is a result of the study undertaken in chapter 3 where we showed that, up to changes of the order of β (the ratio between the satellite and light motions $\sim 10^{-5}$), the same expressions are obtained both in the Earth- and the satellite-fixed frames.
When preforming the spatio-temporal interferometry, one is interested in measuring the time-dependent electric field sampled over a predefined integration time τ and over which the Fourier-transformation is performed (figure 4.2).

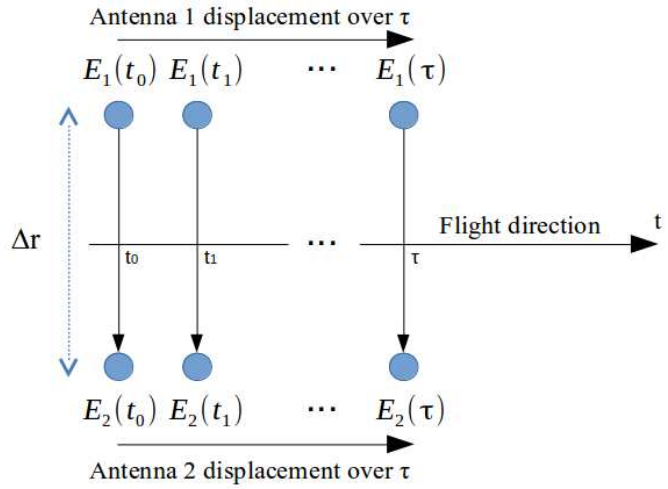

Figure 4.2: Spatio-temporal interferometry

4.2.2 Fluctuations of sources

We assume that the current fluctuations of sources at the Earth's surface can presumably be described by Random Gaussian Processes (RGPs). Based on this, we introduce the following assumption on sources deduced from the *Fluctuation-Dissipation Theorem* (FDT) detailed in the appendix.

FDT assumption: *Sources at different positions* $\boldsymbol{r}_1'', \boldsymbol{r}_2''$*, with different frequencies* ω_1, ω_2*, or with different polarizations* i, j *are uncorrelated,*

$$\left\langle \tilde{j}_i(\mathbf{r}_1'', \omega_1)\tilde{j}_i^*(\mathbf{r}_2'', \omega_2)\right\rangle = \delta_{ij}\frac{l_c^3}{T_c}\delta(\mathbf{r}_1'' - \mathbf{r}_2'')\delta(\omega_1 - \omega_2)\left\langle |\tilde{j}_i^*(\mathbf{r}_2'', \omega_2)|^2\right\rangle, \tag{4.4}$$

where l_c, T_c refer to the correlation dimensions and the average $\left\langle \dots \right\rangle$ is over an ensemble of realizations of the stochastic processes which can be reduced to a temporal average by assuming ergodicity.

4.3 Fourier Correlation Imaging

4.3.1 Introduction

Here, we describe the new correlation approach to be termed with the spatio-temporal interferometric concept. It is based on cross-correlating the Fourier components of the time-dependent signals measured by a pair of antennas separated by a distance Δr at two different frequencies. The Fourier components of the received signals are computed by Fourier-transforming the temporal fields sampled over an integration time τ (figure 4.3). Thanks to this methodology, the classical purely 2D-spatial aperture synthetic reconstruction problem in SMOS is reduced to a combined 1D-spatial/1D-temporal problem.

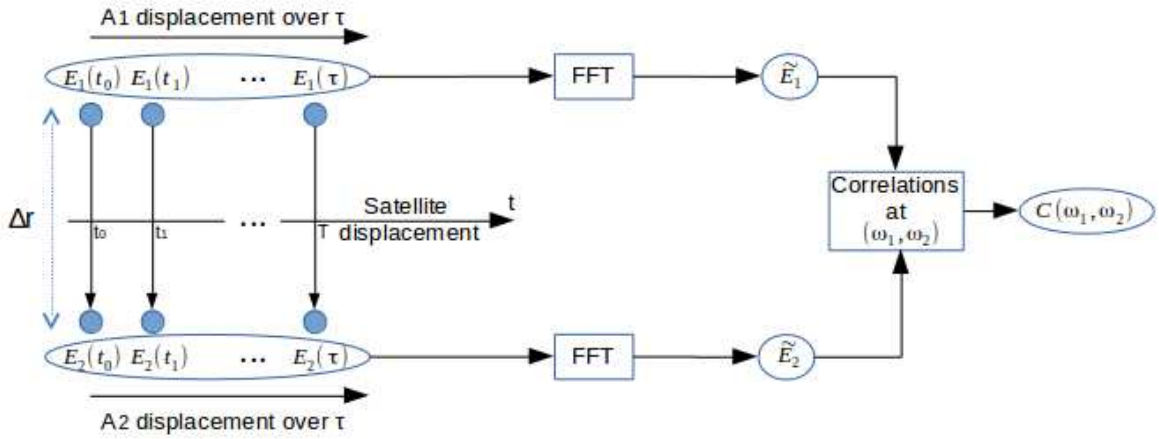

Figure 4.3: Concept of Fourier Correlation Imaging

4.3.2 Electric field spectrum

The spectrum of the electric fields is obtained by Fourier-transforming the acquired temporal signals by each antenna sampled over an integration time τ which corresponds to the inverse of the frequency bandwidth. In the following theoretical analysis, time and frequency integrations will be considered as infinite.

Now, Fourier-transforming the expression (4.3) of the electric field,

$$\tilde{\mathbf{E}}_{\mathbf{r}_1}(\omega) = \frac{1}{\sqrt{2\pi}} \int_{-\infty}^{\infty} dt_1 e^{-i\omega t} \mathbf{E}_{\mathbf{r}_1}(t),$$

gives

$$\tilde{\mathbf{E}}_{\mathbf{r}_1}(\omega) = K_1 \int dt \int d\omega' \int d^3\mathbf{r}'' \frac{i\omega'}{|R(t)|} \tilde{\mathbf{j}}(\mathbf{r}'', \omega') e^{i(\omega'-\omega)t} e^{-i\omega'|R(t)|/c}, \tag{4.5}$$

where $K_1 = -\mu_0/(8\pi^2)$.

For completeness, we push further the analysis of the spectrum (4.5). First, an approximation of the distance $|R(t)| = |\mathbf{r} + \mathbf{v}_s t - \mathbf{r}''|$ to first order in $v_s t/|\mathbf{r} - \mathbf{r}''| \ll 1$, with $v_s = |\mathbf{v}_s|$, gives

$$\begin{aligned} |\mathbf{r} + \mathbf{v}_s t - \mathbf{r}''| &= \sqrt{(\mathbf{r} + \mathbf{v}_s t - \mathbf{r}'')^2} = |\mathbf{r} - \mathbf{r}''| \sqrt{1 + 2\frac{(\mathbf{r} - \mathbf{r}'') \cdot \mathbf{v}_s t}{|\mathbf{r} - \mathbf{r}''|^2} + \frac{\mathbf{v}_s^2 t^2}{|\mathbf{r} - \mathbf{r}''|^2}} \\ &\simeq |\mathbf{r} - \mathbf{r}''| \left(\frac{(\mathbf{r} - \mathbf{r}'') \cdot \mathbf{v}_s t}{|\mathbf{r} - \mathbf{r}''|^2} \right) = |\mathbf{r} - \mathbf{r}''| + \hat{e}_{\mathbf{r}-\mathbf{r}''} \cdot \mathbf{v}_s t, \end{aligned} \tag{4.6}$$

which yields, by neglecting time-dependent corrections to the amplitude,

$$\begin{aligned} \tilde{\mathbf{E}}_{\mathbf{r}_1}(\omega) &\simeq K_1 \int_{-\infty}^{\infty} dt \int_{-\infty}^{\infty} d\omega' \int d^3\mathbf{r}'' \frac{i\omega' \tilde{\mathbf{j}}(\mathbf{r}'', \omega')}{|\mathbf{r} - \mathbf{r}''|} e^{i(\omega'-\omega)t} e^{-i\frac{\omega'}{c}(|\mathbf{r}-\mathbf{r}''| + \hat{e}_{\mathbf{r}-\mathbf{r}''} \cdot \mathbf{v}_s t)} \\ &= iK_1 \int_{-\infty}^{\infty} d\omega' \omega' \int d^3\mathbf{r}'' \frac{\tilde{\mathbf{j}}(\mathbf{r}'', \omega')}{|\mathbf{r} - \mathbf{r}''|} e^{-i\frac{\omega'}{c}|\mathbf{r}-\mathbf{r}''|} \int_{-\infty}^{\infty} dt e^{-i\omega t} e^{i\omega'(1-\hat{e}_{\mathbf{r}-\mathbf{r}''} \cdot \beta)t} \end{aligned} \tag{4.7}$$

where we have introduced $\boldsymbol{\beta} = \mathbf{v}_s/c$. The time integral in (4.7) thus boils down to

$$\begin{aligned}\int_{-\infty}^{\infty} dt e^{-i\omega t} e^{i\omega'(1-\hat{e}_{\mathbf{r}-\mathbf{r}''}\cdot\boldsymbol{\beta})t} &= 2\pi\delta(-\omega+\omega'(1-\hat{e}_{\mathbf{r}-\mathbf{r}''}\cdot\boldsymbol{\beta})) \\ &= 2\pi\delta(\omega'-\omega(1-\hat{e}_{\mathbf{r}-\mathbf{r}''}\cdot\boldsymbol{\beta})^{-1})\frac{1}{|1-\hat{e}_{\mathbf{r}-\mathbf{r}''}\cdot\boldsymbol{\beta}|},\end{aligned} \tag{4.8}$$

which, to first order in $v_s/c \simeq 10^{-5}$ to get $(1-\hat{e}_{\mathbf{r}-\mathbf{r}''}\cdot\boldsymbol{\beta})^{-1} \simeq (1+\hat{e}_{\mathbf{r}-\mathbf{r}''}\cdot\boldsymbol{\beta})$, and by neglecting once more corrections to the amplitude, yields

$$\begin{aligned}\tilde{\mathbf{E}}_{\mathbf{r}_1}(\omega) &\simeq iK_1\int_{-\infty}^{\infty} d\omega'\omega'\int d^3\mathbf{r}''\frac{\tilde{\mathbf{j}}(\mathbf{r}'',\omega')}{|\mathbf{r}-\mathbf{r}''|}e^{-i\frac{\omega'}{c}|\mathbf{r}-\mathbf{r}''|}\delta(\omega'-\omega(1+\hat{e}_{\mathbf{r}-\mathbf{r}''}\cdot\boldsymbol{\beta})) \\ &= iK_1\omega(1+\hat{e}_{\mathbf{r}-\mathbf{r}''}\cdot\boldsymbol{\beta})\int d^3\mathbf{r}''\frac{\tilde{\mathbf{j}}\Big(\mathbf{r}'',\omega(1+\hat{e}_{\mathbf{r}-\mathbf{r}''}\cdot\boldsymbol{\beta})\Big)}{|\mathbf{r}-\mathbf{r}''|}e^{-i\frac{\omega}{c}(1+\hat{e}_{\mathbf{r}-\mathbf{r}''}\cdot\boldsymbol{\beta})|\mathbf{r}-\mathbf{r}''|} \\ &\simeq iK_1\omega\int d^3\mathbf{r}''\frac{\tilde{\mathbf{j}}\Big(\mathbf{r}'',\omega(1+\hat{e}_{\mathbf{r}-\mathbf{r}''}\cdot\boldsymbol{\beta})\Big)}{|\mathbf{r}-\mathbf{r}''|}e^{-i\frac{\omega}{c}(1+\hat{e}_{\mathbf{r}-\mathbf{r}''}\cdot\boldsymbol{\beta})|\mathbf{r}-\mathbf{r}''|}.\end{aligned} \tag{4.9}$$

In equation (4.9), we clearly notice the effect of the Doppler shift, arising from the motion of the observer with respect to the source, through the frequency translation $\omega \to \omega(1+\hat{e}_{\mathbf{r}-\mathbf{r}''}\cdot\boldsymbol{\beta})$. This shows furthermore the linkage between the frequency ω of the electric field spectrum and the frequencies of source's fluctuations ω' by means of the Doppler shift.

4.3.3 Correlation function

The correlation, or visibility, function is obtained by cross-correlating the Fourier components given by (4.5) of the observed electric field fluctuations by a pair of antennas at different frequencies ω_1 and ω_2,

$$C(\mathbf{r}_1,\mathbf{r}_2,\omega_1,\omega_2) = \Big\langle \tilde{\mathbf{E}}_{\mathbf{r}_1}(\omega_1)\tilde{\mathbf{E}}^*_{\mathbf{r}_2}(\omega_2)\Big\rangle, \tag{4.10}$$

where $\Big\langle \dots \Big\rangle$ is an average over an ensemble of uncorrelated realizations of the stochastic process defining sources' fluctuations. This average will be briefly discussed in chapter 5 section 2.
Using the FDT assumption introduced earlier, we derive the correlation function between the acquired spectrums by the pair of antennas of original positions $\mathbf{r}_1$, $\mathbf{r}_2$,

$$\begin{aligned}C(\mathbf{r}_1,\mathbf{r}_2,\omega_1,\omega_2) =& K_2\int dt_1\int dt_2\int d\omega'\int d^3\mathbf{r}''\omega'^2\frac{\Big\langle\Big|\tilde{\mathbf{j}}\Big(\mathbf{r}'',\omega'\Big)\Big|^2\Big\rangle}{|\mathbf{r}_1+\mathbf{v}_s t_1-\mathbf{r}''||\mathbf{r}_2+\mathbf{v}_s t_2-\mathbf{r}''|} \\ &\times e^{-i\frac{\omega'}{c}(|\mathbf{r}_1+\mathbf{v}_s t_1-\mathbf{r}''|-|\mathbf{r}_2+\mathbf{v}_s t_2-\mathbf{r}''|)}e^{i\omega'(t_1-t_2)}e^{-i(\omega_1 t_1-\omega_2 t_2)},\end{aligned} \tag{4.11}$$

where $K_2 = K_1^2 l_c^3/T_c$.

In reality, each antenna provides a voltage $\tilde{V}_{\mathbf{r}}(\omega)$ which is the result of the filtering of the captured signal both in space, by the antenna dimensions, and in frequency, by the intermediate and low-pass filters present in the processing channel. If we denote the frequency response of the whole chain by $H(\omega)$, the delivered voltage by the antenna is expressed as follows: $\tilde{V}_{\mathbf{r}}(\omega) = H(\omega)\tilde{\mathbf{E}}_{\mathbf{r}}(\omega)$. In a first step, we will restrict the analytical derivation of the correlation function to its unfiltered version, obtained by cross-correlating the unfiltered versions of the electric field spectrums, which enters in the definition of

the filtered version as follows

$$C^F(\mathbf{r}_1,\mathbf{r}_2,\omega_1,\omega_2) = \left\langle \tilde{V}_{\mathbf{r}_1}(\omega_1)\tilde{V}^*_{\mathbf{r}_2}(\omega_2)\right\rangle \\ = C(\mathbf{r}_1,\mathbf{r}_2,\omega_1,\omega_2)H(\omega_1)H^*(\omega_2). \tag{4.12}$$

We show furthermore in [3] that the intensity of current fluctuations $I(\mathbf{r}'',\omega') \equiv \left\langle \left|\tilde{\mathbf{j}}\left(\mathbf{r}'',\omega'\right)\right|^2 \right\rangle$ appearing in the expression of the correlation function (4.11) is a weakly-dependent function on frequency, such that $I(\mathbf{r}'',\omega') \simeq I(\mathbf{r}'')$, which is related in the microwave regime to the physical temperature of the source at the origin of the current fluctuations $\mathbf{j}(\mathbf{r}'',\omega')$ at position $\mathbf{r}''$.
Besides, satellite-based aperture synthesis imagers retrieve the values of the position-dependent brightness temperatures radiated from sources at the ground, which are related to the physical temperatures by means of the emissivity (see chapter 1), from the measured correlation values. Correspondingly, we are interested in this section in deriving a suitable relationship that links the correlation values measured by means of the FouCoIm concept to the brightness temperatures.

For simplicity, we take at a first assumption the satellite to be moving in the x-direction, such that $\mathbf{v}_s = v_s\hat{e}_x$ where $\hat{e}_x$ is the unit vector.

Now, based on equation (4.11), one may be tempted to reduce the phase of the correlation function Φ,

$$\Phi = -\frac{\omega'}{c}(|\mathbf{r}_1 + \mathbf{v}_s t_1 - \mathbf{r}''| - |\mathbf{r}_2 + \mathbf{v}_s t_2 - \mathbf{r}''|) + \omega'(t_1 - t_2) - (\omega_1 t_1 - \omega_2 t_2). \tag{4.13}$$

to a more convenient form comprised of common variables of both antennas. Thus, if we define the following relative and center-of-mass frequency and time variables

$$\begin{cases} \omega_c = (\omega_1+\omega_2)/2 \\ \Delta\omega = \omega_2 - \omega_1 \end{cases}, \begin{cases} t_c = (t_1+t_2)/2 \\ \Delta t = t_2 - t_1 \end{cases},$$

and introduce a new spatial variable $\mathbf{r}_t \equiv \mathbf{r}'' - \mathbf{v}_s t_c$, which implies $\mathbf{r}_1 + \mathbf{v}_s t_1 - \mathbf{r}'' = \mathbf{r}_1 - \mathbf{v}_s\Delta t/2 - \mathbf{r}_t$ and $\mathbf{r}_2 + \mathbf{v}_s t_2 - \mathbf{r}'' = \mathbf{r}_2 + \mathbf{v}_s\Delta t/2 - \mathbf{r}_t$, the total phase Φ becomes

$$\Phi = (-\omega' + \omega_c)\Delta t + \Delta\omega t_c - \frac{\omega'}{c}(|\mathbf{r}_1 - \mathbf{v}_s\Delta t/2 - \mathbf{r}_t| - |\mathbf{r}_2 + \mathbf{v}_s\Delta t/2 - \mathbf{r}_t|). \tag{4.14}$$

Next, we change the integration variables from t_1, t_2 to $t_c, \Delta t$ and from $\mathbf{r}''$ to $\mathbf{r}_t$ in order to get

$$C(\mathbf{r}_1,\mathbf{r}_2,\omega_1,\omega_2) \simeq K_2 \int dt_c \int d\Delta t \int d\omega' \int d^3\mathbf{r}_t \omega'^2 \frac{I(\mathbf{r}_t + \mathbf{v}_s t_c)}{|\mathbf{r}_1 - \mathbf{v}_s\Delta t/2 - \mathbf{r}_t||\mathbf{r}_2 + \mathbf{v}_s\Delta t/2 - \mathbf{r}_t|} \\ \times \exp\left[i\Big(\Delta t(-\omega' + \omega_c) + t_c\Delta\omega - \frac{\omega'}{c}(|\mathbf{r}_1 - \mathbf{v}_s\Delta t/2 - \mathbf{r}_t| - |\mathbf{r}_2 + \mathbf{v}_s\Delta t/2 - \mathbf{r}_t|)\Big)\right]. \tag{4.15}$$

By rearranging equation (4.15), the integral over t_c is thus reduced to a 1D Fourier transform of the current intensity function following the variable t_c. Besides, using the assumption on the flight direction (in x-direction), one has $I(x'',y'') = I(x_t + x, y_t)$ with $x = v_s t_c$. With all of this, the integral over t_c becomes

$$\int_{-\infty}^{\infty} dt_c I(\mathbf{r}_t + \mathbf{v}_s t_c) e^{i\Delta\omega t_c} = \frac{1}{v_s}\int_{-\infty}^{\infty} dx I(x_t + x, y_t) e^{i\frac{\Delta\omega}{v_s}x} = \frac{\sqrt{2\pi}}{v_s}\tilde{I}_{x_t,y_t}(\kappa_x), \tag{4.16}$$

where $I(x_t + x, y_t) \equiv I_{x_t,y_t}(x)$ and $\kappa_x = \Delta\omega/v_s$ is the variable conjugate of x. With (4.16), equation (4.15) thus reads

$$C(\mathbf{r}_1, \mathbf{r}_2, \omega_1, \omega_2) \simeq K_3 \int d\Delta t \int d\omega' \int d^3\mathbf{r}_t \omega'^2 \frac{\tilde{I}_{\mathbf{r}_t}(\kappa_x)}{|\mathbf{r}_1 - \mathbf{v}_s\Delta t/2 - \mathbf{r}_t||\mathbf{r}_2 + \mathbf{v}_s\Delta t/2 - \mathbf{r}_t|} \times \exp\Big[i\Big((-\omega' + \omega_c)\Delta t - \frac{\omega'}{c}(|\mathbf{r}_1 - \mathbf{v}_s\Delta t/2 - \mathbf{r}_t| - |\mathbf{r}_2 + \mathbf{v}_s\Delta t/2 - \mathbf{r}_t|)\Big)\Big]. \quad (4.17)$$

where $K_3 = \sqrt{2\pi}K_2/v_s$. Again, if we neglect the weak dependence on frequency of the Fourier transform of the current intensities and the weak variation of ω'^2 compared to the rapid oscillations of the phase factors, which can pulled out of the integral as ω_0^2, the integral over ω' boils down to

$$\int d\omega' \exp\Big[-i\omega'\Big(\Delta t + \frac{1}{c}(|\mathbf{r}_1 - \mathbf{v}_s\Delta t/2 - \mathbf{r}_t| - |\mathbf{r}_2 + \mathbf{v}_s\Delta t/2 - \mathbf{r}_t|)\Big)\Big] \quad (4.18)$$

$$= 2\pi\delta\Big(\Delta t + \frac{1}{c}(|\mathbf{r}_1 - \mathbf{v}_s\Delta t/2 - \mathbf{r}_t| - |\mathbf{r}_2 + \mathbf{v}_s\Delta t/2 - \mathbf{r}_t|)\Big). \quad (4.19)$$

Next, we derive the following approximations to first order in $\mathbf{v}_s\Delta t/|\mathbf{r} - \mathbf{r}_t|$ (valid for $\Delta t \leq h/v_s \sim 100$ s using the standard parameters),

$$|\mathbf{r}_1 - \mathbf{v}_s\Delta t/2 - \mathbf{r}_t| \simeq |\mathbf{r}_1 - \mathbf{r}_t| - \mathbf{v}_s \cdot \hat{\mathbf{e}}_{\mathbf{r}_1 - \mathbf{r}_t}\Delta t/2, \quad (4.20)$$

$$|\mathbf{r}_2 + \mathbf{v}_s\Delta t/2 - \mathbf{r}_t| \simeq |\mathbf{r}_2 - \mathbf{r}_t| + \mathbf{v}_s \cdot \hat{\mathbf{e}}_{\mathbf{r}_2 - \mathbf{r}_t}\Delta t/2, \quad (4.21)$$

and introduce new relative and center-of-mass variables of antennas' initial positions, $\Delta\mathbf{r} = \mathbf{r}_2 - \mathbf{r}_1$ and $\mathbf{r}_c = (\mathbf{r}_1 + \mathbf{r}_2)/2$. Previous approximations (4.20), (4.21) give

$$|\mathbf{r}_1 - \mathbf{v}_s\Delta t/2 - \mathbf{r}_t| - |\mathbf{r}_2 + \mathbf{v}_s\Delta t/2 - \mathbf{r}_t| \simeq (|\mathbf{r}_1 - \mathbf{r}_t| - |\mathbf{r}_2 - \mathbf{r}_t|) - \mathbf{v}_s \cdot \hat{\mathbf{e}}_{\mathbf{r}_c - \mathbf{r}_t}\Delta t \simeq -(\boldsymbol{\Delta r} + \mathbf{v}_s\Delta t) \cdot \hat{\mathbf{e}}_{\mathbf{r}_c - \mathbf{r}_t}, \quad (4.22)$$

and

$$|\mathbf{r}_1 - \mathbf{v}_s\Delta t/2 - \mathbf{r}_t||\mathbf{r}_2 + \mathbf{v}_s\Delta t/2 - \mathbf{r}_t| \simeq |\mathbf{r}_1 - \mathbf{r}_t||\mathbf{r}_2 - \mathbf{r}_t| \simeq |\mathbf{r}_c - \mathbf{r}_t|^2. \quad (4.23)$$

With all of this, equation (4.18) is thus transformed into

$$\int d\omega' \exp\big[\dots\big] \simeq 2\pi\delta\Big(\Delta t(1 - \boldsymbol{\beta} \cdot \hat{\mathbf{e}}_{\mathbf{r}_c - \mathbf{r}_t}) - \frac{1}{c}\boldsymbol{\Delta r} \cdot \hat{\mathbf{e}}_{\mathbf{r}_c - \mathbf{r}_t}\Big), \quad (4.24)$$

with $\beta = |\boldsymbol{\beta}| \sim 10^{-5}$ using the standard parameters. By noticing that $1/(1 - \boldsymbol{\beta} \cdot \hat{\mathbf{e}}_{\mathbf{r}_c - \mathbf{r}_t}) \simeq (1 + \boldsymbol{\beta} \cdot \hat{\mathbf{e}}_{\mathbf{r}_c - \mathbf{r}_t})$, one is left with

$$\int d\omega' \exp\big[\dots\big] \simeq \frac{1}{|1 - \boldsymbol{\beta} \cdot \hat{\mathbf{e}}_{\mathbf{r}_c - \mathbf{r}_t}|} 2\pi\delta\Big(\Delta t - \frac{1}{c}\boldsymbol{\Delta r} \cdot \hat{\mathbf{e}}_{\mathbf{r}_c - \mathbf{r}_t}(1 + \boldsymbol{\beta} \cdot \hat{\mathbf{e}}_{\mathbf{r}_c - \mathbf{r}_t})\Big). \quad (4.25)$$

Neglecting changes to the amplitude, the expression (4.17) of the correlation function thus becomes

$$C(\mathbf{r}_1, \mathbf{r}_2, \omega_1, \omega_2) \simeq 2\pi K_3\omega_0^2 \int d^3\mathbf{r}_t \frac{\tilde{I}_{\mathbf{r}_t}(\kappa_x)}{|\mathbf{r}_c - \mathbf{r}_t|^2} \exp[i\omega_c \frac{1}{c}\boldsymbol{\Delta r} \cdot \hat{\mathbf{e}}_{\mathbf{r}_c - \mathbf{r}_t}(1 + \boldsymbol{\beta} \cdot \hat{\mathbf{e}}_{\mathbf{r}_c - \mathbf{r}_t})] \simeq K_4 \int d^3\mathbf{r}_t \frac{\tilde{I}_{\mathbf{r}_t}(\kappa_x)}{|\mathbf{r}_c - \mathbf{r}_t|^2} \exp[i\omega_c \frac{\boldsymbol{\Delta r} \cdot \hat{\mathbf{e}}_{\mathbf{r}_c - \mathbf{r}_t}}{c}], \quad (4.26)$$

where we have neglected in the phase the second order term $\omega_c\beta/c$ and introduced $K_4 = 2\pi K_3\omega_0^2$.

Moreover, since the variables x_t and x are independent, the 1D Fourier transform of the intensity of current fluctuations $\tilde{I}_{\mathbf{r}_t}(\kappa_x)$ can be further reduced to

$$\begin{aligned}\tilde{I}_{\mathbf{r}_t}(\kappa_x) &= \frac{1}{\sqrt{2\pi}}\int_{-\infty}^{\infty} dx I_{x_t,y_t}(x)e^{i\kappa_x x} = \frac{1}{\sqrt{2\pi}}\int_{-\infty}^{\infty} dx I_{0,y_t}(x_t+x)e^{i\kappa_x x} \\ &= \frac{1}{\sqrt{2\pi}}\int_{-\infty}^{\infty} dx' I_{0,y_t}(x')e^{i\kappa_x x'}e^{-i\kappa_x x_t} = e^{-i\kappa_x x_t}\tilde{I}_{0,y_t}(\kappa_x). \end{aligned} \tag{4.27}$$

Equation (4.26) together with (4.27) yield the final expression of the correlation function obtained by means of the FouCoIm concept,

$$C(\mathbf{r}_1,\mathbf{r}_2,\omega_1,\omega_2) \simeq K_4 \int dx_t \int dy_t \frac{\tilde{I}_{0,y_t}(\kappa_x)}{|\mathbf{r}_c-\mathbf{r}_t|^2} e^{-i\kappa_x x_t} e^{i\frac{\boldsymbol{\Delta r}\cdot\hat{\mathbf{e}}_{\mathbf{r}_c-\mathbf{r}_t}}{c}\omega_c}. \tag{4.28}$$

On the face of the expression (4.28), it seems that the position-dependent intensities of sources' current fluctuations are linked to the measured correlation values by means of the FouCoIm approach via a 2D integral-transformation.

4.3.4 Properties of the correlation function

We describe hereafter a different derivation of the outcome of the FouCoIm concept leading to a remarkable property of the obtained correlation function.

Starting from the expression (4.11) of the correlation function established earlier and using the property that the current intensities, which are weakly dependent on frequency, are related to the absolute temperature in the microwave regime as follows [3]

$$\left\langle |\tilde{\mathbf{j}}(\mathbf{r}'',\omega')|^2 \right\rangle \equiv I(\mathbf{r}'') = K_3 T(\mathbf{r}''), \tag{4.29}$$

where K_3 is a constant. Equation (4.11) together with (4.29) yield

$$\begin{aligned} C(\mathbf{r}_1,\mathbf{r}_2,\omega_1,\omega_2) = K_2K_3 \int dt_1 \int dt_2 \int d\omega' \int d^3\mathbf{r}'' \frac{\omega'^2 T(\mathbf{r}'')}{|R_1(t_1)||R_2(t_2)|} e^{i\omega'(t_1-t_2)} e^{-i(\omega_1 t_1-\omega_2 t_2)} \\ \times e^{-i\frac{\omega'}{c}(|R_1(t_1)|-|R_2(t_2)|)}. \end{aligned} \tag{4.30}$$

Next, by considering the following approximations (valid for $\Delta t \leq 100$ s)

$$|R_1(t_1)| \simeq |\mathbf{r}_1-\mathbf{r}''| + \mathbf{v}_s\cdot\hat{\mathbf{e}}_{\mathbf{r}_1-\mathbf{r}''}t_1, \quad |R_2(t_2)| \simeq |\mathbf{r}_2-\mathbf{r}''| + \mathbf{v}_s\cdot\hat{\mathbf{e}}_{\mathbf{r}_2-\mathbf{r}''}t_2, \tag{4.31}$$

one gets by letting as earlier $\Delta t = t_2 - t_1$, $\mathbf{r}_c = (\mathbf{r}_1+\mathbf{r}_2)/2$ and $\boldsymbol{\Delta r} = \mathbf{r}_2 - \mathbf{r}_1$,

$$|R_1(t_1)| - |R_2(t_2)| \simeq -(\boldsymbol{\Delta r} + \mathbf{v}_s\Delta t)\cdot\hat{\mathbf{e}}_{\mathbf{r}_c-\mathbf{r}''}. \tag{4.32}$$

By inserting (4.32) in (4.30), one is left with

$$\begin{aligned} C(\mathbf{r}_1,\mathbf{r}_2,\omega_1,\omega_2) \simeq & K_4 \int dt_1 \int dt_2 \int d^3\mathbf{r}'' \frac{T(\mathbf{r}'')}{|R_1(t_1)||R_2(t_2)|} e^{-i(\omega_1 t_1-\omega_2 t_2)} \\ & \times \int d\omega' e^{-i\omega'\Delta t} e^{i\frac{\omega'}{c}(\boldsymbol{\Delta r}+\mathbf{v}_s\Delta t)\cdot\hat{\mathbf{e}}_{\mathbf{r}_c-\mathbf{r}''}}, \end{aligned} \tag{4.33}$$

with $K_4 = \omega_0^2 K_2 K_3$ and where we have pulled out ω'^2 from the integral as ω_0^2 since it weakly varies compared to the phase.

As previously, by introducing the time and frequency center-of-mass $t_c = (t_1 + t_2)/2$, $\omega_c = (\omega_1 + \omega_2)/2$ and the frequency difference $\Delta\omega = \omega_2 - \omega_1$, one can switch the variables t_1, t_2 in (4.33) into $t_c, \Delta t$ by noticing that $\omega_1 t_1 - \omega_2 t_2 = -(\omega_c \Delta t + \Delta\omega t_c)$,

$$\begin{aligned} C(\mathbf{r}_1, \mathbf{r}_2, \omega_1, \omega_2) \simeq & K_4 \int dt_c \int d\Delta t \int d^3\mathbf{r}'' \frac{T(\mathbf{r}'')}{|R_1(t_c - \Delta t/2)||R_2(t_c + \Delta t/2)|} e^{i(\omega_c \Delta t + \Delta\omega t_c)} \\ & \times \int d\omega' e^{-i\omega' \Delta t} e^{i\frac{\omega'}{c}(\boldsymbol{\Delta r} + \mathbf{v}_s \Delta t)\cdot \hat{\mathbf{e}}_{\mathbf{r}_c - \mathbf{r}''}}. \end{aligned} \tag{4.34}$$

The frequency integral in the preceding expression of the correlation function leads to a precise value of the time difference Δt,

$$\begin{aligned} \int d\omega' e^{-i\omega' \Delta t} e^{i\frac{\omega'}{c}(\boldsymbol{\Delta r} + \mathbf{v}_s \Delta t)\cdot \hat{\mathbf{e}}_{\mathbf{r}_c - \mathbf{r}''}} &= 2\pi \delta\Big(\Delta t - \frac{1}{c}(\boldsymbol{\Delta r} + \mathbf{v}_s \Delta t)\cdot \hat{\mathbf{e}}_{\mathbf{r}_c - \mathbf{r}''}\Big) \\ &\simeq \frac{2\pi}{|1 - \boldsymbol{\beta}\cdot \hat{\mathbf{e}}_{\mathbf{r}_c - \mathbf{r}''}|} \delta\Big(\Delta t - \frac{1}{c}\boldsymbol{\Delta r}\cdot \hat{\mathbf{e}}_{\mathbf{r}_c - \mathbf{r}''}(1 + \boldsymbol{\beta}\cdot \hat{\mathbf{e}}_{\mathbf{r}_c - \mathbf{r}''})\Big) \\ &\simeq 2\pi \delta\Big(\Delta t - \frac{1}{c}\boldsymbol{\Delta r}\cdot \hat{\mathbf{e}}_{\mathbf{r}_c - \mathbf{r}''}\Big). \end{aligned} \tag{4.35}$$

With (4.35), equation (4.34) becomes

$$C(\mathbf{r}_1, \mathbf{r}_2, \omega_1, \omega_2) \simeq K_5 \int dt_c \int d^3\mathbf{r}'' \frac{T(\mathbf{r}'')}{|R_1(t_c)||R_2(t_c)|} e^{i(\omega_c \tau_R + \Delta\omega t_c)}, \tag{4.36}$$

where $K_5 = 2\pi K_4$ and $\tau_R = \frac{1}{c}\boldsymbol{\Delta r}\cdot \hat{\mathbf{e}}_{\mathbf{r}_c - \mathbf{r}''} \sim 10^{-7}$. Besides, through the satellite's motion the temperature T becomes dependent of the time variable t_c as follows: $T(\mathbf{r}'' + v_s t_c) = T(x'' + x, y'')$. Based on this, equation (4.34) can thus be rearranged as follows

$$C(\mathbf{r}_1, \mathbf{r}_2, \omega_1, \omega_2) \simeq K_5 \int d^3\mathbf{r}'' e^{i\omega_c \tau_R} \int dt_c \frac{T(\mathbf{r}'', t)}{|R_1(t_c)||R_2(t_c)|} e^{i\Delta\omega t_c}. \tag{4.37}$$

In practice, the signal received at the level of each antenna is Fourier-transformed by integration over a fixed integration time τ, such that $v_s \tau \ll h$, and is afterwards filtered in the allowed Earth observation frequency bandwidth of 20 MHz of central frequency $\omega_0 = 2\pi \times 1.4135$ GHz. One may subsequently approximate the distance product by

$$|R_1(t)||R_2(t)| \simeq |\mathbf{r}_1 - \mathbf{r}''||\mathbf{r}_2 - \mathbf{r}''| \simeq |\mathbf{r_c} - \mathbf{r}''|^{\mathbf{2}}, \tag{4.38}$$

to finally obtain

$$C(\mathbf{r}_1, \mathbf{r}_2, \omega_1, \omega_2) \simeq \sqrt{2\pi} K_5 \int d^3\mathbf{r}'' \frac{e^{i\omega_c \tau_R}}{|\mathbf{r_c} - \mathbf{r}''|^{\mathbf{2}}} \tilde{T}(\mathbf{r}'', \Delta\omega), \tag{4.39}$$

where we have introduced the Fourier transform of the x-dependent temperature field,

$$\tilde{T}(\mathbf{r}'', \Delta\omega) = \frac{1}{\sqrt{2\pi}} \int dt_c T(\mathbf{r}'', t_c) e^{i\Delta\omega t_c}. \tag{4.40}$$

Equation (4.39) expresses differently the obtained correlation function using the FouCoIm concept compared (4.28). This expression depicts the remarkable property that when cross-correlating the observed Fourier-transformed signals (by integration over times not exceeding 100 s) by a pair of antennas imaging a scene at the surface of the Earth, the obtained correlation function bears a 2D information. In other words, thanks to this imaging technique, in addition to the standard information borne by the auto-correlation (in the ω_c-direction), an additional correlation information exists in a second dimension over small frequency differences (in the $\Delta\omega$-direction) (figure 4.4).

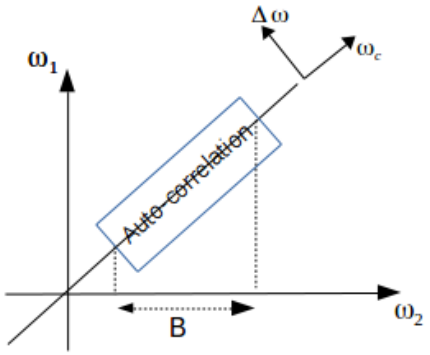

Figure 4.4: 2D information of the correlation function

4.3.5 General expression of the correlation function

Now, we derive the general expression of the correlation function in the case of a random positioning of the pair of antennas.
We assimilate the Earth's surface to a plane located at $z'' = 0$ and introduce antennas' and sources' coordinates, $\mathbf{r}_1 = (x_1, y_1, z_1)$, $\mathbf{r}_2 = (x_2, y_2, z_2)$ and $\mathbf{r}'' = (x'', y'', 0)$, respectively. We thus have $\mathbf{r}_c = (x_c, y_c, z_c) = \Big((x_1 + x_2)/2, (y_1 + y_2)/2, (z_1 + z_2)/2\Big)$, $\Delta r = (dx, dy, dz) = (x_2 - x_1, y_2 - y_1, z_2 - z_1)$ and $\mathbf{r}''_t = (x_t, y_t, 0) = (x'' - v_s t_c, y'', 0)$. With all of this, equation (4.28) is expressed in the general case as follows

$$C_{ij}(\mathbf{r}_1, \mathbf{r}_2, \omega_1, \omega_2) \simeq K_4 \delta_{ij} \int dx_t e^{-i\kappa_x x_t} \int dy_t \frac{\exp\left[i\frac{\omega_c}{c}\left(\frac{dx(x_t - x_c) + dy(y_t - y_c) - dz z_c}{\sqrt{(x_t - x_c)^2 + (y_t - y_c)^2 + z_c^2}}\right)\right]}{(x_t - x_c)^2 + (y_t - y_c)^2 + z_c^2} \tilde{I}_{0,y_t}(\kappa_x). \tag{4.41}$$

In the general case of an array of N antennas, one gets $N(N-1)/2$ different antenna-pairs and the corresponding correlation function to the pair (A_m, A_n) is deduced from (4.41) as follows

$$C_{ij}(\mathbf{r}_m, \mathbf{r}_n, \omega_1, \omega_2) \simeq K_4 \delta_{ij} \int dx_t e^{-i\kappa_x x_t} \int dy_t \frac{\exp\left[i\frac{\omega_c}{c}\left(\frac{dx_{mn}(x_t - x_{mn}) + dy_{mn}(y_t - y_{mn}) - dz_{mn} z_{mn}}{\sqrt{(x_t - x_{mn})^2 + (y_t - y_{mn})^2 + z_{mn}^2}}\right)\right]}{(x_t - x_{mn})^2 + (y_t - y_{mn})^2 + z_{mn}^2} \tilde{I}_{0,y_t}(\kappa_x). \tag{4.42}$$

4.3.6 Simplified expression of the correlation function

In the perspective of a more detailed study of the FouCoIm concept, we derive a simplified form of the expression (4.28) of the correlation function under the condition of a pair of antennas arranged perpendicularly to the flight direction (y-direction) and $\boldsymbol{\Delta r}$ from antenna 1 to antenna 2 such that $\boldsymbol{\Delta r} = \Delta r \hat{e}_y$ with $\Delta r = |\boldsymbol{\Delta r}|$ denoting the spatial separation between both antennas. Also, we denote

the initial center-of-mass position of antennas at $(x_0, 0)$. Based on this, the phase term in (4.28) is thus reduced to

$$\frac{\boldsymbol{\Delta r}\cdot\hat{\mathbf{e}}_{\mathbf{r}_c-\mathbf{r}_t}}{c}\omega_c = -\frac{\Delta r y_t}{\sqrt{(x_t-x_0)^2+y_t^2+h^2}}\frac{\omega_c}{c} \tag{4.43}$$

Integrating (4.43) in (4.28) yields the following

$$\begin{aligned} C(\mathbf{r}_1,\mathbf{r}_2,\omega_1,\omega_2) \simeq & K_4\int dx_t\int dy_t \frac{\tilde{I}_{0,y_t}(\kappa_x)e^{-i\kappa_x x_t}}{(x_t-x_0)^2+y_t^2+h^2}\exp[-i\frac{\Delta r y_t}{\sqrt{(x_t-x_0)^2+y_t^2+h^2}}\frac{\omega_c}{c}] \\ = & K_4 e^{-i\kappa_x x_0}\int dx_t\int dy_t \frac{\tilde{I}_{0,y_t}(\kappa_x)e^{-i\kappa_x x_t}}{x_t^2+y_t^2+h^2}\exp[-i\frac{\Delta r y_t}{\sqrt{x_t^2+y_t^2+h^2}}\frac{\omega_c}{c}]. \end{aligned} \tag{4.44}$$

By switching to dimensionless variables $\xi = x_t/\Delta r, \eta = y_t/\Delta r$ and $\theta = h/\Delta r$, one is left with

$$C(\mathbf{r}_1,\mathbf{r}_2,\omega_1,\omega_2) \simeq K_4 e^{-i\kappa_x x_0}\int d\xi\int d\eta \frac{\tilde{I}_{0,y_t}(\kappa_x)e^{-i\kappa_x\Delta r\xi}}{\xi^2+\eta^2+\theta^2}\exp[-i\frac{\Delta r\eta}{\sqrt{\xi^2+\eta^2+\theta^2}}\frac{\omega_c}{c}], \tag{4.45}$$

which, by applying the change of variables $\xi \to \xi/\sqrt{\eta^2+\theta^2}$, reads

$$C(\mathbf{r}_1,\mathbf{r}_2,\omega_1,\omega_2) \simeq K_4 e^{-i\kappa_x x_0}\int \frac{d\eta}{\sqrt{\eta^2+\theta^2}}\mathcal{K}\{\alpha(\eta),\beta(\eta)\}\tilde{I}_{0,y_t}(\kappa_x), \tag{4.46}$$

where we have introduced the integral kernel

$$\mathcal{K}\{\alpha(\eta),\beta(\eta)\} = \int d\xi \frac{e^{-i(\alpha(\eta)\xi+\frac{\beta(\eta)}{\sqrt{\xi^2+1}})}}{\xi^2+1}, \tag{4.47}$$

with $\alpha(\eta) = \kappa_x\Delta r\sqrt{\eta^2+\theta^2}$ and $\beta(\eta) = (\Delta r\omega_c/c)(\eta/\sqrt{\eta^2+\theta^2})$.

Equation (4.46) constitutes the central equation for the study of the FouCoIm concept. It highlights the remarkable relationship linking the measured correlation values at a pair of frequencies (ω_1,ω_2) to the Fourier-transform (FT) of the position-dependent intensities of sources at the surface of the Earth by means of a 1D *highly oscillatory integral* (HOI) kernel $\mathcal{K}$ defined by integration in x-direction. Based on this, if we assume that the HOI kernel can be approximated, the reconstruction of the FT of current intensities, and hence the brightness temperatures, is thus reduced to an inversion problem in y-direction.
We show furthermore that (4.46) leads to a 2D mapping of the intensity of current fluctuations as function of position by means of a frequency-dependent (on ω_c and $\Delta\omega$) integral kernel function.
As a matter of fact, reconstructing $\tilde{I}_{0,y'}(\kappa_x)$ depends on the ability of inverting the correlation function equation and hence approximating the HOI kernel. Suppose an inverse integration kernel can be found, one obtains $\tilde{I}_{0,y_t}$ for all y_t as function of κ_x which, by taking the inverse Fourier transform in x-direction, yields the reconstruction of the full (x'',y'')-dependent brightness temperature map.

4.3.7 Study of the HOI kernel

4.3.7.1 Approximation of the HOI kernel

The HOI kernel (4.47) linking the correlation values to the brightness temperatures is unlikely to give an exact analytical value, one is therefore interested in determining an acceptable approximation of it.

Due to the dependence of the HOI on α and β, four regimes need to be distinguished: 1) $\alpha \gg \beta\,(\beta \sim 1)$, 2) $\beta \gg \alpha\,(\alpha \sim 1)$, 3) $\alpha \sim \beta\,(\alpha, \beta \gg 1)$, and 4) $\alpha \sim \beta \sim 1$ (intermediate regimes will be discussed in next chapter). Hereafter, we give a brief study of the HOI kernel and for more details about the analytical and numerical derivation of the kernel one should refer to the first section of chapter 5.

In the first regime, by expanding $\exp(-i\beta/\sqrt{1+\xi^2})$ into a power series, one can derive a straightforward analytical approximation of (4.47) using a term-by-term integration,

$$\mathcal{K}(\alpha,\beta) = \sqrt{2\pi\alpha}\sum_{n=0}^{\infty}\frac{(-i\beta)^n}{n!}\sqrt{\Big(\frac{\alpha}{2}\Big)^n}\frac{K_{(n+1)/2}(\alpha)}{\Gamma(1+n/2)}, \tag{4.48}$$

where $K_n(z)$ is the modified Bessel function of the second kind of order n defined as

$$K_n(z) = \frac{(2z)^n}{\sqrt{\pi}}\Gamma(n+\frac{1}{2})\int_0^{\infty}\frac{\cos x}{(\alpha^2+z^2)^{(n+1/2)}}dx. \tag{4.49}$$

In the second regime, the HOI kernel (4.47) is rearranged in the following standard form

$$I[f] = \int f(x)e^{i\omega g(x)}dx, \tag{4.50}$$

that defines HOIs and where f and g are smooth functions. In this regime, f and g are respectively defined as $\exp(-i\alpha\xi)/(1+\xi^2)$ and $-1/\sqrt{1+\xi^2}$, and ω is set to β. By noticing furthermore that g has a stationary point at $\xi = 0$, one may derive an analytical approximation of the HOI kernel (4.47) using a *stationary phase approximation* as follows

$$\begin{aligned}\mathcal{K}(\alpha,\beta) &\simeq \sqrt{\frac{2\pi}{\beta|g''(0)|}}f(0)e^{i\beta g(0)}e^{i\,\mathrm{sign}(g''(0))\frac{\pi}{4}}\\ &= \sqrt{\frac{2\pi}{\beta}}e^{-i\beta}e^{i\frac{\pi}{4}}.\end{aligned} \tag{4.51}$$

In the third regime, a similar stationary phase method can be applied for $f(\xi) = 1/(1+\xi^2)$ and $g(\xi) = -(\xi + \delta/\sqrt{1+\xi^2})$, with $\beta = \delta\alpha$ and ω set to α. It appears that g has two real stationary points ξ_1, ξ_2 for each value of η which are determined using for instance *Sotta-method*. The stationary phase approximation of the HOI kernel in this regime is thus obtained through

$$\mathcal{K}(\alpha,\beta) \simeq \sum_{i=1}^{2}\sqrt{\frac{2\pi}{\alpha|g''(\xi_i)|}}f(\xi_i)e^{i\alpha g(\xi_i)}e^{i\,\mathrm{sign}(g''(\xi_i))\frac{\pi}{4}}. \tag{4.52}$$

Finally in the fourth regime, the integral kernel (4.47) is not anymore a HOI and a classical rectangular approximation is sufficiently correct to derive an approximation of it,

$$\mathcal{K}(\alpha,\beta) \simeq \sum_{\xi}\frac{e^{-i(\alpha\xi+\frac{\beta}{\sqrt{\xi^2+1}})}}{\xi^2+1}. \tag{4.53}$$

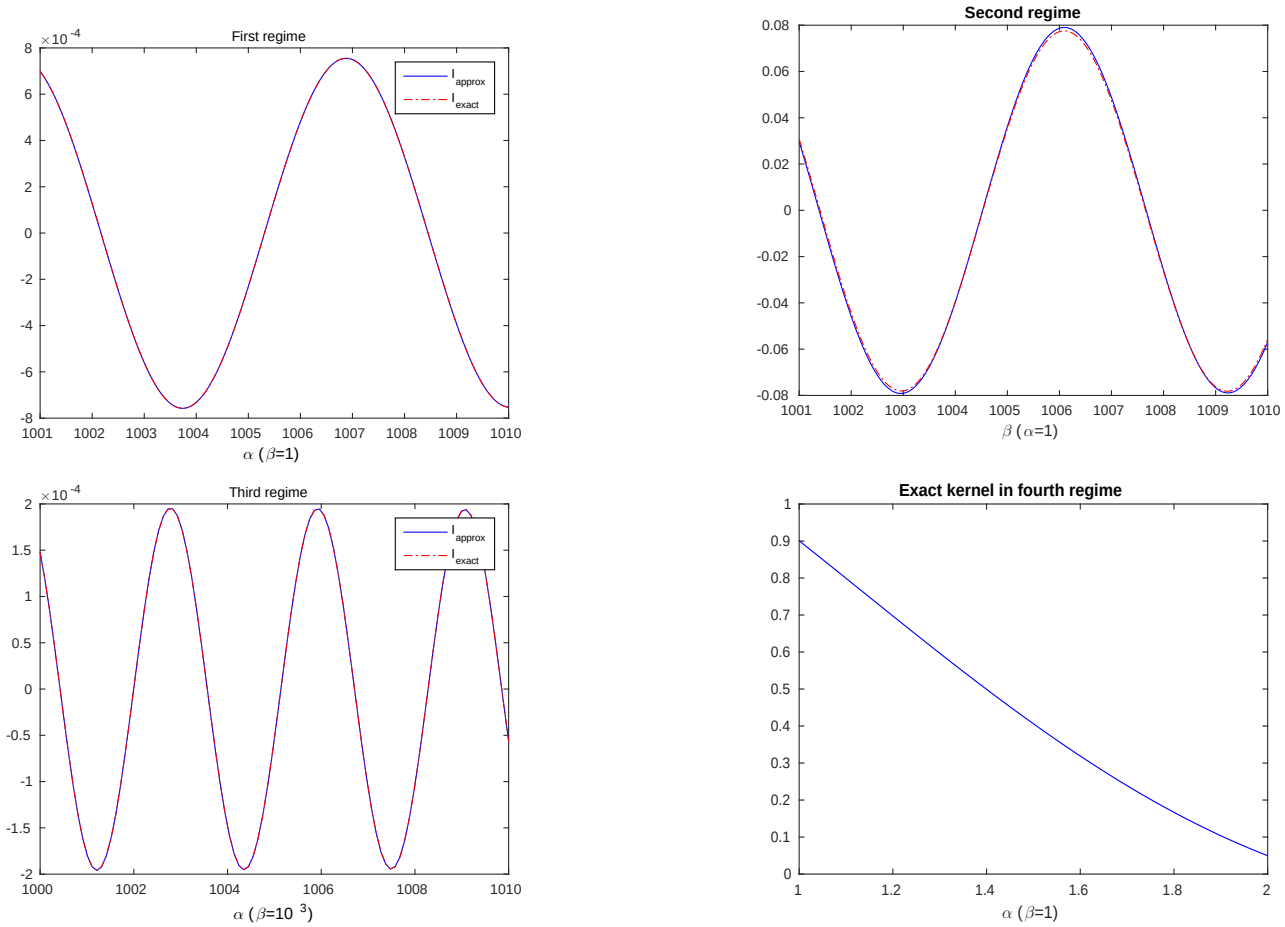

Figure 4.5: Exact and approximate forms of the HOI kernel in the 1^{st}, 2^{nd} and 3^{rd} regimes in addition to the exact form in the 4^{th} regime

Shown in figure 4.5 the numerical results of the quadrature of the HOI kernel in the different frequency regimes. Based on previous figures, one may notice that the contributions from the first and third regimes to the HOI kernel are much lower than those from the second and fourth regimes. We show furthermore in chapter 5 that the fourth regime is restricted to a very tiny η-interval. This means that only the second regime significantly contribute to the HOI kernel and thus to the correlation function. In other words, the correlation function can be correctly considered to be non-zero only within the second regime. Under those circumstances, only the second regime is going to be considered in the following analytical developments.

4.3.7.2 Analytical inversion of the HOI kernel

As previously announced, the only relevant regime in the definition of the HOI kernel is $\beta \gg \alpha$. This condition of α and β induces a more stringent inversion condition on the integration variable η,

$$\begin{aligned}
\beta \gg \alpha \Rightarrow \beta \geq \alpha \quad & \text{(in the minimal case)} \\
\Leftrightarrow \frac{\Delta r \omega_c}{c} \frac{\eta}{\sqrt{\eta^2+\theta^2}} & \geq \frac{\Delta\omega}{v_s} \Delta r \sqrt{\eta^2+\theta^2} \\
\Leftrightarrow \Delta\omega & \leq \frac{v_s}{c} \frac{\eta}{\eta^2+\theta^2} \omega_c \\
\Leftrightarrow \eta_1 \leq \eta & \leq \eta_2, \qquad (4.54)
\end{aligned}$$

where $\eta_{1,2} = (1 \pm \sqrt{1 - 4\delta^2\tilde{h}^2})/(2\delta)$ with $\delta = c\Delta\omega/(v_s\omega_c)$. Figure 4.6 shows the inversion domain of the HOI kernel.

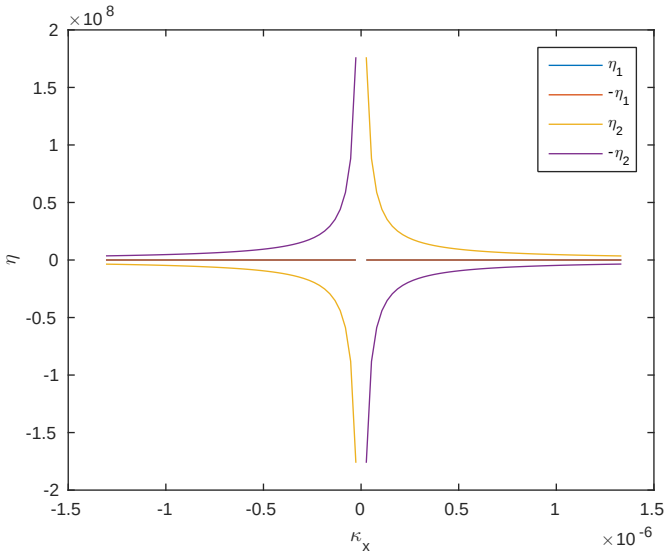

Figure 4.6: Inversion domain

Or equivalently a condition on the frequency difference $\Delta\omega$ by considering the maximum value of $\eta/(\eta^2 + \theta^2)$ reached at $\eta = \theta$,

$$\Delta\omega \leq \frac{v_s\omega_c}{2\theta c}. \tag{4.55}$$

The condition (4.55) suggests that the correlation function is likely to be non-zero only within a small frequency interval $\Delta\omega$ around the auto-correlation (figure 4.4). This condition is sufficient but not necessary in the inversion of the HOI kernel. Using standard parameters and a spacing between antennas $\Delta r = 50$ m, one finds that in addition to the auto-correlation, the correlation function bears additional information within a small frequency interval $\Delta\omega$ up to 1.17 Hz. Besides, the condition (4.54) implies that by means of the analytical inversion of the HOI kernel, one has only access to the brightness temperatures at positions verifying (4.54) (figure 4.7).

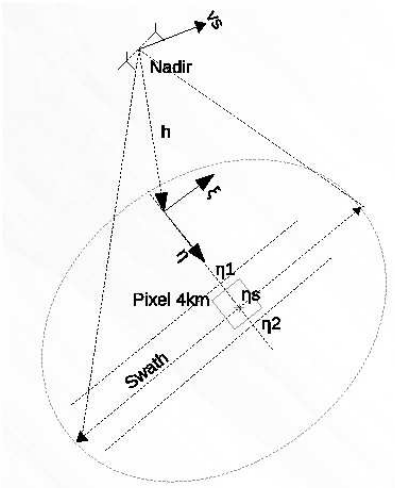

Figure 4.7: Inversion condition on η

In summary, the analytical derivation of the integral kernel confirms the previously established remarkable property of a borne 2D information by the correlation function for the measurement of the position-dependent brightness temperature. Besides, we show that this property is most likely to be valid within a small frequency interval $\Delta\omega$ of the order of one Hertz.

4.3.8 Analytical inversion of the correlation function

4.3.8.1 Reconstructed source function

Based on the established inversion conditions of the HOI kernel (4.54),(4.55), equation (4.47) can be replaced by its approximate form (4.51) in the regime $\beta \gg \alpha$ which can be further extended to $\beta < 0$ through

$$\mathcal{K}(\alpha,\beta) \simeq \sqrt{\frac{2\pi}{|\beta|}} e^{-i\beta} e^{i\,\mathrm{sign}(\beta)\frac{\pi}{4}}. \tag{4.56}$$

Next, by introducing the following variables $\kappa = (\Delta\omega/v_s)\Delta r$, $\tilde{k}_c = \Delta r \omega_c/c$ and $\zeta = \eta/\sqrt{\eta^2+h^2} \in [-1,1]$, the expression (4.46) of the correlation function is thus transformed to

$$C(\kappa,\tilde{k}_c) \simeq \sqrt{2\pi}\frac{K_4 e^{-i\kappa_x x_0}}{\sqrt{|\tilde{k}_c|}} \int_{-\infty}^{\infty} d\zeta F(\zeta) e^{-i\tilde{k}_c\zeta}, \tag{4.57}$$

where

$$\begin{aligned} F\Big(\zeta\Big) &= \frac{1}{\sqrt{|\zeta|}(1-\zeta^2)}[e^{i\,\mathrm{sign}(\tilde{k}_c)\frac{\pi}{4}} w(\zeta_1,\zeta_2,\zeta) + e^{-i\,\mathrm{sign}(\tilde{k}_c)\frac{\pi}{4}} w(-\zeta_1,-\zeta_2,\zeta)]\tilde{I}_{0,\zeta\theta/\sqrt{1-\zeta^2}}(\kappa_x) \\ &\equiv \frac{1}{\sqrt{|\zeta|}(1-\zeta^2)}[e^{i\,\mathrm{sign}(\tilde{k}_c)\frac{\pi}{4}} w_{\zeta_1}^{\zeta_2}(\zeta) + e^{-i\,\mathrm{sign}(\tilde{k}_c)\frac{\pi}{4}} w_{-\zeta_1}^{-\zeta_2}(\zeta)]\tilde{I}_{0,\zeta\theta/\sqrt{1-\zeta^2}}(\kappa_x), \end{aligned} \tag{4.58}$$

with $w(\zeta_1,\zeta_2,\zeta)$ a windowing function equal to one for $\zeta_1 \le \zeta \le \zeta_2$ and zero elsewhere. It may be tempted based on (4.57) to recover $\tilde{I}$ through an inverse Fourier transform. However, the sign functions in F prevent (4.57) from being a direct Fourier transform. Besides, in reality one has only access to the filtered version of the correlation function C^F defined over the protected frequency bandwidth in the L-band $B = 20$ MHz centered at $\omega_0 = 2\pi \times 1.4135$ GHz.

Now, we assume that the received signal by each antenna is filtered by a Gaussian filter of full width at half maximum (fwhm) $b \equiv 2\pi B$ both at positive and negative frequencies. The filter function is expressed as follows

$$H(\omega) = \Big(G(\omega;-\omega_0,b) + G(\omega;\omega_0,b)\Big)\sqrt{b}\pi^{1/4}, \tag{4.59}$$

with $G(\omega;\omega_0,b) = \exp\Big(-(\omega-\omega_0)^2/(2b^2)\Big)/(\sqrt{2\pi}b)$ and where $\sqrt{b}\pi^{1/4}$ serves as a normalization factor of $H(\omega)$. The filtered version of the correlation function is thus defined as

$$C^F(\kappa,\tilde{k}_c) = C(\kappa,\tilde{k}_c) H(\omega_1) H^*(\omega_2). \tag{4.60}$$

By reminding that $\Delta\omega \ll \beta \ll \omega_0$ and considering that only terms with the same sign ($\mathrm{sign}(\omega_1) = \mathrm{sign}(\omega_2)$) contribute to the product $H(\omega_1)H^*(\omega_2)$, we show that

$$\begin{aligned} C^F(\kappa,\tilde{k}_c) &\simeq \frac{1}{2} C(\kappa,\tilde{k}_c)\Big(G(\tilde{k}_c;-\tilde{k}_{c0},\frac{\tilde{b}}{\sqrt{2}}) + G(\tilde{k}_c;\tilde{k}_{c0},\frac{\tilde{b}}{\sqrt{2}})\Big) \\ &\equiv \frac{1}{2} C(\kappa,\tilde{k}_c)\Big(G^{-\tilde{k}_{c0}}_{\tilde{b}/\sqrt{2}}(\tilde{k}_c) + G^{+\tilde{k}_{c0}}_{\tilde{b}/\sqrt{2}}(\tilde{k}_c)\Big), \end{aligned} \tag{4.61}$$

where $\tilde{k}_{c0} = \Delta r \omega_0/c$ and $\tilde{b} = \Delta r b/c$.

In order to recover the expression of the reconstructed source function, we replace the correlation function in (4.57) by its filtered version (4.61) and derive the following Fourier transform with respect to $\tilde{k}_c$ (denoted $\mathcal{F}_{\tilde{k}_c\to\zeta}$),

$$\mathcal{F}_{\tilde{k}_c\to\zeta}\Big\{\sqrt{\frac{|\tilde{k}_c|}{2\pi}}\frac{e^{i\kappa_x x_0}}{K_4}C^F(\kappa,\tilde{k}_c)\Big\} = \frac{1}{2}\mathcal{F}_{\tilde{k}_c\to\zeta}\Big\{\Big(G^{-\tilde{k}_{c0}}_{\tilde{b}/\sqrt{2}}(\tilde{k}_c) + G^{+\tilde{k}_{c0}}_{\tilde{b}/\sqrt{2}}(\tilde{k}_c)\Big)\int_{-\infty}^{\infty} d\zeta F(\zeta)e^{-i\tilde{k}_c\zeta}\Big\}. \tag{4.62}$$

First, the Fourier transform of the Gaussian filter functions gives

$$\begin{aligned}
\mathcal{F}_{\tilde{k}_c\to\zeta}\Big\{G^{\pm\tilde{k}_{c0}}_{\tilde{b}/\sqrt{2}}(\tilde{k}_c)\Big\} =& \frac{1}{\sqrt{2\pi}}\int\frac{d\tilde{k}_c}{\sqrt{\pi}\tilde{b}}e^{-(\tilde{k}_c\pm\tilde{k}_{c0})^2/\tilde{b}^2}e^{-i\tilde{k}_c\zeta}\\
=& \frac{1}{\sqrt{2}\pi\tilde{b}}e^{\pm i\tilde{k}_{c0}\zeta}\int dK_c e^{-K_c^2/\tilde{b}^2}e^{-iK_c\zeta}, \quad K_c = \tilde{k}_c \pm \tilde{k}_{c0}\\
=& \frac{1}{\sqrt{2}\pi\tilde{b}}e^{\pm i\tilde{k}_{c0}\zeta}\int dK_c \exp[-(\frac{K_c}{\tilde{b}} + i\frac{\zeta\tilde{b}}{2})^2 - (\frac{\zeta\tilde{b}}{2})^2]\\
=& \frac{1}{\sqrt{\pi}\tilde{b}}e^{\pm i\tilde{k}_{c0}\zeta}e^{-\zeta^2\tilde{b}^2/4}\frac{1}{\sqrt{2\pi}}\frac{\tilde{b}}{\sqrt{2}}\underbrace{\int dz e^{-z^2/2}}_{=\sqrt{2\pi}}, \quad z = \sqrt{2}(\frac{K_c}{\tilde{b}} + i\frac{\zeta\tilde{b}}{2})\\
=& \frac{1}{\sqrt{2\pi}}e^{\pm i\tilde{k}_{c0}\zeta}e^{-\zeta^2\tilde{b}^2/4} = \frac{\sqrt{2}}{\tilde{b}}e^{\pm i\tilde{k}_{c0}\zeta}G^0_{\sqrt{2}/\tilde{b}}(\zeta).
\end{aligned} \tag{4.63}$$

Then, integrating (4.63) in (4.62) yields

$$\begin{aligned}
\mathcal{F}_{\tilde{k}_c\to\zeta}\left\{\sqrt{\frac{|\tilde{k}_c|}{2\pi}}\frac{e^{i\kappa_x x_0}}{K_4}C^F(\kappa,\tilde{k}_c)\right\} =& \frac{\sqrt{2}}{\tilde{b}}\Bigg[\Big(e^{-i(\tilde{k}_{c0}\zeta-\pi/4)} + e^{i(\tilde{k}_{c0}\zeta-\pi/4)}\Big)G^0_{\sqrt{2}/\tilde{b}}(\zeta)\star w^{\zeta_2}_{\zeta_1}(\zeta)\frac{\tilde{I}_{0,\zeta\theta/\sqrt{1-\zeta^2}}(\kappa_x)}{\sqrt{|\zeta|}(1-\zeta^2)}\\
&+ \Big(e^{-i(\tilde{k}_{c0}\zeta+\pi/4)} + e^{i(\tilde{k}_{c0}\zeta+\pi/4)}\Big)G^0_{\sqrt{2}/\tilde{b}}(\zeta)\star w^{-\zeta_2}_{-\zeta_1}(\zeta)\frac{\tilde{I}_{0,\zeta\theta/\sqrt{1-\zeta^2}}(\kappa_x)}{\sqrt{|\zeta|}(1-\zeta^2)}\Bigg]\\
=& \frac{\sqrt{2}}{\tilde{b}}\sum_{\sigma=\pm}\left(G^0_{\sqrt{2}/\tilde{b}}(\zeta)\cos(\tilde{k}_{c0}\zeta+\sigma\frac{\pi}{4})\right)\star\left[w^{\zeta_2}_{\zeta_1}(\sigma\zeta)\frac{\tilde{I}_{0,\zeta\theta/\sqrt{1-\zeta^2}}(\kappa_x)}{\sqrt{|\zeta|}(1-\zeta^2)}\right].
\end{aligned} \tag{4.64}$$

Based on equation (4.64), $\tilde{I}_{0,\eta}$ can be finally recovered cut by two windowing functions, multiplied with $1/\sqrt{|\zeta|}(1-\zeta^2)$ and convoluted with the product of a Gaussian of width $\sqrt{2}/\tilde{b}$ and a cosine function. We thus define the reconstructed source through

$$\begin{cases}
\mathcal{F}_{\tilde{k}_c\to\zeta>0}\left\{\sqrt{\frac{|\tilde{k}_c|}{2\pi}}\frac{e^{i\kappa_x x_0}}{K_4}C^F(\kappa,\tilde{k}_c)\right\} \equiv \frac{\sqrt{2}}{\tilde{b}}\left(G^0_{\sqrt{2}/\tilde{b}}(\zeta)\cos(\tilde{k}_{c0}\zeta+\frac{\pi}{4})\right)\star\left[w^{\zeta_2}_{\zeta_1}(\zeta)\frac{\tilde{I}_{0,\zeta\theta/\sqrt{1-\zeta^2}}(\kappa_x)}{\sqrt{|\zeta|}(1-\zeta^2)}\right]\\
\mathcal{F}_{\tilde{k}_c\to\zeta<0}\left\{\sqrt{\frac{|\tilde{k}_c|}{2\pi}}\frac{e^{i\kappa_x x_0}}{K_4}C^F(\kappa,\tilde{k}_c)\right\} \equiv \frac{\sqrt{2}}{\tilde{b}}\left(G^0_{\sqrt{2}/\tilde{b}}(\zeta)\cos(\tilde{k}_{c0}\zeta-\frac{\pi}{4})\right)\star\left[w^{\zeta_2}_{\zeta_1}(-\zeta)\frac{\tilde{I}_{0,\zeta\theta/\sqrt{1-\zeta^2}}(\kappa_x)}{\sqrt{|\zeta|}(1-\zeta^2)}\right]
\end{cases}, \tag{4.65}$$

or more generally by

$$\tilde{I}_{rec}(\kappa,\zeta) \equiv \frac{\tilde{b}}{\sqrt{2}}\mathcal{F}_{\tilde{k}_c\to\zeta}\left\{\sqrt{\frac{|\tilde{k}_c|}{2\pi}}\frac{e^{i\kappa_x x_0}}{K_4}C^F(\kappa,\tilde{k}_c)\right\}. \tag{4.66}$$

Starting from equation (4.66), a derivation of the reconstructed source function of a single source point is detailed in the following section, based on which, a theoretical value of the geometric resolution will be extracted.

4.3.8.2 Analytical inversion in the case of a single source point

Consider a single source point of intensity I_0 located at the surface of the Earth at position $x'' = 0, y'' = \eta_s \Delta r$ where η_s lies within the inversion condition (4.54). We thus have

$$I(\mathbf{r}'') = I_0\delta(x'')\delta(y'' - \eta_s\Delta r)\Delta r^2, \tag{4.67}$$

and using (4.16), one gets

$$\tilde{I}_{0,\eta}(\kappa_x) = \frac{I_0\Delta r}{\sqrt{2\pi}}\delta(\eta - \eta_s). \tag{4.68}$$

We next derive the expression of the correlation function due to one single source with respect to the inversion condition (4.54), equivalent to

$$\kappa \le \kappa_m(\eta) \equiv \frac{\omega_c\Delta r}{c}\frac{\eta}{\eta^2+\theta^2} \le \kappa_M \equiv \frac{\omega_c\Delta r}{2c\theta}, \tag{4.69}$$

using the approximate form of the HOI kernel (4.56),

$$C(\kappa,\tilde{k}_c) = K_4 I_0 \Delta r \frac{e^{-i\kappa_x x_0}e^{i\,\mathrm{sign}(\tilde{k}_c)\pi/4}}{\sqrt{|\tilde{k}_c|\eta_s}(\eta_s^2+\theta^2)^{1/4}} e^{-i\tilde{k}_c\frac{\eta_s}{\sqrt{\eta_s^2+\theta^2}}}\Pi\Big(\kappa_m(\eta_s) - |\kappa|\Big), \tag{4.70}$$

where Π is the Heaviside function enforcing the correlation function to zero outside the allowed range (4.69).

From (4.66) and by means of a Fourier-transformation in $\kappa \equiv \kappa_x\Delta r$, one obtains the expression

$$I_{rec}(x,y) = \frac{\tilde{b}}{\sqrt{2}}\frac{1}{2\pi K_4\Delta r}\int d\tilde{k}_c\int d\kappa\sqrt{\frac{|\tilde{k}_c|}{2\pi}}C^F(\kappa,\tilde{k}_c)e^{-i\kappa(\tilde{x}-\tilde{x}_0)}e^{i\tilde{k}_c\zeta}, \tag{4.71}$$

which, by integrating the filtered version of (4.70), yields

$$\begin{aligned} I_{rec}(x,y) =& \frac{\tilde{b}}{\sqrt{2}}\frac{I_0}{2(2\pi)^{3/2}}\int d\tilde{k}_c\frac{e^{i\tilde{k}_c\zeta}e^{i\,\mathrm{sign}(\tilde{k}_c)\pi/4}}{\sqrt{\eta_s}(\eta_s^2+\theta^2)^{1/4}}e^{-i\tilde{k}_c\frac{\eta_s}{\sqrt{\eta_s^2+\theta^2}}}\frac{1}{2}\Big(G^{-\tilde{k}_{c0}}_{\tilde{b}/\sqrt{2}}(\tilde{k}_c) + G^{+\tilde{k}_{c0}}_{\tilde{b}/\sqrt{2}}\Big) \\ &\times\int d\kappa e^{-i\kappa\tilde{x}}\Pi\Big(\kappa_m(\eta_s) - |\kappa|\Big) \\ =& \frac{\tilde{b}}{\sqrt{2}}\frac{I_0}{(2\pi)^{3/2}}\frac{\kappa_m(\eta_s)}{\sqrt{\eta_s}(\eta_s^2+\theta^2)^{1/4}}e^{-(\zeta-\zeta_s)^2\tilde{b}^2/4}\cos\Big(\tilde{k}_{c0}(\zeta-\zeta_s)+\frac{\pi}{4}\Big)\mathrm{sinc}\Big(\kappa_m(\eta_s)\tilde{x}\Big). \end{aligned} \tag{4.72}$$

One finally gets by introducing the filter function

$$I_{rec}(x,y) = \frac{I_0}{2\pi}\frac{\Delta r\omega_c}{c}\frac{\sqrt{|\zeta_s|}(1-\zeta_s^2)}{\theta^2}G^{\zeta_s}_{\sqrt{2}/\tilde{b}}(\zeta)\cos\Big(\tilde{k}_{c0}(\zeta-\zeta_s)-\frac{\pi}{4}\Big)\mathrm{sinc}\Big(\kappa_m(\eta_s)\tilde{x}\Big), \tag{4.73}$$

where $\mathrm{sinc}(x) \equiv \sin(x)/x$.

Equation (4.73) represents the 2D reconstructed source function of a single source located at $(0, y_s)$. The reconstructed image is shaped as a sinc-function in x-direction (along-track direction) and as a product of a Gaussian of width $\sqrt{2}/\tilde{b}$ centered at ζ_s and a rapidly oscillating cosine function in y-direction (cross-track direction) (figure 4.8).

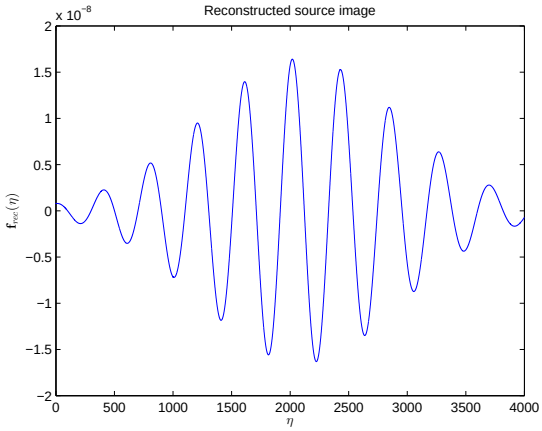

Figure 4.8: Reconstructed source function of a single source point in the cross-track direction

Based on (4.73), a straightforward estimation of the achievable spatial resolution is only possible in x-direction which is not the case in y-direction due the rapidly oscillating cosine function weighted by the Gaussian. In fact, the spatial resolution in y-direction seems to vary between a minimal value set by the width of the central pic of the cosine function and a maximal value dictated by the width of the Gaussian.

4.3.9 Estimation of the geometric resolution

The resolution in x-direction $\mathcal{R}_x$ is dictated by the position-dependent factor

$$\kappa_{max}(\eta_s) = (\Delta r\omega_c/c)(\eta_s/(\eta_s^2+\theta^2))$$

in the sinc function, which reaches its maximal value at $\eta_s = \theta$. This gives the best achievable resolution in the along-track direction,

$$\mathcal{R}_x(\eta_s) = \frac{\Delta r}{\kappa_m(\eta_s)} \geq \mathcal{R}_{x_{min}} = \frac{\Delta r}{\kappa_M} = \frac{2hc}{\omega_0\Delta r}. \tag{4.74}$$

An expression of the spatial resolution in y-direction cannot be directly extracted from the expression of the reconstructed source function (4.73). It seems nevertheless to range between the maximal value

set by the Gaussian,

$$
\begin{aligned}
G^{\zeta_s}_{\sqrt{2}/\tilde{b}}(\zeta) &= \frac{\tilde{b}}{2\sqrt{\pi}} \exp\Big[-(\zeta-\zeta_s)^2 \frac{\tilde{b}^2}{4}\Big] \\
&= \frac{\tilde{b}}{2\sqrt{\pi}} \exp\Big[-(\frac{\eta}{\sqrt{\eta^2+\theta^2}} - \frac{\eta_s}{\sqrt{\eta_s^2+\theta^2}})^2 \frac{\tilde{b}^2}{4}\Big] \\
&\simeq \frac{\tilde{b}}{2\sqrt{\pi}} \exp\Big[-(\eta-\eta_s)^2 \frac{\tilde{b}^2}{4(\eta_s^2+\theta^2)}\Big],
\end{aligned} \tag{4.75}
$$

where we have considered that the Gaussian is strongly localized at $\eta = \eta_s$, and given by

$$
\mathcal{R}_{y_{max}}(\eta_s) \equiv 2\frac{\sqrt{\eta_s^2+\theta^2}}{\tilde{b}} \Delta r \leq 2\sqrt{2}\frac{\theta}{\tilde{b}}\Delta r = 2\sqrt{2}\frac{hc}{\Delta r b} \equiv \mathcal{R}_{y_{Max}}, \tag{4.76}
$$

and the minimal value set by the cosine function. Its value can be further deduced using the definition of the spectral resolution of a diffraction image from a double slit defined to be the smallest shift in the source's position that makes a peak of the reconstructed image move into the next trough. Using the argument of the cosine function, this minimal shift is determined as follows

$$
\tilde{k}_{c0}\frac{\partial}{\partial\eta}\frac{\eta}{\sqrt{\eta^2+\theta^2}}|_{\eta=\eta_s}\Delta\eta \simeq \pi \Rightarrow \Delta\eta \simeq \frac{\pi(\eta_s^2+\theta^2)^{3/2}}{\tilde{k}_{c0}\theta^2}. \tag{4.77}
$$

Hence, one derives the best achievable value of the geometric resolution in the cross-track direction,

$$
\mathcal{R}_{y_{min}}(\eta_s) \equiv \Delta r \frac{\pi(\eta_s^2+\theta^2)^{3/2}}{\tilde{k}_{c0}\theta^2} \geq \frac{\pi hc}{\Delta r \omega_0} \equiv \mathcal{R}_{y_{Min}}. \tag{4.78}
$$

An other way to directly extract an estimation of the geometrical resolution in the cross-track direction is to calculate the average over a set of reconstructed source functions for different values of the spacing Δr between the antennas. Varying the value of Δr engenders a set of cosine functions of different periods which, when averaged, tend towards a sinc-function whose full width at half maximum (fwhm) determines the spatial resolution (figure 4.9).
Based on this approach, the different spacings Δr need to be intelligently chosen so as to reach the optimal value (4.78) of the spatial resolution.

All things considered, we conclude that the best achievable spatial resolution in both directions is of the order of $hc/(\Delta r\omega_0) \sim 3$ km using standard parameters and for $\Delta r = 50$ m.

4.3.10 Discussion

A new *spatio-temporal interferometric* concept is proposed as the new generation of Earth observation systems using aperture synthesis. Combined with an innovative *Fourier Correlation Imaging* procedure, based on correlating the Fourier components of the observed electric field fluctuations at different frequencies, this concept yields a remarkable relationship linking the correlation values to the 2D position-dependent brightness temperatures by means of a *highly oscillatory integral kernel*. We show furthermore that starting from a 1D instrument geometry, the obtained correlation function bears a 2D pixel-dependent information of the observed scene, which leads, when inverted, to a mapping of the 2D brightness temperatures.

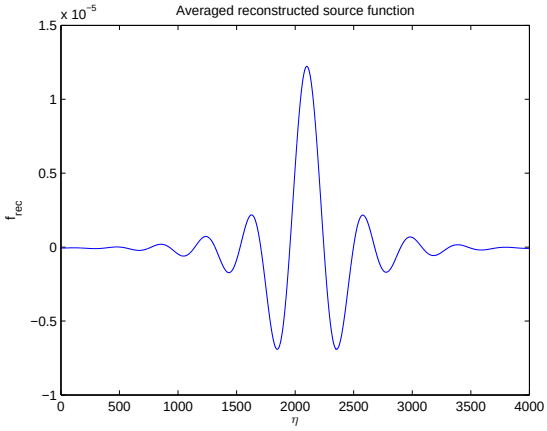

Figure 4.9: Average of a set of reconstructed source function using different values of Δr

The theoretical derivation of the functional parameters of the FouCoIm concept, comprised of a pair of antennas separated by a distance Δr, operating at a frequency ω_0, and flying at a height h with a speed v_s, optimally yields equivalent spatial resolutions in both directions of the order of few kms ($hc/(\Delta r \omega_0)$ with a value of Δr of 50 m and using the standard parameters).

A first theoretical derivation of the radiometric sensitivity in the simple case of a single source point (not presented here) yielded unexpected values and didn't allow to conclude. The question whether the achieved radiometric sensitivity using the FouCoIm concept meets the predefined requirement is still open. Based on the theoretical derivation, we weren't able to state on the radiometric performance of the concept in hand, but we hope that a further numerical achievement shall give clearer results (see chapter 5).

One of the important hypothesis at the basis of the feasibility of the FouCoIm concept is the necessity of having access to a set of a considerable number of realizations of the stochastic process modeling the source's fluctuations (equation (4.4)). This condition is not fulfilled in the real case of a spaceborne implementation since one only has access to a unique realization per satellite's passage. In this perspective, we proposed within the framework of this thesis a possible way to bypass this difficulty (briefly discussed in chapter 5) using either a pseudo-random permutation or a vector subdivision approach.

4.4 Appendix: Thermal fluctuations and their fundamental laws

We derive the fundamental law of nature that describes the quantum fluctuations of sources at the origin of Earth's radiations based on the so-called *Fluctuation-Dissipation Theorem* (FDT) [4].

In remote sensing and astrophysical applications, observations are made of the thermal radiation of distant objects. This quantity informs about the physical relationship between the measured radiation and the internal thermal structure of the object and its physical, chemical, or geometric features.

Any object with a physical temperature other than the absolute zero is continuously emitting a fluctuating electromagnetic field, covering a very broad range of wavelengths, as a result of the spontaneous transitions between vibration-rotation levels of molecules. The radiated field contains both a wave (far) field, carrying the energy from the object's body, and a quasi-stationary (near) thermal field, which is concentrated in a layer adjacent to the surface of thickness of the order of the wavelength.

A close relation resides between the present noise in electric systems and thermal radiations owing to the fact that the radiated electromagnetic fields by physical objects are the result of the thermal electric fluctuations. Nevertheless, thermal radiations are quantum and cannot be straightforwardly described within the framework of the classical Maxwellian theory of electromagnetism. The fluctuating electromagnetic field is represented as the field generated by random 'detached' sources of Langevinian type distributed in a medium, and in order to calculate the energy characteristics of the fluctuating field it is necessary to know the spatial correlation of the spectral amplitudes of these random currents. In this manner, the FDT allows to associate the correlation functions of detached fields to the dissipative properties of a system described using macroscopic Maxwell equations (in the Gaussian system units):

$$\mathrm{rot}\mathbf{H} = \frac{\partial \mathbf{D}}{\partial t} + \frac{4\pi}{c}\mathbf{j}_e, \tag{4.79}$$

$$\mathrm{rot}\mathbf{E} = -\frac{\partial \mathbf{B}}{\partial t} - \frac{4\pi}{c}\mathbf{j}_m, \tag{4.80}$$

where $\mathbf{j}_e$ and $\mathbf{j}_m$ are the detached fluctuating currents (electric and magnetic) at the origin of the thermal fluctuations. The spatial and spectral amplitudes of these random currents for an isotropic medium give

$$\overline{\mathbf{j}_{ej}(\mathbf{r}) \cdot \mathbf{j}_{ek}(\mathbf{r}')} = -\frac{j\omega\Theta(\omega, T)}{8\pi^2}\delta_{jk}\delta(\mathbf{r} - \mathbf{r}')[\dot{\epsilon}^*(\mathbf{r}) - \dot{\epsilon}(\mathbf{r}')], \tag{4.81}$$

where subscripts j and k denote spatial components ($j = k = 1, 2, 3$), Θ is the mean energy of the quantum oscillator defined as

$$\Theta(\omega, T) = \frac{\hbar\omega}{2} + \frac{\hbar\omega}{\exp(\hbar\omega/kT) - 1}, \tag{4.82}$$

and $\dot{\epsilon} = \epsilon' + j\epsilon''$ is the so-called general susceptibility. Equation (4.81) can be further simplified into

$$\overline{|\mathbf{j}_e(\mathbf{r})|}^2 = \frac{\omega\Theta(\omega, T)}{4\pi^2}\epsilon''(\mathbf{r}). \tag{4.83}$$

Equation (4.83) represents the essence of the FDT, namely the relationship linking the intensity of the electromagnetic fluctuations to the macroscopic dissipation properties in a physical system. In other words, the spatial features of a medium will directly inform about the correlation properties of intensity of the surface-based detached sources and, consequently, on the field of thermal properties.

The time-dependent fluctuating sources at the surface of the Earth can be mathematically modeled using random Gaussian processes (RGP). Consider several realizations ($\sim 10^4$) of the current fluctuations

of two sources at the Earth's surface, figures 4.10,4.11 show the average over the set of realizations of the auto-correlation of one source and the correlation of both sources.

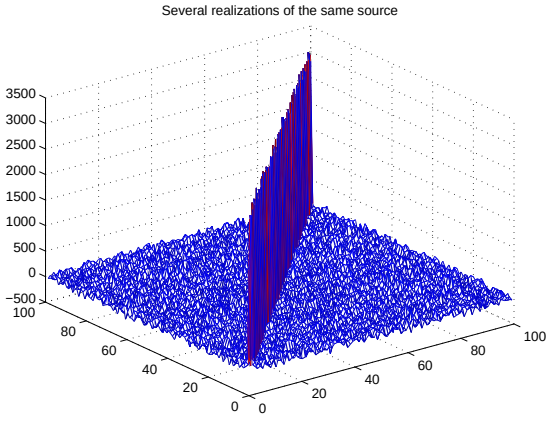

Figure 4.10: Average of auto-correlations

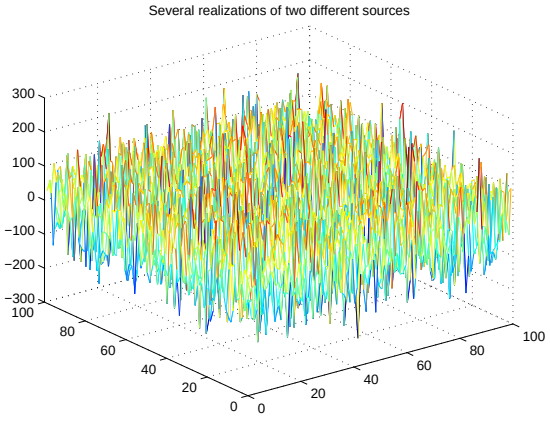

Figure 4.11: Average of correlations

Figure 4.10 shows the property that the only remaining contribution in the average of the auto-correlations is located at the diagonal (same frequencies). While the second figure shows that sources at different positions, described by different RGPs, are totally uncorrelated and the average is completely random (no correlation remains).

Bibliography

[1] D. Braun, Y. Monjid, B. Rougé, and Y. Kerr, "Generalization of the Van Cittert-Zernike theorem: observers moving with respect to sources," *Measurement and Science Technology*, November, 2015.

[2] D. Braun, "Fourier Correlation Imaging," Unpublished, 2012.

[3] D. Braun, Y. Monjid, B. Rougé, and Y. Kerr, "Fourier-Correlation Imaging," *to be submitted soon.*

[4] E. A. Sharkov, "Passive Microwave Remote Sensing of the Earth: Physical Foundations". *Springer*, Chichester, UK, 2003.

Chapter 5

FOURIER CORRELATION IMAGING: NUMERICAL DERIVATION

Contents

5.1 Introduction

The subject the present chapter, which constitutes the second main contribution entirely developed within the framework of this thesis, is two-fold: i) based on the introduced theoretical derivations in chapter 4, a first section is exclusively dedicated to the detailed study of the theoretical and numerical quadrature of the highly oscillatory integral kernel appearing in the expression of the correlation function (4.46), which will serve as a partial basis to a second section that concerns ii) the theoretical and numerical derivation of three versions of a complete numerical processor.

As it is usually the case in Earth observation missions, the objective of the previous numerical processor is three-fold: i) the reconstruction of surface temperatures starting from the measured correlation values by means of the Fourier correlation imaging instrument, ii) the numerical derivation of the functional parameters of interest, namely the radiometric and spatial resolutions, with the intent of a numerical validation of the studied concept, and finally iii) to be employed in the practical case termed with an experimental or even a spaceborne implementation of the Fourier correlation imaging approach.

A discussion on the FDT assumption (equation (4.4)), whose verification is paramount for the spaceborne implementation of the FouCoIm concept, is presented at the end of the second section.

The entire developments of the present chapter will be subject to a publication which is in current preparation at the time of the writing of this report [1].

5.2 Numerical quadrature of the highly oscillatory integral kernel

5.2.1 Introduction

In chapter 4, the spatio-temporal interferometric concept was combined with a new *Fourier Correlation Imaging* methodology with the hope of achieving much higher spatial resolutions. The theoretical derivation of the resulting correlation function yielded a new formulation of the Van Cittert-Zernike theorem indicating that the measured correlation values by means of the preceding imaging approach are linked to the interesting brightness temperatures by means of a Highly Oscillatory Integral (HOI) kernel. A consequence to which, the reconstructing procedure boils down to a matrix inversion problem constructed through the numerical quadrature of the HOI kernel.

The quadrature of HOIs is of crucial importance in many scientific fields which involve the modeling of wave phenomena, e.g. derivation of Maxwell's equations. In the field of Earth observation using remote sensing, for instance, the electric fields received by a pair of antennas are cross-correlated to derive the *correlation function* which defines the Fourier transform of the intensity distribution of current fluctuations in the observed scene [2]. Such a calculation procedure gives rise to highly oscillatory problems which are widely perceived as "difficult" as the integral becomes more and more oscillatory.

In the present section we explore the application of several numerical methods for the quadrature of the HOI kernel encountered in the analytical derivation of the Fourier Correlation Imaging concept set as a mandatory step in the reconstruction procedure of brightness temperatures. The kernel is analytically and numerically approximated within different frequency regimes using highly oscillatory asymptotic and numerical quadrature methods such as the *asymptotic expansion*, the *Filon-type* method [3, 4], and the *Levin-type collocation* method [5, 6].

Here, we explore the relevance of the different frequency regimes and we demonstrate all in all based on the numerical results that only one regime contributes significantly to the correlation function of interest. Besides, in the light of the analytical developments derived in this chapter, a numerical processor is under implementation for the reconstruction of temperatures using the quadrature of the HOI kernel in all frequency regimes (see next section).

This numerical processor is intended to be employed to allow a general reconstruction of temperatures when employing the FouCoIm procedure. It was initially thought to get rid of the high computational effort required to allow a direct inversion of the correlation function and to extract the different concept's functional parameters when dealing with signals in the L-band (oscillating signals at 1.4 GHz).

5.2.2 Theoretical model

A *Fourier correlation imaging* concept was recently proposed as the new generation of satellite-based passive radiometers operating in the protected frequency band 1400-1427 MHz. By cross-correlating the Fourier components of the electric field fluctuations received by a pair of antennas, separated by a distance Δr and flying on board of a satellite at height h and of speed v_s at different frequency components ω_1, ω_2, a new formulation of the most-used theorem in passive Earth observation, the *Van Cittert–Zernike* theorem [7], is derived. This formulation links the two-frequency measured correlation values,

$$C(\omega_1, \omega_2) \simeq K \int_{-\infty}^{\infty} dy' I(a, b, c) \tilde{\mathcal{I}}(\kappa_x), \tag{5.1}$$

to the Fourier transform of the intensity distribution of the observed scene

$$\tilde{\mathcal{I}}(\kappa_x) = \frac{1}{\sqrt{2\pi}} \int_{-\infty}^{\infty} dx \mathcal{I}(x) e^{i\kappa_x x}, \tag{5.2}$$

by means of a HOI kernel $I(a, b, c)$ defined as

$$I(a, b, c) = \int_{-\infty}^{\infty} dx' \frac{e^{-i(ax' + \frac{b}{\sqrt{x'^2 + c^2}})}}{x'^2 + c^2}, \tag{5.3}$$

where $\kappa_x = (\omega_2 - \omega_1)/v_s$, $a = \kappa_x$, $b = (\Delta r \omega_c / c_l) y' = \tilde{k}_c y'$, $c = \sqrt{y'^2 + h^2}$, $\omega_c = (\omega_1 + \omega_2)/2$, c_l the speed of light, and K a constant.
The expression (5.3) of the HOI kernel can be reduced to

$$I(a, b, c) = \frac{1}{c} I(ac, b/c, 1) = \frac{1}{c} I(\alpha, \beta, 1), \tag{5.4}$$

where $\alpha = \kappa_x \sqrt{y'^2 + h^2}$ and $\beta = \tilde{k}_c y' / \sqrt{y'^2 + h^2}$. In what follows, we will be interested in the theoretical and numerical quadrature of the following simplified form of the integral kernel

$$I(\alpha, \beta, 1) = \int_a^b dx \frac{e^{-i(\alpha x + \frac{\beta}{\sqrt{x^2+1}})}}{x^2 + 1}. \tag{5.5}$$

5.2.3 Quadrature methods for highly oscillatory integrals

5.2.3.1 Introduction

Here, we give an overview of the different methods used for the evaluation of HOIs of the form

$$\mathcal{I}[f] = \int_a^b f(x) e^{i\omega g(x)} dx, \tag{5.6}$$

where f and g are smooth functions, and ω refers to the frequency of oscillations which can be very large.

The need for sophisticated methods in the quadrature of HOIs is the result of the failure of most traditional methods as the frequency of oscillations increases. Most non-oscillatory and standard quadrature methods, mostly consisting in approximating the integral with a weighted summation at a finite set of discrete points,

$$\int_a^b f(x) e^{i\omega x} dx \simeq \sum_{i=1}^{n} w_i f(x_i) e^{i\omega x_i}, \tag{5.7}$$

fail in approximating the integral (5.6) for increasing ω and fixed n. Nevertheless, increasing n with ω yields an approximation of the HOI with a limited accuracy until a stage where the computational cost becomes considerable. An alternative to standard methods are the asymptotic methods, namely the *asymptotic expansion* and the *steepest descent method*. Although their increasing convergence accuracy with frequency, these methods present, however, the inconvenient of a limited accuracy for a fixed frequency. As a result, sophisticated numerical methods were developed with the intent of reaching an arbitrary high accuracy for fixed frequencies, namely *Filon* and *Levin collocation methods*.

In this section, we give an introduction to both *asymptotic methods*, by focusing on the *stationary phase method* and the *asymptotic expansion*, and *numerical quadrature methods*, including the *Filon* and *Levin collocation methods*.

5.2.3.2 Asymptotics

5.2.3.2.1 Stationary phase method: The stationary phase method is an analytical procedure for the evaluation of HOIs of the form (5.6) in the particular case where the function g presents stationary points [8].
Let us assume, for simplicity, that g' cancels at some point $\xi \in [a,b]$ and $g'(x) \neq 0$ everywhere else. We suppose moreover that $g''(\xi) \neq 0$ and $f(\xi) \neq 0$, ξ is called a first-order *stationary point*. In order to remove the singularity at ξ, the HOI $\mathcal{I}[f]$ can be rewritten as follows

$$\mathcal{I}[f] = e^{i\omega g(\xi)} \int_a^b f(x) e^{i\omega[g(x)-g(\xi)]} dx. \tag{5.8}$$

It is interesting to note that as the frequency increases, oscillations give rise to a cancellation of the contributions of the integral whose behavior becomes essentially dictated by the behavior of the integrand at the neighborhood of the stationary point ξ. Based on this, the integration interval $[a,b]$ can be expended to $]-\infty,\infty[$ as follows

$$\mathcal{I}[f] \simeq e^{i\omega g(\xi)} f(\xi) \int_{-\infty}^{\infty} e^{i\omega[g(x)-g(\xi)]} dx. \tag{5.9}$$

We next expand the function g in the neighborhood of ξ using a Taylor expansion,

$$\begin{aligned} g(x) &= g(\xi) + g'(\xi)(x-\xi) + \frac{g''(\xi)}{2}(x-\xi)^2 + \mathcal{O}\Big((x-\xi)^2\Big) \\ &= g(\xi) + \frac{g''(\xi)}{2}(x-\xi)^2 + \mathcal{O}\Big((x-\xi)^2\Big). \end{aligned}$$

to finally get

$$\begin{aligned} \mathcal{I}[f] &\simeq e^{i\omega g(\xi)} f(\xi) \int_{-\infty}^{\infty} e^{i\frac{\omega}{2} g''(\xi)(x-\xi)^2} dx \\ &\simeq e^{i\omega g(\xi)} f(\xi) \sqrt{\frac{2\pi i}{\omega g''(\xi)}} \\ &= e^{i\omega g(\xi)} f(\xi) \sqrt{\frac{2\pi}{\omega |g''(\xi)|}} \sqrt{i \operatorname{sign}\Big(g''(\xi)\Big)} \\ &= \sqrt{\frac{2\pi}{\omega |g''(\xi)|}} f(\xi) e^{i\omega g(\xi)} e^{i \operatorname{sign}(g''(\xi))\frac{\pi}{4}}, \quad \text{as} \quad \omega \to \infty. \end{aligned} \tag{5.10}$$

Equation (5.10) represents the general approximate form of the HOI kernel (5.6) in the case of a single stationary point of g at ξ using the stationary phase approximation. More generally in the presence of several stationary points, it is convenient to add the contribution of each one. Equation (5.10) thus becomes

$$\mathcal{I}[f] \simeq \sum_{\xi} \sqrt{\frac{2\pi}{\omega |g''(\xi)|}} f(\xi) e^{i\omega g(\xi)} e^{i \operatorname{sign}(g''(\xi))\frac{\pi}{4}}, \quad \text{as} \quad \omega \to \infty. \tag{5.11}$$

5.2.3.2.2 Asymptotic expansion: We first assume that $f, g \in \mathcal{C}^\infty([a,b])$ and g has no stationary points ($g'(x) \neq 0$, $\forall x \in [a,b]$), the full asymptotic expansion of (5.6) is derived by means of a set of iterated integrations by parts [8],

$$Q^A[f] \sim -\sum_{k=1}^{\infty} \frac{1}{(-i\omega)^m} \left[\frac{e^{i\omega g(b)}}{g'(b)} \sigma_{m-1}[f](b) - \frac{e^{i\omega g(a)}}{g'(a)} \sigma_{m-1}[f](a) \right], \tag{5.12}$$

where

$$\sigma_0[f](x) = f(x)$$
$$\sigma_{m+1}[f](x) = \frac{d}{dx}\left[\frac{\sigma_m[f](x)}{g'(x)}\right], \quad m = 0, 1, ... \tag{5.13}$$

Interestingly, this expansion depends on the values of f, g and their derivatives at the endpoints a, b. It is shown furthermore in [9] that a truncation of the asymptotic expansion at an order s,

$$Q_s^A[f] = -\sum_{k=1}^{s} \frac{1}{(-i\omega)^m}\left[\frac{e^{i\omega g(b)}}{g'(b)}\sigma_{m-1}[f](b) - \frac{e^{i\omega g(a)}}{g'(a)}\sigma_{m-1}[f](a)\right], \tag{5.14}$$

approximates oscillatory integrals of the form (5.6) with a relative accuracy of $\mathcal{O}(\omega^{-s-1})$.
In the presence of at least one single stationary point ξ, the previous expansion is not anymore valid since the function f/g' is not continuously differentiable. One way to get rid this indetermination is suggested in [9] in the case of a single first-order stationary point ξ ($g'(\xi) = 0$ and $g''(\xi) \neq 0$) by noticing that the function $(f - f(\xi))/g'$ has a removable singularity and

$$\mathcal{I}[f] = f(\xi)\mathcal{I}[1] + \mathcal{I}[f - f(\xi)]. \tag{5.15}$$

In the case of a r-order stationary point ξ, the singularity can be removed by subtracting a r-term Taylor expansion of f [10],

$$Q^A[f] = \sum_{k=0}^{r-1} \frac{1}{k!} f^{(k)}(\xi)\mathcal{I}[(. - \xi)^k] + \int_a^b \Big(f(x) - \sum_{k=0}^{r-1} \frac{1}{k!} f^{(k)}(\xi)(x - \xi)^k\Big)e^{i\omega g(x)}dx, \tag{5.16}$$

which leads to the following truncated s-order asymptotic expansion

$$\begin{aligned} Q_s^A[f] =& \sum_{j=0}^{r-1} \frac{1}{j!}\mu_j(\omega;\xi) \sum_{m=0}^{s-j-1} \frac{1}{(-i\omega)^m}\rho_m^{(j)}[f](\xi) \\ &- \sum_{m=1}^{s-1} \frac{1}{(-i\omega)^m}\left[\frac{e^{i\omega g(b)}}{g'(b)}\Big(\rho_{m-1}[f](b) - \rho_{m-1}[f](\xi)\Big) - \frac{e^{i\omega g(a)}}{g'(a)}\Big(\rho_{m-1}[f](a) - \rho_{m-1}[f](\xi)\Big)\right], \end{aligned} \tag{5.17}$$

where

$$\rho_0[f](x) = f(x),$$
$$\rho_{k+1}[f](x) = \frac{d}{dx}\frac{\rho_k[f](x) - \sum_{j=0}^{r-1} \frac{1}{j!}\rho_k[f]^{(j)}(\xi)(x - \xi)^j}{g'(x)}, \quad \text{for} \quad k \geq 0, \quad \text{and} \tag{5.18}$$
$$\mu_m(\omega;\xi) = I[x^m] = \int_a^b (x - \xi)^m e^{i\omega g(x)}, \quad m \geq 0. \tag{5.19}$$

This expression, known as the Iserles and Nørsett asymptotic expansion in the presence of stationary points, approximates oscillatory integrals with a quadrature error of $\mathcal{O}(\omega^{-s-1/(r+1)})$ [11]. It presents, however, the inconvenient of a limited accuracy for a fixed frequency in contrary to the numerical quadrature methods presented hereafter.

5.2.3.3 Numerical quadrature methods

If applied correctly, one shows that the numerical quadrature methods yield a higher convergence accuracy, and the more ω is increased the less a considerable computational effort is required [10].

Two cases are to be distinguished when applying such numerical methods: integrals with stationary points (points where $g'(x) = 0$) and those without.

5.2.3.3.1 Filon-type methods Filon method, as originally developed, consisted in dividing the integration interval into a set of subintervals over which the function f is interpolated by a quadratic [12]. This original approach has been progressively generalized to the so-called Filon-type methods using higher degree polynomials for the interpolation of the function f [13].

We start by assuming that the function g has no stationary points within the integration interval ($g'(x) \neq 0, \forall x \in [a,b]$). Let $\{x_k\}_0^\nu$ be a set of nodes such that $a = x_0 < x_1 < \ldots < x_\nu = b$ of corresponding multiplicities $\{m_k\}_0^\nu$. We define the *Filon-type approximation* of the HOI (5.6) for an interpolated function f, using the Hermite interpolation, by the polynomial $\tilde{f} = \sum_{k=0}^{n} c_k x^k$ where $n = \sum_{k=0}^{\nu} m_k$, solution to the following system of equations

$$\tilde{f}(x_k) = f(x_k),\ \tilde{f}'(x_k) = f'(x_k),\ \ldots,\ \tilde{f}^{(m_k)}(x_k) = f^{(m_k)}(x_k),$$

for each integer $0 \leq k \leq \nu$, as follows

$$Q^F[f] \equiv \mathcal{I}[\tilde{f}] = \sum_{k=0}^{n} c_k \mathcal{I}[x^k]. \tag{5.20}$$

The accuracy of the Filon-type method method is largely dependent on the interpolation precision which is subject to improvement by adding additional node points and multiplicities. By letting $s = min\{m_0, m_\nu\}$, one shows that the quadrature order of this method is of the order of $\mathcal{O}(\omega^{-s-1})$ in the absence of stationary points [14].

By noticing that the asymptotic behavior of the Filon-type method strongly depends on the local behavior of the integrand at the stationary points and at the endpoints of the integration interval [9], Filon-type methods can be extended to the case of the presence of stationary points.
For simplicity we assume a single $(r-1)$-order stationary point ξ of g, i.e. $g^{(k)}(\xi) = 0, \forall k \in \{1, \ldots, r-1\}$ and $g^{(r)}(\xi) \neq 0$. Let $\tilde{f}(x) = \sum_{k=0}^{n} c_k \phi_k(x)$ an interpolating polynomial of f using a set of basis functions $\{\phi_k\}_0^n$, independent from ω and n, at a sequence of node points $\{x_k\}_0^\nu$ of corresponding multiplicities $\{m_k\}_0^\nu$ where $n = \sum_{k=0}^{\nu} m_k$. We assume furthermore that $x_0 = a, x_\eta = \xi$ and $x_\nu = b$.
By firstly deriving the interpolation coefficients c_k, solutions the following system of equations

$$\tilde{f}(x_k) = f(x_k), \tilde{f}'(x_k) = f'(x_k), \ldots, \tilde{f}^{(m_k)}(x_k) = f^{(m_k)}(x_k), \quad k = 1, \ldots, \eta, \ldots, \nu,$$

the Filon-type approximation of the HOI in the presence of a single stationary point is found to be defined as follows

$$Q^F[f] \equiv I[\tilde{f}] = \sum_{k=0}^{n} c_k \mathcal{I}[\phi_k]. \tag{5.21}$$

Besides, one shows that the expression (5.21) presents a quadrature error of the order of $\mathcal{O}(\omega^{-s-1/(r+1)})$ where $s = min\{m_0, m_\nu\}$ [9].
The basis functions ϕ_k are typically defined to be x^{k-1} using a standard polynomial interpolation since the moments $I[x^k]$ are most likely to be known. In contrary, the employment of complex interpolations, such as Hermite or Lagrangian interpolations, may result in a great difficulty in the analytical calculation of previous moments which prevents Filon-type methods from providing any approximation. Owing to the complexity of the Filon-type approximations, new moment-free methods were developed in the perspective of bypassing the need of moment calculations, such as the Levin-type collocation methods.

5.2.3.3.2 Levin collocation method: The Levin collocation method is mainly based on the idea of approximating HOIs without the use of moments [15]. Its approach consists in finding a function F verifying $\frac{d}{dx}[Fe^{i\omega g}] = fe^{i\omega g}$ in a way to have

$$\mathcal{I}[f] = \int_a^b f(x)e^{i\omega g(x)}dx = \int_a^b \frac{d}{dx}[F(x)e^{i\omega g(x)}]dx = F(b)e^{i\omega g(b)} - F(a)e^{i\omega g(a)}.$$

This procedure is equivalent to employ a *collocation* with an operator $\mathcal{L}$ satisfying $\mathcal{L}[F] = f$ and where

$$\mathcal{L}[F] = F' + i\omega g' F. \tag{5.22}$$

The only difficulty of this collocation method resides in the approximation of F which, once F is derived, allows a direct quadrature of the HOI $\mathcal{I}[f]$.
More particularly, by letting $\tilde{f}(x) = \sum_{k=0}^{n} c_k \phi_k(x)$ a polynomial interpolating, at a set of node points $\{x_k\}_0^\nu$ of corresponding multiplicities $\{m_k\}_0^\nu$, the function f and its derivatives for some suitable basis $\{\phi_k\}_0^n$ where $n = \sum_{k=0}^{\nu} m_k$. The interpolation coefficients c_k are determined through the collocation system

$$\mathcal{L}[\tilde{f}](x_k) = f(x_k), \ldots, \mathcal{L}[\tilde{f}]^{(m_k-1)}(x_k) = f^{(m_k-1)}(x_k), \quad k = 1, \ldots, \nu, \tag{5.23}$$

and the Levin-type $Q^L[f]$ gives

$$Q^L[f] = \int_a^b \mathcal{L}[\tilde{f}](x)e^{i\omega g(x)}dx = \int_a^b \frac{d}{dx}[\tilde{f}(x)e^{i\omega g(x)}]dx = \tilde{f}(b)e^{i\omega g(b)} - \tilde{f}(a)e^{i\omega g(a)}. \tag{5.24}$$

One shows using the asymptotic expansion that the expression (5.24) approximates the HOI with a quadrature error of the order of $\mathcal{O}(\omega^{-s-1})$, where $s = min\{m_0, m_\nu\}$. Interestingly, the Levin-type method allows the same quadrature as the Filon-type method but with the undeniable advantage that no moment is required to be calculated. Besides, for a fixed ω, the asymptotic order of the Levin collocation method seems to solely depend on the used derivatives' order at the endpoints of the integration interval [11].

In the presence of stationary points of g, the same singularity removal principle (5.15) is employed, and one shows that the quadrature accuracy of Levin-type methods, when a set of r-order stationary points is present, is of the order of $\mathcal{O}(\omega^{-s-1/(r+1)})$ [14].

5.2.4 Analytical derivations of the quadrature

We now apply the previously described asymptotic and numerical methods for the approximation of the HOI kernel (5.5). The detailed analytical derivation of the different approximations in this paragraph will serve as a basis to a further numerical implementation. In this perspective, we start by expressing (5.5) in the form of a HOI (5.6) in which the smooth functions f and g need to be distinguished.

5.2.4.1 Frequency regimes

Due to the dependence of the oscillatory behavior of the integral kernel (5.5) on both variables α and β, the determination of the functions f and g passes through the distinction of four main frequency regimes (figure 5.1). Intermediate regimes are also discussed in the following.

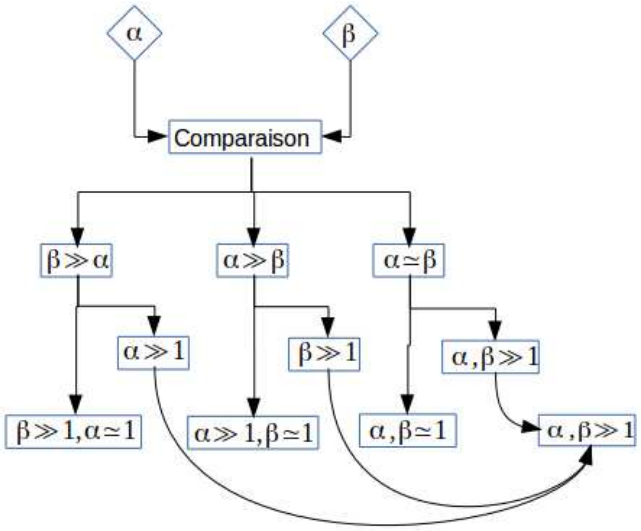

Figure 5.1: Frequency regimes of the HOI kernel

5.2.4.1.1 First regime: In the regime where $\beta \gg \alpha$ and $\alpha \simeq 1$, a plot of the integrand of (5.5) (figure 5.2) shows that oscillations become smooth in the neighborhood of zero. Based on this, we split the integral kernel into a smooth and a highly oscillatory integrals in the case where $a < 0 < b$,

$$\begin{aligned}\mathcal{I}[f] &= \mathcal{I}_1[f] + \mathcal{I}_2[f] \\ &= \int_{-e}^{e} f(x)e^{i\beta g(x)}dx + \int_{[a,b]\setminus[-e,e]} f(x)e^{i\beta g(x)}dx. \end{aligned} \tag{5.25}$$

with $\omega = \beta$, and $f(x) = e^{-i\alpha x}/(1+x^2)$ and $g(x) = -1/\sqrt{1+x^2}$ are smooth functions where e refers to the condition $x \sim 0 \Leftrightarrow |x| < e$ ($e \sim 1/\beta$).

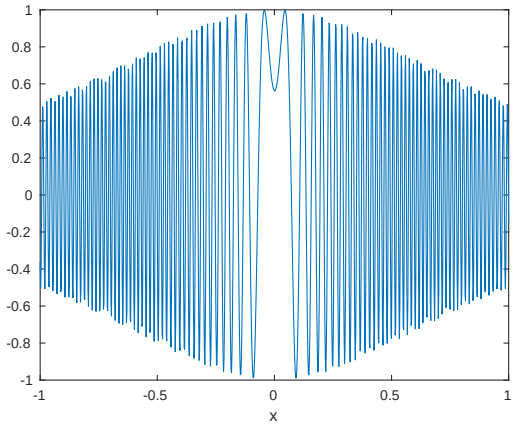

Figure 5.2: Integrand of the integral kernel in the first regime

Based on (5.25), the quadrature of the integral kernel in the first regime is performed using a simple trapezoidal rule for the calculation of $\mathcal{I}_1[f]$ (owing its non-oscillatory behavior) and a highly oscillatory quadrature method for what regards $\mathcal{I}_2[f]$. Besides, by considering the change of variables

$X = -1/\sqrt{1+x^2}$ ($\forall x \in \mathbf{R},\ X \in [-1, 0]$), the second half of the integral kernel becomes

$$\mathcal{I}_2[f] = \int_{-1/\sqrt{1+a^2}}^{-1/\sqrt{1+e^2}} F(X)e^{i\beta X}dX + \int_{-1/\sqrt{1+b^2}}^{-1/\sqrt{1+e^2}} F(X)e^{i\beta X}dX, \quad a \leq -e,\ b \geq e, \tag{5.26}$$

where $F(X) = e^{-i\alpha\sqrt{\frac{1}{X^2}-1}}/(X\sqrt{\frac{1}{X^2}-1})$.

5.2.4.1.2 Second regime: In the regime where $\alpha \gg \beta$ and $\beta \simeq 1$, the integral kernel is written in the form of a HOI where $f(x) = e^{-i\beta/\sqrt{1+x^2}}/(1+x^2)$, $\omega = \alpha$ and $g(x) = -x$. Additionally, if we consider the change of variables $X = -x$, the expression of the integral kernel becomes

$$\mathcal{I}[f] = \int_{-a}^{-b} F(X)e^{i\alpha X}dX, \tag{5.27}$$

where $F(X) = e^{-i\beta/\sqrt{1+X^2}}/(1+X^2)$.

5.2.4.1.3 Third regime: In the regime where $\alpha \simeq \beta \simeq 1$, the integral kernel is not anymore a HOI, a consequence to which neither of previous methods is needed for the quadrature, and only a classical trapezoidal rule using a set of N nodes such that $x_0 = a < x_1 < \ldots < x_N = b$ is suitably sufficient,

$$\mathcal{I}[f] \simeq \frac{b-a}{N}\sum_{i=0}^{N-1}\frac{f(x_i)e^{i\omega g(x_i)} + f(x_{i+1})e^{i\omega g(x_{i+1})}}{2}, \tag{5.28}$$

where $\omega = \alpha$, $\beta = \epsilon\alpha$, $f(x) = 1/(1+x^2)$ and $g(x) = -(x + \epsilon/\sqrt{1+x^2})$.

5.2.4.1.4 Fourth regime: In the regime where $\beta \simeq \alpha$ and $\alpha, \beta \gg 1$, the integral kernel is written in the form of a HOI where $\omega = \alpha$, $\beta = \epsilon\alpha$, $f(x) = 1/(1+x^2)$ and $g(x) = -(x + \epsilon/\sqrt{1+x^2})$. In this regime, in contrast to previous ones, the expression of the HOI kernel cannot be easily transformed into the following simpler form of HOIs

$$\mathcal{I}[f] = \int_a^b F(x)e^{i\omega x}, \tag{5.29}$$

which allows a straightforward application of Filon or Levin-type methods.

One may notice furthermore that the regime $\alpha, \beta \gg 1$ includes in the definition of f and g in the intermediate frequency regimes $\alpha \gg \beta \gg 1$ and $\beta \gg \alpha \gg 1$.

In the next section, in each of the four frequency regime both an asymptotic and a numerical method are applied for the quadrature of the HOI kernel of interest.

5.2.4.2 Analytical derivation of the approximations

5.2.4.2.1 Using asymptotic methods: We derive hereafter a set of analytical approximations of the integral kernel (5.5) using asymptotic methods that will constitute a basis against which the results of the application of the numerical methods will be subsequently compared in the numerical step.
Depending on the frequency regimes, and hence the corresponding functions f and g of the HOI form, either a direct approximation using Bessel functions or a stationary phase approximation are applied in order to analytically derive an approximation to the integral kernel (5.5).

In the **first regime**, an analytical approximation is derived using the stationary phase approximation. The corresponding g-function to this regime presents a single stationary point at $\xi = 0$ (since $g'(x) = x/(1+x^2)^{3/2}$). With (5.10), the application of the stationary phase approximation leads to the following approximate form

$$I(\alpha, \beta, 1) \simeq \sqrt{\frac{2\pi}{\beta |g''(\xi)|}} f(\xi) e^{i\beta g(\xi)} e^{i \operatorname{sign}(g''(\xi))\frac{\pi}{4}} = \sqrt{\frac{2\pi}{\beta}} e^{-i\beta} e^{i\frac{\pi}{4}}. \tag{5.30}$$

In the **second regime**, the stationary phase method cannot be applied since the corresponding g-function has no stationary point. Instead, one obtains by expanding $\exp(-i\beta/\sqrt{1+x^2})$ into a serie of powers and using a term-by-term integration the following approximation

$$I(\alpha, \beta, 1) = \sqrt{2\pi\alpha} \sum_{n=0}^{\infty} \frac{(-i\beta)^n}{n!} \sqrt{\left(\frac{\alpha}{2}\right)^n} \frac{K_{(n+1)/2}(\alpha)}{\Gamma(1+n/2)}, \tag{5.31}$$

where $K_n(z)$ is the n-order modified Bessel function of the second kind defined as

$$K_n(z) = \frac{(2z)^n}{\sqrt{\pi}} \Gamma(n+\frac{1}{2}) \int_0^{\infty} \frac{\cos x}{(\alpha^2+z^2)^{(n+1/2)}} dx, \tag{5.32}$$

with

$$\Gamma(z) = \int_0^{\infty} t^{z-1} e^{-t} dt. \tag{5.33}$$

In the **third regime**, there is no need of the application of an asymptotic method since the integral kernel is not a HOI.

In the **fourth regime**, an analytical approximation to the HOI kernel can be derived by using either the stationary phase method (5.11) or the asymptotic expansion (5.12). The application of the asymptotic expansion is straightforward, while the stationary phase method requires the determination of the stationary points of the g-function.
We start by studying the function derivative of g, $g'(x) = -(1-\epsilon x/(1+x^2)^{3/2})$. For $x \neq 0$, the existence of a stationary point is governed by a condition on ϵ as follows

$$g'(x) = 0 \Leftrightarrow \forall x \in \mathbf{R},\ |\epsilon| > \sqrt{\frac{1+3x^2+3x^4+x^6}{x^2}}. \tag{5.34}$$

Shown in figure 5.3 a plot of the function $h : x \to \sqrt{(1+3x^2+3x^4+x^6)/x^2}$ defining the condition (5.34) on ϵ for positive values of x. Based on this, one determines the minimal value of h that reduces the condition (5.34) to simply $|\epsilon| \gtrsim 2.6$. Figure 5.4, in turn, represents a plot of the function derivative of g where it is clearly seen that for values of ϵ such that $|\epsilon| < \sqrt{(1+3x^2+3x^4+x^6/)x^2}$, the g-function has no stationary points ($g(x) \neq 0$).

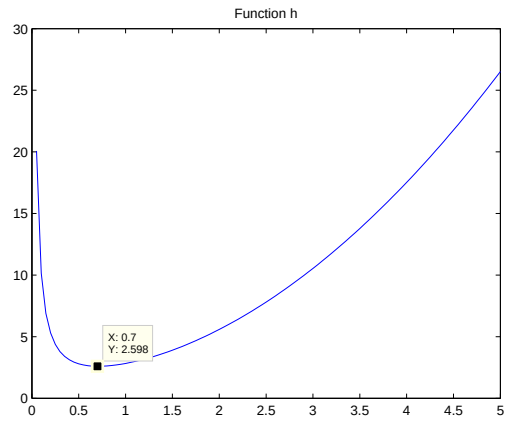

Figure 5.3: h-function for positive values of x

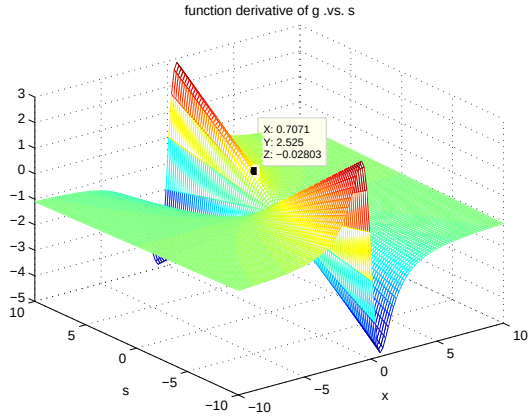

Figure 5.4: Function derivative of g for different values of ϵ

In the absence of stationary points ($|\epsilon| < 2.6$), an approximation to the integral kernel is obtained using the asymptotic expansion,

$$I(\alpha, \beta, 1) \simeq \frac{f(b)}{i\alpha g'(b)} e^{i\alpha g(b)} - \frac{f(a)}{i\alpha g'(a)} e^{i\alpha g(a)}, \tag{5.35}$$

while in the other case ($|\epsilon| \gtrsim 2.6$), the stationary points of g-function must be determined by resolving the following equation

$$g'(x) = 0 \Leftrightarrow 1 - \frac{\epsilon x}{(1+x^2)^{3/2}} = 0 \tag{5.36}$$

$$\Leftrightarrow x^6 + 3x^4 + (3 - \epsilon^2)x^2 + 1 = 0. \tag{5.37}$$

To do so, two different methods can be applied:

a) **Direct method**
First, let $X = x^2$, $a = 1$, $b = 3$, $c = 3 - \epsilon^2$, and $d = 1$, one obtains

$$g'(x) = 0 \Leftrightarrow P(X) = aX^3 + bX^2 + cX + d = 0, \tag{5.38}$$

which, with $X = y + h$, reduces the solving of (5.36) to the following polynomial roots finding problem

$$P(X) = P(y+h) = ay^3 + (3ah + b)y^2 + (3ah^2 + 2bh + c)y + ah^3 + bh^2 + ch + d. \tag{5.39}$$

The basic idea of the direct method is to cancel the coefficient of y^2. Thus, by setting h to $-b/(3a)$ and introducing $p = (3ah^2 + 2bh + c)/a$ and $q = -(ah^3 + bh^2 + ch + d)/a$, (5.39) becomes

$$P(y+h) = a(y^3 + py - q). \tag{5.40}$$

Hence,

$$P(X) = 0 \Leftrightarrow P(y+h) = 0 \Leftrightarrow y^3 + py = q. \tag{5.41}$$

Next, let $y = u + v$, with $u, v \in \mathbf{C}$, one is therefore left with

$$y^3 + py - q = 0 \Leftrightarrow u^3 + v^3 + (3uv + p)(u + v) = q, \tag{5.42}$$

which, if we set $uv = -p/3$, yields the following system of equations

$$\begin{cases} u^3 + v^3 = q \\ u^3 v^3 = (-\frac{p}{3})^3 \cdot \end{cases} \tag{5.43}$$

From (5.43), we deduce that u^3 and v^3 are solutions to the following second-degree equation

$$Z^2 - qZ + \Big(-\frac{p}{3}\Big)^3 = 0, \tag{5.44}$$

of discriminant $\Delta = q^2 + 4p^3/27$, and respective solutions

$$u^3 = \frac{q - i^{\frac{1-\mathrm{sign}(\Delta)}{2}}\sqrt{|\Delta|}}{2}, \quad v^3 = \frac{q + i^{\frac{1-\mathrm{sign}(\Delta)}{2}}\sqrt{|\Delta|}}{2}.$$

In the case where $u^3, v^3 \in \mathrm{R}$, we finally deduce the expression of the first solution x_1 to the equation (5.39),

$$\begin{aligned} x_1 &= y + h = u + v + h \\ &= \left(\frac{q - \sqrt{q^2 + 4p^3/27}}{2}\right)^{1/3} + \left(\frac{q + \sqrt{q^2 + 4p^3/27}}{2}\right)^{1/3} - \frac{b}{3a}. \end{aligned} \tag{5.45}$$

Next, by factorizing the polynomial P in the following form

$$P(X) = (X - x_1)P_2(X) = (X - x_1)(\alpha X^2 + \beta X + \delta), \tag{5.46}$$

where $\alpha = a$, $\beta = b + ax_1$ and $\delta = c + (b + ax_1)x_1$, the Remaining solutions are afterwards found from (5.46) by solving the equation $P_2(X) = 0$ of discriminant $\Delta_2 = \beta^2 - 4\alpha\delta = (3+x_1)^2 - 4[(3-s^2)+(3+x_1)x_1]$ and respective solutions

$$\begin{cases} x_2 = \dfrac{-\beta + i^{\frac{1-\mathrm{sign}(\Delta_2)}{2}}\sqrt{|\Delta_2|}}{2\alpha} = \dfrac{-(3+x_1) + i^{\frac{1-\mathrm{sign}(\Delta_2)}{2}}\sqrt{|\Delta_2|}}{2} \\ x_3 = \dfrac{-\beta - i^{\frac{1-\mathrm{sign}(\Delta_2)}{2}}\sqrt{|\Delta_2|}}{2\alpha} = \dfrac{-(3+x_1) - i^{\frac{1-\mathrm{sign}(\Delta_2)}{2}}\sqrt{|\Delta_2|}}{2} \end{cases}.$$

With all of this, we finally have

$$P(X) = 0 \Leftrightarrow X \in \{x_1; x_2; x_3\}. \tag{5.47}$$

Since we are only interested in real stationary points in the stationary phase approximation and giving that $X = x^2$, we only keep real non-negative x_i. Consequently,

$$g'(x) = 0 \Leftrightarrow x \in \Big\{ \underbrace{\sqrt{x_i}}_{\xi_i}, x_i \in \mathbf{R}^+ \Big\}_i. \tag{5.48}$$

b) **Sotta method**
As previously, we let $X = x^2$ in order to get

$$g'(x) = 0 \Leftrightarrow P(X) = aX^3 + bX^2 + cX + d = 0. \tag{5.49}$$

The method of Sotta allows the solving of the equation $P(x) = 0$ for $c \neq 0$ using the described algorithm in figure 5.5, where $j = e^{i2\pi/3}$, $\alpha = s^2(bs - 3ar)$ and $\beta = q^2(bq - 3ap)$, with p/q and r/s solutions to the Sotta resolvent defined as

$$(b^2 - 3ac)x^2 + (bc - 9ad)x + (c^2 - 3bd) = 0, \tag{5.50}$$

and verifying $ps - rq \neq 0$ and $pqrs \neq 0$. The obtained $\{x_1, x_3, x_3\}$ are the final solutions to equation (5.49).

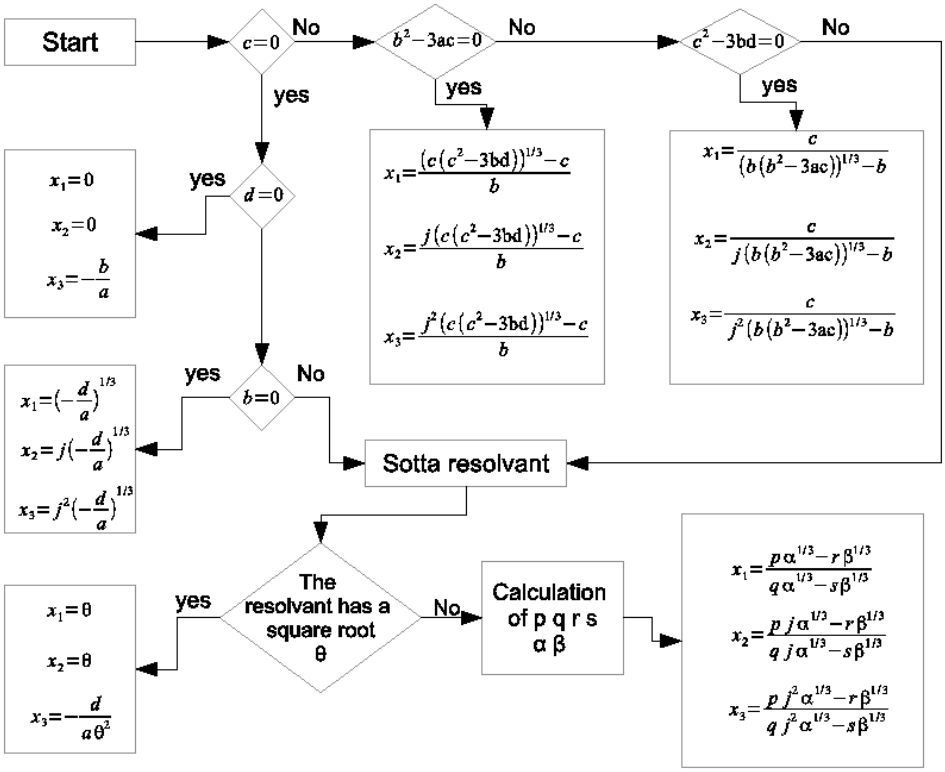

Figure 5.5: Sotta algorithm

Similarly to the direct method, we only keep real non-negative solutions in the determination of the stationary points of function g,

$$g'(x) = 0 \Leftrightarrow x \in \Big\{ \underbrace{\sqrt{x_i}}_{\xi_i}, x_i \in \mathbf{R}^+ \Big\}_i. \tag{5.51}$$

All things considered, the integral kernel (5.5) is finally approximated in the **fourth regime** by means of the stationary phase method as follows

$$I(\alpha, \beta, 1) \simeq \sum_{\xi_i} \sqrt{\frac{2\pi}{\alpha |g''(\xi_i)|}} f(\xi) e^{i \operatorname{sign}(g''(\xi_i)) \frac{\pi}{4}} e^{ig(\xi_i)\alpha}, \tag{5.52}$$

using the derived set of stationary points.

5.2.4.2.2 Using numerical methods: Previous asymptotic approximations of the HOI kernel constitute a comparative basis against which the results of the application of sophisticated numerical methods will be compared. In the following, we introduce a detailed analytical derivation of the quadrature of the integral kernel (5.5) using highly oscillatory numerical methods.

In the **first regime**, additionally to the straightforward calculation of the first non-oscillatory part of the integral kernel (5.25), a Filon-type method is applied for the quadrature of the second highly oscillatory part (5.26) using a *Hermite interpolation* of F within the integration interval $[x_0, x_1]$, where x_0, x_1 refer to the integration limits.
Let a cubic polynomial H expressed as

$$H(x) = a + b(x - x_0) + c(x - x_0)^2 + d(x - x_0)^2(x - x_1), \tag{5.53}$$

and satisfying $F(x_0) = H(x_0)$, $F'(x_0) = H'(x_0)$, $F(x_1) = H(x_1)$, and $F'(x_1) = H'(x_1)$. With $h = x_1 - x_0$, one gets $a = F(x_0)$, $b = F'(x_0)$, $c = \Big(F(x_1) - F(x_0) - hF'(x_0)\Big)/h^2$, and $d = [2(F(x_0) - F(x_1))/h + F'(x_0) + F'(x_1)]/h^2$.
The application of the Filon-type method consists in substituting F in the expression of the integral kernel (5.26) by its Hermite interpolation H as follows

$$Q^F[F] = \int_{x_0}^{x_1} H(x)e^{i\beta x}, \tag{5.54}$$

which, given the introduced change of variables in (5.26), can be analytically computed by means of classical integral calculations. One easily obtains

$$Q^F[F] = c_1F(x_0) + c_2F(x_1) + c_3F'(x_0) + c_4F'(x_1), \tag{5.55}$$

where

$$\begin{cases} c_1 = q_1 - \dfrac{1}{h^2}q_3 + \dfrac{2}{h^3}q_4 \\ c_2 = \dfrac{1}{h^2}q_3 - \dfrac{2}{h^3}q_4 \\ c_3 = q_2 - \dfrac{1}{h}q_3 + \dfrac{1}{h^2}q_4 \\ c_4 = \dfrac{1}{h^2}q_4 \end{cases}, \quad \begin{cases} q_1 = m_1 \\ q_2 = m_2 - x_0m_1 \\ q_3 = m_3 - 2x_0m_2 + x_0^2m_1 \\ q_4 = m_4 - (2x_0 + x_1)m_3 \\ \quad + (x_0^2 + 2x_0x_1)m_2 - x_0^2x_1m_1 \end{cases}, \quad \begin{cases} m_1 = \dfrac{1}{i\beta}(e^{i\beta x_1} - e^{i\beta x_0}) \\ m_2 = \dfrac{1}{i\beta}(x_1e^{i\beta x_1} - x_0e^{i\beta x_0} - m_1) \\ m_3 = \dfrac{1}{i\beta}(x_1^2e^{i\beta x_1} - x_0^2e^{i\beta x_0} - m_2) \\ m_4 = \dfrac{1}{i\beta}(x_1^3e^{i\beta x_1} - x_0^3e^{i\beta x_0} - m_3) \end{cases}.$$

In the **second regime**, a similar Filon-type method is applied using, this time, a second-order *Lagrangian interpolation* of F at the endpoints $x_0 = -b, x_1 = -a$ defined as

$$\Pi_2[F](x) = \frac{x - x_1}{x_0 - x_1}F(x_0) + \frac{x - x_0}{x_1 - x_0}F(x_1). \tag{5.56}$$

Substituting again F by its interpolation (5.56) in the expression of the integral kernel (5.27) yields the following Filon-type approximation

$$Q^F[F] = \int_{x_0}^{x_1} \Pi(x)e^{i\alpha x}. \tag{5.57}$$

With $h = x_1 - x_0$, one easily shows using classical integral calculations that

$$Q^F[F] = l_1 F(x_0) + l_2 F(x_1), \tag{5.58}$$

where

$$\begin{cases} l_1 = -\dfrac{1}{h}(n_2 - x_0 n_1) \\ l_2 = \dfrac{1}{h}(n_2 - x_1 n_1) \end{cases}, \quad \begin{cases} n_1 = \dfrac{1}{i\alpha}(e^{i\alpha x_1} - e^{i\alpha x_0}) \\ n_2 = \dfrac{1}{i\alpha}(x_1 e^{i\alpha x_1} - x_0 e^{i\alpha x_0}) - \dfrac{1}{i\alpha} n_1 \end{cases}.$$

As previously, In the **third regime** there is no need of the application of a numerical method since the integral kernel is not a HOI.

In the **fourth regime**, the complex expression of the g-function does not permit a direct application of the Filon-type method since the thus generated moments cannot be analytically computed. An alternative way to get rid of the calculation of moments is to use the moment-free Levin-type collocation method.
As mentioned before, the only complexity of Levin-type methods resides in the approximation of F. As a matter of fact, a direct derivation of F using the exact expressions of f and g in this frequency regime is unlikely to give an analytical expression. That is, instead of using the exact expressions of F and f, one way could be to consider a polynomial approximation of each.
By letting L a N-order Lagrangian interpolation of f expressed as

$$L(x) = \sum_{k=1}^{N} l_k x^k,$$

one is interested in deriving an approximation of F of the form $\tilde{F}(x) = \sum_{k=1}^{N} c_k x^k$ satisfying $\mathcal{L}[\tilde{F}] = L$. Based on this, the coefficients $\{c_k\}_k$ are determined by resolving the following system of equations

$$\begin{aligned} \mathcal{L}[\tilde{F}](x) = L(x) \Leftrightarrow \tilde{F}'(x) + i\omega g'(x)\tilde{F}(x) = L(x) \Leftrightarrow \sum_{k=2}^{N} k c_k x^{k-1} + i\omega \sum_{k=1}^{N} l_k g'(x) x^k = \sum_{k=1}^{N} l_k x^k \\ \Leftrightarrow \begin{cases} i\omega c_1 g'(x) + 2c_2 & = l_1 \\ & \vdots \\ i\omega c_{N-1} g'(x) + N c_N & = l_{N-1} \\ i\omega c_N g'(x) & = l_N \end{cases}, \end{aligned} \tag{5.59}$$

and one easily finds for $g'(x) \neq 0$

$$\begin{cases} c_1(x) & = \dfrac{1}{i\omega g'(x)}\Big(l_1 - 2\dfrac{l_2}{i\omega g'(x)}\Big) \\ & \vdots \\ c_{N-1}(x) & = \dfrac{1}{i\omega g'(x)}\Big(l_{N-1} - N\dfrac{l_N}{i\omega g'(x)}\Big) \\ c_N(x) & = \dfrac{l_N}{i\omega g'(x)} \end{cases}. \tag{5.60}$$

Once the approximation $\tilde{F}$ is derived, the Levin-type approximation is afterwards obtained using the property $\frac{d}{dx}[F(x)e^{i\omega g(x)}] = \mathcal{L}[F](x)e^{i\omega g(x)}$ and by substituting F by $\tilde{F}$ in the expression of the HOI kernel. One is thus left with

$$\begin{aligned} Q^L[f] &= \int_a^b \mathcal{L}[F](x)e^{i\omega g(x)}dx \simeq \int_a^b \mathcal{L}[\tilde{F}](x)e^{i\omega g(x)}dx = \int_a^b \frac{d}{dx}[\tilde{F}(x)e^{i\omega g(x)}]dx \\ &= \tilde{F}(b)e^{i\omega g(b)} - \tilde{F}(a)e^{i\omega g(a)}. \end{aligned} \tag{5.61}$$

Besides, in the presence of stationary points of g within the integration interval, a similar Levin-type method is applied termed with the property (5.15) which allows the removal of the singularity at the level of each stationary point.

So far, the analytical derivation of the application of both the asymptotic and numerical methods for the quadrature of the HOI kernel was established. In the following, we will be interested in the numerical implementation of the resulting approximate expressions in the various frequency regimes.

5.2.5 Quadrature simulation results

Here, we present the obtained numerical results of the quadrature of the HOI kernel (5.5), mainly in the three frequency regimes where the integral kernel is considered to be highly oscillatory. At each frequency regime, the derived approximations in previous section are numerically compared to the "exact" form the HOI kernel obtained by means of a classical trapezoidal rule,

$$\mathcal{I}[f] \sim \frac{b-a}{N}\sum_{i=0}^{N-1}\frac{f(x_i)e^{i\alpha g(x_i)} + f(x_{i+1})e^{i\alpha g(x_{i+1})}}{2}, \tag{5.62}$$

using a set of node points $\{x_i\}_i$ within the integration interval $[a,b]$. Of course, when employing a standard trapezoidal rule as a comparative basis, the considered frequency range needs to be as lower as possible to allow an acceptable approximation of the HOI kernel.

In the following numerical simulations, we set the integration interval $[a,b]$ to $[-T/2, T/2]$, where $T = 1$.

5.2.5.1 First regime

Shown in figures 5.6,5.7 the quadrature results of the HOI kernel in the first regime ($\beta \gg \alpha$, $\alpha \simeq 1$) using both the Filon/Levin-type and asymptotic approximations as well as the "exact" form by means of the trapezoidal rule approximation.

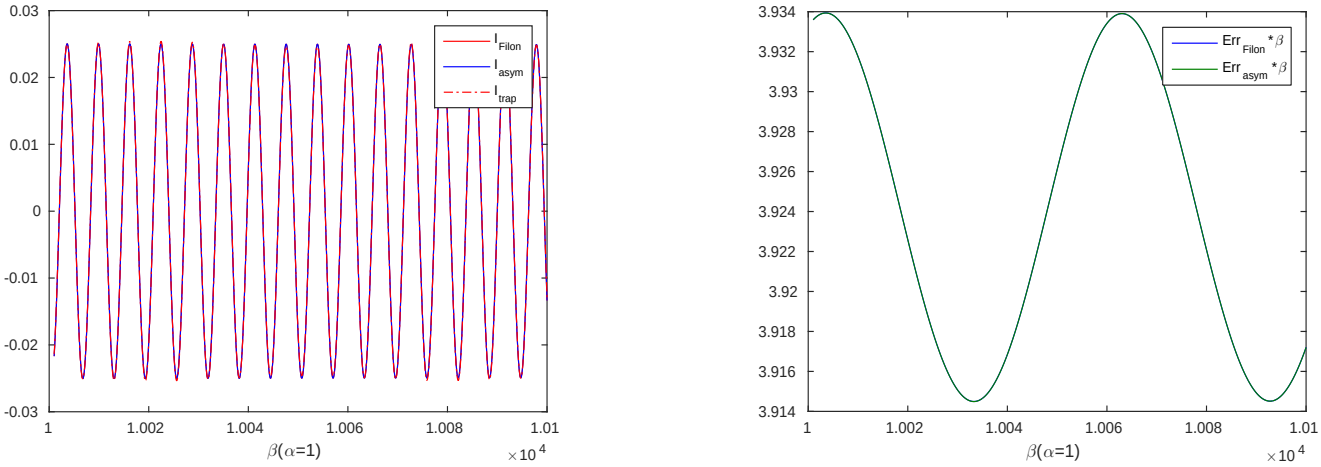

Figure 5.6: (left) Results of the quadrature of the HOI kernel in the first regime using the Filon-type, the stationary phase and the trapezoidal rule approximations. (right) The quadrature error of the Filon-type and the stationary phase approximations scaled by β.

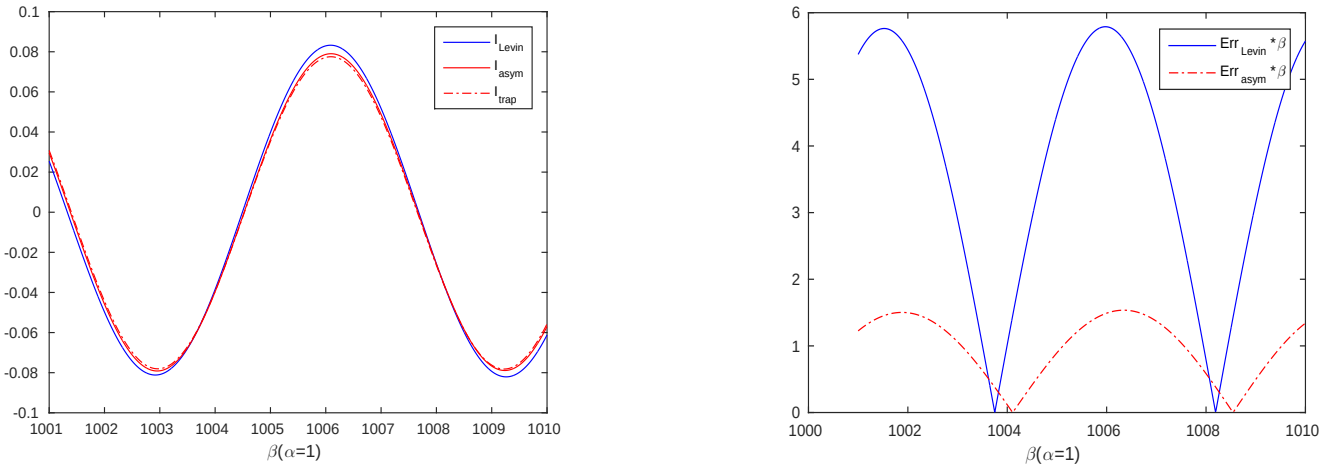

Figure 5.7: (left) Results of the quadrature of the HOI kernel in the first regime using the Levin-type, the stationary phase and the trapezoidal rule approximations. (right) The quadrature error of the Levin-type and the stationary phase approximations scaled by β.

As expected, the Levin and Filon-type approaches approximate the HOI kernel in the first regime with a quadrature error of the order of $\mathcal{O}(\beta^{-1})$.

5.2.5.2 Second regime

Similarly, figure 5.8 compares the results of the quadrature of the HOI kernel in the second regime ($\alpha \gg \beta$, $\beta \simeq 1$), obtained using the Filon-type method and the expression (5.31), to the "exact" trapezoidal form.

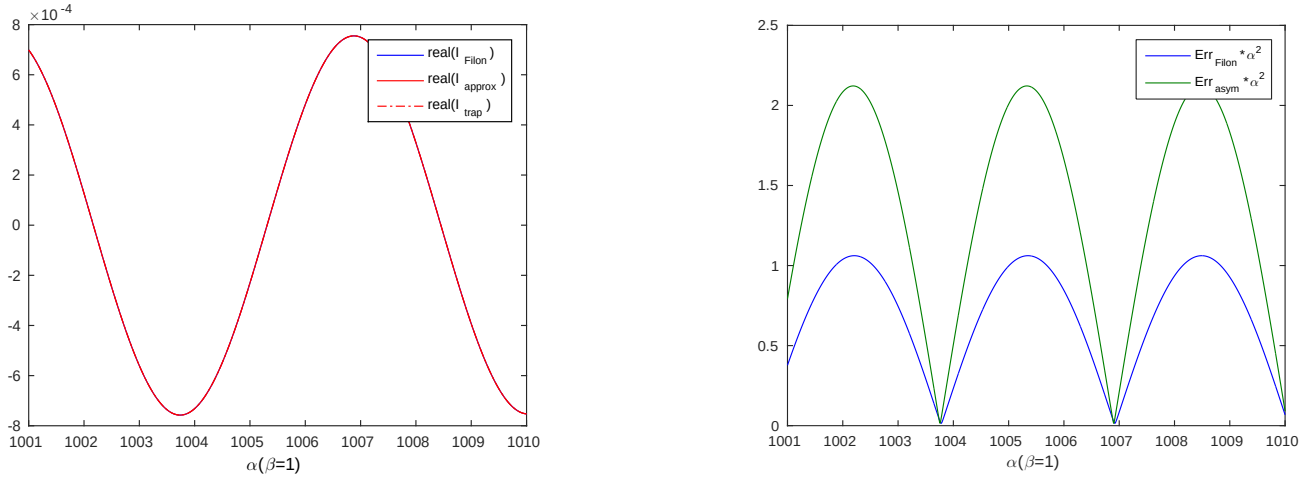

Figure 5.8: (left) Results of the quadrature of the HOI kernel in the second regime using the Filon-type, the asymptotic and the trapezoidal rule approximations. (right) The quadrature error of the Filon-type and the asymptotic approximations scaled by β^2.

Based on previous figures, one obtains in the second regime in the absence of stationary points a quadrature error of the order of $\mathcal{O}(\alpha^{-2})$.

5.2.5.3 Fourth regime

The quadrature of the HOI kernel in the fourth regime ($\beta \simeq \alpha$, $\alpha, \beta \gg 1$) is performed using both asymptotic (the stationary phase approximation and the asymptotic expansion) and numerical (Levin-type) methods in the absence and the presence of stationary points, respectively.

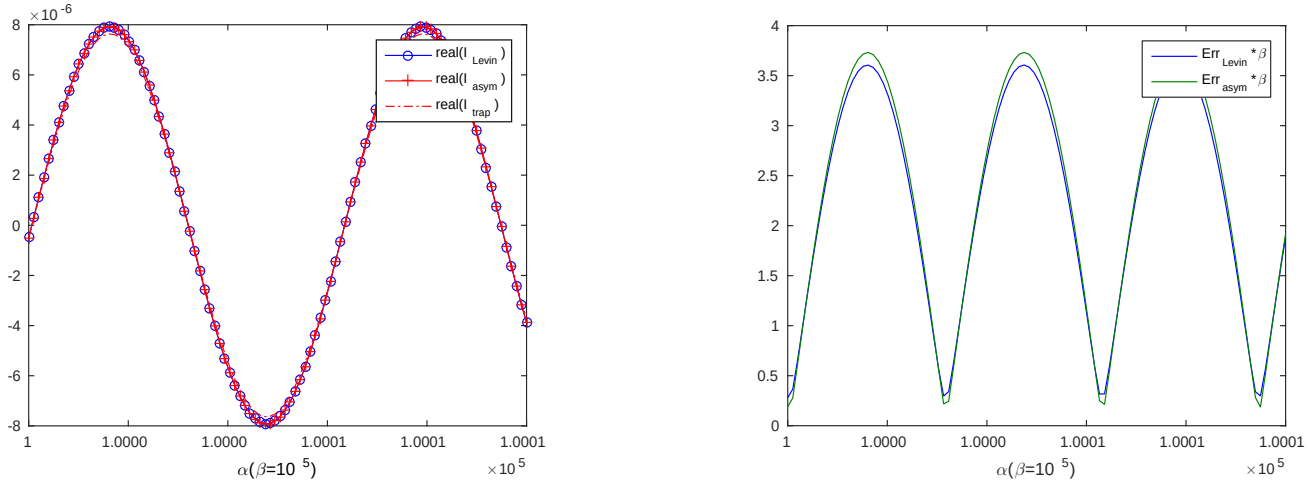

Figure 5.9: (left) Results of the quadrature of the HOI kernel in the fourth regime in the absence of stationary points ($|\epsilon| < 2.6$) using the Levin-type, the asymptotic and the trapezoidal rule approximations. (right) The quadrature error of the Levin-type and the stationary phase approximations scaled by β.

On one hand, in the absence of stationary points, figure 5.11 depicts an accuracy of the Levin-type method of the order of $\mathcal{O}(\beta^{-1})$.

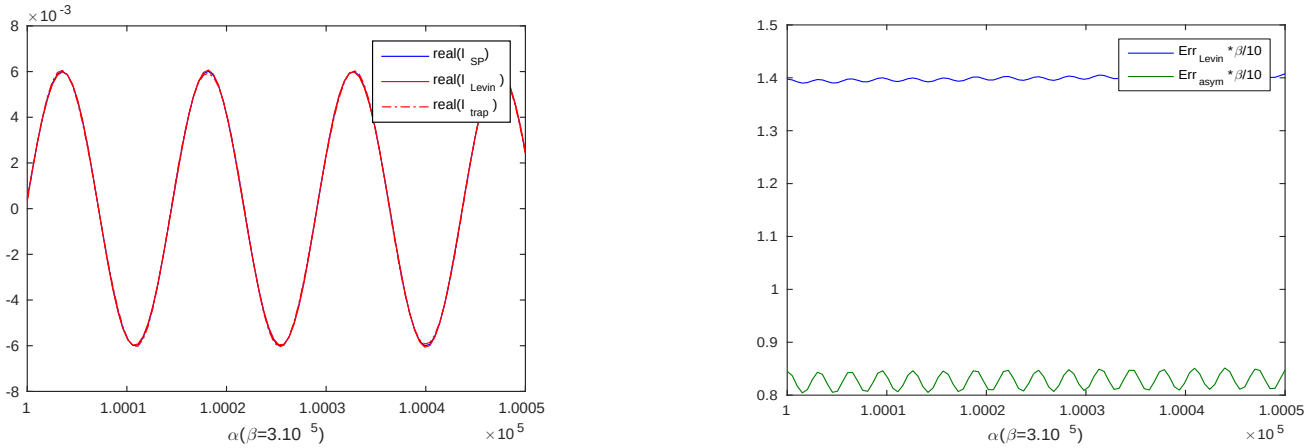

Figure 5.10: (left) Results of the quadrature of the HOI kernel in the fourth regime in the presence of stationary points ($|\epsilon| \geq 2.6$) using the Levin-type, the asymptotic and the trapezoidal rule approximations. (right) The quadrature error of the Levin-type and the stationary phase approximations scaled by β.

On the other hand, in the presence of stationary points, a lower accuracy is achieved by both the asymptotic and the Levin-type methods compared to the case where no stationary point is present, namely $\mathcal{O}(10 \times \beta) = \mathcal{O}(10^{-4})$.

5.2.6 Discussion

Based on the obtained numerical results of the quadrature of the HOI kernel in the various frequency regimes, one may notice that the values of the integral kernel in the regime $\beta \gg \alpha$ are at least two orders higher than those in the other regimes. Besides, the $\alpha \sim \beta \sim 1$ gives comparable values to the first regime (figure 5.11) but one shows that this regime contributes to the integral kernel only within a very tiny η-interval, which renders its contributions negligible.

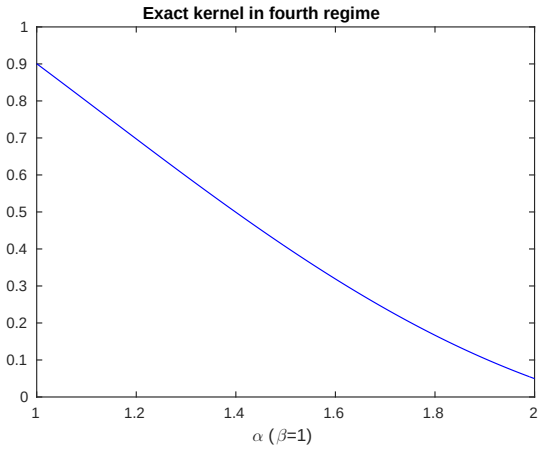

Figure 5.11: Integral kernel in the regime $\alpha \sim \beta \sim 1$

With all of this, one can state that the only relevant regime that efficiently contributes to the HOI kernel is the first regime ($\beta \gg \alpha$).

5.2.7 Conclusions

In the context of Earth observation from space, recent space-based passive interferometric systems have been largely used on board of satellites with the aim of a global and repetitive coverage of the key parameters of the Earth. These key parameters, namely *soil moisture* [16] and *ocean salinity* [17], are directly derived from the emitted *brightness temperatures* [18] from the Earth's surface/atmosphere system, which is, in turn, reconstructed from the cross-correlation values of the measured signals at the level the satellite's antennas using inversion techniques [19].

The theoretical derivation of the correlation function obtained by means of the FouCoIm concept gives rise to a direct relationship that links the measured correlation values to the brightness temperatures through a **highly oscillatory integral kernel**. Therefore, the reconstruction procedure is strictly dependent of the ability of inverting the correlation function equation, and hence the numerical quadrature of the HOI kernel.

In this section, both asymptotic and numerical quadrature methods were employed for the quadrature of the HOI kernel of interest in order to allow a general derivation of the correlation values obtained by means of the FouCoIm concept and a simpler reconstruction of temperatures detailed in the next section.

5.3 Numerical processor: derivation & results

5.3.1 Introduction

We previously showed that the use of the FouCoIm approach resulted in a new formulation of the correlation function including a highly oscillatory integral kernel term linking the quantities of interest. Starting from the established expression of the correlation function, the reconstruction procedure of the brightness temperatures is therefore an attempt to reformulate the correlation function equation in a invertible form.

This section mainly focuses on the numerical transformation of the correlation function so as to build an efficient numerical reconstruction procedure of brightness temperatures. We firstly derive a detailed numerical implementation of the different physical quantities required for the computation of the correlation values before going through the considered inversion methodology so far implemented in the numerical processor.

A particular attention must be, nevertheless, drawn to the range of frequencies used in the calculation of quantities of interest. As a matter of fact, passive Earth remote sensing is exclusively fashioned in the protected frequency band (1400-1427 MHz), and the filtering processes using such high frequencies requires a quite high sampling rate. That is, this section includes three methodologies to bypass the need for a high computational effort in the inversion procedure. First, one expects, using a frequency translation procedure, to translate the calculation to much lower frequency band and thus notably reduce the required sampling rate. Second, we introduce a reconstruction procedure exploiting the quadrature of the HOI kernel detailed in the previous section while keeping the realistic problem dimensions. And finally, we propose to translate the calculations to frequencies in the ultra-sound domain while taking care of introducing convenient dimensions allowing the same approximations as in the theoretical derivation. This final approach introduces the idea of a practical experimental validation of the FouCoIm concept.

5.3.2 Numerical simulations using frequency translation

5.3.2.1 Current density

Sources of temperature at the surface of the Earth are assumed to be randomly emitting in the whole frequency spectrum in the transverse direction. Their current fluctuations are described by stochastic processes that can be numerically modeled using Random Gaussian Processes (RGP).
Now, if we consider a source at the surface of the Earth located at a position $\mathbf{r}''$ and of temperature T_0, its frequency-dependent transverse current fluctuations can be expressed as a RGP of variance T_0 (or of standard deviation $\sqrt{T_0}$) with a mean of 0,

$$\tilde{\mathbf{j}}^t(\mathbf{r}'', \omega') = \mathcal{N}(0, \sqrt{T_0}). \tag{5.63}$$

Moreover, the Fourier-transform of (5.63) gives the density of the time-dependent transverse current fluctuations,

$$\mathbf{j}^t(\mathbf{r}'', t) = \frac{1}{\sqrt{2\pi}} \int d\omega' e^{i\omega' t} \tilde{\mathbf{j}}^t(\mathbf{r}'', \omega'). \tag{5.64}$$

In the following numerical developments, the frequency-dependent transverse current fluctuations of sources of temperature will be numerically modeled using (5.63).

5.3.2.2 Electric field

We propose hereafter a way to possibly compute the Fourier components of the electric fields using a translation to much lower frequencies than those in the L-band.

The time-dependent electric field due to a current density $\mathbf{j}$ at the surface of the Earth observed by an on-board antenna of original position $\mathbf{r}_1$ is expressed as follows

$$\mathbf{E}_{\mathbf{r}_1}(t_1) = \frac{K_1}{\sqrt{2\pi}} \int d\omega' \int d^3\mathbf{r}'' \frac{i\omega'}{|R_1(t_1)|} \tilde{\mathbf{j}}^t(\mathbf{r}'', \omega') e^{i\omega'(t_1 - \frac{|R_1(t_1)|}{c})}, \tag{5.65}$$

where $K_1 = -\mu_0/(4\pi)$ and $R_1(t) = \mathbf{r}_1 + \mathbf{v}_s t - \mathbf{r}''$. This expression is filtered over a frequency bandwidth B centered at ω_0,

$$\mathbf{E}_{\mathbf{r}_1}(t_1) = \frac{K_1}{\sqrt{2\pi}} \int_{\omega_0 - B/2}^{\omega_0 + B/2} d\omega' \int d^3\mathbf{r}'' \frac{i\omega'}{|R_1(t_1)|} \tilde{\mathbf{j}}^t(\mathbf{r}'', \omega') e^{i\omega'(t_1 - \frac{|R_1(t_1)|}{c})}, \tag{5.66}$$

which can be written as

$$\mathbf{E}_{\mathbf{r}_1}(t_1) = \frac{K_1}{\sqrt{2\pi}} \int d^3\mathbf{r}'' \Big\{ \int_{-B/2}^{B/2} dW' i(W' + \omega_0) \tilde{\mathbf{j}}^t(\mathbf{r}'', W' + \omega_0) e^{iW'(t_1 - \frac{|R_1(t_1)|}{c})} \Big\} \frac{e^{i\omega_0(t_1 - \frac{|R_1(t_1)|}{c})}}{|R_1(t_1)|}. \tag{5.67}$$

By letting

$$e(\mathbf{r}'', t_1) = \int_{-B/2}^{B/2} dW' i(W' + \omega_0) \tilde{\mathbf{j}}^t(\mathbf{r}'', W' + \omega_0) e^{iW'(t_1 - \frac{|R_1(t_1)|}{c})},$$

which needs to be numerically implemented using a Shannon-Nyquist temporal sampling of $F_s = 2B$, one obtains

$$\mathbf{E}_{\mathbf{r}_1}(t_1) = \frac{K_1}{\sqrt{2\pi}} \int d^3\mathbf{r}'' e(\mathbf{r}'', t_1) \frac{e^{i\omega_0(t_1 - \frac{|R_1(t_1)|}{c})}}{|R_1(t_1)|}. \tag{5.68}$$

Now, the Fourier component of the electric field received by the antenna 1 is obtained by Fourier transforming (5.68),

$$\tilde{\mathbf{E}}_{\mathbf{r}_1}(\omega_1) = \frac{K_1}{2\pi} \int d^3\mathbf{r}'' \int dt_1 e(\mathbf{r}'', t_1) e^{i(\omega_0 - \omega_1)t_1} \frac{e^{-i\omega_0 \frac{|R_1(t_1)|}{c}}}{|R_1(t_1)|}. \tag{5.69}$$

By using the previously established approximation,

$$|R_1(t_1)| = |\mathbf{r}_1 + \mathbf{v}_s t_1 - \mathbf{r}''| \simeq |\mathbf{r}_1 - \mathbf{r}''| + \mathbf{v}_s \cdot \hat{\mathbf{e}}_{\mathbf{r}_1 - \mathbf{r}''} t_1, \tag{5.70}$$

equation (5.69) is consequently transformed into

$$\tilde{\mathbf{E}}_{\mathbf{r}_1}(\omega_1) \simeq \frac{K_1}{2\pi} \int d^3\mathbf{r}'' e^{-i\omega_0 \frac{|\mathbf{r}_1 - \mathbf{r}''|}{c}} \int dt_1 e(\mathbf{r}'', t_1) e^{i(\omega_0 - \omega_1)t_1} \frac{e^{-i\omega_0 \boldsymbol{\beta} \cdot \hat{\mathbf{e}}_{\mathbf{r}_1 - \mathbf{r}''} t_1}}{|R_1(t_1)|}, \tag{5.71}$$

where $\boldsymbol{\beta} = \mathbf{v}_s/c$ with $\beta \simeq 2.5.10^{-5}$. Again, by letting

$$\tilde{e}(\mathbf{r}'', \omega_1) = \int dt_1 e(\mathbf{r}'', t_1) e^{i(\omega_0 - \omega_1)t_1} \frac{e^{-i\omega_0 \boldsymbol{\beta} \cdot \hat{\mathbf{e}}_{\mathbf{r}_1 - \mathbf{r}''} t_1}}{|R_1(t_1)|},$$

which is, in turn, computed for $\omega_1 \in [\omega_0 - B/2, \omega_0 + B/2]$ (hence $\omega_1 - \omega_0 \in [-B/2, B/2]$) and a maximal Doppler shift $\omega_0 \beta \simeq 35$ KHz using the same Nyquist-Shannon temporal sampling F_s. The final expression of the Fourier component of the Electric field fluctuations as seen by the antenna 1 is finally given by

$$\tilde{\mathbf{E}}_{\mathbf{r}_1}(\omega_1) \simeq \frac{K_1}{2\pi} \int d^3\mathbf{r}'' \tilde{e}(\mathbf{r}'', \omega_1) e^{-i\omega_0 \frac{|\mathbf{r}_1 - \mathbf{r}''|}{c}}. \tag{5.72}$$

5.3.2.3 Correlation function

Equation (4.10) together with the FDT assumption (equation (4.4)) yield the following expression of the correlation function

$$C(\mathbf{r}_1,\mathbf{r}_2,\omega_1,\omega_2) \simeq (\frac{K_1}{2\pi})^2 \int d^3\mathbf{r}'' e^{-i\frac{\omega_0}{c}(|\mathbf{r}_1-\mathbf{r}''|-|\mathbf{r}_2-\mathbf{r}''|)} \Bigg\{ \int_{-B/2}^{B/2} dW' (W'+\omega_0)^2 \times k_1(W',\omega_1,\mathbf{r}'') k_2^*(W',\omega_2,\mathbf{r}'') \Big\langle |\tilde{\mathbf{j}}^t(\mathbf{r}'',W'+\omega_0)|^2 \Big\rangle \Bigg\}, \tag{5.73}$$

where

$$k_i(W',\omega_i,\mathbf{r}'') = \int dt_i e^{i(\omega_0-\omega_i)t_i} e^{iW'(t_i-\frac{|R_i(t_i)|}{c})} \frac{e^{-i\omega_0 \boldsymbol{\beta}\cdot\hat{\mathbf{e}}_{\mathbf{r}_i-\mathbf{r}''} t_i}}{|R_i(t_i)|}, \quad i=\{1,2\}. \tag{5.74}$$

The time integration in the preceding expression shall be numerically computed over an integration time τ. Equation (5.74) thus becomes

$$k_i(W',\omega_i,\mathbf{r}'') = \int_{-\tau/2}^{\tau/2} dt_i e^{i(\omega_0-\omega_i)t_i} e^{iW'(t_i-\frac{|R_i(t_i)|}{c})} \frac{e^{-i\omega_0 \boldsymbol{\beta}\cdot\hat{\mathbf{e}}_{\mathbf{r}_i-\mathbf{r}''} t_i}}{|R_i(t_i)|}, \quad i=\{1,2\}. \tag{5.75}$$

We assume furthermore that $(W'+\omega_0)^2 \Big\langle \Big| \tilde{\mathbf{j}}^t\Big(\mathbf{r}'', (W'+\omega_0)\Big)\Big|^2 \Big\rangle$, which is related to the brightness temperature, depends only weakly on frequency (compared to the rapid oscillations of the phase as function of ω) over the bandwidth B, $(W'+\omega_0)^2 \Big\langle \Big| \tilde{\mathbf{j}}^t\Big(\mathbf{r}'', (W'+\omega_0)\Big)\Big|^2 \Big\rangle \simeq \omega_0^2 \Big\langle \Big| \tilde{\mathbf{j}}^t\Big(\mathbf{r}'', \omega_0\Big)\Big|^2 \Big\rangle$. The expression (5.73) is thus reduced to

$$C(\mathbf{r}_1,\mathbf{r}_2,\omega_1,\omega_2) \simeq (\frac{K_1}{2\pi})^2 \omega_0^2 \int d^3\mathbf{r}'' e^{-i\frac{\omega_0}{c}(|\mathbf{r}_1-\mathbf{r}''|-|\mathbf{r}_2-\mathbf{r}''|)} \Big\langle |\tilde{\mathbf{j}}^t(\mathbf{r}'',\omega_0)|^2 \Big\rangle \times \Bigg\{ \int_{-B/2}^{B/2} dW' k_1(W',\omega_1,\mathbf{r}'') k_2^*(W',\omega_2,\mathbf{r}'') \Bigg\}, \tag{5.76}$$

and even more simplified as follows

$$C(\mathbf{r}_1,\mathbf{r}_2,\omega_1,\omega_2) \simeq \int d^3\mathbf{r}'' K(\omega_1,\omega_2,\mathbf{r}'') \Big\langle |\tilde{\mathbf{j}}^t(\mathbf{r}'',\omega_0)|^2 \Big\rangle, \tag{5.77}$$

where

$$K(\omega_1,\omega_2,\mathbf{r}'') = (\frac{K_1}{2\pi})^2 \omega_0^2 e^{-i\frac{\omega_0}{c}(|\mathbf{r}_1-\mathbf{r}''|-|\mathbf{r}_2-\mathbf{r}''|)} \int_{-B/2}^{B/2} dW' k_1(W',\omega_1,\mathbf{r}'') k_2^*(W',\omega_2,\mathbf{r}''). \tag{5.78}$$

5.3.2.4 Correlation matrix

If we consider that both frequencies ω_1, ω_2 are similarly sampled within the bandwidth B using $N_\omega = B \times F_s$ frequency samples $\{\omega_i\}_{i\in\{1\dots N_\omega\}}$. The integral over $\mathbf{r}''$ in the expression (5.77) of the correlation function can be discretized and transformed into a 2D summation over sources' positions (since we assumed the Earth's surface as a plane at $z=0$),

$$C(\mathbf{r}_1,\mathbf{r}_2,\omega_i,\omega_j) \simeq \sum_{\mathbf{r}''} K(\omega_i,\omega_j,\mathbf{r}'') \Big\langle |\tilde{\mathbf{j}}^t(\mathbf{r}'',\omega_0)|^2 \Big\rangle, \tag{5.79}$$

leading to the definition of the $(i,j)-$component of the correlation matrix. We furthermore define a kernel matrix K where the (i,j)-th component is expressed for each source position $\mathbf{r}''$ by $K(\omega_i,\omega_j,\mathbf{r}'')$.

This gives rise to a square kernel matrix for each source position.
In order to derive a matrix equation of the correlation function, we define a reshaped matrix of the correlation function as a column matrix and a global kernel matrix defined as a set of column matrices for each source position. Now, if we consider N_s sources of temperature of positions $\{\mathbf{r}''_k\}_{k\in\{1\dots N_s\}}$, equation (5.79) is thus equivalent to the following matrix equation

$$\mathcal{C} \simeq \mathcal{K} \times \mathcal{T}, \tag{5.80}$$

where

$$\mathcal{C} = \begin{pmatrix} C(\mathbf{r}_1, \mathbf{r}_2, \omega_1, \omega_1) \\ \vdots \\ C(\mathbf{r}_1, \mathbf{r}_2, \omega_1, \omega_{N_\omega}) \\ \vdots \\ C(\mathbf{r}_1, \mathbf{r}_2, \omega_{N_\omega}, \omega_{N_\omega}) \end{pmatrix} = \begin{pmatrix} C_{11} \\ \vdots \\ C_{1N_\omega} \\ \vdots \\ C_{N_\omega N_\omega} \end{pmatrix},$$

$$\mathcal{K} = \begin{pmatrix} K(\omega_1, \omega_1; \mathbf{r}''_1) & \dots & K(\omega_1, \omega_1; \mathbf{r}''_{N_s}) \\ \vdots & & \vdots \\ K(\omega_1, \omega_{N_\omega}; \mathbf{r}''_1) & \dots & K(\omega_1, \omega_{N_\omega}; \mathbf{r}''_{N_s}) \\ \vdots & & \vdots \\ K(\omega_{N_\omega}, \omega_{N_\omega}; \mathbf{r}''_1) & \dots & K(\omega_{N_\omega}, \omega_{N_\omega}; \mathbf{r}''_{N_s}) \end{pmatrix} = \begin{pmatrix} K_{11}(\mathbf{r}''_1) & \dots & K_{11}(\mathbf{r}''_{N_s}) \\ \vdots & & \vdots \\ K_{1N_\omega}(\mathbf{r}''_1) & \dots & K_{1N_\omega}(\mathbf{r}''_{N_s}) \\ \vdots & & \vdots \\ K_{N_\omega N_\omega}(\mathbf{r}''_1) & \dots & K_{N_\omega N_\omega}(\mathbf{r}''_{N_s}) \end{pmatrix},$$

and

$$\mathcal{T} = k \begin{pmatrix} \left\langle |\tilde{\mathbf{j}}^t(\mathbf{r}''_1, \omega_0)|^2 \right\rangle \\ \vdots \\ \left\langle |\tilde{\mathbf{j}}^t(\mathbf{r}''_{N_r}, \omega_0)|^2 \right\rangle \end{pmatrix} = \begin{pmatrix} T_1 \\ \vdots \\ T_{N_s} \end{pmatrix},$$

where k is a constant that links the current fluctuations intensities to brightness temperatures (see [20]). Here, time and frequency integrations in the expression of each K_{ij} are to be replaced by summations in the numerical derivation.

5.3.2.5 Reconstruction procedure using frequency translation

Starting from the thus defined matrix equation of the correlation function, the brightness temperature map of an observed scene can be reconstructed from the measured correlation values by inverting (5.80). Based on this, the T_B reconstruction boils down to a matrix inversion problem.
That is, the reconstruction procedure, resulted from the integrals' discretization, allows the reconstruction of temperatures over a predefined spatial grid of sources' positions. This is equivalent to assume a *a priori* constant temperature over a whole pixel of central position $\mathbf{r}''$, which yields the establishment of a distribution map of sources' positions.
More particularly, the global kernel matrix $\mathcal{K}$ is easily constructed using equation (5.78). Next, by constructing and reshaping the measurement-based correlation matrix one is able of reconstructing the brightness temperatures of the observed scene following the predefined distribution map through

$$\mathcal{T} \simeq \mathcal{K}^\dagger \times \mathcal{C}, \tag{5.81}$$

where $\mathcal{K}^\dagger$ refers to the Moore-Penrose pseudo-inverse of the kernel matrix $\mathcal{K}$.

5.3.2.6 Simulation results

5.3.2.6.1 Reconstruction of temperatures: The preceding reconstruction procedure was implemented in the simple case of few localized source points at the surface of the Earth. For each source point of position $\mathbf{r}''$ of temperature T_s, we define a corresponding source vector as a Random Gaussian Process (RGP) of standard deviation the square root of the temperature (or equivalently the intensity $I_s = K_3 T_s$ (equation (4.29))). We assume furthermore that one possesses a set of N_r uncorrelated realizations of each source vector over which the average $< \ldots >$ in the expression of the correlation function (5.73) is computed.
We consider an observer flying at a height h with a speed v_s and comprised of a pair of antennas separated by a distance Δr and arranged perpendicularly to the flight direction.
The Fourier components of the electric field fluctuations as seen by the antenna-pair are computed by means of the expression (5.72) for each sources' realization and are cross-correlated to construct a realization-dependent correlation matrix. Next, a global correlation matrix is computed by averaging the set of realization-dependent correlation matrices.
In the meantime, the global kernel matrix $\mathcal{K}$ of sources' positions dependent columns is numerically constructed.

Now, let $N_r = 10^3$ uncorrelated realizations of four source points located at the surface of the Earth as described in figure 5.12. We firstly perform the computation over a frequency bandwidth $B = 1$ KHz sampled using a frequency $F_e = 3$ KHz $> 2\times$B.

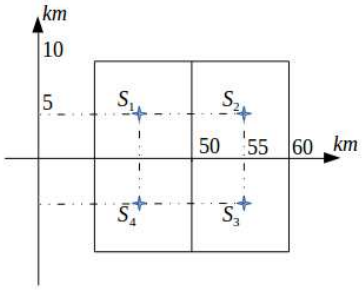

Figure 5.12: Sources' positions

For an integration time τ, the described reconstruction procedure yields the following values of reconstructed temperatures $\{T_{rec_1}, T_{rec_2}, T_{rec_3}, T_{rec_4}\}$ (table 5.1).

Table 5.1: Reconstructed temperatures

τ(s)	T_s(K)	Source	T_{rec}(K)	Std
5	300	$\{S_1, S_2, S_3, S_4\}$	$\{307.90, 300.94, 315.77, 293.15\}$	$\{0.026, 0.003, 0.052, 0.022\}$

Next, simulations are pushed a bit further in order to model the inversion accuracy as function of source's position. We consider an integration time $\tau = 10$ s, a frequency bandwidth $B = 1$ KHz and $N_r = 10^3$ different realizations of a source point of temperature 300 K located at the surface of the Earth iteratively over a grid of $10^3 \times 10^3$ km^2 as described in figure 5.13.

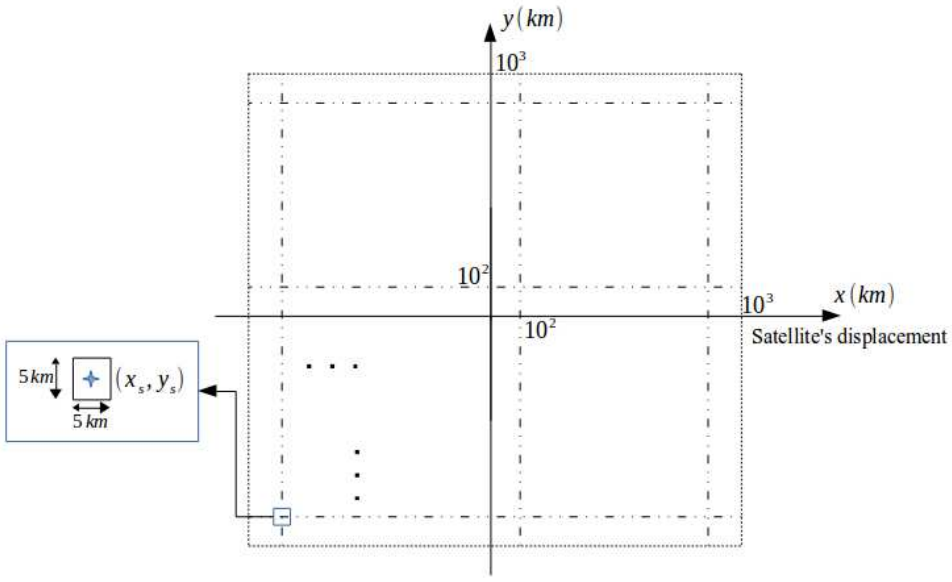

Figure 5.13: Source's positions

Hereafter are plotted the results of the reconstruction of temperatures all over the grid of $10^3 \times 10^3$ km^2. The following figures depict an acceptable reconstruction accuracy of temperatures using the frequency translation approach.

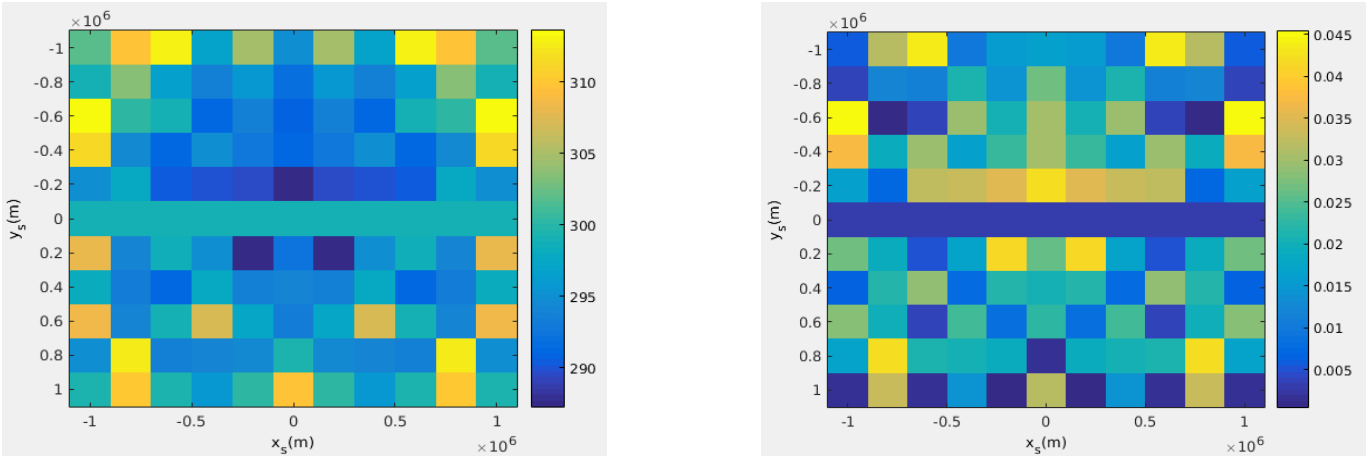

Figure 5.14: (left) Reconstructed temperatures and (right) reconstruction errors as function of source's position in the microwave regime

One is interested in determining the effect of N_r (the number of the different realizations of the stochastic process modeling the source fluctuations) on the reconstruction accuracy. Let a source point located at $(0, y_s = 100$ km$)$ of temperature 300 K, figure 5.15 shows the reconstructed temperatures as function of N_r. Based on this, the higher N_r is the more accurate the reconstruction will be until a stage of stabilization ($N_r > 3000$).

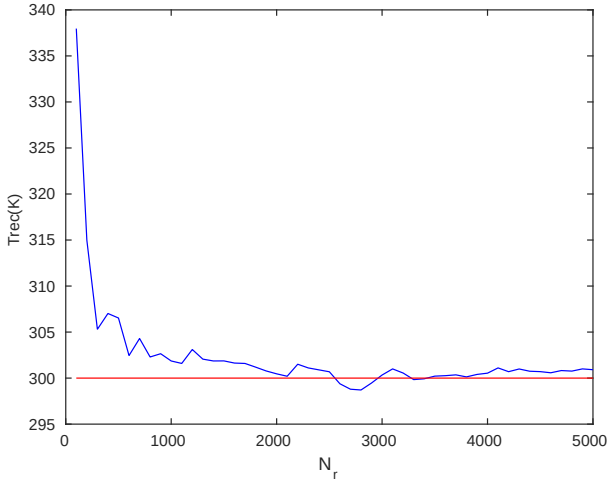

Figure 5.15: Reconstruction accuracy .vs. N_r

5.3.2.6.2 Reconstructed source function: Besides the direct reconstruction of temperatures, we are interested in deriving the shape of the reconstructed source function (or point-spread function (PSF)) of a single source point which is to be compared with the theoretical expression derived earlier in chapter 4.

In this perspective, starting from a single source point we perform the reconstruction of temperatures over a spatial profile in the neighborhood of the source position y_s. More particularly, we construct the kernel matrix over the set of spatial positions ($y \in \{y_1, \ldots, y_s, \ldots, y_N\}$) which, when inverted and multiplied with the correlation matrix in the position of the source point, yields the reconstructed source function by the FouCoIm concept of a single source point,

$$f_{rec} = [\mathcal{K}(y_1), \ldots, \mathcal{K}(y_s), \ldots, \mathcal{K}(y_N)]^{\dagger} \times \mathcal{C}(y_s). \tag{5.82}$$

Based on this function, one is further able of extracting the value of the achievable geometric resolution. In reality, the direct use of the pseudo-inverse doesn't allow a correct inversion of equation (5.80) over a spatial profile starting from one single point due the singularity of the kernel matrix. As a result, a Thickonov regularization approach was employed in such way to get rid of the singularity and allow a more controlled inversion.

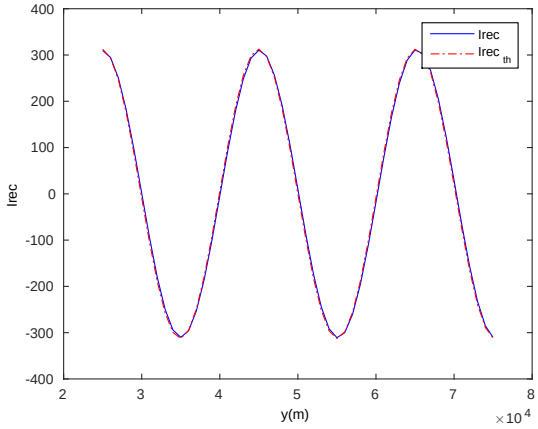

Figure 5.16: Reconstructed source function in the microwave regime

Shown in figure 5.16 the reconstructed source function as obtained both numerically, by means of the frequency translation procedure, and theoretically, as derived in chapter 4.

The applied Gaussian filtering in the numerical simulations of the expressions of the electric fields isn't noticed in the figure 5.16 (compared to figure 4.8) since the considered frequency bandwidth B of 1 KHz yields an inverse Gaussian function in the spatial domain of a higher width ($\sqrt{2}/\tilde{b} = \sqrt{2}c/(2\pi\Delta r B)$) than the considered spatial profile (figure 5.17 where the amplitude of the inverse Gaussian function is constantly equal to 1). That is, in order to see the effect of the Gaussian functions, the numerical calculation needs to be performed using a 20-MHz bandwidth.

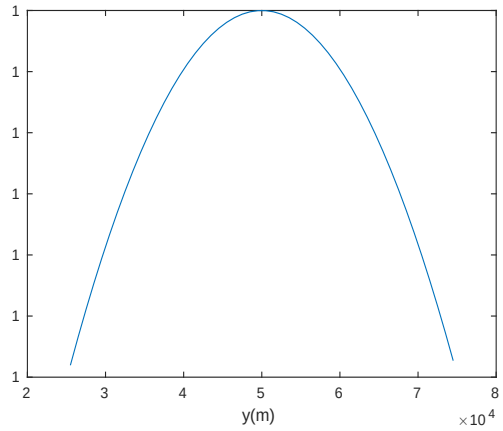

Figure 5.17: Inverse Gaussian function

5.3.2.6.3 Geometric resolution (GR): Once the reconstructed source function is numerically derived, a value of the GR can thus be extracted using the introduced definition in chapter 4 in the case of a single source point. The best achievable value of the GR is defined to be the minimal required shift in the source position making a peak of the reconstructed source function move into the next trough. Figure 5.18 shows the reconstructed source functions corresponding to three positions in the cross-track direction of the source point $\{50, 55, 60\}$ km. Based on this, a 10-km shift of the source position seems to verify the definition of the GR.

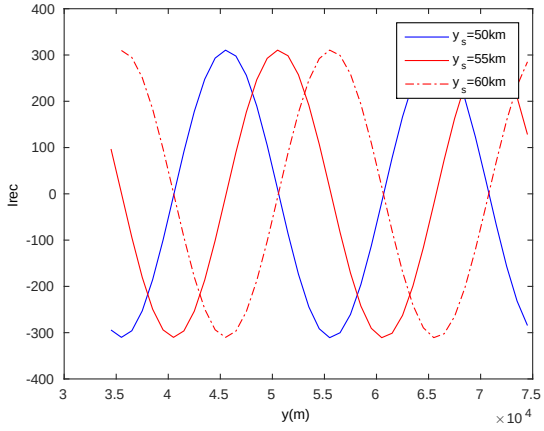

Figure 5.18: Extraction of the value of the geometric resolution in the microwave regime

Besides, the theoretical expression of the GR in the cross-track direction derived in chapter 4,

$$R_y = \frac{\pi c}{\Delta r \omega_0} \frac{(y_s^2 + h^2)^{3/2}}{h^2}, \tag{5.83}$$

gives an equivalent value of 10.069 km for a source position $y_s = 50$ km.

5.3.2.6.4 Radiometric sensitivity (RS): Besides the GR, the RS is the second important parameter to be evaluated. It is defined at a source position y_s in the case of ideal receivers (absence of the receiver's noise) as the following ratio

$$\mathrm{RS}(y_s) \equiv \frac{\sigma(T_{rec}(y_s))}{T_{rec}(y_s)} \equiv \frac{\sqrt{\Delta(T_{rec}(y_s))}}{T_{rec}(y_s)} = \frac{\sqrt{< T_{rec}^2(y_s) > - < T_{rec}(y_s) >^2}}{T_{rec}(y_s)}, \tag{5.84}$$

where $< ... >$ is the average over the thermal ensemble which is numerically performed by considering the average over a set of different realizations of the stochastic process modeling the thermal radiations emitted by a source of temperature. T_{rec} refers to the reconstructed source's temperature for each realization of the stochastic process.
We thus proceed in the same manner as in the reconstruction of temperatures when dealing with the RS. Figure 5.19 shows the variations of the RS over the same spatial profile as in figure 5.13 using $N_r = 10^3$ realizations. A RS that ranges between 0.2 and 1 depicts a fluctuation level of the correlations of the order of source's temperature (300 K) which reveals a degraded radiometric performance of the FouCoIm concept. A possible improvement of the RS using an array of antennas is later briefly discussed and should be deeply investigated in the future.

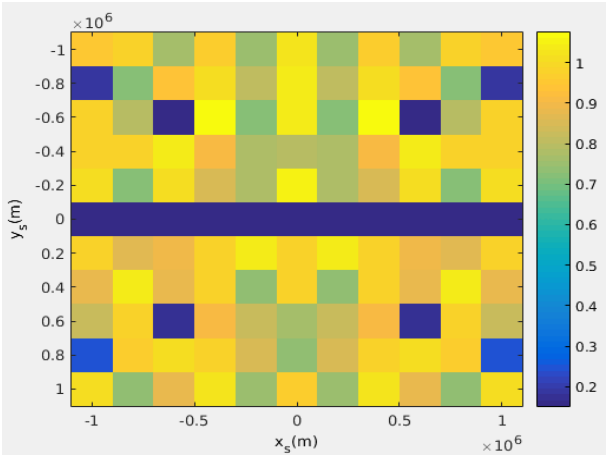

Figure 5.19: Radiometric sensitivity as function of source's position in the microwave regime

5.3.2.7 Discussion

This first reconstruction methodology using a frequency translation approach allows a simple numerical implementation and derivation of the functional parameters of the FouCoIm concept. However, the reconstruction of temperatures using the frequency translation approach is only applicable in the case of a set of few source points, otherwise the chosen sampling rate wouldn't be sufficient due to the highly oscillating phase factor in (5.71).

Besides, this approach presents the inconvenient of the need of an access to sources' frequencies ω' so as the filtering in (5.67) can be performed. This requirement is unlikely to be fulfilled in the real case

since one only controls the frequencies of the filtered version of the electric fields ω. Though, as shown in chapter 4, ω' are related to ω by means of the source's position-dependent Doppler shift induced by the satellite's displacement. This is equivalent to say that the frequency bandwidth B of ω equals the frequency bandwidth B' of ω' augmented by twice the Doppler shift.

In brief, the application of such a procedure cannot be applied in the generalized real case of the reconstruction of maps of temperatures, but was mainly intended to derive a first overview of the reconstruction results.

5.3.3 Numerical simulations using the quadrature of the HOI kernel

5.3.3.1 Introduction

Here, we give an overview of the under-implementation reconstruction algorithm that includes the numerical quadrature of the HOI kernel linking the correlation values to the brightness temperatures. This reconstruction approach is mainly based on establishing a discretized form of the correlation function by integrating the quadrature of the HOI kernel described in the first section of this chapter.

The quadrature of the HOI kernel allows to bypass the required high computational effort in the inversion of the correlation function equation when dealing with signals in the microwave regime. As a matter of fact, starting from the established expression of the correlation function (equation (4.46)), the brightness temperatures can be easily reconstructed in all frequency regimes without the need of the high sampling rate dictated by the considered range of frequencies thanks to the quadrature of the HOI kernel, which incorporates the main oscillating phase factors of the correlation function.

5.3.3.2 Correlation function

In chapter 4, we derived the following expression of the correlation function obtained by means of the FouCoIm concept

$$C(\omega_1,\omega_2) = k\int dy' I(y',\omega_1,\omega_2)\tilde{T}(y',\omega_1,\omega_2), \tag{5.85}$$

where

$$I(y',\omega_1,\omega_2) = \int dx' \frac{e^{i(\alpha x'+\beta/\sqrt{1+x'^2})}}{1+x'^2}, \tag{5.86}$$

and

$$\tilde{T}(y',\omega_1,\omega_2) = \frac{1}{\sqrt{2\pi}v_s}\int dx e^{i\kappa_x x}T(y',x), \tag{5.87}$$

with k a constant, $\alpha = \kappa_x \Delta r/\sqrt{y'^2+h^2}$, $\beta = \tilde{k}_c y'/\sqrt{y'^2+h^2}$, $\kappa_x = (\omega_2-\omega_1)/v_s$, $\tilde{k}_c = \Delta r(\omega_1+\omega_2)/(2c)$, and $x = v_s t$.
Equation (5.85) can be rearranged in a more convenient form,

$$C(\omega_1,\omega_2) = \frac{k}{\sqrt{2\pi}v_s}\int dy' \int dx I(y',\omega_1,\omega_2)e^{i\kappa_x x}T(y',x). \tag{5.88}$$

One should not confuse the variable x', that refers to the integration variable in the definition of the HOI kernel, and the variable x which defines the Fourier-transform variable in (5.87).
Equation (5.88) suggests that using the quadrature of the HOI kernel, the correlation function is linked to the brightness temperatures through a double integration over y' and x. All things considered, the reconstruction of brightness temperatures from the correlation values boils down to a 2D inversion problem.

5.3.3.3 Correlation matrix

If we consider that both frequencies ω_1, ω_2 are similarly sampled within the bandwidth B using N_ω frequency samples $\{\omega_i\}_{i\in\{1\dots N_\omega\}}$. Equation (5.88) is numerically implemented by discretizing the integrals over y' and x,

$$C(\omega_i,\omega_j) \simeq \frac{k}{\sqrt{2\pi}v_s}\sum_{y'}\sum_{x} I(y',\omega_i,\omega_j)e^{i\kappa_{x_{ij}}x}T(y',x) \equiv \sum_{y'}\sum_{x} K(y',x,\omega_i,\omega_j)T(y',x), \tag{5.89}$$

where $\kappa_{x_{ij}} = (\omega_j-\omega_i)/v_s$ and $K(y',x,\omega_i,\omega_j) \equiv (k/\sqrt{2\pi}v_s)I(y',\omega_i,\omega_j)e^{i\kappa_{x_{ij}}x}$.
Letting $N_{y'}$ and N_x samples of y' and x, for each frequency couple (ω_1,ω_2) the correlation value $C(\omega_i,\omega_j)$ is obtained through the following matrix equation

$$C(\omega_i,\omega_j) \simeq \mathcal{K}(\omega_i,\omega_j) \times {}^t\mathcal{T}, \tag{5.90}$$

where

$$\mathcal{K}(\omega_i,\omega_j) = \begin{pmatrix} K(y'_1,x_1,\omega_i,\omega_j) & \dots & K(y'_1,x_{N_x},\omega_i,\omega_j) & \dots K(y'_{N_{y'}},x_{N_x},\omega_i,\omega_j)\end{pmatrix},$$

and

$$\mathcal{T} = \begin{pmatrix} T(y'_1,x_1) & \dots & T(y'_1,x_{N_x}) & T(y'_{N_{y'}},x_{N_x})\end{pmatrix}.$$

With all of this, we define a correlation matrix equation for the whole set of frequencies as follows

$$\mathcal{C} \simeq \mathcal{K} \times {}^t\mathcal{T}, \tag{5.91}$$

where $\mathcal{K}$ refers to the global kernel matrix defined as

$$\mathcal{K} = \begin{pmatrix} K(y'_1,x_1,\omega_1,\omega_1) & \dots & K(y'_{N_{y'}},x_{N_x},\omega_1,\omega_1) \\ \vdots & & \vdots \\ K(y'_1,x_1,\omega_1,\omega_{N_\omega}) & \dots & K(y'_{N_{y'}},x_{N_x},\omega_1,\omega_{N_\omega}) \\ \vdots & & \vdots \\ K(y'_1,x_1,\omega_{N_\omega},\omega_{N_\omega}) & \dots & K(y'_{N_{y'}},x_{N_x},\omega_{N_\omega},\omega_{N_\omega})\end{pmatrix} \equiv \begin{pmatrix} K_{11}(y'_1,x_1) & \dots & K_{11}(y'_{N_{y'}},x_{N_x}) \\ \vdots & & \vdots \\ K_{1N_\omega}(y'_1,x_1) & \dots & K_{1N_\omega}(y'_{N_{y'}},x_{N_x}) \\ \vdots & & \vdots \\ K_{N_\omega N_\omega}(y'_1,x_1) & \dots & K_{N_\omega N_\omega}(y'_{N_{y'}},x_{N_x})\end{pmatrix},$$

and

$${\mathcal{C}} = {}^t\begin{pmatrix} C(\omega_1,\omega_1) & \dots & C(\omega_1,\omega_{N_\omega}) & \dots & C(\omega_{N_\omega},\omega_{N_\omega})\end{pmatrix} \equiv {}^t\begin{pmatrix} C_{11} & \dots & C_{1,N_\omega} & \dots & C_{N_\omega,N_\omega}\end{pmatrix}.$$

5.3.3.4 Highly oscillatory reconstruction procedure

Based on equation (5.91), the reconstruction procedure of the brightness temperatures boils down to a matrix inversion problem. More precisely, the strategy is the following (figure 5.20):

- determine the quadrature regime of the HOI using a comparison matrix of the values of α and β for each frequency couple with respect to the regimes defined in the first section,
- compute the values of the HOI kernel for each frequency couple based on the comparison matrix,
- construct the global kernel matrix for the whole set of frequency couples,
- construct the correlation matrix for the whole set of frequency couples, and finally

- reconstruct the T_B vector, defined for all y' and x samples, as follows

$$^t\mathcal{T} \simeq \mathcal{K}^\dagger \times \mathcal{C}, \tag{5.92}$$

where $\mathcal{K}^\dagger$ refers to the Moore-Penrose pseudo-inverse of the kernel matrix $\mathcal{K}$.

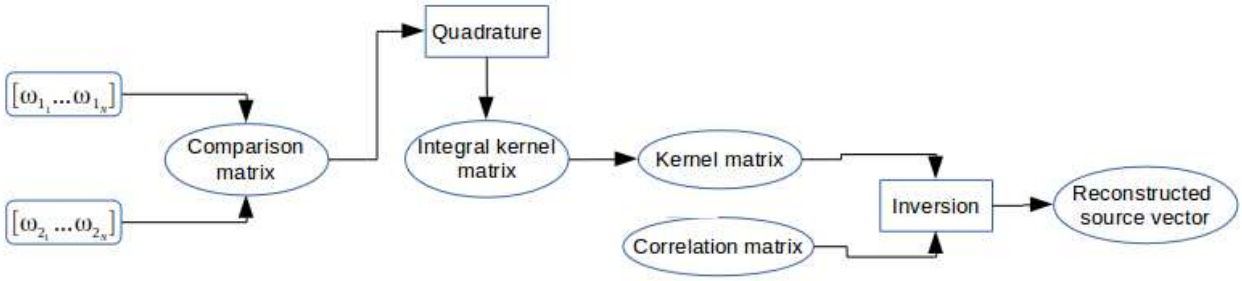

Figure 5.20: Reconstruction algorithm using the quadrature of the HOI kernel

5.3.3.5 Simulations results

In what follows, we present some results of the reconstruction procedure using the quadrature of the HOI kernel described earlier. We focus nevertheless the numerical derivation to the regime where $\beta \gg \alpha$ whose contributions to the integral kernel are predominant compared to other regimes.
Now, if we plot the corresponding matrices to

$$\alpha = (\omega_2 - \omega_1)\sqrt{y_s^2 + h^2}/v_s \quad \text{and} \quad \beta = (\omega_1 + \omega_2)(\Delta r/c)(y_s/\sqrt{y_s^2 + h^2}),$$

using the standard parameters of SMOS and a source point located at (x_s, y_s), the regime $\beta \gg \alpha$ is reached in the neighborhood of the matrices' diagonal (figure 5.21).

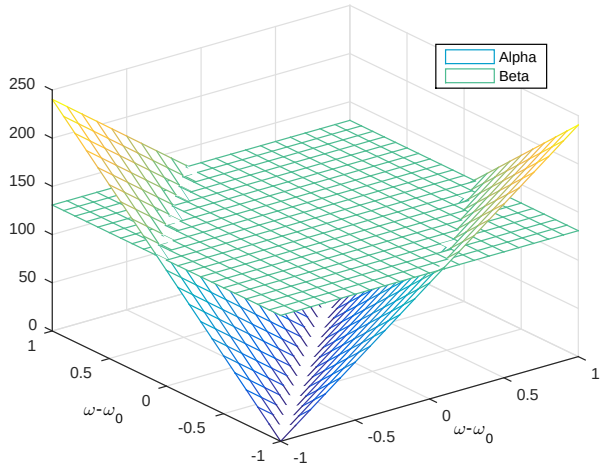

Figure 5.21: α and β matrices for all frequency couples

Based on this, we construct the kernel matrix using the quadrature of the HOI kernel in the regime $\beta \gg \alpha$ (see the first section of this chapter) whose diagonal is compared with the kernel matrix diagonal

derived using the frequency translation approach. Figure 5.22 shows that, after a rescaling of the amplitude, the quadrature of the HOI kernel in the regime of interest yields a quite good approximation and hence an equivalent reconstruction accuracy.

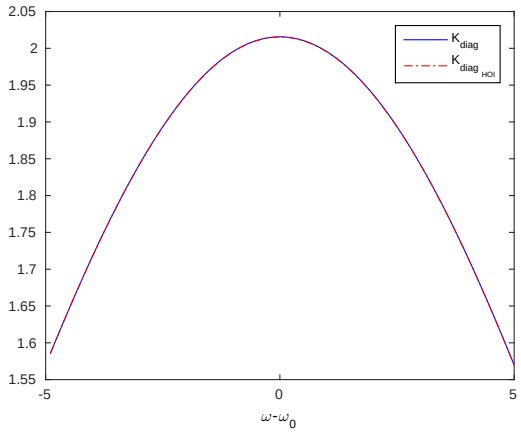

Figure 5.22: Exact overlapping of the diagonals of the produced kernel matrices using the frequency translating and the HOI quadrature approaches

5.3.3.6 Discussion

So far, the employment of the quadrature of the HOI kernel in the reconstruction of temperatures in the context of the FouCoIm concept was successfully performed within the predominant frequency regime $\beta \gg \alpha$.

At the time of the writing of this report, the related numerical processor to the HOI quadrature reconstruction approach is under final verifications and will be the subject of a publication.

5.3.4 Numerical simulations in the ultra-sound regime

5.3.4.1 Introduction

In the present section, we study the alternative idea of performing the numerical simulations using frequencies in the ultra-sound regime. This is the result of the noticed high complexity of calculations when dealing with emissions in the microwave regime in addition to the validity of the Maxwell's theory even at the ultra-sound frequency regime. One hopes by means of this approach to retrieve the same behavior of correlations even though at two different frequency regimes and then indirectly derive the different functional quantities, namely the radiometric and geometric resolutions, by deduction from the numerical results in the simple ultra-sound case.

This idea originally rose from the proposal of an experimental validation of the FouCoIm concept in the ultra-sound domain. The passage to the ultra-sound domain allows the reduction of the problem's dimensions for a simpler technical implementation. Based on the obtained numerical results in the ultra-sound regime (even we will be considering frequencies lower than in the ultra-sound band), one should verify if the same properties of the FouCoIm are retrieved even at a such lower frequencies. This should furthermore informs about the relevance of the experimental validation of the FouCoIm concept in the ultra-sound regime.

5.3.4.2 Model

So as to retrieve the same behavior of the correlation function in both the ultra-sound and microwave domain, the functional parameters must be translated in a linear fashion in such a way to keep the same order of ratios between both domains, namely $h/\Delta r$, ω_0/B and c/v_s, to ensure the validity of all considered approximations (table 5.2).

Table 5.2: Standard parameters

Variable	Microwave regime	Ultra-sound regime
Wave speed c (m/s)	3.10^8	343.2
Instrument speed v_s (m/s)	$7{,}5.10^3$	2
Central frequency ω_0 (Hz)	$1.4135.10^9$	5.10^2
Instrument height h (m)	750.10^3	10^2
Spacing between antennas Δr (m)	50	20
Frequency bandwidth B (Hz)	20.10^6	1

First, the maximal Doppler shift possibly induced by the platform motion expressed as

$$\mathrm{Dp}_{max} = \frac{v_s}{c}\frac{h}{\sqrt{2h^2 + (\Delta r/2)^2}}\omega_0, \tag{5.93}$$

is of the order of 25 KHz and 2 Hz respectively in both frequency regimes. This value represents the frequency shift in sources' emissions when traveling from the surface to the platform's reference. Hence, when computing the temporal components of the electric fields as observed by the antennas, one must take account of the Doppler effect. Since the Doppler shift can be either positive or negative depending the respective positions of the emitting source and the platform, the considered frequency band B must be augmented by twice the maximal Doppler shift ($B' = B + 2\mathrm{Dp}_{max} = 3$ Hz in the ultra-sound regime). Next, we set an integration time τ of 10 s and a sampling frequency $F_s = 1.5.10^3$ Hz $> 2(\omega_0 + B'/2)$ respecting the Nyquist-Shannon sampling criterion.

In what follows, we assimilate the amplitude of an ultra-sound signal to a temperature and will be dealing with reconstructed temperatures.

5.3.4.3 Direct reconstruction procedure

Similarly to the frequency translation approach, the reconstruction procedure in the ultra-sound regime is built in the same manner without the need of a translation to lower frequencies. Based on the expression (4.30) of the correlation function, the (ω_1, ω_2)-dependent coefficient of the correlation matrix,

by considering N_s source points, is expressed as follows

$$\begin{aligned}\mathcal{C}(\omega_1,\omega_2) &\simeq \mathcal{K}(\omega_1,\omega_2)\times {}^t\mathcal{T}\\ &= \Big(\mathcal{K}\big((\omega_1,\omega_2);\mathbf{r}''_1\big),\ldots,\mathcal{K}\big((\omega_1,\omega_2);\mathbf{r}''_{N_s}\big)\Big)\times {}^t\Big(\mathcal{T}(\mathbf{r}''_1),\ldots,\mathcal{T}(\mathbf{r}''_{N_s})\Big),\end{aligned} \tag{5.94}$$

with $\mathcal{T}(\mathbf{r}''_1)\simeq\left\langle|\tilde{\mathbf{j}}^t(\mathbf{r}'',\omega_0)|^2\right\rangle/K_3$ (equation (4.29) with the assumption that the temperature depends only weakly on frequency) and where the (ω_1,ω_2)-dependent coefficient of the kernel matrix $\mathcal{K}$ at source's position $\mathbf{r}''_i$ reads

$$\mathcal{K}\big((\omega_1,\omega_2);\mathbf{r}''_i\big)\simeq K_2\omega_0^2\int dt_1\int dt_2\int d\omega'\int\frac{e^{-i\frac{\omega'}{c}(|R_1(t_1)|-|R_2(t_2)|)}}{|R_1(t_1)||R_2(t_2)|}e^{i\omega'(t_1-t_2)}e^{-i(\omega_1t_1-\omega_2t_2)}, \tag{5.95}$$

with $|R_2(t_2)|=|\mathbf{r}_2+\mathbf{v}_st_2-\mathbf{r}''_i|$ and $|R_1(t_1)|=|\mathbf{r}_1+\mathbf{v}_st_1-\mathbf{r}''_i|$.
The kernel matrix is afterwards constructed column-by-column for each source's position $\mathbf{r}''$. Each column contains the whole set of frequency couples (ω_1,ω_2). Based on this construction, one is left with the following global correlation matrix equation

$$\mathcal{C}\simeq\mathcal{K}\times{}^t\mathcal{T}, \tag{5.96}$$

which, when inverted by means of a multiplication with the Moore-Penrose pseudo-inverse of the kernel matrix $\mathcal{K}^\dagger$, allows the reconstruction of the vector of temperatures over the set of spatial positions.

5.3.4.4 Inversion in the case of a single source point

Using the previously described reconstruction procedure, we invert the correlation function in the case of a single source point located at different positions all over the 2D plane $[-500m,500m]$ in both directions and using the functional parameters in the ultra-sound frequency regime (table 5.2).
In figure 5.23 are plotted the outcome and the accuracy of the reconstruction procedure in the ultra-sound regime of a single source point of temperature $T_0=300$ K iteratively located at different spatial locations over a 2D-[-500m,500m] grid.

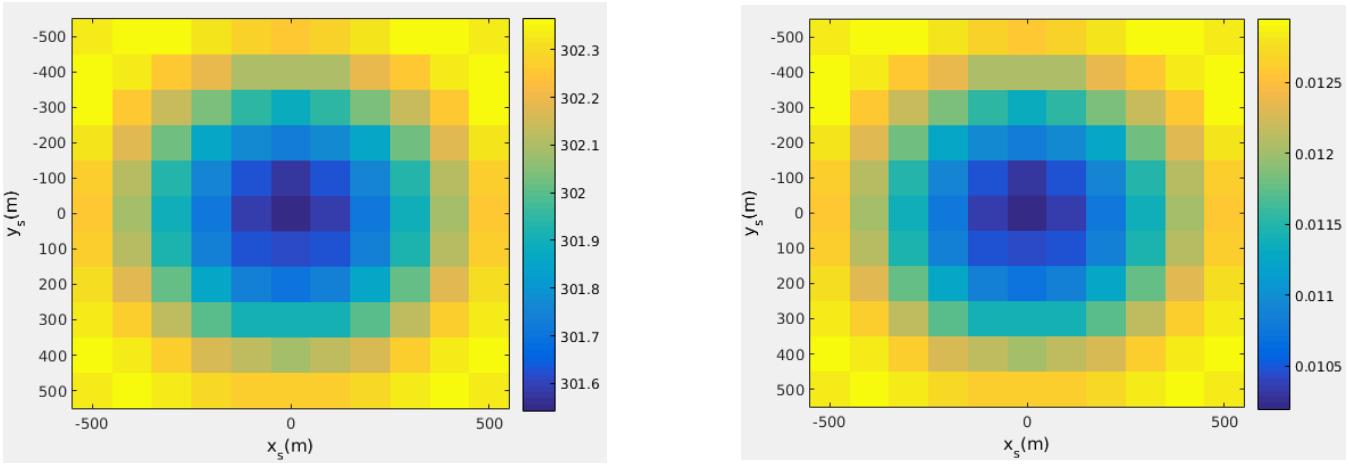

Figure 5.23: (left) Reconstructed temperatures and (right) reconstruction errors ($\epsilon(x_s,y_s)=|T_{rec}(x_s,y_s)-T_0|/T_0$) as function of source's position in the ultra-sound regime

The reconstruction error seems to linearly increase when moving away from the nadir. This behavior wasn't noticed in the microwave regime and may probably be the result of the consideration of the correct sampling rates in the ultra-sound case.

5.3.4.5 Reconstructed source function

We employ hereafter the direct numerical reconstruction procedure termed with the reconstruction over a spatial profile to derive the reconstructed source function (or the point-spread function (PSF)) of a single source point located at $(0, y_s = 100 \text{ m})$ in the ultra-sound domain using the quoted parameters in table 5.2.

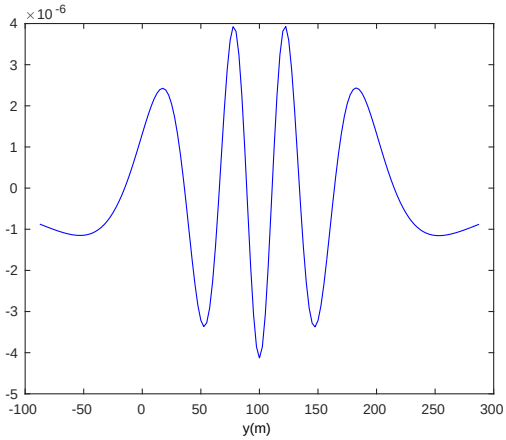

Figure 5.24: Reconstructed source function of a single source point in the ultra-sound regime

As depicted in the theoretical derivation, figure 5.24 plots the particular form of the reconstructed source function by means of the FouCoIm approach as a cosine function weighted by a Gaussian centered at the position of the point source.

5.3.4.6 Geometric resolution

We numerically derive the value of the geometric resolution in the ultra-sound domain with the perspective of demonstrating the theoretical expression derived in chapter 4. To do so, we apply the same described methodology in chapter 4 for the derivation of the value of the geometric resolution, namely the determination of the minimal shift in the source position making a peak of the reconstructed source function coincide with the next trough.
Shown in figure 5.25 the superposition of the reconstructed source functions for two different source's positions $y_s = 77.5$ m and $y_s = 100$ m.

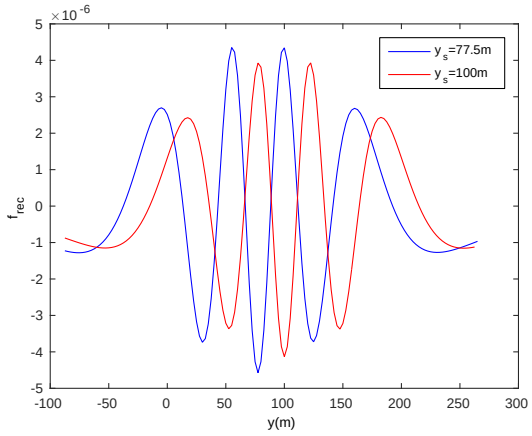

Figure 5.25: Reconstructed source functions for $y_s = 77.5$ m and $y_s = 100$ m in the ultra-sound regime

On the other hand, the theoretical expression of the geometric resolution in the cross-track (5.83) gives a similar value of the order of 22 m for a source position $y_s = 100$ m. We clearly see that shifting the source position by R_y makes each peak of the reconstructed source function move to the next trough. This goes in the sense of strengthening the choice of using the ultra-sound frequencies as an experimental way of validation of the FouCoIm concept's outcome.

5.3.4.7 Radiometric sensitivity (RS)

The radiometric sensitivity is expressed for ideal antennas (by solely including the thermal nature of the radiated fields of sources at the Earth's surface) as follows [21]

$$\text{SNR} = \frac{\sqrt{< T_{rec}^{S^2} > - < T_{rec}^{S} >^2}}{< T_{rec}^{S} >} = \frac{\sigma(T_{rec}^{S})}{< T_{rec}^{S} >}, \tag{5.97}$$

where $< ... >$ is the average over N_r different realizations of the stochastic process and T_{rec}^{S} the reconstructed source's temperature at each realization.
Following simulations concern the evaluation of the variation of the RS for a changing source position in the ultra-sound domain. We apply the direct reconstruction procedure for a single source of temperature $T_s = 25°\text{C}$ $(= 273.15 + 25$ K) whose position is iteratively changing over a 2D spatial grid. A linear dependence of the RS (computed using (5.97)) on the source's position is also highlighted by figure 5.26.

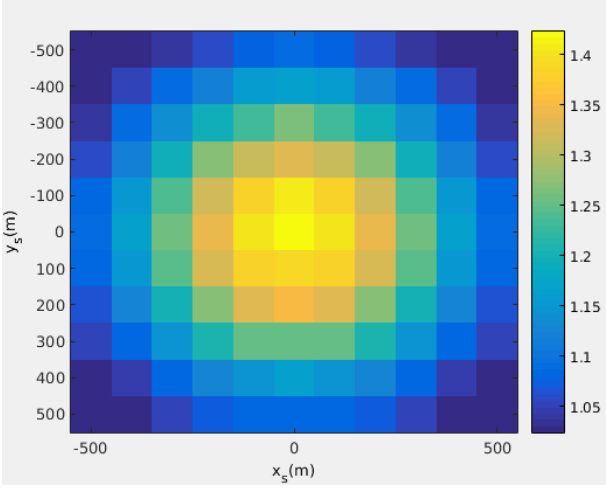

Figure 5.26: Radiometric sensitivity as function of source's position in the ultra-sound regime

A mean value of the radiometric sensitivity of the order of unity obtained from the numerical study of the FouCoIm concept in the ultra-sound regime depicts a degraded radiometric performance similarly to what has been noted in the microwave regime. This was, nonetheless, to be expected since a pair of antennas doesn't allow to acquire the minimal required flux for an acceptable detection of changes in temperature.

5.3.5 Discussion on the FDT assumption

One may wonder whether the requirement on having access to a set of N_r different realizations of the stochastic process of source's fluctuations (FDT hypothesis (equation (4.4))) is fulfilled in the practical case. This question is unfortunately to be answered to the negative. This owes to the correlation process of the FouCoIm concept that exploits the whole frequency information included in the electric field spectrums obtained by Fourier-transforming the time-dependent electric fields which, in turn, dispose of a unique vector of fluctuations per satellite's passage.

Two different methods were proposed to bypass this difficulty but weren't deeply studied and detailed within the framework of this thesis. One proposes to use a pseudo-random permutation (PRP) method on the vector of each electric field's spectrum as much time as needed to derive uncorrelated realizations of the same vector. Such a method clearly doesn't create additional information about sources but simply generates, in a controlled way, a set of uncorrelated vectors which, when averaged, allow to go through the FDT assumption which is paramount in our theoretical derivation. This first method was briefly verified in the case of the reconstruction of the temperature of a single source point, but needs to be validated in a real case using broad sources.

Another way could be to subdivide the spectrum vectors into a set of sub-vectors that are by definition uncorrelated owing to the random Gaussianity of the global vectors. The FDT assumption is next fulfilled by averaging over the set of sub-vectors.

That being said, the practical implementation of the FouCoIm concept for a spaceborne use is strictly dependent on the ability of fulfilling the FDT assumption. Based on this, the validation of previous methods is crucial.

These methods are under investigation at the time of the writing of this report and will be subject to further verifications in the future.

5.3.6 Conclusions

Three different numerical approaches have been considered in the numerical study of the FouCoIm concept. These approaches introduce three different ways to bypass the need of a high sampling rate for the numerical expression of the physical quantities of the problem, namely the electric field spectrums observed in the L-band by a pair of antennas.

A first frequency translation approach introduces a tricky way for the numerical implementation of the expression of the electric fields' spectrums using a lower frequency band in the simple case of the presence of only a single source point at the Earth's surface. Next, using the quadrature of the HOI kernel figuring in the expression of the correlation function, a direct numerical implementation in the L-band is therefore achievable and thus allows a general reconstruction of temperatures in all frequency regimes. Finally, a simpler, but cautious, implementation in the ultra-sound regime has allowed to verify the retrieval of the same properties of the correlation function even in lower frequencies. This final approach will serve as a numerical basis against which the idea of an experimental validation of the FouCoIm concept should be confronted.

Based on our numerical achievements, we were able to state on both the geometric and radiometric performances of the FouCoIm concept. The best optimistic achievable spatial resolution of the FouCoIm concept consisting of a pair of antennas separated by a distance Δr flying on board of a satellite at a height h is of the order of $hc/(\Delta r \omega_0)$ both in the cross- and along-track directions. This optimally yields sub-kilometric resolutions in the standard case of SMOS and using a 100-m separated pair of antennas.

For what concerns the radiometric sensitivity, the simple use of a pair of antennas is far from satisfactory and an in-depth study is needed to answer the question of whether the radiometric performance of this concept can be enhanced in the case of the use of an array of antennas. This should probably increase the captured flux by the observer and respectively ameliorate its sensitivity, but the question whether this approach yields a proportional improvement as function of the number of the included antennas in the array can only be answered through a detailed theoretical study. A study of the degree of coherence of the captured signals by each antenna is particularly to be conducted in the future.

The numerical simulations in the ultra-sound domain allowed the derivation of the functional parameters of the FouCoIm concept. Due to lack of time, these results couldn't be experimentally verified as initially programmed. The experimental step is of crucial importance in the validation of the FouCoIm concept and therefore need to be implemented in the future.

Bibliography

[1] Y. Monjid, D. Braun, B. rougé, and Y. H. Kerr, "Numerical quadrature of a highly oscillatory integral kernel," *in preparation*.

[2] C. S. Ruf, C. T. Swift, A. B. Tanner, and D. M. Le Vine, "Interferometric synthetic aperture microwave radiometry for the remote sensing of the Earth," *IEEE Trans. Geosci. Remote Sensing*, vol. 26, pp. 597-611, Sept. 1988.

[3] A. Deano and D. Huybrechs, "Complex Gaussian quadrature of oscillatory integrals," *Numerische Mathematik*, 112 (2009), pp. 197-219.

[4] A. Iserles and S. P. Nørsett, "Quadrature methods for multivariate highly oscillatory integrals using derivatives," *Math. Comp.*, 75 (2006), pp. 1233-1258.

[5] D. Levin, "Fast integration of rapidly oscillatory functions," *J. Comput. Appl. Math.*, 67 (1996), pp. 95-101.

[6] S. Olver, "Moment-free numerical integration of highly oscillatory functions," *IMA J. of Numer. Anal.*, 26 (2006), pp. 213-227.

[7] I. Corbella, N. Duffo, M. Vall-llossera, and A. Camps, "The visibility function in interferometric aperture synthesis radiometry," *IEEE Transaction on Geoscience and Remote Sensing*, vol. 42, No. 8, pp. 1677-1682, ISSN: 0278-0062.

[8] F. W. J. Olver, "Asymptotics and Special Functions," *Academic Press*, New York, 1974.

[9] A. Iserles and S. P. Nørsett, "Efficient quadrature of highly oscillatory integrals using derivatives," *Proc. Roy. Soc. A.*, 461 (2005), pp. 1383-1399.

[10] Andreas Asheim, "Numerical Methods for Highly Oscillatory Problems," *Doctoral thesis at NTNU*, Trondheim, May 2010.

[11] D. Huybrechs and S. Olver, "Highly oscillatory quadrature," *Isaac Newton Institute for Mathematical Sciences*.

[12] G. Jeffery and L. N. G. Filon, *Obituary Notices of Fellows of the Royal Society*, 2(7), 500-509.

[13] Y. L. Luke, "On the computation of oscillatory integrals," *Proc. Cambridge Phil. Soc.*, 50, 269-277.

[14] Sheehan Olver, "Numerical Approximation of Highly Oscillatory Integrals," *Doctoral thesis of the University of Cambridge*, June 14, 2008.

[15] D. Levin, "Procedure for computing one- and two-dimensional integrals of functions with rapid irregular oscillations," *Math. Comp.*, 38(158), 531-538.

[16] Lingli WANG and John J. QU. "Satellite remote sensing applications for surface soil moisture monitoring: A review". *Front. Earth Sci.* China 2009, 3(2):237-247.

[17] C.J. Koblinsky, P. Hildebrand, Y. Chao, A. deCharon, W. Edelstein, G. Lagerloef, D. LeVine, F. Pellerano, Y. Rahmat-Samii, C. Ruf, F. Wentz, W. Wilson, and S. Yueh. "SEA SURFACE SALINITY FROM SPACE: SCIENCE GOALS AND MEASUREMENT APPROACH". *Radio Sci.*, vol. 38, p. 8064, 2003.

[18] K. S. Rao, G. Chandra and P. V. N. Rao, "The relationship between brightness temperature and soil moisture Selection of frequency range for microwave remote sensing". *International Journal of Remote Sensing*, vol. 8, issue 10, p. 1531-1545, 1987.

[19] E. Anterrieu and A. Khazaal, "Regularized image reconstruction for the SMOS space mission". *Journal of Physics: Conference Series 135*, (2008) 012008.

[20] D. Braun, Y. Monjid, B. Rougé, and Y. Kerr, "Fourier-Correlation Imaging," *to be submitted soon.*

[21] D. M. Le Vine, "The Sensitivity of Synthetic Aperture Radiometers for Remote Sensing Applications From Space," *NASA Technical Memorandum 1C0741*, December, 1989.

Conclusions & Perspectives

Assurer la continuité en provision en données d'observation de la terre, si ce n'est pouvoir proposer des produits encore plus optimisés, sont là les objectifs moteurs à l'origine de la course vers le développement de nouveaux concepts d'observation de la terre de plus en plus novateurs poussant les technologies actuelles à leurs limites. S'ajoute à cela le besoin sans précédent d'une parfaite compréhension des phénomènes climatiques modulant la vie humaine sur terre.

L'observation de la terre depuis l'espace a connu un grand essor au sein de la communauté scientifique durant les dernières décennies. Ceci est dû essentiellement à la capacité des missions spatiales à produire une information à la fois globale, fréquente et récurrente sur les paramètres géophysiques de la terre, et à l'applicabilité des produits d'observation de la terre à un large spectre d'applications scientifiques.

Du fait de ce grand essor, de nouvelles applications scientifiques de plus en plus exigeantes en produits d'observation de la terre continuent de voir le jour engendrant ainsi un besoin continuel. En outre, les missions actuelles semblent atteindre leurs limites en terme de la résolution spatiale de leurs produits quand elles sont confrontées à des applications hydrologiques à l'échelle locale où des résolutions kilométriques sont exigées. Tout cela combiné au fait que la plupart des missions actuelles ont largement dépassé leurs durées de vie estimées créé un fort besoin en une nouvelle génération de missions capables à la fois d'assurer la provision en produits d'observation de la terre et de proposer des mesures de meilleure qualité.

Dans le cadre des travaux de cette thèse, un nouveau concept a été proposé comme une nouvelle perspective à l'observation de la terre depuis l'espace. Ce concept, basé sur une nouvelle méthodologie interférométrique, a fait l'objet d'une étude détaillée que ce soit du point de vue analytique ou numérique. En s'inspirant du concept SMOS employant une interférométrie purement spatiale, la nouvelle méthode a opté pour une interférométrie spatio-temporelle par l'intégration de la variable temps dans le traitement.

En partant des premiers principes en électromagnétisme, le premier volet des travaux de thèse a permis la généralisation du plus important théorème en synthèse d'ouverture et la dérivation théorique des différents paramètres fonctionnels d'intérêt par la mise en évidence d'une nouvelle mesure jusqu'à lors jamais exploitée. Un deuxième volet numérique a servi d'une base de validation et de vérification des résultats théoriques et a permis de pousser l'étude du concept encore plus loin.

La nouvelle méthodologie interférométrique a été testée dans le cas simple d'une paire d'antennes séparées d'une d'une centaine de mètres à bord d'un satellite en orbite basse observant une source ponctuelle à la surface de la terre. Il en a découlé une forme complexe de la *fonction d'étalement du*

point induisant par optimisation une résolution spatiale kilométrique dans les deux directions. La sensibilité radiométrique, quant à elle, reste à ce jour une question ouverte et on a été incapable durant ces travaux de thèse de statuer analytiquement sur la performance radiométrique d'un tel concept mais une évaluation numérique a permis des indications partielles. Ceci ouvre toutefois le champ à deux nombreuses possibilités d'amélioration et d'optimisation, citant par exemple l'utilisation de réseaux d'antennes ou d'antennes plus directives.

Un autre point qui a été partialement traité lors des ces travaux de thèse concerne l'une des hypothèses fondamentales du concept de corrélation dans l'espace fréquentiel, à savoir la nécessité d'avoir à chaque instant accès à plusieurs réalisations décorrélées des vecteurs fluctuations des sources à la surface de la terre (l'hypothèse FDT (equation (4.4))). Cette hypothèse est réduite dans le cas temporel par ergodicité à un simple échantillonnage temporel, alors que dans le cas fréquentiel l'analyse est plus complexe du fait de la considération totale de l'information temporelle dans le calcul des transformées de Fourier. La capacité à vérifier cette hypothèse a un impact directe sur la réalisation pratique en spatial du concept de corrélation dans l'espace fréquentiel.

Une première méthode consistant en la subdivision des spectres des signaux en plusieurs bandes fines (qui sont à priori décorrélées vu le caractère stochastique des signaux) a été proposée pour pallier au manque d'information et n'a malheureusement pas été finalisée par manque de temps. Grâce à cette méthode, chaque signal correspondant à une sous-bande est considéré comme quasi-totalement indépendant, ainsi en inter-corrélant les différentes sous-bandes entres elles, l'hypothèse peut être vérifiée. Cette dernière a été numériquement vérifiée par la reconstruction d'un seul point source mais reste toutefois à être validée sur des cas plus réalistes de sources étendues.

Une deuxième méthode encore plus originale a été proposé dans cette perspective. Celle-ci repose sur l'utilisation de permutations pseudo-aléatoires (PRP: pseudo-random permutation) afin de générer à partir d'une seule réalisation du vecteur spectre du champ électrique plusieurs vecteurs totalement décorrélés. L'avantage de la méthode PRP est sa capacité à générer d'une manière contrôlée des réalisations décorrélées du même vecteur et ainsi permettre de passer à travers l'hypothèse FDT. Cette méthode a été rapidement testée dans le cas de la reconstruction d'un point source, mais reste à être validée sur un cas réaliste de source étendue.

Une validation expérimentale du concept de corrélation dans l'espace fréquentiel a été prévue dans le cadre des travaux de cette thèse mais, par manque de temps, elle s'est vue réduite à uniquement une validation numérique, qui reste à être consolidée par des études plus détaillées du point de vue de la sensibilité radiométrique. La validation expérimentale représente une étape essentielle dans la démonstration de la faisabilité d'un tel concept sortant de l'ordinaire pour l'observation de la terre depuis l'espace. Similairement au cas numérique, il est proposé d'implémenter un concept expérimental miniature permettant de représenter notre concept réel d'étude et d'en vérifier la pertinence, et pour y parvenir on a opté pour l'utilisation des signaux en ultra-son au lieu des mirco-ondes. Par ce biais, il est possible de réduire d'une manière intéressante les dimensions du problème pour une implémentation réaliste sans pour autant affecter la physique du problème.

Grâce à cette expérimentation, on souhaite avant tout démontrer la découverte au cœur du concept de corrélation dans l'espace de Fourier, à savoir l'existence d'une corrélation entre des fréquences légèrement différentes. Cette propriété nouvelle peut être expliquée physiquement par le fait que la paire d'antennes voient les fluctuations d'un point source à la surface de la terre à des fréquences différentes à cause d'un effet Doppler différent au niveau de chaque antenne. La différence exploitable entre les fréquences est très faible (de l'ordre du hertz) ce qui induit un défit technologique considérable d'échantillonnage fréquentiel. En effet, il est nécessaire d'échantillonner à des ordres 10 fois au-delà du

critère de Shannon (2×1.4135 GHz) afin d'avoir une information exploitable.

Vu la complexité et la non maturité de la méthodologie d'interférométrie spatio-temporelle, un concept plus classique a été proposé durant les derniers mois de la thèse comme solution à implémentation rapide pour pallier au besoin dans le cas de la perte de la mission SMOS qui a, depuis un certain temps, dépassé sa durée de vie estimée. La nouvelle idée reprend les points forts de l'ancienne mission tout en proposant des solutions aux problèmes mis en évidence après le lancement. Elle apporte plus particulièrement une solution innovante à l'aliasing observé dans les images produites par SMOS, dû essentiellement à l'espacement insuffisant entre les antennes pour respecter le critère de Shannon, par l'intermédiaire d'une disposition géométrique astucieuse. Combiné à cela, le concept intègre plusieurs nouvelles techniques de traitement d'image, telle que la méthode de débruitage "Non-Local Means", dans le but d'améliorer le rapport signal-à-bruit et ainsi la performance radiométrique du concept.